Electrochemomechanics of lithium metal and alloy anodes for solid-state batteries



Jack Aspinall

Oriel College

University of Oxford

A thesis submitted for the degree of

Doctor of Philosophy

Trinity 2023

Preface

This thesis is the result of my work carried out in the Department of Materials, at the University of Oxford between October 2019 and August 2023, under the supervision of Professor Mauro Pasta.

No part of this thesis has been previously submitted for a degree at this or any other university. The work of other authors has been drawn upon and has been referenced and acknowledged in the text. A list of references is given at the end of the thesis.

Some of the work in the thesis has been reported in the following publications and at the following conferences:

Publications

Lithium indium alloys as a counter and reference electrode for solid-state batteries Jack Aspinall, Yvonne Chart, Hua Guo, Pranay Shrestha, Johannes Ihli, and Mauro Pasta (In preparation)

Lithium magnesium alloys: a framework for investigating lithium alloy anodes for solid-state batteries Jack Aspinall, Krishnakanth Sada, Hua Guo, Sudarshan Narayanan, Yvonne Chart, Ben Jagger, Souhardh Kotakadi, Emily Milan, Laurence Brassart, David Armstrong, and Mauro Pasta *Research Square*, 2023 (Pre-print available, in submission/review)

Elastic and Plastic Mechanical Properties of Lithium measured by nanoindentation Ed Darnbrough, Jack Aspinall, Mauro Pasta, David Armstrong *Materials Design* (Volume 233, September 2023, 112200) doi.org/10.1016/j.matdes.2023.112200

EBSD-coupled indentation: nanoscale mechanics of lithium metal Jack Aspinall, David Armstrong, Mauro Pasta *Materials Today Energy* (Volume 30, December 2022, 101183) doi.org/10.1016/j.mtener.2022.101183

On the Relative Importance of Li Bulk Diffusivity and Interface Morphology in Determining the Stripped Capacity of Metallic Anodes in Solid-State Batteries Marco Siniscalchi, Liu Junliang, Joshua S. Gibson, Stephen Turrell, Jack Aspinall, Robert Weatherup, Mauro Pasta, Susannah C. Speller, Chris R. M. Grovenor *ACS Energy Letters* (Volume 7, October 2022, 3593–3599) doi.org/10.1021/acsenergylett.2c01793

In situ and operando characterisation of Li metal–Solid electrolyte interfaces Sudarshan Narayanan, James S Gibson, Jack Aspinall, Robert Weatherup, Mauro Pasta *Current Opinion in Solid State and Materials Science* (Volume 26, Issue 2, April 2022, 100978) doi.org/10.1016/j.cossms.2021.100978

A red phosphorus-graphite composite as anode material for potassium-ion batteries Isaac Capone, Jack Aspinall, Hyeon Jeong Lee, Albert Xiao, Johannes Ihli, Mauro Pasta *Materials Today Energy* (Volume 21, September 2021, 100840) doi.org/10.1016/j.mtener.2021.100840

Electrochemo-Mechanical Properties of Red Phosphorus Anodes in Lithium, Sodium, and Potassium Ion Batteries Isaac Capone, Jack Aspinall, Ed Darnbrough, Ying Zhao, Tae-Ung Wi, Hyun-Wook Lee, Mauro Pasta *Matter* (Volume 3, Issue 6, December 2020, 2012–2028) doi.org/10.1016/j.matt.2020.09.017

Conferences

244th ECS Meeting 2023: Magnesium Alloys: A Framework for Investigating Lithium Alloy Anodes for Solid State Batteries - Oral Presentation

Faraday Institution Conference 2023: A Framework for Investigating Lithium Alloy Anodes for Solid State Batteries

Faraday Institution Early Career Researcher Conference: Mechanics of Lithium Metal at Nanoscale by EBSD Coupled Nanoindentation

MRS Fall Meeting 2022: Mechanics of Lithium Metal at Nanoscale by EBSD Coupled Nanoindentation - Oral Presentation

Nanobrüken 2022 Nanomechanical Testing Conference: Mechanics of lithium metal at nanoscale by in-situ EBSD coupled nanoindentation - Oral presentation

Acknowledgements

I would like to thank the following people, without whom I would not have been able to complete this research.

I'd like to thank the Faraday Institution for funding the project and providing a training programme that has broadened my battery expertise beyond the cell level. I'd also like to thank all the funding bodies, including the Henry Royce Institute, who have provided funding for the exceptional facilities and equipment at the Department of Materials, and Nissan Motor Co. Ltd. with whom I look forward to collaborating further.

I'm extremely grateful to the Pasta group, especially to my supervisor Prof. Mauro Pasta, whose insight and guidance steered me through the research and kept me on topic. A special thanks go to Yvonne Chart, Dr. Isaac Capone, Dr. Jack Fawdon, Dr. Krishnakanth Sada, Dr. Sudarshan Narayanan, Dr. Hua Guo, Emily Milan, Souhardh Kotakadi and Ben Jagger whose expertise helped take the experimental investigations to the next level. To all the members of the group, both past and present, thanks for making Rex Richards a lively, fun place to work.

I would also like to thank Prof. Dave Armstrong, Dr Ed Darnbrough, and the Oxford Micromechanics Group, who provided expertise and help with nanoindentation that were invaluable, and the group's members including Bradley Young, Pedr Charlesworth, Johann Perera, and Robert Scales who have become close and valued friends.

Thank you to my friends, of whom there are too many to list here, who have kept me sane and supported me throughout my studies. Hopefully, I'll be more fun now this thesis is written.

My biggest thanks go to my family. Both of my grandparents passed during the last four years. I hope Granddad would be proud of me "keeping up the good work", and that Mama is satisfied that I have (finally) finished studying. I hope the work never took priority over spending moments with them. Most importantly I want to thank my mum. I feel very fortunate, and her countless sacrifices over the two decades spent raising us are the reason that it is possible. Thank you.

And for my wife Harriet, thank you for your endless love, support, encouragement and understanding. I'm excited to meet our daughter in December, she has provided the best motivation to get this thesis finished.

Abstract

The fracture of ceramic solid electrolytes, driven by the plating of lithium within cracks, has been identified as one of the fundamental issues to successfully develop solid-state batteries. Understanding the mechanics of lithium at the nanoscale is therefore essential. In the first experimental chapter, the elastic and plastic properties of lithium are measured by nanoindentation within an electron microscope. Lithium metal samples are characterized by electron backscattered diffraction before and after indentation to understand the dependence of the mechanical properties on crystallographic orientation and determine the stiffness tensor components, moduli, and Poisson's ratio using a method first proposed by Vlassak and Nix. The measured stiffness tensor components are C_{11} = 13.3, C_{12} = 11.2, and C_{44} = 8.8 GPa. Hardness measurements show a clear size effect with hardness in excess of 100 MPa observed for indent depths below 300 nm, which could contribute toward observed lithium filament propagation.

Lithium alloys have the potential to overcome anode-side challenges in solid-state batteries. In the second experimental chapter, lithium-rich magnesium alloys are synthesised and characterised, quantifying the changes in mechanical properties, transport, and surface chemistry that impact electrochemical performance. Increases in hardness, stiffness, adhesion, and creep resistance are quantified by nanoindentation as a function of magnesium content. A decrease in diffusivity is quantified with ^{6}Li pulsed field gradient nuclear magnetic resonance spectroscopy and chronopotentiometry, and an increase in interfacial impedance due to the presence of magnesium is identified with electrochemical impedance spectroscopy which is correlated with x-ray photoelectron spectroscopy data. Throughout, changes in properties are linked to electrochemical performance. This work provides a framework to investigate other lithium alloy systems.

The performance limitations of lithium metal are holding back the development of solid-state cathodes and lithium-free anodes. In the final experimental chapter, indium-lithium alloys are explored as a combined counter and reference electrode for all-solid-state batteries. They enable high current densities without shorting, fast discharge capacity, and high cycle stability. The performance is attributable to very fast diffusion kinetics in the InLi intermetallic, D_{Li}^{298K}=5.8×10^{-7} cm^{2}s^{-1}. The indium metal phase is essentially ion-blocking, so the performance is tied

to the microstructure, which evolves during charge and discharge. A two-layer microstructure is proposed which offers good accessible capacity and good cycle life at high current densities.

Contents

1 Introduction **1**

1.1 Context for work 1

1.2 Lithium Batteries Background 3

1.2.1 Lithium Metal 5

1.2.2 Solid Electrolytes 6

1.2.3 Lithium alloys 10

1.3 Mechanical properties in solid-state batteries. 11

1.4 Outline of thesis 14

2 Method fundamentals **16**

2.1 Scanning electron microscopy 16

2.1.1 EBSD: Electron backscatter diffraction 17

2.2 Nanoindentation 18

2.3 Electrochemical testing 21

2.3.1 Cell Assembly 21

2.3.2 EIS: Electrochemical impedance spectroscopy 22

2.4 PFG-NMR: Pulsed-field gradient nuclear magnetic resonance spectroscopy 24

2.5 XPS: X-ray photoelectron spectroscopy 25

2.6 Other techniques 26

3 Elastic and plastic properties of lithium metal from EBSD coupled nanoindentation **27**

3.1 Introduction 28

3.2 Surface Preparation 29

3.2.1 Ion milling 29

3.2.2 Grind and polish 29

3.2.3 Microtome 30

3.3 Modelling of the lithium-electron interaction 33

3.4 EBSD of Lithium Metal 36

3.5 EBSD of other Alkali metals. 37

3.5.1 Potassium metal 37

3.5.2 Sodium metal . . . 38
3.6 Optimisation of indentation parameters . . . 39
3.6.1 Frequency of continuous stiffness measurement. . . . 40
3.6.2 Characterising indentation tip . . . 40
3.6.3 Machine compliance calibration . . . 43
3.6.4 Pile up correction . . . 44
3.7 Elastic Mechanical Response . . . 44
3.7.1 Variation in indentation modulus with crystal orientation . . 46
3.7.2 Euler Angles . . . 47
3.7.3 Fitting to modulus data . . . 48
3.8 Plastic Mechanical Response . . . 51
3.9 Adhesion . . . 54
3.10 Impact of measured nanoscale hardness. . . . 55
3.11 Conclusions . . . 58

4 Developing an alloy anode investigation framework using the lithium magnesium alloy system. 62
4.1 Introduction . . . 63
4.2 Synthesis of magnesium alloy anodes. . . . 65
4.3 Characterisation of magnesium alloy anodes. . . . 67
4.3.1 SEM Imaging . . . 67
4.3.2 Electron backscattered diffraction. . . . 67
4.3.3 X-ray diffraction. . . . 71
4.4 Mechanical properties of lithium magnesium alloys. . . . 72
4.4.1 Elastic anisotropy . . . 72
4.4.2 Plastic properties . . . 74
4.4.3 Adhesion . . . 76
4.4.4 Creep of lithium magnesium alloys . . . 77
4.4.5 Summary of lithium magnesium mechanics. . . . 85
4.5 Surface chemistry . . . 86
4.5.1 Open-circuit voltage . . . 86
4.5.2 Electrochemical Impedance Spectroscopy . . . 87
4.6 Diffusion . . . 94
4.6.1 PFG-NMR on ^{6}Li Alloys . . . 94
4.6.2 Diffusivity measured by time of flight secondary ion mass spectrometry (TOF-SIMS). . . . 97
4.7 Chronopotentiometry . . . 97
4.8 Cross-sectional imaging of stripped lithium magnesium alloy anodes. 104
4.8.1 Cross-sectional imaging of stripped and plated lithium magnesium alloy anodes. . . . 107
4.9 Conclusions. . . . 108

5 Indium lithium alloys as a counter/reference electrode. 111
5.1 Introduction . . . 112
5.2 Synthesising phase pure InLi. . . . 113
5.3 Mechanical characterisation . . . 115
5.3.1 Berkovich Indentation . . . 115
5.3.2 Cube corner indentation . . . 117
5.4 Diffusion of InLi intermetallic. . . . 119
5.5 In metal on charge . . . 120
5.5.1 First cycle coulombic efficiency of pure indium metal . . . 124
5.6 Indium-lithium on discharge . . . 125
5.6.1 Cast indium lithium two-phase alloy electrode . . . 126
5.6.2 In + InLi two layer alloy electrode . . . 131
5.6.3 Characterising delithiated microstructure . . . 134
5.7 Electrodes formed by combining indium and lithium foils . . . 138
5.8 Cycling two-layer InLi electrode. . . . 142
5.8.1 Electrochemical Impedance Spectroscopy before cycling . . . 143
5.8.2 Cycling two-layer InLi electrode . . . 144
5.9 Conclusions . . . 147

6 Conclusions 149

References 153

1 Introduction

Contents

1.1 Context for work 1
1.2 Lithium Batteries Background 3
1.2.1 Lithium Metal 5
1.2.2 Solid Electrolytes 6
1.2.3 Lithium alloys 10
1.3 Mechanical properties in solid-state batteries. 11
1.4 Outline of thesis 14

1.1 Context for work

Better batteries are a key component in decarbonisation policy[1]. Road transport, which accounts for a fifth of CO_2 emissions [2], requires a portable source of energy. Traditionally, petrol or diesel have been used and internal combustion engine (ICE) cars make up the majority of UK car registrations [3]. The combustion of these hydrocarbons leads to the emission of greenhouse gases, which drive climate change[4], and air pollutants, which cause large numbers of deaths – primarily from premature cardiovascular disease[2].

Batteries are an alternate portable energy storage technology. The constituent cells spatially separate the oxidation and reduction components of a redox reaction,

forcing electrons around an external circuit so that work can be done, driven by the potential difference of the combined reaction. Over the past 6 decades, commercial battery energy density has increased by around 3% a year and, over the last decade alone, pack level cost has decreased 87%[5–7]. As a result, battery-powered electric cars are now competitive with traditional combustion engine cars.

Electric vehicles (EV) have zero tailpipe emissions, are more efficient, and have significantly lower greenhouse gas emissions than conventional vehicles - even when accounting for electricity and battery production[8]. They sit at the centre of the UK government's strategy towards a zero-emission transport sector[1], alongside deep grid decarbonisation[9].

At the beginning of the period of work detailed in this thesis, EV accounted for just 2% of new UK car registrations[3], with pioneering companies providing medium to high-end models, based on lithium-ion chemistry, with excellent performance but around half the range of equivalent ICE vehicles. The prevailing wisdom in 2019 was that low-medium cost, smaller electric cars, competitive with modern ICE vehicles would require a significant reduction in battery pack cost, weight, and size, underpinned by a cell chemistry change [10]. Now it seems that progressive advances in lithium-ion batteries are sufficient to drive this transition. The expected UK EV market share in 2023 has increased to 18% despite supply chain constraints and reluctance to transition from industry incumbents. This technological revolution has demonstrated the benefits of high energy density batteries and driven investment in battery research across the globe.

Looking forward, the electrification of long-distance heavy goods transport and long-distance aerospace requires around a twofold increase in cell-specific energy density[11]. As the incumbent lithium-ion chemistry (transition metal oxide cathode and graphite anode) is fast approaching its theoretical energy density limit, continued improvement relies on replacing it with superior alternative chemistry. A promising approach is the use of a lithium metal anode that electroplates and strips on successive cycles. This architecture is called a lithium metal battery (LMB)[12].

1.2 Lithium Batteries Background

The first publication concerning lithium metal batteries was published in 1913 [13], decades before lithium-ion was developed. The Li^+/Li reduction potential was found to be -3.04V versus the standard hydrogen electrode (SHE), meaning protic solvents such as water were readily reduced. The development of more stable non-aqueous electrolytes in the fifties and sixties led to numerous patent submissions, summarised by Jasinki in 1970[14]. In 1972, whilst researching at Exxon, Dr Stanley Whittingham, created a lithium battery which used a titanium sulphide cathode[15, 16]. TiS_2 is a layered structure into which lithium intercalates. This was followed in 1977 with the proposal of a graphite intercalation anode by Basu and colleagues[17, 18], providing an alternative to lithium metal at the anode. The intercalation was later shown to be reversible[19] whilst using a polymer electrolyte. Both lithium metal and graphite lithium-ion intercalation anodes showed unexpected, electrolyte-dependent, stability against non-aqueous electrolytes, graphite much more so. To explain this, in 1979 Peled proposed a solid interphase layer (SEI) was forming from the decomposition products of the electrolyte that then prevented further decomposition, by being both electrically insulative whilst still ionically conductive[20]. In 1980 Whittingham collaborated with, now fellow Nobel laureate, John B. Goodenough to improve the battery using metal oxide cathodes[21]. Akira Yoshino patented an assembled prototype cell with a transition metal oxide cathode and graphite anode in 1986 [22]. Finally, Sony commercialised the lithium-ion battery in 1991[23].

Commercialised lithium-ion battery specific energy density has approximately doubled since 1991[24]. Yet the graphite anode has remained mostly unchanged throughout the years of lithium-ion. The lithiation onset potential of graphite is around 0.05V above Li^+/Li. This is a double edged sword, as cell voltage (energy per ion) is high, but the small headway to Li/Li^+ means overpotential must be controlled to avoid lithium plating and the associated battery failure[25, 26]. This limits high power use. On cycling, lithium ions intercalate between the graphite layers to form LiC_6[19]. The carbon scaffold minimises volume change on cycling to

13% [27], which avoids current collector delamination and minimises mechanical stresses on the SEI layer. But, the low lithium packing density leads to a low specific and volumetric capacity of 372 mAh g^{-1} and 840 mAh cm^{-3}. These are insufficient for the needs of industry in the coming decades. Therefore, it's widely accepted that the graphite anode needs replacing[28, 29]. Lithium metal is an attractive choice for a future commercial anode because it has the highest theoretical capacity (3860 mAh g^{-1} or 2061 mAh cm^{-3}) and lowest reduction potential (-3.04V versus the SHE) of all alkali metal candidates.

Modern, commercial, high quality lithium-ion cells, such as those used in electric cars, have the following characteristics:

- Cost below 100 $/kWh [30]
- Cycle life of greater than 2000 cycles. [31]
- Failure rates below one in 10 million.[32]
- Operating temperature of 0-50 Celsius.
- Energy density of 260 Wh/kg and 730 Wh/L
- Areal energy density near 6 mAh/cm^2.
- Sustained current densities of 2.3 mA/cm^2.
- Transient current densities up to 32 mA/cm^2.

These are hugely impressive but also are the prerequisite conditions for profitable electric vehicle commercialisation. For lithium metal anodes to replace graphite intercalation anodes, similar standards must be achieved for cycle life and safety, whilst demonstrating battery pack level energy density superiority.

The safety requirements are particularly important. Despite the extremely low statistical failure rates, safety concerns persist. In the aerospace industry, 261 air/airport incidents have been recorded involving lithium-ion batteries since 2006[33] and numerous personal electronics product recalls have due to battery

safety concerns[32]. As demonstrated by Airbus 787 issues and the 737 max debacle, companies suffer hugely from small numbers of failure events, and are therefore rightly hesitant to use any new battery technology unless it's failure rate is well below 1 in 10 million. Li-ion safety issues include mechanical failure, lithium dendrite growth and thermal runaway, mostly originating from the unwanted plating of lithium metal onto the anode[25].

1.2.1 Lithium Metal

Lithium metal anodes have a high theoretical capacity (3860 mAh g^{-1} and 2061 mAh cm^{-3}) owing to its high lithium packing density and very low reduction potential (-3.04V versus the SHE) [34]. Batteries can be made using lithium metal and a liquid electrolyte but they suffer from three key issues. First, the low potential readily decomposes all known liquid electrolytes depositing an SEI layer that modifies the deposition morphology and consumes the electrolyte, leading to low coulombic efficiency and poor cycle life. Second, the deposition morphology at even moderate currents is mossy, leading to significant electrolyte consumption. During fast charging the lithium forms sub-nanometre filaments, which grow from their tip (lithium dendrites). These can short the cell. Last, there is a large volume change associated with plating and stripping of lithium, which leads to repeated SEI breakage and repair consuming both lithium metal and electrolyte, directly reducing capacity [35, 36] and to lithium becoming electrically separated from the anode (dead lithium)[37, 38].

Battery cycle life is defined as the cycle number where the battery is at 80% of its original capacity. Achieving 1000 cycles requires a coulombic efficiency above 99.98%, defined as the ratio of capacities before and after each cycle[39, 40]. The highest lab-based liquid-electrolyte lithium metal publication to date reported 99.6% coulombic efficiency[41] at a current density of 2mAcm^{-}2 using a carbon nano-tube modified anode. Recently, a team at Samsung reported a 99.8% coulombic efficiency[42] using a solid-state electrolyte and silver-carbon composite layer modified anode and a high nickel content cathode. These two publications

are standout examples. Most publications are far lower, with only a handful of studies reporting true coulombic efficiencies above 0.99[40].

Although there continues to be progress, over a century of research[43] has failed to safely implement lithium metal liquid electrolyte cells. Therefore research focus has steadily shifted towards the use of solid-state electrolytes.

1.2.2 Solid Electrolytes

It was in the early 1990s that the first lithium-ion solid conducting ceramic was demonstrated[44]. Because solid electrolytes have a single fixed interface, their use mostly removes the issue of continual performance degradation and capacity fade due to SEI formation on the large surface area of plated lithium metal. Monroe and Newman in their highly cited theoretical work proposed that high stiffness materials (E $>$ 15 GPa) could act to prevent dendrite formation, by increasing the local nucleation overpotential in undesired locations to a point where it is avoided[45]. If they enable the use of lithium metal anodes (theoretical capacity 3860 mAh·g^{-1} and 2061 mAh·cm^{-3}) [46], solid state cells can have gravimetric and volumetric energies upwards of 400 Wh·kg^{-1} and 1000 Wh·L^{-1} [47].

Solid lithium ion conductors can broadly be split into inorganic ceramics and organic polymers (eg. polyethylene oxide (PEO))[48]. The ionic conductivity of polymer electrolytes remains too low to be practical. The ceramics are typically classified by their crystal structure. The notable classes researched today include sulphides[49](e.g. lithium germanium phosphorous sulphur (LGPS))[50] and garnets[51] (e.g. LLZO), with some interest in perovskites[52] and anti-perovskites[53].

Today, the best solid ionic conductors demonstrate room temperature ionic conductivity of the order 10^{-2} Scm^{-1} for the best sulphides[49, 54] and 10^{-3} Scm^{-1} for the best oxides [55]. These are comparable to liquid electrolytes and sufficient for use in batteries. But the materials must also have high electronic resistivity[56], high ionic selectivity, a wide electrochemical stability window[57], good chemical, thermal and mechanical stability during cycling and ideally have an easy manufacturing/battery assembly route, whilst being safe and low cost[58].

Finding materials that fulfil all these requirements and finding ways to produce batteries with them successfully, is an ongoing challenge. Solids are fundamentally more complex than liquids. Porosity[59], differences between grain boundary, free surface and bulk properties[60], impurities and internal stresses[61], can all substantially affect the performance of the electrolyte.

Unlike in liquid electrolytes, lithium ions are the only mobile species within solid electrolytes so no concentration overpotential occurs[46]. However, there are other challenges. Firstly uneven lithium stripping generates voids which lead to increased local current density on the remaining anode area, facilitating dendrite growth[62]. Secondly, solid electrolytes are susceptible to mechanical failure which can lead to battery short-circuiting [63, 64]. The use of solid electrolytes necessitates, for the first time, a thorough understanding of material mechanical properties within battery research[65]. Thirdly, the use of solid electrolytes brings difficulty to constructing electrodes such that high-capacity lithium materials are co-located with ionic and electronic pathways [66].

Unfortunately, the current lithium metal-solid-state batteries struggle to meet the performance requirements for EVs in terms of cycle life, capacity retention, and charge rate capability. The issues are summarised in the schematic figure 1.1 reproduced from Narayanan et al. 2022 [67]. On charge, despite Monroe and Newman's predictions, high current densities drive lithium filament formation [74] leading to electrolyte fracture [75, 76]. This unexpected failure has been attributed to material porosity[77], grain boundary conductivity[56], changes occurring on stripping [62], sub-micron mechanical properties of lithium[78], and other factors. The mechanical suppression of dendritic growth remains an active research area [79] as it seems counter-intuitive for filaments of lithium metal, one of the softest metals [80], to be able to fracture stiff ceramics. On discharge, slow diffusion kinetics and insufficient creep of lithium metal [81] lead to voiding or contact loss on stripping [72]. These processes, as schematically highlighted in the left and lower panels of figure 1.1 are tied tightly to the mechanical properties of lithium [82] - particularly at the nanoscale. Nanopillar compression work suggests that the hardness of lithium

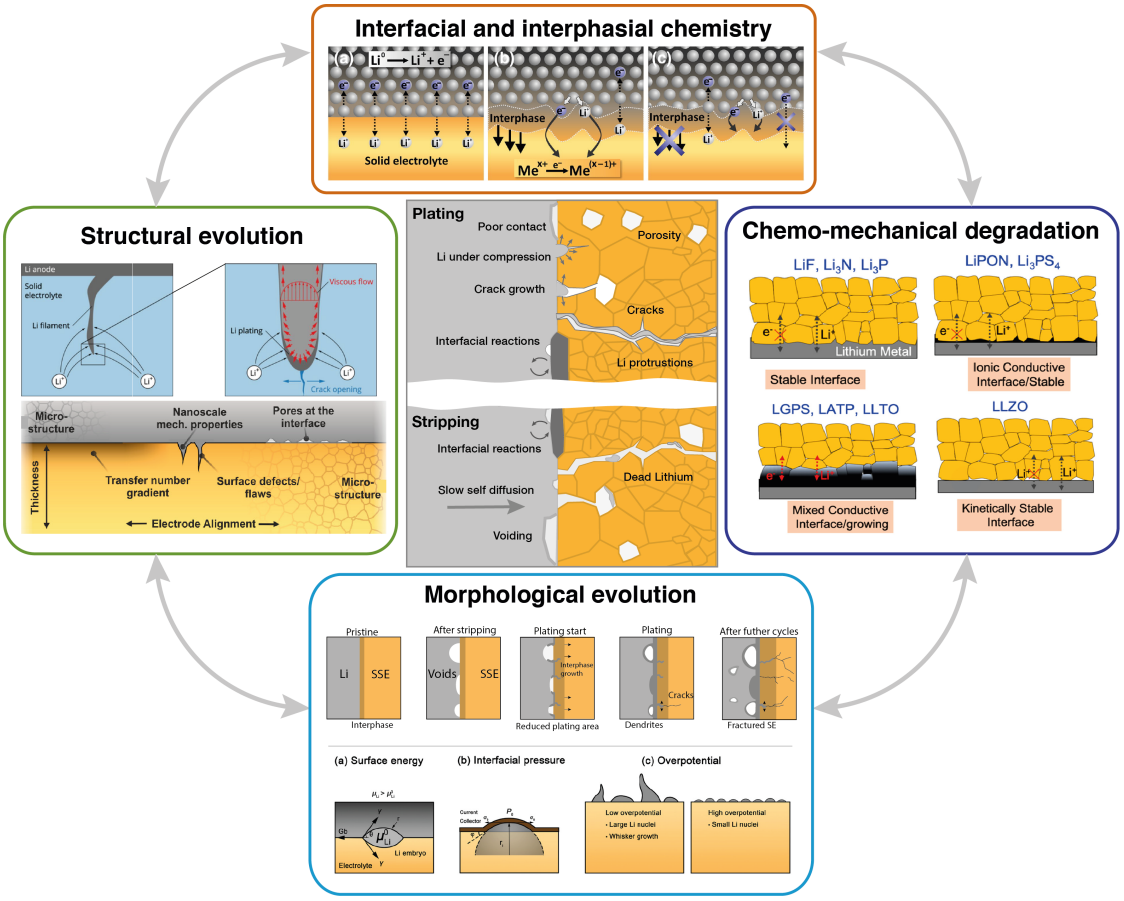


Figure 1.1: Reproduced from [67]. A representation of electro-chemo-mechanical processes occurring at the Li metal-solid electrolyte interface during plating and stripping. Schematic for chemo-mechanical degradation - Reprinted and adapted with permission from [68]; Copyright 2020 American Chemical Society. Schematic for Structural evolution - Reprinted and adapted with permission from [69], Copyright 2020 American Chemical Society and Reproduced with permission from [70]. Schematic for Morphological evolution - Reproduced and adapted with permission from ref [71] Copyright 2021 John Wiley & Sons, Inc., and ref [72] Copyright 2019 Springer Nature. Schematic for Interfacial and interphasial chemistry - Reprinted from [73], Copyright 2015, with permission from Elsevier.

at the nanoscale is orders of magnitude higher than bulk hardness [78], but the dependence on crystallographic orientation, changes in nanoscale creep compared to bulk creep [70, 83] and nanoscale adhesion are unclear.

As is the case for liquid electrolytes, the stability of effective solid-state electrolytes against lithium metal is not the result of intrinsic thermodynamic stability but instead results from kinetic stabilisation from the poor electronic conductivity of formed interphase layers[84]. Various solid electrolytes' SEI can be broadly

characterised into three categories (a) ionically and electronically conductive, which results in continuous degradation, (b) ionically conductive but electronically insulative, where spontaneous decomposition occurs upon contact with Li metal, forming a passivating layer (c) stable due either to thermodynamic stability with lithium metal, or kinetically very low electronic conductivity preventing significant reduction.[67, 85]. Examples are given in the right-hand side panel of figure 1.1. Category A materials lead to high interfacial resistances [86]. But some such as Li_6PS_5Cl are category B, create passivating, high-performance interphase layers[57, 87] despite the potential of lithium metal being below the SE stability window [85, 88]. The performance of an SEI depends on its composition and nanostructure which can be characterised by techniques such as x-ray photoelectron spectroscopy (XPS) [89, 90], Raman spectroscopy [91] and Fourier transformed infrared spectroscopy (FTIR) [92]. Characterisation techniques, which we summarise in this review paper [67], can be correlated with electrochemical data, specifically electrochemical impedance spectroscopy [93], to identify the impact of structural differences on electrochemical processes at the interface. This builds an understanding of the link between structure and performance, enabling rationally driven electrolyte selection for high-performance interphase formation. One aspect that has not been investigated enough is the effect of changing the anode composition by alloying [94–96], or by the use of an alloy interlayer between the deposited lithium and solid electrolyte [42] on the SEI structure and the resultant performance.

At room temperature and practical pressures, the accessible capacity during discharge of pure lithium metal anodes is very limited [81] with a progressive loss of contact occurring [97, 98]. Higher temperature operation can alleviate some of these issues [99], but regulating a higher temperature within a battery pack requires a heating/cooling system which will reduce pack-level energy density. Fundamental changes are needed to aid contact retention at the lithium-metal solid electrolyte interface [100] and increase the transport rate within the anode itself.

1.2.3 Lithium alloys

The material properties of lithium metal determine its electrochemical performance, so lithium-rich alloys are interesting [94] as alloying modifies the physical properties of lithium metal such as the diffusion rate [101–103], mechanics [104], chemistry at the interface, and the material microstructure. This is achieved with only a small reduction of energy density compared to pure lithium [95]. Anodes which involve lithium alloying with a metallic particle on charge have been widely pursued in lithium-ion cells [105].

Under an applied potential lithium can alloy with many elements, successively forming the equilibrium room temperature intermetallics seen on phase diagrams[106]. When fully lithiated, these materials have packing densities comparable to, or even higher than, metallic lithium[107], giving excellent volumetric charge densities. The diffusion kinetics of lithium within alloys are typically fast (D_{Li} $\approx 10^{-7}$-10^{-9} cm^2s^{-1}). The electrode operation voltage is well above the potential of metallic lithium, which avoids lithium plating and lowers the demands of extreme electrolyte stability. Both silicon and aluminium have lithiation onset voltages 0.3-0.4 V above Li^+/Li. This moderate voltage, sitting between lithium metal (0V vs Li^+/Li) or nearby graphite (0.05V vs Li^+/Li) and an alternative such as lithium titanium oxide [LTO] (1.5 vs Li^+/Li), trades a small energy penalty per ion for a large increase in safety[25, 108].

But these materials expand on lithiation, often doubling or tripling in size. Successive expansions and contractions lead to current collector separation[109], an alloy-electrolyte specific process of dynamic SEI breakage and repair[110], and particle/layer disintegration[111]. This results in low first cycle coulombic efficiencies, and significant capacity fade thereafter. The primary advances since this fundamental work, are the use of nanoparticles[112], to reduce the magnitude of stresses, and the design of the host matrix to accommodate the expansion. Nearly all binary alloy systems have been studied, as too have some ternary systems. The

system most studied is lithium with silicon[113–115]. Nanostructured graphite-silicon composite anodes are a key component of increasing energy density in current commercial electric car batteries.

A novel approach is constructing a lithium-rich anode microstructure, which acts as an ideal framework for further lithiation [116, 117], and facilitates discharge at higher rates; with the objective of mitigating the issues in solid-state [94]. Lithium-magnesium binary alloys have been considered one of the most promising alloy anode candidates [94] due to their high energy density, unique wide solid solubility in the lithium-rich phase and similarity in processing to lithium metal. Conflicting literature reports on diffusivity [96] have contributed to this interest. Two works, using different methods, have identified similar decreases in lithium diffusivity with increasing magnesium alloy content [101, 102], but recently Krauskopf. et al. and Siniscalchi et al. [96, 102], both with an LLZO solid electrolyte, demonstrated improved stripping performance with increased magnesium content. This result is surprising and shows that measurement of the diffusivity alone is insufficient to understand the behaviour of alloy anodes. Diffusivity, mechanical properties, surface chemistry and microstructure all contribute to the electrochemical performance. The lithium magnesium system is also the simplest alloy system, with a wide solid solubility region on the lithium-rich side (0<at%Mg<69) and magnesium-rich side (0<at%Li<15%); meaning the impact of microstructure on electrochemical performance is small. Once an effective framework for investigating alloy performance is established with the magnesium system, it can be adapted and applied to thoroughly understand the more complex multiphase lithium alloy systems such as indium [118], aluminium [119], gallium, calcium and silver [95]. The developed fundamental understanding will allow rational alloy anode design to maximise performance, whilst minimising the penalties of energy density, and manufacturing cost.

1.3 Mechanical properties in solid-state batteries.

Four works have measured the three independent elastic constants of lithium metal (C_{11}, C_{12} and C_{44}); which together fully describe the material's anisotropic elastic

response [120–123]. Overall, these works suggest tensor components in the range C_{11}=12.3-14.5 GPa, C_{12}=10.2-11.3, and C_{44}=8.5-8.9 GPa. This suggests lithium is a highly elastically anisotropic material (Anisotropy factor, A≈8).

Most mechanical works on lithium metal have studied polycrystals, with Young's modulus values ranging from 4.97 GPa [124] to 9.8 GPa [125]. Notably, several studies have measured values close to 7.8 GPa [83, 126, 127]. Given lithium's high elastic anisotropy, it is surprising that there is such strong agreement between measurements of polycrystalline Young's modulus in studies with different sample preparation and testing methodologies. Taking the average of prior single crystal studies (C_{11}=13.4, C_{12}=11.0, C_{44}=8.7 GPa) gives a Hill estimate of 10.8 GPa, which is typically a good estimate for untextured polycrystalline moduli [128]. 7.8 GPa lies 28% below this expected value. The disparity between single-crystal and polycrystalline elastic properties as well as the range of single-crystal values reported in the literature justifies new work quantifying the stiffness tensor.

Lithium's plastic response is complex, depending on the mobility of micron-scale dislocations. At small length scales relevant for lithium filaments, the number of dislocations within the stressed volume is limited and therefore size-dependent hardness is expected. Several works have studied plasticity in lithium in micron-scale to bulk samples, and at a range of strain rates. This is summarised well in the recent paper by Fincher et al. [82]. Collectively, studies find bulk lithium has a yield stress of 0.6 MPa, increasing by around a factor of two with a high strain rate [70, 82, 83, 127, 129].

With decreasing plastic zone size, the hardness of lithium increases by over an order of magnitude. Xu et al. performed nanopillar compression to investigate size-dependent hardness, measuring an increase in yield stress from 15 to 105 MPa [123] as pillar size decreases from 9.45 μm to 1.39 μm. The pillars were prepared by focused ion beam milling (FIB) which raises concerns that ion-implantation from pillar machining [130] is contributing to an increase in hardness, especially for the small pillars. The contribution of the FIB-damaged shell to the observed hardness is unclear. Nevertheless, the trend agrees with micro indentation work [82, 125] and

similar experiments on other metals [131]. In the sub-micron region relevant for lithium filament initiation there is a broad spread of results, with yield stress varying from 8 MPa [125] to over 100 MPa [123] between different studies. More work is needed at this length scale to quantify size-dependent plasticity in lithium metal.

The mechanical properties of SEI layers have been identified as a key factor in determining lithium metal plating dynamics[34, 132]. Despite this, there is little literature accurately characterising their mechanics. The elastic properties of specific liquid state SEI layers have been experimentally measured by AFM [133–135] and computationally predicted[135–138], revealing a fine mosaic microstructure comprising of constituent components who's elastic moduli span three orders of magnitude. There's significant scope to build on this and extend the measurements to SEI formed with solid-state electrolytes [67].

The elastic, plastic and fracture properties of various solid electrolytes have been measured. Superionic ceramics tend to be stiff, the Young's modulus of LLZO is 150 GPa and of lithium aluminium titanium phosphate (LATP) is 115 GPa [64] but they are also brittle: $K_{1C} \approx 1$ MPa $m^{0.5}$. The mechanical properties of Li_6PS_5Cl were recently published with a Young's modulus of 28.0±1.8 GPa, a hardness of 921±196 MPa and a fracture toughness K_{1C}=0.91±0.12 $MPam^{0.5}$, making it comparatively soft [139]. Thus far, the mechanical properties of an electrolyte have been investigated as an afterthought following the demonstration of good lithium diffusion kinetics and electrochemical stability. But as solid-state batteries often fail due to electrolyte fracture[50, 140], it is likely that the mechanical properties of candidate solid electrolytes will gain research attention going forward.

The brief literature review provided here is not exhaustive. Many excellent review papers have been published over the last few years on lithium metal and solid-state batteries which highlight the work done in the field and outline the research frontier [47, 66, 141–144]. Relevant literature is referenced throughout.

1.4 Outline of thesis

Chapter 2 provides a brief overview of the theoretical background and experimental settings for the key techniques used in the project.

Chapter 3 details a nanoindentation study on pure lithium. By directly probing the mechanical properties using nanoindentation, we can better understand the mechanical interaction occurring between lithium metal and the solid electrolyte, leading to electrolyte fracture. Given lithium is highly anisotropic, it was necessary to correlate indentation measurements with the material's crystallographic orientation measured by electron backscattered diffraction (EBSD). A novel surface preparation technique for EBSD is detailed. As the lightest metal, lithium is the weakest electron backscattering metal and therefore is a limit case for EBSD. The implications of this on EBSD resolution are explored. The indentation study measures the full stiffness tensor of pure lithium and the length-scale dependent plastic response.

In Chapter 4, I investigate the link between materials properties and electrochemical performance in the lithium-magnesium alloy system in combination with argyrodite, Li_6PS_5Cl, sulphide solid electrolyte. I synthesise and microstructurally characterise alloys of three magnesium compositions; then measure the mechanical stiffness, hardness, adhesion, and creep of these alloys by nanoindentation – quantifying the change with the magnesium content. The effect of magnesium on interfacial chemistry is explored with electrochemical impedance spectroscopy (EIS) and x-ray photoelectron spectroscopy (XPS). Diffusivity is measured using ^{6}Li pulsed field gradient nuclear magnetic resonance spectroscopy (PFG-NMR). These properties are correlated with electrochemical tests for varied magnesium content, performed in tightly controlled, realistic conditions (30°C, 50–100-micron thick anodes, 5 MPa stack pressure), with corresponding cross-sectional electron microscopy used to understand the underlying processes more clearly. The measure of diffusivity by electrochemistry and by NMR is compared. The work is presented as a framework that can be applied to other alloy systems, enabling the rapid development of alloy anodes and solid-state batteries.

In Chapter 5, I investigate the indium-rich two-phase region of the indium-lithium alloy system to develop a counter/reference electrode. This chapter follows the framework established in the previous chapter to establish the link between materials properties, microstructure, and performance. A synthesis method for the intermetallic phase is developed, then its mechanical properties and diffusion kinetics are measured, followed by an electrochemical investigation into the behaviour and performance of a range of two-phase microstructures to understand the achieved performance. Optimised indium-lithium anodes show resistance to lithium filament formation, large usable capacities, and low polarisation even at high discharge/charge rates. The understanding gained informs future studies using indium-based counter electrodes.

Overall the work deepens the understanding of the microstructural changes, diffusion kinetics, and mechanics on the lithium metal-solid electrolyte side of a solid-state battery. The EBSD coupled indentation study identifies and quantifies the extreme relative strength of lithium metal at the nano-scale, explaining the observed fracture of solid electrolytes during cycling. The lithium-magnesium study identifies the impact of diffusivity and other materials' properties on performance and provides a framework by which lithium-rich alloy anodes can be developed to overcome this limitation. The final chapter provides a near-ideal counter/reference electrode that can be used in the research effort going forward and contributes to the understanding of two-phase alloy anodes.

2
Method fundamentals

Contents

2.1 Scanning electron microscopy 16
2.1.1 EBSD: Electron backscatter diffraction 17
2.2 Nanoindentation 18
2.3 Electrochemical testing 21
2.3.1 Cell Assembly 21
2.3.2 EIS: Electrochemical impedance spectroscopy 22
2.4 PFG-NMR: Pulsed-field gradient nuclear magnetic resonance spectroscopy 24
2.5 XPS: X-ray photoelectron spectroscopy 25
2.6 Other techniques 26

The main experimental techniques used in this thesis are scanning electron microscopy (SEM) including electron-backscatter diffraction (EBSD), nanoindentation, electrochemical testing, including impedance spectroscopy, nuclear magnetic resonance spectroscopy and x-ray photoelectron spectroscopy. This chapter provides a brief overview of each technique and provides experimental details to allow result reproduction.

2.1 Scanning electron microscopy

Scanning electron microscopy (SEM) was used throughout the project.

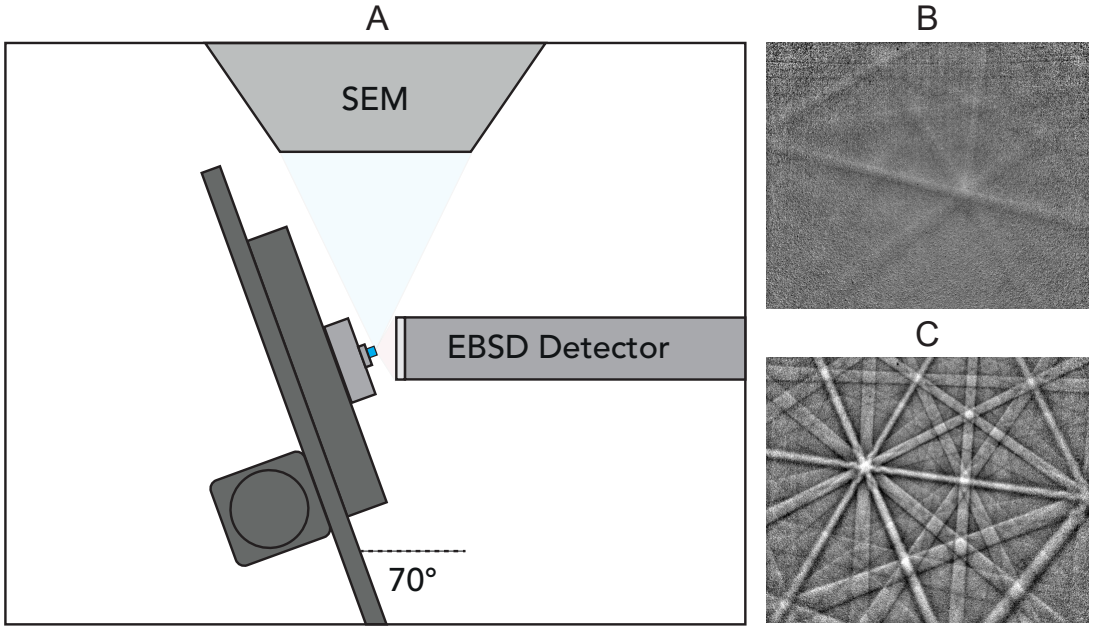


Figure 2.1: (a) EBSD setup schematic (b) Kikuchi pattern of lithium metal at 20kV. (c) Kikuchi pattern of indium metal at 20 kV.

The microscope used was a Tescan Mira-3 FEG-SEM with Oxford Instruments EBSD and EDS detectors. The SEM chamber opens into a dedicated MBraun argon glovebox, enabling sample change without air exposure.

2.1.1 EBSD: Electron backscatter diffraction

EBSD is a diffraction imaging technique which allows the crystallographic structure and orientation of each point on the surface of a sample to be determined [145, 146]. An EBSD map is formed by moving a focused electron beam over a grid of points on a bulk sample surface. At each point the electrons inelastically scatter in all directions due to lattice interactions. Because the incident electron beam is diffusely scattered in all directions, every plane has some electrons travelling at the Bragg angle, leading to diffraction, forming a Kossel cone of high electron intensity. Some of the scattered electrons exit out of the sample surface (backscatter). As is shown in figure 2.1A, the sample is generally tilted 70° to maximise the backscatter signal. A fraction of these backscattered electrons are collected by a detector, typically 30-40 mm in size, held close to the sample, consisting of a scintillator screen coupled to a charge-coupled device (CCD) camera to form an EBSD pattern.

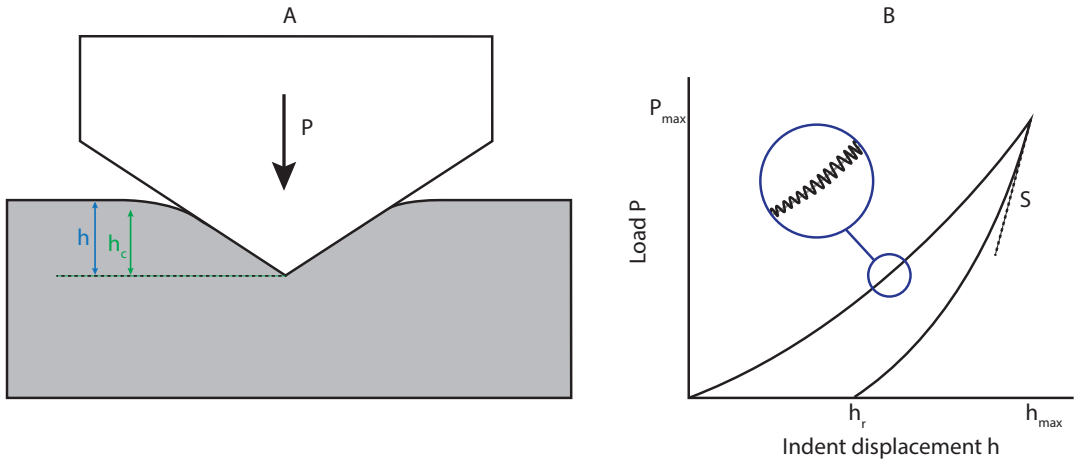


Figure 2.2: Indentation fundamentals. (a) Schematic of indent tip and material in contact. (b) Typical load-displacement curve showing key values and continual stiffness measurement principle.

The pattern consists of the projection of intersecting Kossil cones, which we observe as near-straight bands called Kikuchi bands. The locations and relative orientation of the bands is determined by the crystallographic structure and orientation at the mapped point. Sophisticated software packages integrated into the detector's software rapidly index the patterns, giving the crystal structure and orientation. EBSD requires smooth surfaces, free of mechanical damage; as the EBSD pattern is generated from a thin surface layer of material, typically below 50nm [145].

The EBSD of lithium metal is challenging due to its low atomic number, softness and high reactivity. Typical Kikuchi patterns for lithium and indium, with identical sample surface preparation, are shown in figure 2.1B and C respectively. A discussion of the challenges of lithium EBSD is included in Chapter 3. EBSD was performed at a beam voltage of 20 kV, current of 500 nA, tilt of 70 degrees and a working distance of 15 mm unless explicitly stated otherwise. EBSD patterns were automatically indexed using Oxford Instrument's Aztec software package. The MTEX Matlab package was used to plot and analyse EBSD data.

2.2 Nanoindentation

Building on Hertzian contact mechanics, nanoindentation is an effective technique to determine the mechanical properties of a material by measuring the force (P) and

displacements (h) during the indentation of the material with a small hard tip, this is schematically shown in figure 2.2A. Many of the physical properties measured depend on the contact area between the tip and the sample. There is always some elastic deflection of the sample surface which means it does not perfectly conform to the indenter tip. The nominal indent depth is related to the true contact depth by equation 2.1, which is valid where there is minimal pile-up or sink-in. Knowing the indenter tip area cross-sectional area as a function of distance from its point, allows the contact area to be calculated from the contact depth.

$$h_c = h - \epsilon\frac{P}{S} \tag{2.1}$$

A schematic of a typical load-displacement curve is plotted in figure 2.2B, some key measured values are peak load (P_{max}), depth at peak load (h_{max}), unload contact stiffness ($S = \frac{dP}{dh}$) and the depth at complete unload (h_r). The key properties of modulus and hardness can be calculated from this information using equation 2.2 and equation 2.3 where β is a tip-geometry specific factor around one. The measured modulus E_r is a measure of the combined stiffness of both the tip and sample, therefore for stiff samples, the contribution of the tip has to be removed using equation 2.4 where ν is the Poisson's ratio, and subscript i denotes indenter tip material properties (E_i = 1140, ν_i=0.07).

$$H = P/A_c \tag{2.2}$$

$$E_r = \frac{S\sqrt{\pi}}{2\beta\sqrt{A_c}} \tag{2.3}$$

$$\frac{1}{E_r} = \frac{(1-\nu^2)}{E} + \frac{(1-\nu_i^2)}{E_i} \tag{2.4}$$

Continual stiffness measurement (CSM) [147] is a method integrated into the indenter testing software, whereby a small sinusoidal signal is superimposed onto the loading curve as shown in figure 2.2B. A resultant response is observed in the measured displacement with an amplitude and phase shift from which the material

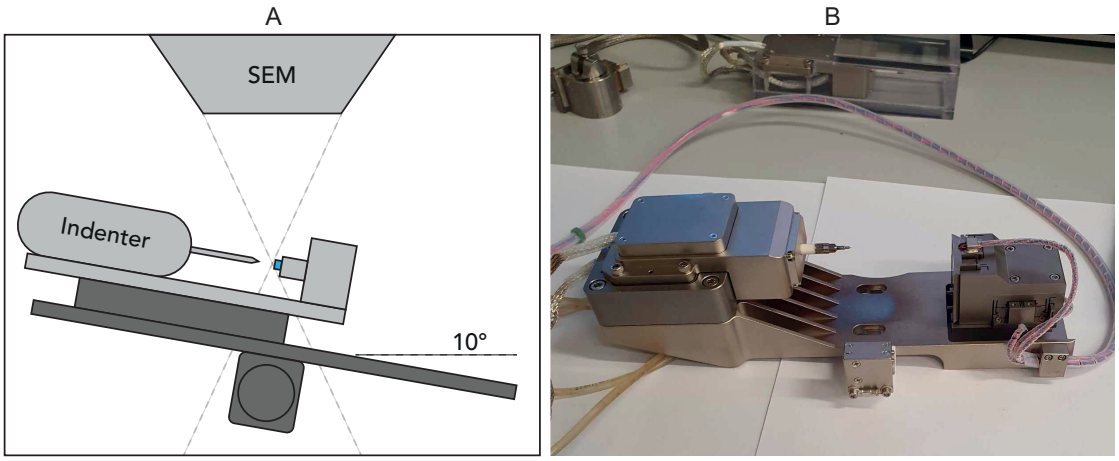


Figure 2.3: Indentation setup. (a) Schematic of indention within SEM chamber. (b) Photograph of PI88 Indenter

stiffness can be calculated. As the frequency of testing is much faster than the indentation time, the stiffness is measured as a function of indentation depth. The material hardness can also be calculated as a function of depth from this data. The CSM technique is used for all indents in this project unless stated otherwise.

Nanoindentation was performed within a single contained system depicted schematically in figure 2.3A consisting of a Bruker Hysitron PI88 in-situ nanoindenter shown in figure 2.3B, with a five-axis sample stage mounted to the five-axis stage of the Tescan Mira-3 FEG-SEM. The two five-axis stages of the indentation setup allow the sample to be rotated between EBSD and indentation positions (Tilt accuracy of $<0.33°$, rotation accuracy $< 0.12°$). The SEM was used to align the sample surface perpendicular to the indenter in both axes of freedom. The system allows indents to be performed at targeted sites. Two transducers are used, first the low-load transducer with a maximum load of 25 mN with CSM capability, and second the high-load transducer with a maximum load of 500 mN, but no CSM capability. A diamond Berkovich indentation tip was used unless it is stated otherwise. The indenter was calibrated carefully following the manufacturer's instructions before each indentation session. Machine compliance was measured to be 8.02 nm/mN using a fused silica calibration sample. Prior to each test, thermal drift rate was measured in contact, with preload of 10 μN, over 40 seconds. The first 20 seconds

were given as time for the system to stabilise after initial contact, and the last 20 seconds were sampled to calculate the mean drift rate, assumed constant throughout the indent. For lithium, a large dynamic load amplitude of 50 μN at a target quasistatic load of 1000 μN was used scaling with the square root of quasistatic load to minimise viscoplasticity error whilst retaining indenter contact [148, 149]). These values were scaled for higher hardness materials tested, for which the data quality was less sensitive to the testing parameters.

2.3 Electrochemical testing

All the electrochemical tests reported in the thesis are on solid-state electrochemical cells.

2.3.1 Cell Assembly

Lithium stress relaxes when held under compression at a constant displacement. Given lithium is stiff (E = 10.6 GPa), the elastic strain due to typical stack pressures is well below 1%. A fixed displacement cell setup therefore cannot give reliable and fixed stack pressures. To achieve fixed and controlled stack pressure for electrochemical tests, it is essential to have a compressed spring in mechanical series with the cell, where the spring compression distance is large compared to any cell thickness changes during the test.

All electrochemical measurements were performed within a temperature chamber at a temperature of 30 °C. Li_6PS_5Cl (Ampcera 10 μm.) pellets were pressed with stainless steel plungers, at a pressure of 370 MPa for 300 seconds within custom Macor cell cylinders (diameter = 10 mm) giving a pellet thickness of around 700 μm. Metallic foil electrodes including pure lithium and lithium alloys were calendared down to a thickness of 50-100 μm before 10 mm diameter anodes were hole punched and attached to the solid electrolyte at a pressure of 80 MPa. When assembled, the cell has a compressed spring that maintains a constant stack pressure of 5±0.5 MPa throughout cycling, shown schematically in **??**. This stress can be changed using spacers. Assembled cells were rested at open-circuit for 20 hours

within the temperature chamber, (impedance measured approximately every two hours) before the remaining electrochemical test was performed. Cells were tested with a Biologic VMP3 potentiostat. Before cell assembly, the Macor cylinder and stainless steel plungers were thoroughly cleaned ultrasonically using successively deionised water, isopropanol, and acetone before drying overnight in a vacuum oven at 70°C. I assembled and tested the vast majority of electrochemical cells in this project. A small number of lithium magnesium alloy cells were assembled and tested by Dr. Krishnakanth Sada and Souhardh Kotakadi. The most commonly used electrochemical test was chronopotentiometry whereby a constant unidirectional current is drawn, and the resultant potential is measured, a current density of 0.3 $mAcm^{-2}$ was used unless otherwise stated.

2.3.2 EIS: Electrochemical impedance spectroscopy

Electrochemical impedance spectroscopy EIS enables the measurement of impedance contributions from different electrochemical processes within a cell, which each have characteristic times ($\tau = RC$). EIS can be performed potentiostatically (PEIS) by measuring the current response due to an small oscillating potential signal, or galvanostatically (GEIS) by measuring the potential response due to a small oscillating current signal. All the results reported in this project are PEIS. When the test frequency is much slower than these characteristic times, fast processes appear ohmic. When the frequency is much faster, slow processes do not have time to operate. When the frequency and the characteristic time are similar, there are energy losses associated with the process, leading to a phase shift in the measured current signal. By measuring the real and imaginary components of impedance as a function of frequency, an understanding of the electrochemical processes can be gained. The potential signal can be described by equation 2.5 giving the current response described by equation 2.6. The resultant impedance is given by equation 2.7. Excellent tutorials/reviews of EIS have been published recently [150, 151], the manufacturer's websites such as those of Gamry and Biologic are excellent resources, and reviews of EIS specifically for solid-state batteries [152] are available.

$$E = E_0 exp(j\omega t) \tag{2.5}$$

$$I = I_0 exp(j\omega t - \phi) \tag{2.6}$$

$$Z(\omega) = \frac{E}{I} = Z_0 exp(j\phi) = Z_0(cos\phi + jsin\phi) \tag{2.7}$$

The impedance is plotted throughout this thesis using a Nyquist plot, where the real component of impedance is plotted on the x-axis and the negative of the imaginary component is plotted on the y-axis; such that the magnitude of the vector from the origin to each point gives the total impedance, and the angle of this vector to the x-axis gives the phase angle. Common impedance plots consist of semicircles of varying size and position.

To aid insight, equivalent circuit models (ECM) are used, which have to be carefully designed to be both simple, to enable consistent fitting of EIS data, yet sufficiently complex to accurately capture the experimental reality. I have aired on the side of simplicity throughout.

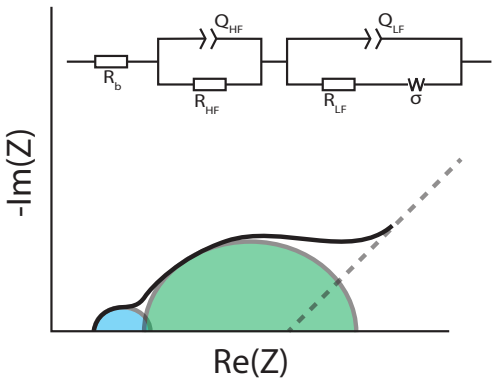


Figure 2.4: EIS Nyquist plot schematic with equivalent circuit model.

PEIS was performed using a biologic VMP3 using a single-sine mode with a frequency range of 50 mHz to 1 MHz with 10 logarithmically spaced frequencies per decade, resulting in a spectra collection time of twenty minutes. Data was fit using Zfit within Biologic EC-lab software and plotted in Matlab. Values of impedance are normalised with the electrode area.

2.4 PFG-NMR: Pulsed-field gradient nuclear magnetic resonance spectroscopy

PFG-NMR was experimentally carried out by Dr Hua Guo, therefore this overview is brief to capture the key principles of the technique to aid the analysis in the text.

The measurement of diffusion using NMR is possible if the magnetic field can be made so that it spatially varies, such that atoms within a crystalline lattice can be put into a spatially varied spin state. Then if the field is removed and the spin-state-bearing atoms diffuse, their motion can be measured. In the pulsed-field gradient technique, a magnetic field gradient, which is intermittently pulsed is superimposed onto a fixed magnetic field giving the nuclear spins a position-dependent phase angle.

A radio frequency (RF) signal is used to excite some of the nuclear spins into a higher energy state. When the signal is switched off, this leads to spin relaxation which emits radiation that can be measured. The intensity of the emission is determined by the original phase angle of the nuclear spins. A series of pulses of magnetic gradients and RF signals can be used to encode and decode the spatial distribution of spin states with a time delta between them. Experimentally the timing of the pulses is kept constant, the gradient strength is varied and the signal strength is measured. The decay in signal strength with gradient strength is related to the diffusion coefficient.

The alloy samples for nuclear magnetic resonance (NMR) tests were prepared with ^{6}Li-enriched lithium metal (95% ^{6}Li, 5% ^{7}Li Chunks, Sigma Aldrich). All the metal bulk were cut into small pieces and packed in NMR tubes that are sealed by J-Young's caps. For the InLi test a sample of the hand-milled InLi powder was loaded into a capillary tube. The ^{6}Li PFG NMR experiments for the alloys and ^{7}Li PFG NMR experiments for the intermetallic were carried out on a Bruker AVANCE III HD spectrometer with a magnetic field of 9.4 T (Larmor frequency of ^{6}Li is 58.89 MHz) equipped with a 5 mm single-axis diffusion probe. A stimulated echo pulse sequence was applied with an effective gradient pulse duration (δ) of 2 ms, a diffusion time (Δ) between 300-800 ms, and gradient amplitudes varying between 0.02 and 25 Tm^{-1}. A pulse delay of 1 s and a scan number of 128-512 were applied for each test.

2.5 XPS: X-ray photoelectron spectroscopy

XPS was experimentally carried out by Dr Sudarshan Narayanan and Ben Jagger, and they fit the raw XPS spectra. Therefore this overview is brief to capture the key principles of the technique to aid the higher-level analysis later in the thesis.

Low-energy x-rays (approximately 1.5 keV) are incident on a sample surface in a vacuum chamber. The x-ray photons interact with atoms on the sample surface, leading to the emission of electrons, with a characteristic energy defined by subtracting the incident photon energy from the electron's binding energy, which itself is determined by the material's bond structure. By measuring the energy and intensity of emitted electrons, we gain insight into the atoms present and their nearest-neighbour bonding in the sample. XPS is a highly surface-sensitive technique, typically probing a few nm of depth, therefore the technique can be coupled with an ion beam (typically argon) to etch away a surface to obtain depth-dependent composition data, or to sputter a material onto the sample surface in order to investigate the reaction products formed.

XPS measurements were made using a PHI Versaprobe III instrument capable of generating focused, monochromatic Al Kα X-rays at 1486.6 eV, under ultrahigh vacuum (chamber pressure $\sim 10^{-7}$ to 10^{-6} Pa) conditions. Alloy samples were prepared within a glovebox in the same way as electrodes by brushing a fresh surface and then calendering. These were then transferred into the XPS chamber using a vacuum transfer vessel (ULVAC PHI GmbH) to avoid contamination and ambient exposure. A 500 µm × 500 µm area from each sample was analysed. XPS data from the surface were collected with the monochromator operating at a power of 25 W and an electron beam voltage of 15 kV. In-built electron and low energy Ar sources were utilised for charge neutralisation. A pass energy of 224 eV was used for wide-sweep survey scans while high resolution core-level spectra were collected using a pass energy of 55 eV. The passivation layer depth-profiling was achieved with consecutive XPS analysis and Ar+ sputtering (4 keV, 3 mm × 3 mm) for a total of 60 minutes. Acquired spectra were fitted, after the application of a Shirley background, with Gaussian-Lorenzian line shapes, except for lithium metal which

was fitted with an asymmetric Voigt line shape, using CasaXPS software [153]. All spectra from alloy samples were charge referenced to the adventitious C 1s peak or the Li_2C_2 at 285 and 282.4 eV [154], respectively. Fitted regions were quantified and relative fractions of components were estimated using the relative sensitivity factors provided by CasaXPS.

For in situ sputtering of Mg, an argyrodite sample pellet was mounted on a special sample holder similar to the setup described by Wenzel et al. [93]. A Mg foil (∼500-700 μm thick), prepared by pressing Mg flakes (Sigma Aldrich, purity 99.9%) in a pellet die at 500 MPa for 5 minutes using a hydraulic press, was then mounted on to the vertical plate. The in situ sputtering of Mg was performed using an Ar+ ion gun at an ion accelerating voltage of 4kV, with the beam being rastered over a 3mm x 3mm area. Photoemission spectra were taken with neutralisers switched off. The spectra collected during in situ sputtering were all charge referenced to Cl $2p_{3/2}$ at 198.5 eV, considering that the position of the spectra remained unchanged throughout the sputtering process. [90, 155].

2.6 Other techniques

Some other techniques were used sparsely throughout this thesis including x-ray diffraction (XRD), atomic force microscopy (AFM) and cross-sectional plasma-focused ion beam milling (PFIB). The methods used are outlined in the experimental chapter alongside the collected data.

3

Elastic and plastic properties of lithium metal from EBSD coupled nanoindentation

Contents

3.1 Introduction 28
3.2 Surface Preparation 29
3.2.1 Ion milling 29
3.2.2 Grind and polish 29
3.2.3 Microtome 30
3.3 Modelling of the lithium-electron interaction 33
3.4 EBSD of Lithium Metal 36
3.5 EBSD of other Alkali metals. 37
3.5.1 Potassium metal 37
3.5.2 Sodium metal 38
3.6 Optimisation of indentation parameters 39
3.6.1 Frequency of continuous stiffness measurement. 40
3.6.2 Characterising indentation tip 40
3.6.3 Machine compliance calibration 43
3.6.4 Pile up correction 44
3.7 Elastic Mechanical Response 44
3.7.1 Variation in indentation modulus with crystal orientation 46
3.7.2 Euler Angles 47
3.7.3 Fitting to modulus data 48
3.8 Plastic Mechanical Response 51
3.9 Adhesion 54
3.10 Impact of measured nanoscale hardness. 55
3.11 Conclusions 58

3.1 Introduction

Much of the work reported in this chapter is published in Materials Today Energy [156].

Failure of solid-state lithium metal batteries occurs due to the penetration of metallic lithium into the solid-state electrolyte [74]. The fact this occurs is somewhat counter-intuitive, lithium is a soft metal akin to butter so normally it shouldn't penetrate a stiff ceramic. Two materials are interacting, lithium metal and the solid-state electrolyte. Measuring and understanding the mechanical properties of both is needed to understand the interaction which leads to failure.

Lithium is highly mechanically anisotropic [104], and therefore accurate nano-mechanical characterisation of lithium metal requires electron backscattered diffraction (EBSD) to map the crystallographic orientation of the surface. Successful EBSD of lithium has been previously reported once, with the surface prepared by broad beam ion milling[157]. The ion implantation associated with this makes it inappropriate for the preparation of a sample for an indentation study and therefore a new method has been developed. Due to the electron-atom cross-section scaling non-linearly with atomic number, lithium represents a limit case in the EBSD of metals; with the low electron cross-section leading to a large interaction volume and therefore low band contrast. Modelling of the electron interaction volume enables us to optimise imaging parameters to maximise the quality of lithium EBSD maps.

The mechanical response of lithium consists of a recoverable/elastic component and a permanent/plastic component. Lithium's elastic response is fully described by its stiffness tensor C, which has three independent components C_{11}, C_{12} and C_{44}. The tensor allows the resultant elastic strain to be calculated from any given stress tensor. Stiffness is independent of the material length scale. The plastic component is captured in simple metals by yield stress and a work-hardening exponent. Lithium's plastic behaviour is more complex due to substantial size dependence and time-dependent deformation.

3.2 Surface Preparation

Metallurgy was revolutionised by the development of surface polishing, grinding and etching methods that enabled optical microscopy of metals and their microstructure. In modern research, surface preparation is essential for techniques such as EBSD and nanoindentation.

3.2.1 Ion milling

Ion milling either by broad-beam or focused ion beam (FIB) is an effective method to prepare flat surfaces for EBSD and indentation in most materials. In typical metals such as molybdenum, the effect of ion-beam damage on measured mechanical properties is negligible [158], but due to lithium's low atomic mass, the penetration depth of milling ions is significantly higher. Stopping range of ions in matter (SRIM [159]) calculations suggest a mean ion implantation depth of 102±20 nm in Li compared to 11±6 nm in Mo with a 30 kV Ga^+ beam. The implantation depth of gallium ions in both lithium and molybdenum was calculated using open-source SRIM-2013 software. The trajectories of 10,000 ions were calculated in each case, with a beam voltage of 30 kV. The phase diagram of lithium and gallium is complex with many intermetallics that may form [160]. The contribution of this damaged layer to the mechanical properties is unclear. In addition, lithium's low melting point and low hardness lead to poor results when milling at non-cryogenic temperatures. I chose to avoid ion milling in the preparation of mechanical test samples.

3.2.2 Grind and polish

Grinding and polishing do not work for lithium metal. Neither water itself nor water-based polishing mediums can be used. With a Mohs hardness of 0.6, pure lithium tends to deform plastically (squash and shear) rather than polish, even if effort is made to minimise the compressive load. A Buehler MiniMet 1000 semi-automatic grinder/polisher was moved into a glovebox. Lithium samples were secured to the holder using superglue. Successive silicon carbide papers of 400, 800, 1200, 2500 and 4000 grit were used for three minutes each with minimal

force and a speed of 30 cycles/min, followed by 9, 3, 1 and 0.1 micron polishing cloths with matching oil-soluble Kemet diamond polishing paste. Pure lithium was too soft for this technique even where the minimal downward force was applied. The final result was a dull finish. The coarser grit sandpapers rapidly removed material, and later sandpapers seemed to stir the upper layer of material, rather than abrade it. Lithium was also found to be reactive with diamond lapping films (Agar scientific Ultraprep) forming a thin black layer.

3.2.3 Microtome

Lithium is as soft as biological tissue ($\sigma_y \approx 1$ MPa [161]). Microtome is a technique widely used in biomedical research to prepare microscopy slides of tissue and bone. The technique involves precisely shearing off a thin layer of material from the surface of the sample using a very sharp blade, leaving a flat surface. The shear deformation is localised to the surface. In biological samples, microtome can achieve very low surface roughness of less than 10nm variation [162]. This technique is particularly valuable for samples with two or more phases of different hardness, such as an alloy with both a solid solution and an intermetallic phase. Microtome removes a flat plane of material, whereas abrasive techniques would preferentially remove the softer phase, leading to depth variation.

In this work the technique was used in reverse, small layers were cut from a mounted lithium metal block, leaving a flat surface behind. The exposed surface is fresh, and therefore free from a reaction layer that would form during any wet polishing or etching process, although a reaction layer naturally forms, even in highly controlled glovebox atmospheres over several hours.

As can be observed in figure 3.1A, the microtomed surface is shiny, with a mirror metallic lustre. The as-prepared surface is fresh but even within the highly controlled glovebox atmosphere, this finish dulls over a day. In an electron microscope, the surface is locally flat and a tabletop vice can be used to guide the blade path during cutting to achieve a single flat plane across the sample. The microtomed surface of lithium metal was characterised using SEM microscopy and atomic force

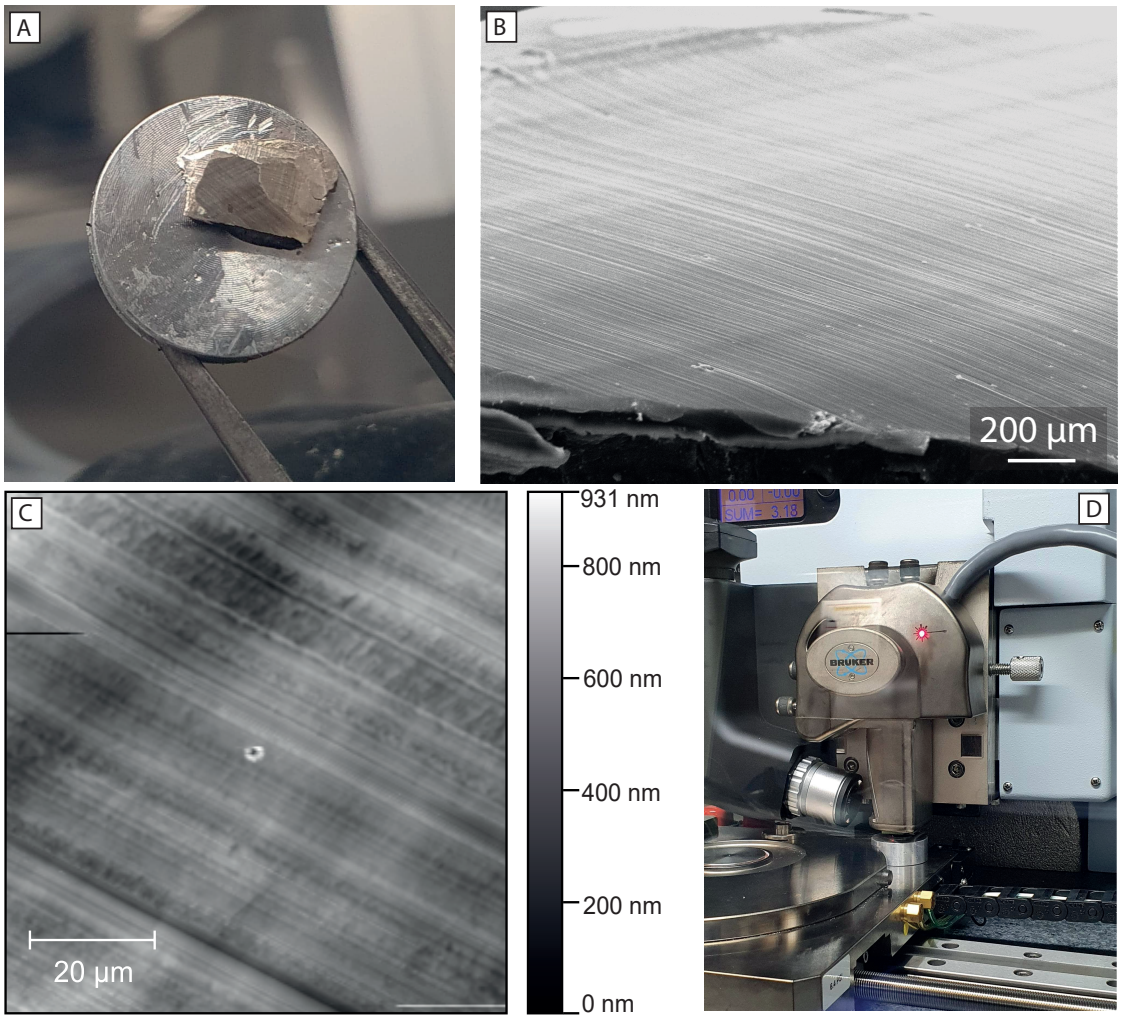


Figure 3.1: Microtomed lithium surface characterisation. (a) Photograph of microtomed lithium metal. (b) SEM micrograph of surface, low magnification. (c) AFM map of surface roughness with 80 micron scan width. (d) Photograph of AFM head during scanning.

microscopy (AFM) with a Bruker Dimension Icon, contained within a dedicated glovebox. Small grooves can be observed in the SEM image shown in figure 3.1B. An example AFM map, collected in PeakForce mode with an 80-micron square scan area, can be seen in figure 3.1C. A photograph of the setup used for AFM characterisation is included in figure 3.1D.

The surface roughness across a range of areas scanned, with their associated area are detailed in table 3.1. The mathematics behind calculating surface roughness are not independent of area, therefore for a larger sampled area, a larger roughness is observed - this is apparent in the results. With a scan size of 25 micron,

Sample	Area	Average R (nm)	RMS R (nm)	Δh (nm)	Width (um)
1	1	34.88	50.70	583.0	25
	2	41.07	54.96	457.2	25
2	3	122.4	156.3	907.0	50
	4	179.6	229.9	1831	92.7
3	5	216.8	272.4	1677	80
	6	157.8	203.7	833.1	80
	7	146.3	182.2	926.4	80
	8	107.0	145.9	1156.6	80
	9	72.2	95.85	637.2	80
All	Mean	119.8	154.7	1000.9	-
	StDev	58.7	72.2	449.1	-

Table 3.1: AFM results of microtomed lithium metal. Average R is mean surface roughness (S_a), and RMS R is root mean square roughness. Δh is the difference between the maxima and minima of the height. The width is square scan size.

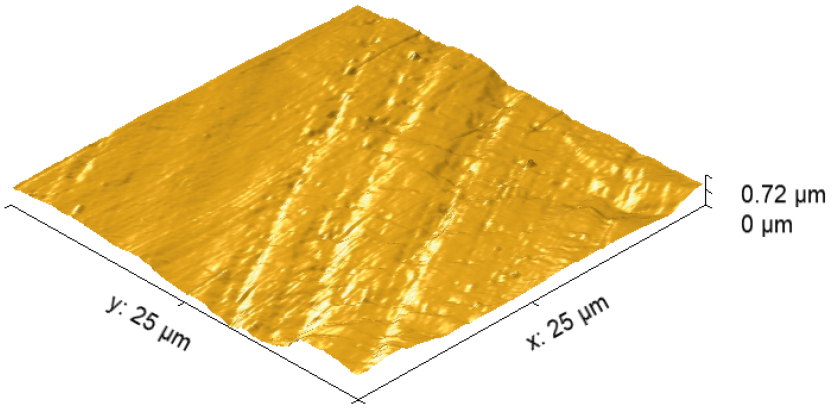


Figure 3.2: 3 dimensional render of microtomed lithium metal surface.

approximately the area of a single indentation, surface roughness well below 100 nm is achieved by manual microtome. This is sufficiently flat for EBSD and indentation studies. There is scope for improvement, microtome machines enable the optimisation of cutting rate, blade angle, material temperature, quantity of material removed per cut and perfectly straight cutting path. This method seems powerful to prepare lithium samples that have fresh surfaces, that are extremely smooth at the nanoscale, and a surface roughness of less than 10nm across a 25 micron scan area seems achievable [162].

3.3 Modelling of the lithium-electron interaction

The electron backscatter cross-section of a material scales non-linearly with atomic number, meaning lithium (Z=3) represents a limit case for EBSD. The low electron cross section leads to a large interaction volume and therefore poor EBSD resolution and low-contrast patterns. In this section, modelling of the electron-lithium interaction is performed. The insights gained from this modelling allow optimisation of imaging parameters. Casino [163] was used to generate predicted electron trajectories in lithium at a sample tilt of 70 degrees. A total of 10,000 incident electrons was used in each simulation. Backscattered electrons were defined as those which exited the sample surface. No filtering for exit angle was applied as the overwhelming majority of these are likely to be captured by the EBSD detector. The trajectories were then processed in Matlab to plot interaction density distributions. In some of the figures, the plotted subset was sampled by backscattered electron energy to investigate the effect of energy filtering on lithium EBSD resolution.

In most metals, for a beam perpendicular to a sample surface, upwards of 30% of incident electrons backscatter. The backscattered electron (BSE) yield from lithium in this geometry is very low, at around 4% across a range of voltages. This reflects the small degree of lithium-electron interaction. At 30 kV, the modal penetration depth of lithium is 34.4 and 24.8 μm for all electrons and backscattered electrons respectively, and at 20 kV the equivalent values are 16.7 and 12.5 μm. By comparison, these penetration depths are over an order of magnitude deeper than for iron (Z=26) at the same beam parameters.

At the high sample tilt of 70 degrees used for EBSD, lithium's backscattered electron yield significantly increases to 23% - underlining the importance of sample tilt in successful EBSD. However, the large penetration depth of electrons in lithium strongly determines EBSD resolution in the axis of specimen tilt. The density of electron-sample interactions predicted by Casino for a 30 kV beam voltage is shown in Figure 3.3A, as well as the resolved density plots in the three Cartesian axes (Figure 3.3B, C and D) – with x in the axis of sample tilt and z normal to the sample surface. The bounding box within which 90% of the interactions are

contained is 26.0 μm x 16.8 μm x 4.5 μm. Penetration depth can be reduced by lowering the SEM beam voltage, which is proportional to the incident electron speed. For a lower beam voltage of 20 kV, the equivalent bounding box is 12.4 μm x 7.9 μm x 2.1 μm – approximately half in all dimensions.

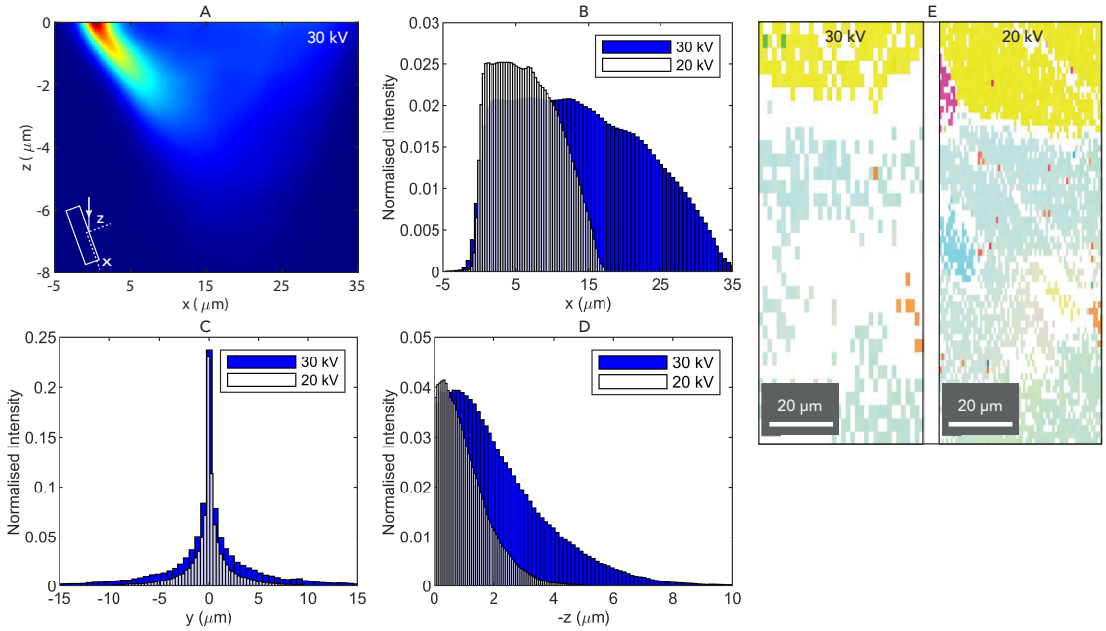


Figure 3.3: EBSD parameter optimisation. (a) Map of electron-sample interaction density of backscattered electrons predicted by CASINO for 30 kV beam voltage. (b, c, d) Density of interactions along x, y and z for 20 kV and 30 kV incident beams. E - EBSD scan of the same region at 30 kV (left) and 20 kV (right) demonstrating a higher rate of indexing at lower beam voltage.

Comparative experimental EBSD maps were taken for the same regions at 20 kV and 30 kV beam voltage, with the current modified to maximise the contrast of the Kikuchi pattern for each case. These maps are shown in Figure 3.3E (images have been stretched to correct for 70-degree tilt). In the 30 kV case, regions with grain boundaries running across the sample (horizontal in figure) are poorly resolved, but grain boundaries running in the direction of tilt (vertical in the figure) are well resolved. This reflects the large penetration depth in the direction of tilt (Figure 3.3B), and the comparatively small lateral beam spread (Figure 3.3C). Reducing the beam voltage to 20 kV, the quality of the EBSD map obtained is greatly improved, with points near grain boundaries running across the sample resolved more frequently and accurately. Lowering the beam voltage further to

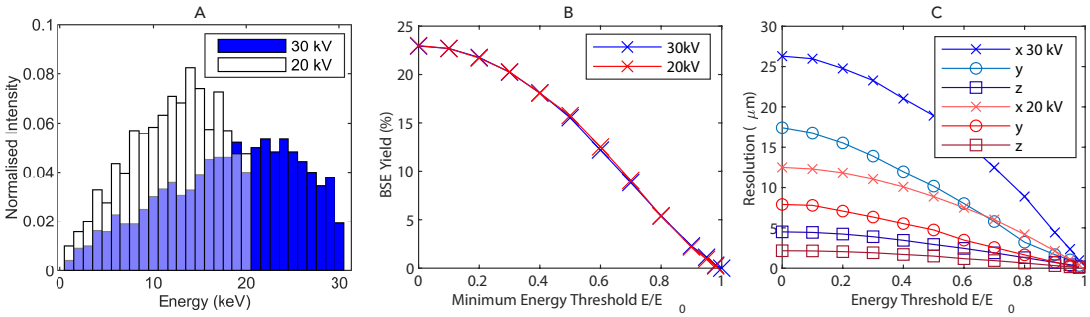


Figure 3.4: Electron backscatter diffraction in lithium metal. (a) Histogram of backscattered electron energies for 20 kV and 30 kV incident beams. (b) BSE yield with minimum energy threshold. (c) Resolution is defined as a bounding box for 90% of BSE interactions in each axis.

10 kV would presumably improve the EBSD resolution further, however, we were unable to resolve a Kikuchi pattern at 10 kV with our detector.

The information on the electron penetration depth from Casino, and the experimental maps in this work, appears to contradict the data presented by Brodusch et al. [157] where the maximum penetration depth of backscattered electrons is calculated to be 350 nm and 50 nm for 30 kV and 10 kV respectively. However, their much smaller penetration depth relies on the assumption that only backscattered electrons losing less than 2% of their energy influence the diffraction pattern, whereas we have presented the data for the full backscattered electron population. As the originally cited paper [164] describes, the contribution of lower energy backscattered electrons to the diffraction pattern becomes greater for materials with lower electron cross sections. Given this trend is established for silicon, iron and iridium, with electron cross-sections 8, 16 and 44 times larger than lithium respectively, the contributions of low energy electrons to the diffraction pattern are substantial in lithium [165].

The effect of energy threshold on both resolution and backscattered yield was investigated. The energy distribution of backscattered electrons for a tilted lithium sample is plotted in Figure 3.4A. For typical materials, with a reasonable electron cross-section, most backscattered electrons have energy close to the incident beam energy [164, 165]. The energy distribution of backscattered electrons from lithium is broad (Figure 3.4A). Whereas the peak of the backscattered energy distribution

with Iron for a 30 kV incident beam is at 29 keV (96% of the incident energy [164]), lithium's is at 22 keV (73% of the incident energy). For iron 55% of all backscattered electrons have energy within 10% of the incident energy, for lithium the value is just 13%. The assumption that only the backscattered electrons with energy within 2% of the incident energy contribute significantly to the Kikuchi patterns is therefore not applicable for lithium. This helps to explain the poor contrast EBSD patterns of lithium metal observed experimentally, despite the considerable BSE yield, with electrons taking a wide range of different pathways through the material all contributing to the diffraction pattern – effectively blurring it [166].

Intuitively, the electrons that lose the most energy whilst interacting with the sample are those that take the longest path through the material. This highlights an opportunity to improve EBSD mapping of lithium metal, and other low-atomic number materials, using energy-filtered EBSD, increasing band contrast for Kikuchi patterns and improving resolution - particularly down the slope of the sample. Figure 3.4B and Figure 3.4C show the effect of applying a minimum threshold on the BSE yield and resolution in each axis. The data shows that a substantial increase in resolution can be achieved but with an associated drop in electron yield. Special energy thresholding detectors are needed to investigate this experimentally.

3.4 EBSD of Lithium Metal

Using microtome blades to prepare the surface, and using imaging parameters based on the electron-lithium modelling, I was able to successfully EBSD lithium metal (Figure 3.5A). The colouring of each pixel denotes the crystal lattice orientation relative to the sample normal at that point, calculated from the Kikuchi diffraction pattern (figure 3.5D). The Kikuchi pattern is blurry compared to a typical metal as discussed. The orientation-colour relationship is shown in the inverse pole figure (Figure 3.5D). In the map shown in Figure 3.5A, 78% of the 29400 points indexed successfully. It can be observed from the map that points near lateral grain boundaries are rarely resolved. The grain size of lithium metal is large, approximately 150 micron.

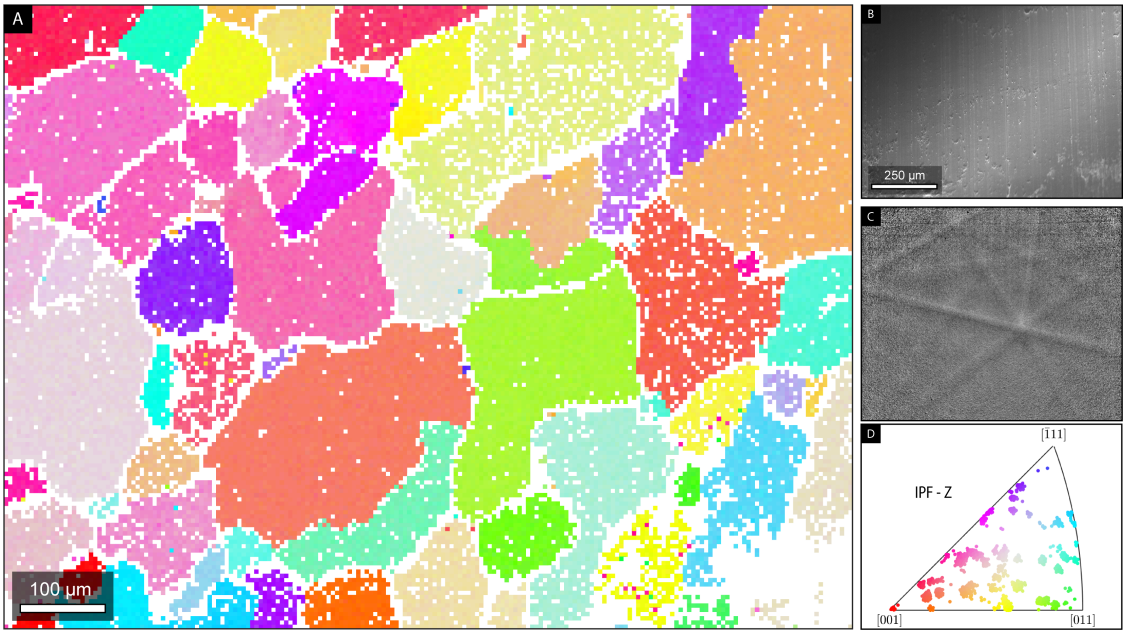


Figure 3.5: EBSD of high purity lithium metal prepared by manual microtome. 20 kV beam voltage.

3.5 EBSD of other Alkali metals.

Having developed this capability with lithium metal, I applied it to both sodium and potassium metal.

3.5.1 Potassium metal

The EBSD of potassium metal is very challenging due to its high reactivity. Figure 3.6A shows an IPF Z EBSD map of a piece of potassium metal (Sigma Aldrich, chunks 99.95%), with the surface prepared by microtome. Using a beam voltage of 30 kV to maximise beam penetration, clear Kikuchi patterns were obtained. The bands are significantly sharper than lithium metal as a direct result of the larger electron cross-section of the material. As can be seen in the map, the grain size of potassium is very large, on the order of millimetres. Figure 3.6B is a photograph of the sample after imaging, with the scanned area marked with a red rectangle. The blue tint of the sample developed over the 4 hours the map took to complete, this is different to the metallic, lustrous surface immediately after the microtome. The grain structure of the sample is visible to the naked eye. Figure 3.6C shows a partial

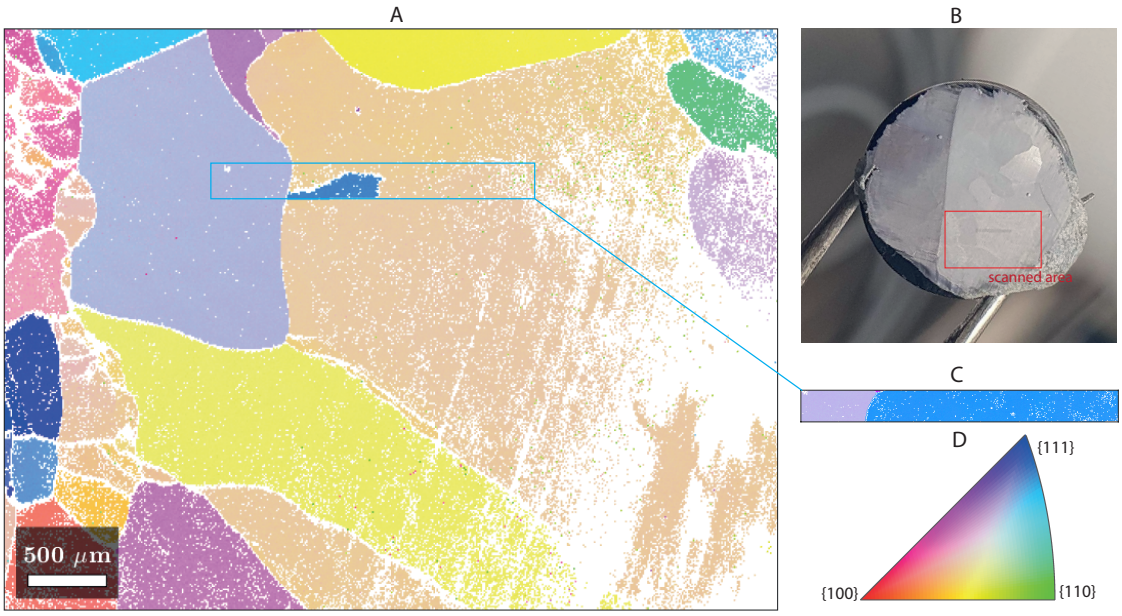


Figure 3.6: EBSD of potassium metal. (a) EBSD map (IPF Z) of potassium metal. (b) Photograph of potassium sample after imaging. (c) EBSD of region highlighted in blue rectangle taken before the main map. (d) Inverse pole figure (IPF) showing the orientation of crystal plane perpendicular to sample normal.

test EBSD map taken immediately before the full map in A was captured. The corresponding region is highlighted in A. As can be seen, the orientations indexed are different in each case, with the blue <111> grain mostly subsumed within the orange grain in the larger map, and the triple junction with the purple having progressed towards the top of the map. This shows that potassium is very thermally active, with the grain structure evolving during the imaging period. Either the vacuum conditions within the SEM chamber or the incident electron beam may be accelerating this process. The ambient pressure melting point of potassium is 63.5 °C. Significant artefacts can be seen on the map, especially in the lower right corner. The increased atomic number increases sensitivity to surface roughness and contamination. As far as I am aware this is the first EBSD of potassium reported.

3.5.2 Sodium metal

EBSD mapping of sodium was also successfully attempted as can be seen in Figure 3.7. The piece of sodium investigated has a wide range of grain sizes, but they are mostly large. The artefacts from the microtome blade scratches

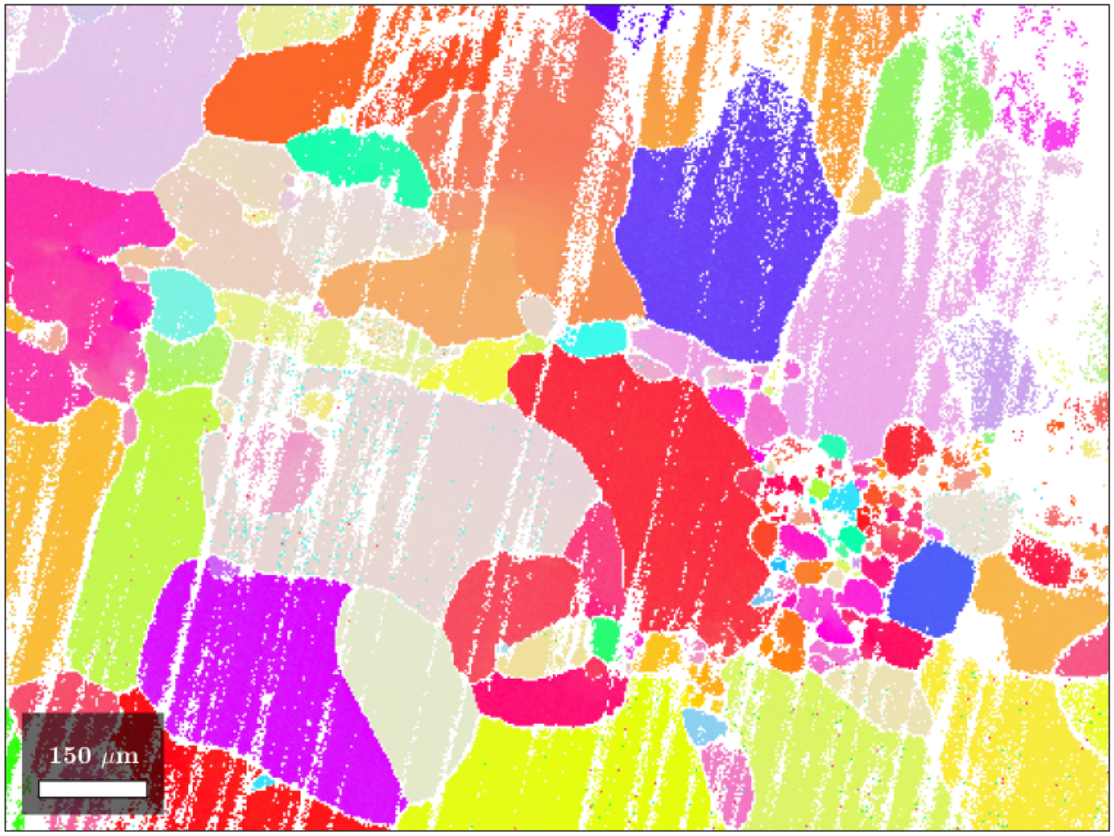


Figure 3.7: EBSD map of sodium metal.

can be seen in this figure, highlighting the potential to achieve superior mapping by using a microtome machine.

3.6 Optimisation of indentation parameters

Obtaining reliable, consistent indentation measurements of lithium metal was challenging compared to the indentation of other materials discussed later in this thesis. This is due to its high stiffness/hardness ratio, viscoplasticity and adhesion. The microtome technique described in the previous chapter minimised the effect of any surface contamination layer and achieved a smooth surface. A large dynamic load amplitude of 50 µN at a target quasistatic load of 1000 µN was used scaling with the square root of quasistatic load to minimize viscoplasticity error while retaining indenter contact [149]. Because the continual stiffness measurement method captures both the load and unload segment of the oscillation, the effect

of creep on measured stiffness is small.

3.6.1 Frequency of continuous stiffness measurement.

The frequency of continuous stiffness measurement (CSM) typically has a small impact on the measured values. However, due to lithium having a relatively low modulus and significant viscoplastic component, resonance was observed for frequencies greater than 150Hz leading to very noisy stiffness data. To select a test frequency, an indent was performed with a peak load held for 300 seconds. The frequency was changed every second during the hold, in a random order, with the resultant displacement amplitude and phase shift between the load and resultant displacement oscillation measured. The results are plotted in figure 3.8 and figure 3.9. A frequency of 70 Hz was selected as this gave a small displacement amplitude and a phase shift near zero, with a tight spread. This minimised the resonant behaviours enabling the elastic response to be measured by the CSM technique.

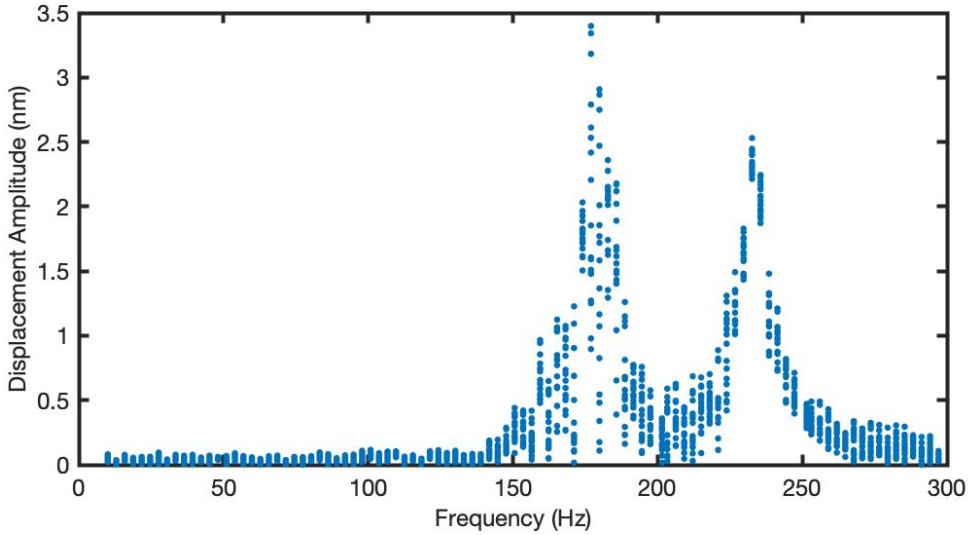


Figure 3.8: Displacement amplitude with CSM frequency, order randomised.

3.6.2 Characterising indentation tip

The shape of the indentation tip is one of the primary sources of uncertainty in indentation tests. Both hardness and modulus depend upon it. Hardness (H) is

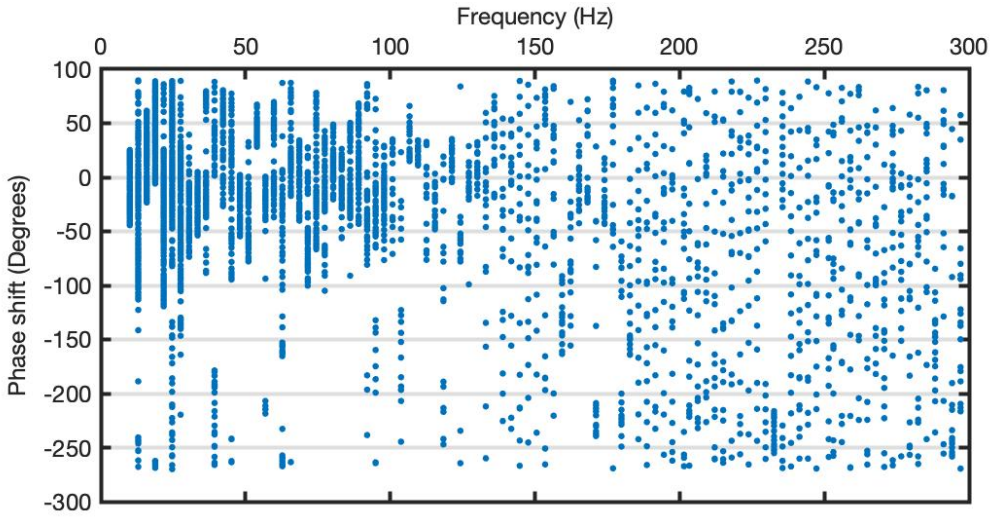


Figure 3.9: Phase shift with CSM frequency, order randomised.

defined by equation 3.1 where P is indentation load and A_c is the contact area. Indentation modulus (M) is defined by equation 3.2 where S is stiffness.

$$H = \frac{P}{A_c} \tag{3.1}$$

$$M = \frac{\sqrt{\pi}}{2} \cdot \frac{S}{\sqrt{A_c}} \tag{3.2}$$

Indent tip shapes are typically calibrated by indenting fused silica. Given fused silica is an amorphous ceramic, it has a constant E/H ratio with depth and both of these values are well known. Therefore performing a series of indents at a range of loads in fused silica allows the tip shape to be back-calculated from the data. As lithium is around 1000x softer than silica (Hardness of fused silica =9.8GPa [167]) the method is not viable, as the indentation depth range in silica indentation is too shallow to map the whole tip depth used for lithium indentation. The area function measured in this method is also sensitive to any other incorrect calibrations of the indentation system.

Instead, the indentation tip shape used for the experiments throughout this chapter was characterised using atomic force microscopy (AFM), to directly measure the tip shape and therefore allow for calculation of the area function. The AFM used

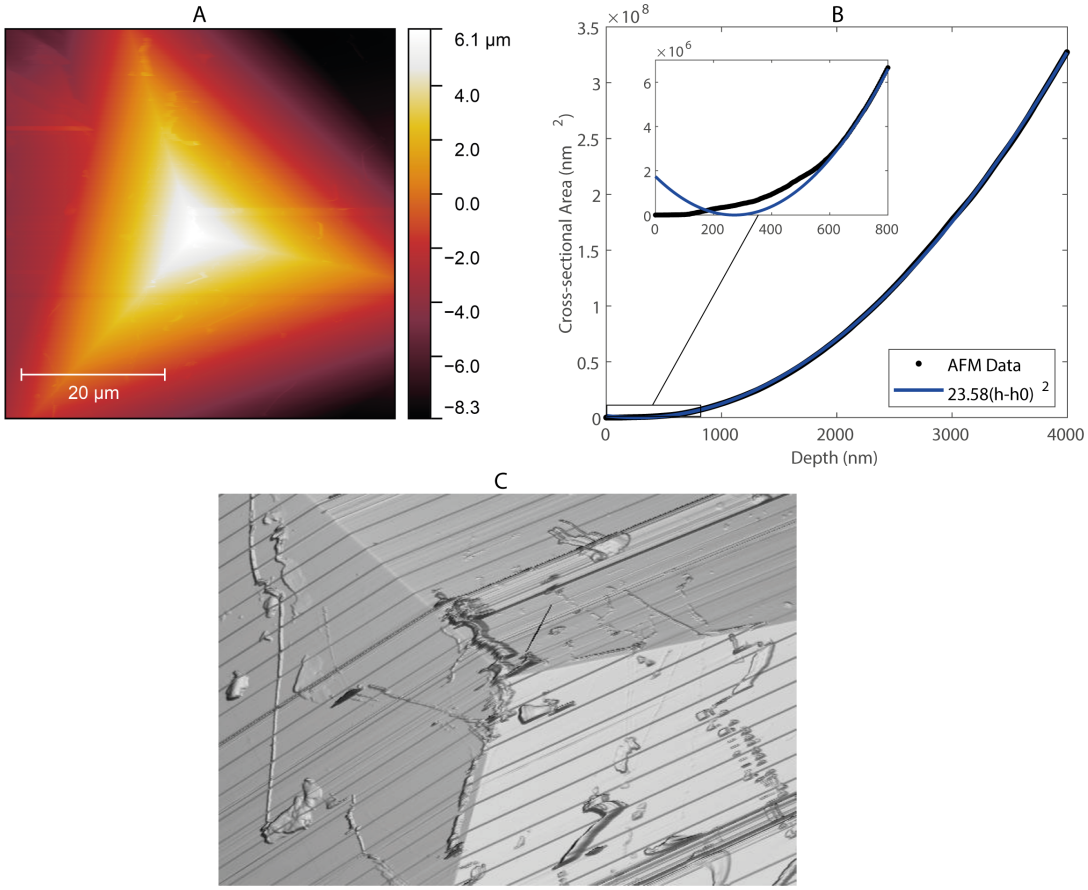


Figure 3.10: AFM of indentation tip. (a) AFM image of indenter tip. (b) Cross-sectional area function. (c) Image of tip processed with openGL lighting in Gwyddion, showing debris at the tip.

was a Bruker Dimension Icon, contained within a dedicated glovebox system. The indentation tip was mounted onto a screw mount provided with the PI88 indentation system, ensuring it was oriented perpendicular to the x-y AFM scan plane.

A scan rate of 0.1Hz was used, with 1024 samples per line over a square area of length 54 micron, with the tip peak approximately in the centre. 3 successive images were captured, with the final one being the cleanest. This is shown in figure 3.10A. The image showed the Berkovich tip was effectively a perfect pyramid, with no tip blunting. The area function reflected this, with the data in figure 3.10B fitting $A = C(h - h0)^2$ well, with a value of C = 23.58 - close to the ideal 24.6. The height offset h0 was needed as a close look at the tip (C) shows that a small amount of dirt was located at the tip during the AFM scan. This is reflected in the area function

with a larger area being measured than the true tip. Based on this data, I concluded that an area function of $A = 23.58h^2$ was the most accurate area function to use.

Cross-sectional contact area strongly determines measured modulus. Any dirt attached to the indent tip significantly affects the measured mechanical response. For most materials, this is not an issue as the modulus of any contaminant is typically far below that of either diamond or the indented material, and the dirt removes itself after a couple of indents. For lithium, its low modulus coupled with its high adhesion, means that dirt can easily get stuck to the tip. Successive indentation does not remove the dirt. Tip cleaning was always done before indentation tests using a cotton bud, with cotton pulled to make soft fibres, under an optical microscope outside of a glovebox before any tests; and the tip was carefully inspected once in the SEM to ensure the tip was free of debris. Due to the possibility of tip contamination during indentation testing, there is uncertainty in the effective area at small indentation depths; therefore where possible, indentation data was fit with data collected deeper than 500 nm depth.

3.6.3 Machine compliance calibration

Quantifying the mechanical contact of the indenter tip and the sample would ideally be done using an infinitely stiff indenter frame. Despite the manufacturer's best efforts, the frame has compliance, meaning for a given contact force, the indenter rig has a finite elastic displacement. This is especially true for in-situ indenters such as the one used in this work, as the frame has to be much smaller to fit within an SEM chamber. To obtain accurate materials property measurements, we must account for machine compliance (C_f) when calculating the material response from the measured stiffness and displacement values. The compliances add linearly, so the correction is of the form in equation 3.3. Machine compliance was measured using fused silica mounted in the same way as the samples, giving a value of 8.02 nmN^{-1}.

$$\frac{1}{S} = \frac{1}{S_{meas}} - C_f \tag{3.3}$$

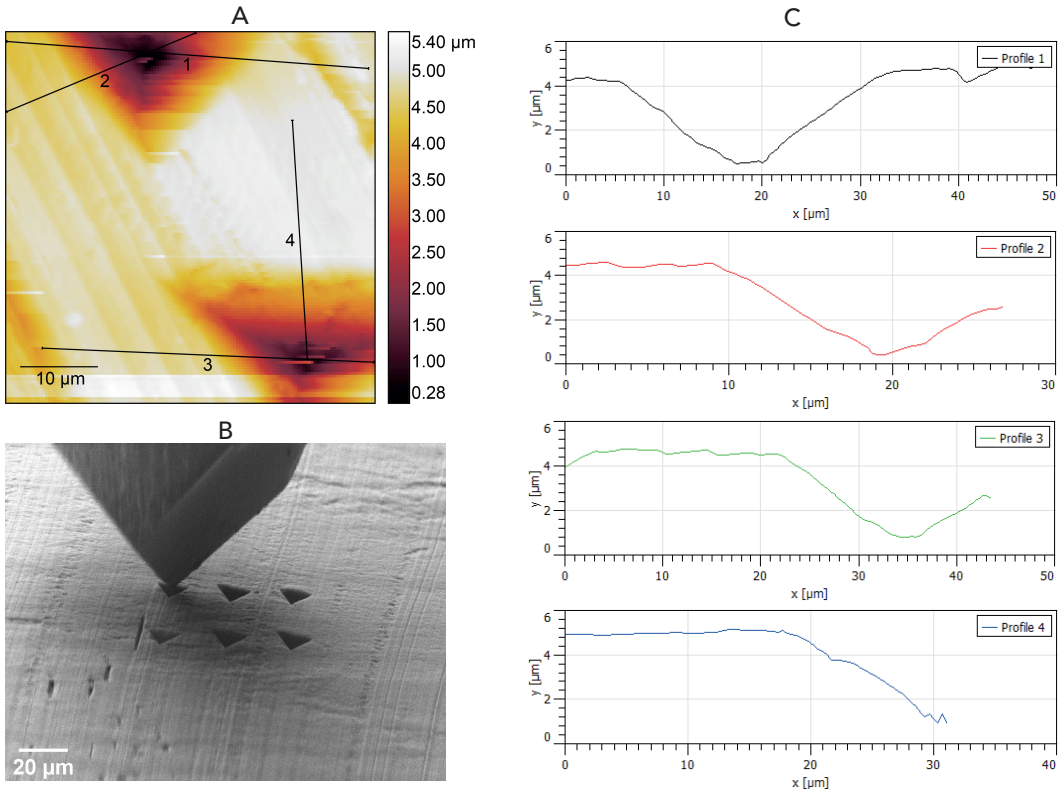


Figure 3.11: Data capturing indentation profile. (a) AFM image of indents in lithium with associated profile lines. (b) SEM image during indentation. (c) Height profiles of indentation.

3.6.4 Pile up correction

In many nanoindentation studies, a correction term of around +10% is applied to the contact area to account for a pile-up of material that gathers around the tip during indentation. During SEM indentation we did not observe any pile up (figure 3.11B). To confirm this we performed atomic force microscopy on the indented lithium surface to map the height profile. As can be seen in the raw image, and in the associated line scans (figure 3.11A and C), no pile-up is observed. We, therefore, have not applied a pile-up correction to the data.

3.7 Elastic Mechanical Response

Having successfully EBSD mapped lithium metal samples, arrays of indents were performed within large grains. Figure 3.12A and B show an example indent array's

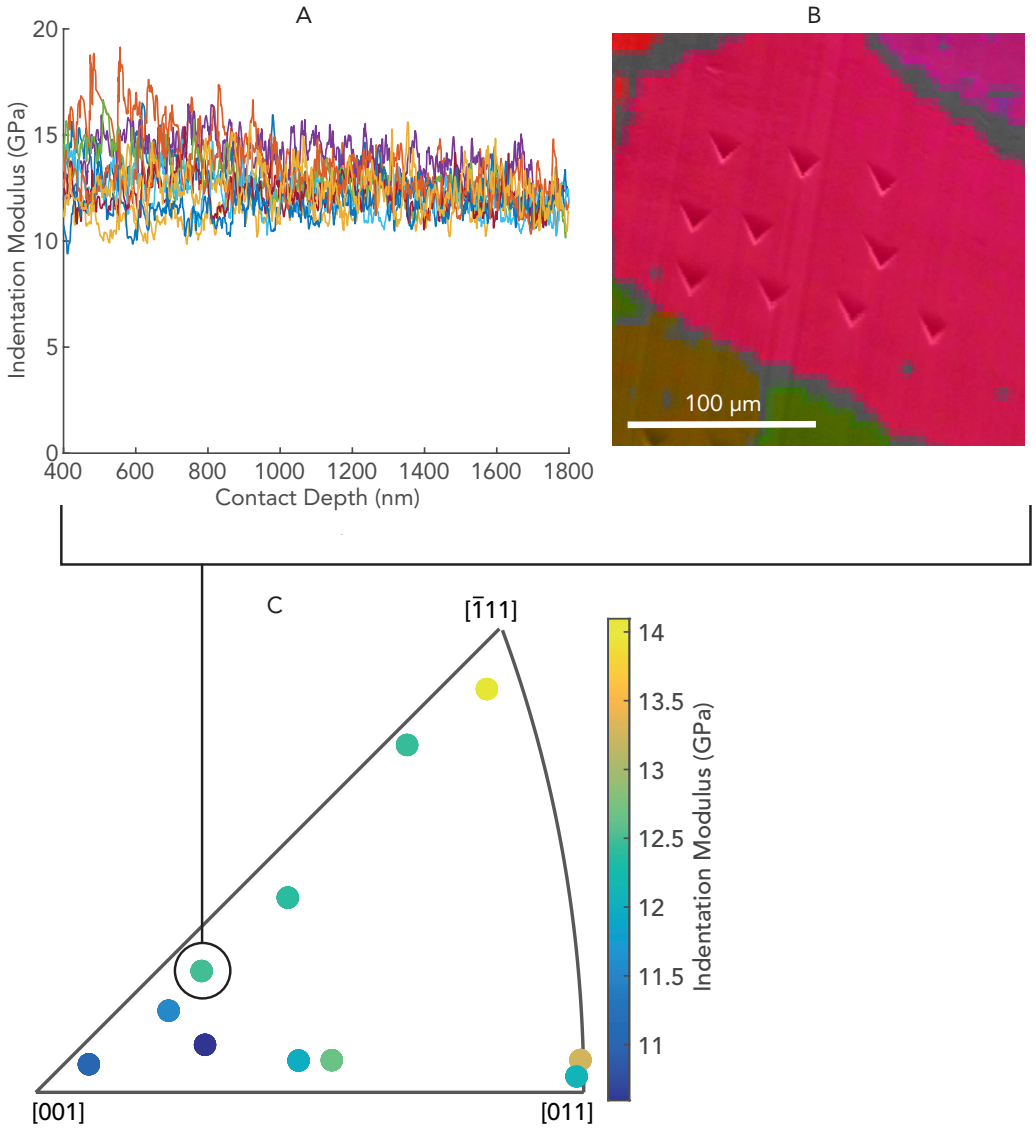


Figure 3.12: Orientation dependent elastic moduli of lithium metal. (a) Measured indentation modulus vs. depth for one grain. (b) Corresponding EBSD map superimposed on SEM image of indented grains. (c) Indentation modulus inverse pole figure showing orientation dependence of measured indentation modulus.

continuous stiffness measure of modulus and the array's corresponding EBSD map. By averaging the modulus data and crystallographic orientation for each grain's dataset, we can obtain a point in surface orientation – modulus space, which is plotted on the inverse pole figure in Figure 3.12C.

The averages of measured indentation modulus for multiple indentations within

grains of differing orientation, plotted in Figure 3.12C, show the expected trend of mechanical indentation anisotropy for cubic crystals, with indents along vectors near the <100> axis of the crystal having lower moduli (11 GPa) than those near the <111> direction (14 GPa).

3.7.1 Variation in indentation modulus with crystal orientation

To extract lithium's stiffness tensor components from this modulus-orientation data, I have repeated the methodology in the 1994 Vlassak and Nix paper[168], which builds on their paper a year earlier [169]. The product of the load distribution under an indenter, and the displacement due to a unit load for a given material stiffness tensor, as derived by Barnett and Lothe [170], is integrated over the half-space boundary. The mathematics involves defining a surface normal to the boundary of an infinite half-space in a coordinate system with its 3 axes along the principle <100> axes of the crystal, before performing the integral in equation 3.4 where gamma is the angle between a vector **t**, which lies in the half-space boundary and starts at the origin, and some fixed datum in the half-space boundary. The original expression assumes a circular contact area to greatly simplify the maths, and therefore a corrective factor of 1.06 is applied to account for the triangular shape of the Berkovich tip [168]. The matrix β is itself defined by the equation 3.5, with **m** and **n** being two perpendicular vectors to **t**, such that they form a right-handed cartesian set, with the integral over φ summing the contributions for all orientations of **m** and **n** in their plane. The matrices of type (**ab**) are defined by the final expression 3.6, with C being the elastic stiffness tensor, with the indices converted by the convention 11 -> 1, 22 -> 2, 33 -> 3, 12-> 4, 23-> 5, 13->6, and a and b being the cosines of the direct angles between the surface normal and the axis of the subscript. Einstein notation is used throughout, such that repeat indices in a single term denote a sum over 1 to 3.

$$M = 1.06 \times 16\pi^2 \left(\int_0^{2\pi} \alpha_m \beta_{km}^{-1}(\gamma) \alpha_k \, d\gamma \right)^{-1} \tag{3.4}$$

$$\beta_{km}(\mathbf{t}) = \frac{1}{8\pi^2}\int_0^{2\pi}\left\{(\mathbf{mm})_{js} - (\mathbf{mn})_{jk}(\mathbf{nn})^{-1}_{kr}(\mathbf{nm})_{rs}\right\}d\varphi \tag{3.5}$$

$$(\mathbf{ab})_{jk} = a_i C_{ijkm} b_m \tag{3.6}$$

Although the maths is laboured, the indentation modulus solely depends on the orientation of the surface normal and the stiffness matrix of the material. The results obtained from these equations have been used across a range of materials systems, giving stiffness tensor values that match other techniques such as single crystal acoustic echo [168, 171]. A Matlab script was written to implement this method, calculating the indentation modulus given the surface crystallographic orientation.

3.7.2 Euler Angles

EBSD mapping of the sample outputs the grain orientations as a set of Euler angles. These are three angles (ϕ, Φ, φ) that define the rotation needed to map the sample coordinate system (x,y,z) onto the crystal coordinate system if they are defined as vertical vectors acted on from the left[146]. The rotation is defined by an anti-clockwise rotation of ϕ about the initial z-axis (z), followed by an anti-clockwise rotation Φ about the new x-axis (x'), followed by a rotation φ about the new z-axis (z").

$$\begin{pmatrix} u \\ v \\ w \end{pmatrix}_c = R_{total}\begin{pmatrix} x \\ y \\ z \end{pmatrix}_s \tag{3.7}$$

$$R_{total} = R_{z''}R_{x'}R_z \tag{3.8}$$

The first rotation about the z axis is easily defined as 3.9:

$$R_z = \begin{pmatrix} cos\phi & -sin\phi & 0 \\ sin\phi & cos\phi & 0 \\ 0 & 0 & 1 \end{pmatrix} \tag{3.9}$$

The rotation matrix about the new x' axis can be obtained from the Rodriques rotation formula 3.11, using the new x-vector to give the matrix in 3.12.

$$x' = \begin{pmatrix} cos\phi \\ sin\phi \\ 0 \end{pmatrix} \tag{3.10}$$

$$R_{\mathbf{w}} = \begin{pmatrix} cos\Phi + w_x^2(1-cos\Phi) & w_x w_y(1-cos\Phi) - w_z sin\Phi & w_y sin\Phi + w_x w_z(1-cos\Phi) \\ w_z sin\Phi + w_x w_y(1-cos\Phi) & cos\Phi + w_y^2(1-cos\Phi) & -w_x sin\Phi + w_y w_z(1-cos\Phi) \\ -w_y sin\Phi + w_x w_z(1-cos\Phi) & w_x sin\Phi + w_y w_z(1-cos\Phi) & cos\Phi + w_z^2(1-cos\Phi) \end{pmatrix} \tag{3.11}$$

$$R_{\mathbf{x'}} = \begin{pmatrix} cos\Phi + cos\phi^2(1-cos\Phi) & cos\phi sin\phi(1-cos\Phi) & sin\phi sin\Phi \\ cos\phi sin\phi(1-cos\Phi) & cos\Phi + sin\phi^2(1-cos\Phi) & -cos\phi sin\Phi \\ -sin\phi sin\Phi & cos\phi sin\Phi & cos\Phi \end{pmatrix} \tag{3.12}$$

The combined rotation matrix is therefore defined as:

$$R_t = R_{x'} R_z \tag{3.13}$$

The surface normal in the crystal coordinate system is independent of the final rotation and therefore we don't need to calculate this rotation matrix. We need to rotate the [001] vector in specimen coordinates into crystal coordinates. So we need to apply the inverse of the total matrix R_t to the [001] vector. This gives the surface normal in crystal coordinates, equation 3.14.

$$n = \begin{pmatrix} sin\phi sin\Phi \\ -cos\phi sin\Phi \\ cos\Phi \end{pmatrix} \tag{3.14}$$

3.7.3 Fitting to modulus data

In the indentation study performed, the crystallographic orientation is measured by EBSD and the indentation modulus is measured by nanoindentation. For each set of indents contained within a grain, the mean measured modulus can be calculated; giving a point on an orientation-modulus plot.

As lithium is cubic, it has three independent stiffness tensor components C_{11}, C_{22} and C_{44}. For a given stiffness tensor, the expected indentation modulus for a specific

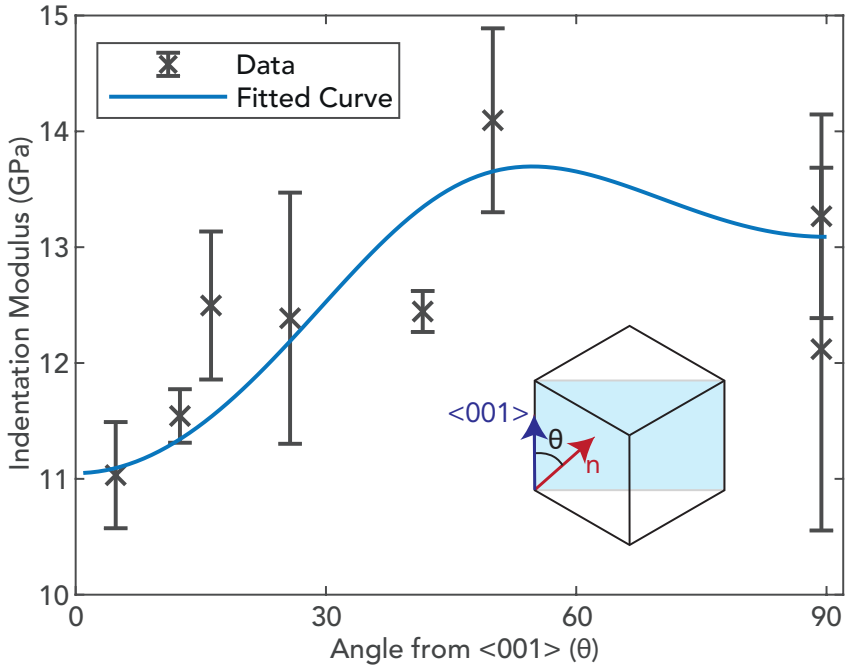


Figure 3.13: Measured moduli for the eight indented grains with surface normal near {110} planes plotted against angle from <001> vectors, this works best-fit trend-line plotted. Schematic inset to show theta definition.

grain orientation (ϕ, Φ, φ) can be calculated. The error between the expected and measured modulus value is found by subtraction. A least-squares sum with each orientation-modulus point weighted by the number of indents in it can be calculated.

$$Err = \sum n_{exp}(M_{exp} - M_{calc})^2 \tag{3.15}$$

The values of C_{11}, C_{22} and C_{44} which minimise the sum of least squares are the best fit. Due to the computational cost of computing the error for a given set of values; it is not realistic to explore the Err(C_{11}, C_{22}, C_{44}) space by brute force to find the minimum value. The function defines a surface in 4d space, where the minima must be found.

A Nelder-Mead algorithm [172], implemented by the fminsearch function in MATLAB was used to find a least-squares fit to the data presented in figure 3.12, giving values of the stiffness tensor outlined in table 3.2. To visualise the resultant fit, the indentation modulus curve for grains with surface normals lying in the (110)

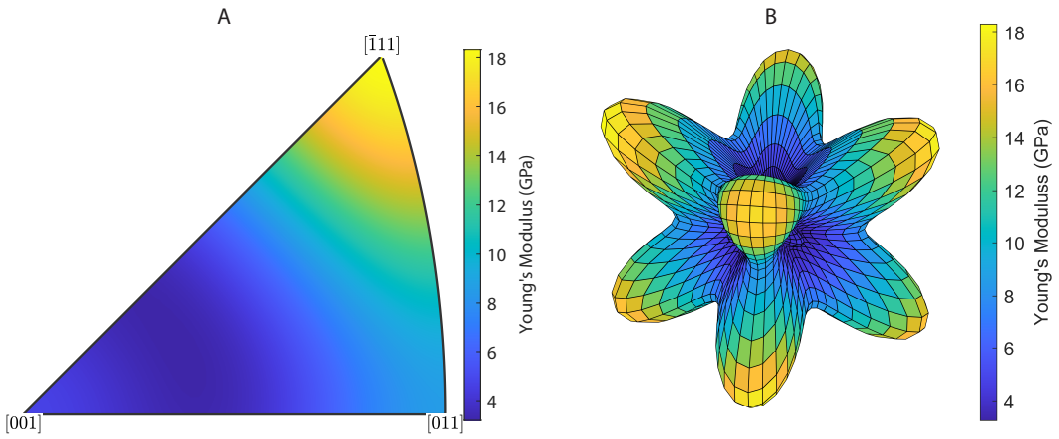


Figure 3.14: Young's modulus anisotropy. (a) inverse pole figure of Young's modulus with orientation. (b) Polar surface plot of Young's modulus with orientation

plane has been calculated, with its maximum along the <111> vector at 54 degrees as shown in Figure 3.13. The eight experimental grain orientations with surface normal lying near the {110} planes (top and right edges of figure 3.12C) have also been plotted. The error bars represent the standard deviation of the indentation modulus values for the indents within each grain's indent set. The three stiffness matrix components fully describe the elastic response of the material, and other values such as polycrystalline Young's, shear and bulk moduli can be calculated from them. In the table, the two extreme single crystal uniaxial Young's moduli values in the [100] and [111] directions have been calculated with approximately a factor of seven difference. Figure 3.14A shows the Young's modulus of a single crystal of lithium with orientation, calculated from the measured stiffness tensor. Figure 3.14B is the same data as presented in A, but plotted as a 3D surface. The degree of elastic anisotropy is clear.

Property	C_{11}	C_{12}	C_{44}	E[100]	E[111]	A	ν	B	E	G
Value	13.34	11.19	8.83	3.1	21.2	8.21	0.28/0.41	11.9	6.41/14.81	2.27/5.73

Table 3.2: Elastic properties results for pure lithium metal tested by nanoindentation. Poisson's ratio (ν), bulk modulus (B), Young's modulus (E) and shear modulus (G) are respectively the Reuss and Voigt polycrystal estimates all given in GPa, except A and ν which are dimensionless.

The elastic stiffness tensor results sit in the middle of the range of measured/calculated indentation results [121–123], and are in very good agreement with the work by the group of Slotwinski and Felice [121, 122]. The work shows lithium is highly elastically anisotropic. Implementing the full stiffness tensor (measured in this work) allows the elastic response of the material to be precisely determined across length scales for any general stress state, with numerical tools such as Abaqus. The knowledge of lithium's elastic anisotropy also allows worst-case mechanical scenarios to be modelled, e.g. single-crystal lithium filaments compressed in the [111] direction will act differently to those compressed in the [100] direction.

Practically, lithium's high elastic anisotropy and large grain size mean that the stiffness of the material is strongly dependent on the texture. The Reuss and Voigt estimates for polycrystalline Young's moduli of lithium using our measured values are 6.41 GPa and 14.81 GPa. We would therefore reasonably expect a true untextured polycrystal to have a Young's modulus of 10.6 GPa (arithmetic mean). The significant difference between the two estimates shows that the arrangement of grains of different orientations can have a substantial effect on a sample's modulus – this is confirmed by the wide range of literature values for the stiffness of polycrystalline lithium. Due to its softness, lithium is typically prepared by rolling which induces strong [100] out-of-plane texture into the material [173], a direction in which its stiffness is much lower. The different polycrystalline moduli values obtained in the literature can be explained by the expected texture in the samples based on the processing method such as wire drawing or foil rolling [70] and the large grain size of lithium ($\approx$100 μm [157]).

3.8 Plastic Mechanical Response

The continuous measurement technique gives hardness (load/contact area) with depth, throughout the indentation. This provides a good approximation for the stresses that evolve during rapid lithium plating within a crack. As can be seen in Figure 3.15A, there is a strong depth dependence on the measured hardness due to the size of the indentation being of the same magnitude as a dislocation. Such

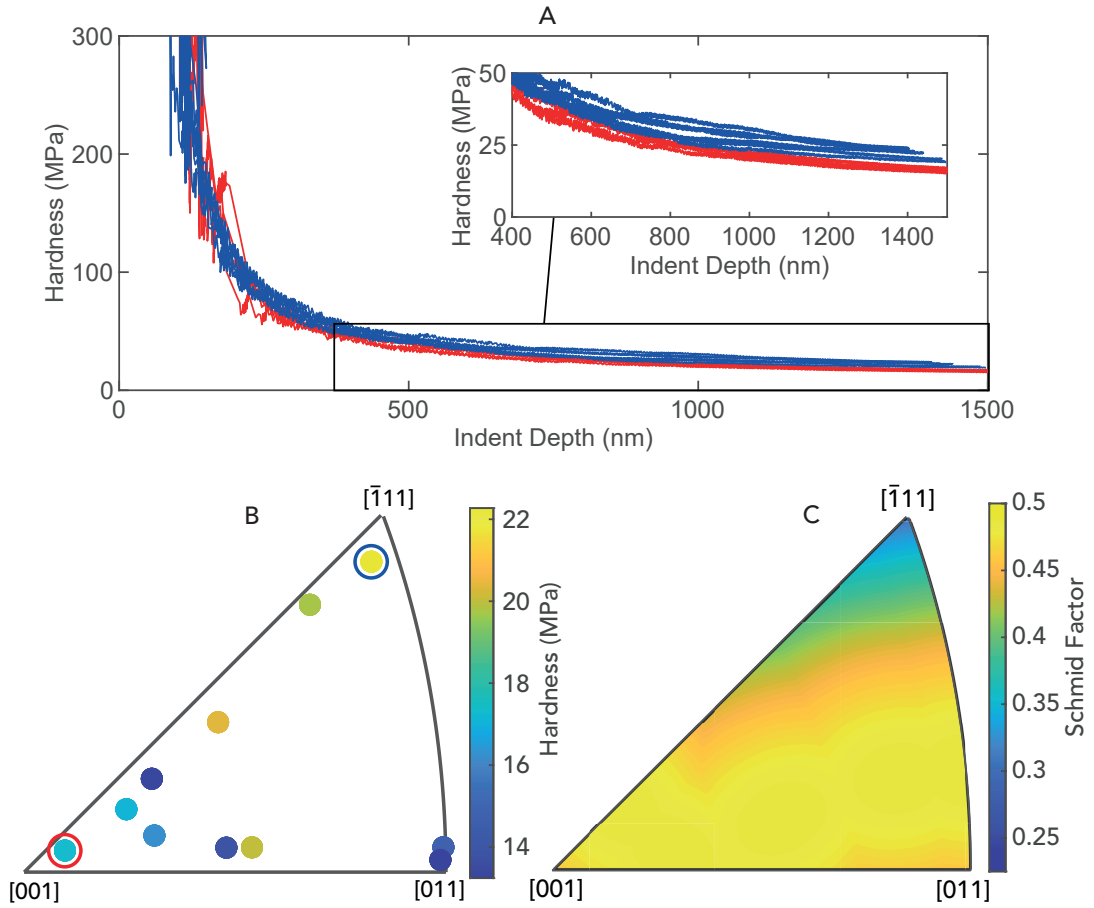


Figure 3.15: Size and orientation dependent hardness of lithium metal measured by nanoindentation. (a) Measured hardness with indentation depth for indents in grains near [100] and [111]; as highlighted in B. (b) Inverse pole figure showing orientation dependence of measured hardness averaged between 1.2 and 1.5 micron. (c) Inverse pole figure showing Schmid factor of lithium metal assuming equal activation energy on {110}, {123} and {112} slip planes.

depth dependence is well described by the equation first put forward by Nix and Gao in 1998 (equation 3.16 [174]), tending to a hardness of H_0 at high depth, with a characteristic decay length h^*. When fitting the data beyond 500 nm, where the indentation error is small, the hardness curves for all indents follow this expression. At low depths (<500nm), where deviation from this trend is often observed [175], measured hardness values slightly exceed the curve. The average values for all indents, and the standard deviations, are H_0=2.01±0.16 MPa and h^*=97.8±42.1 μm.

$$H = H_0\sqrt{1 + \frac{h^*}{h}} \tag{3.16}$$

As can be seen in Figure 3.15A, hardness curves from different grain orientations are broadly similar, but there is a slight hardness anisotropy between lattice orientations observed, with the average hardness between 1.2 and 1.5 micron varying from 22.3 MPa in the <111> indentation axis to 17.2 MPa near <100>, as plotted in Figure 3.15A, with the corresponding points on the inverse pole figure circled in red and blue (Figure 3.15B). The measured anisotropy of hardness corresponds well with the calculated Schmid factor of the axis of indentation, for the {110} <111>, {112} <111> and {123} <111> slip systems of the body-centred cubic (BCC) crystal structure – as shown in the Figure 3.15C. Where the Schmid factor is low, the hardness is high. This is intuitive, given the critically resolved shear stress on the slip plane is proportional to the Schmid factor and the applied stress; therefore, for a lower Schmid factor, a larger normal force is needed to drive slip [176].

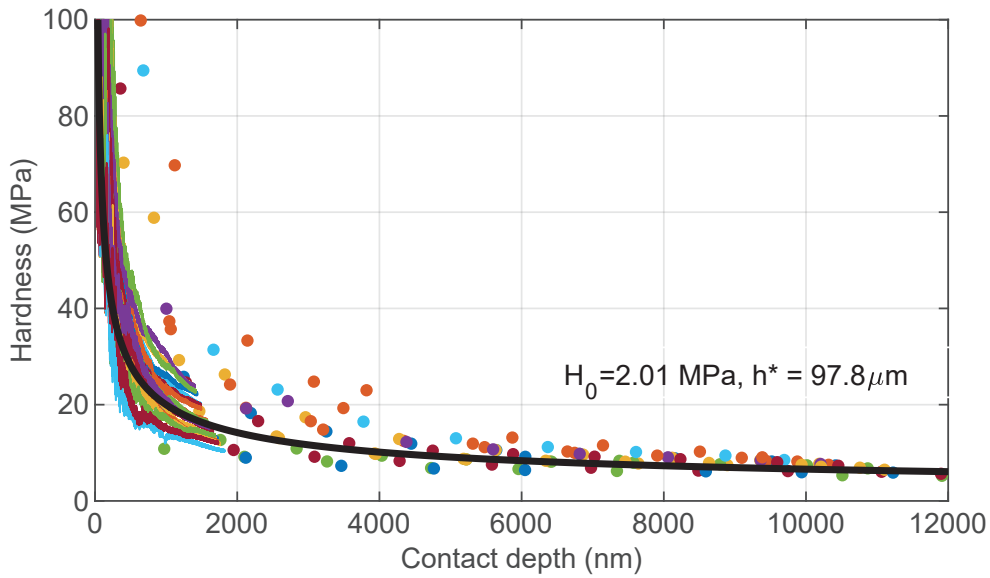


Figure 3.16: Quasistatic partial unload indentation hardness data up to 12000nm depth showing trend fit to low load CSM continues.

Quasi-static (without CSM) indentation with successive partial unloads [147] were performed to confirm the hardness trend continued to deeper depths. 12000 nm was the limit of our indentation tip range. The curve, extrapolated from fits to continuous low load data, fits the quasi-static high load data well. The length scale factor h* scales inversely with the hardness, such that low hardness materials such

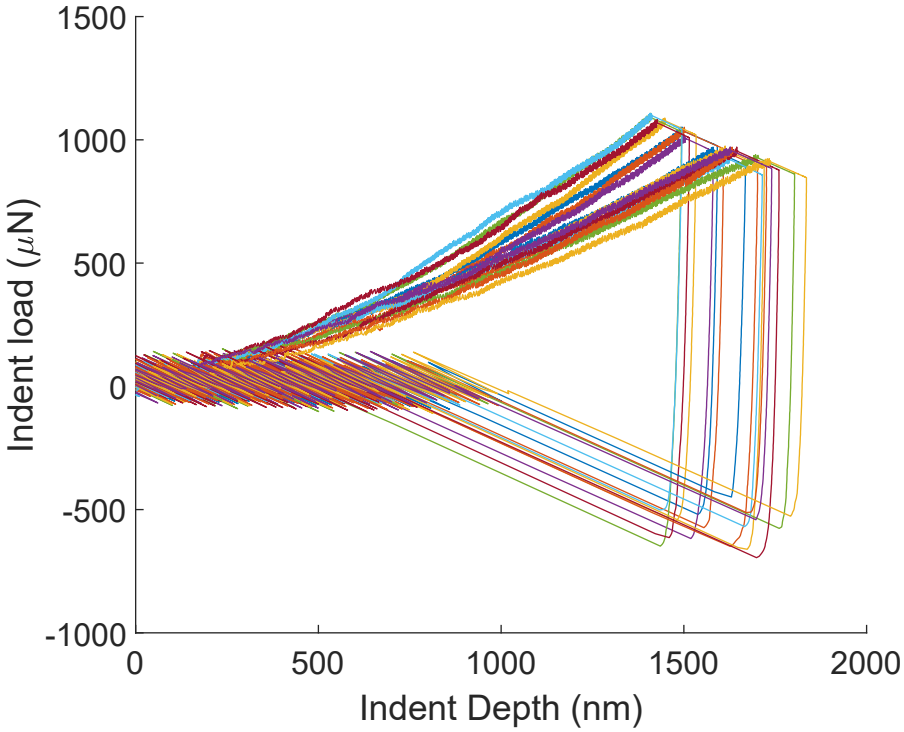


Figure 3.17: Load-displacement plots for indents in lithium with a range of grain orientations.

as lithium have long h* values. Macroscopic lithium samples (> 1mm) in size, will have a hardness of the bulk value H_0, giving a yield stress of approximately a third of this (0.67 MPa), in line with literature values [82]. On the micron scale relevant to microstructural features of lithium within a battery such as lithium filaments, the hardness is considerably higher. The size dependence of lithium metal's plasticity is also relevant to the plastic deformation of thin lithium metal electrodes (typically < 30 microns) as it will be harder than thick bulk lithium foil. The continuously fit hardness values can be used when considering these effects.

3.9 Adhesion

Figure 3.17 shows representative load-displacement curves for the indentations analysed, across a range of crystallographic orientations. The curves are typical, with a loading stage with continuous stiffness measurement performed. The very large stiffness-to-hardness ratio of lithium can be seen, with very little elastic recovery on

unloading. During the two second hold, there is a small amount of creep, followed by unloading. A negative load value is reached at which the indenter tip de-bonds from the sample and jumps from the surface before oscillating towards zero displacement.

The negative load needed to detach the tip from the sample is due to adhesion. The mean value of this pull-off force was -532.6±0.8 μN and by dividing by the contact area, a mean pull-off stress was 7.95±0.02 MPa. No clear trend with orientation was observed. Published work on Berkovich indentation adhesion is limited to ideal elastic systems such as polydimethylsiloxane (PDMS) [177] so the mathematics does not apply to plastic materials such as lithium. Approximating the indenter as a rigid flat punch ($R = \sqrt{A_c/\pi}$) and the metal as elastic using the Kendall model ($P_{off} = \sqrt{8A_c M W_{ad} R}$) [178], the work of adhesion is 9.61±0.03 mJ/m^2. This should only be taken as an estimate as it assumes no plastic work is done by the tensile stresses during pull-off and just considers the stored elastic energy at the pull-off stress. I'm not aware of any other quantitative reports of adhesion with lithium or a mathematical framework for accounting for plasticity during adhesion at the nanoscale.

Does adhesion meaningfully impact measured stiffness values? The oscillating load signal is approximately 5% of the overall load. Any tensile contribution due to adhesion will lead to a slight enhancement in the measured stiffness. This will come from regions that are not fully elastically loaded in compression and therefore which go into tension during each partial unloading. This region will only be at the very outermost edge of the contact area. Because lithium is so soft, compared to its stiffness, the fraction of the contact area which is under partial elastic compression instead of being fully elastically loaded and therefore plastically deformed, will be very small. Therefore any change in measured stiffness measured by CSM should be very small.

3.10 Impact of measured nanoscale hardness.

Size-dependent plasticity is a well-established component of dislocation theory, the effect is widely observed in metallic nanoindentation studies [174] and has recently

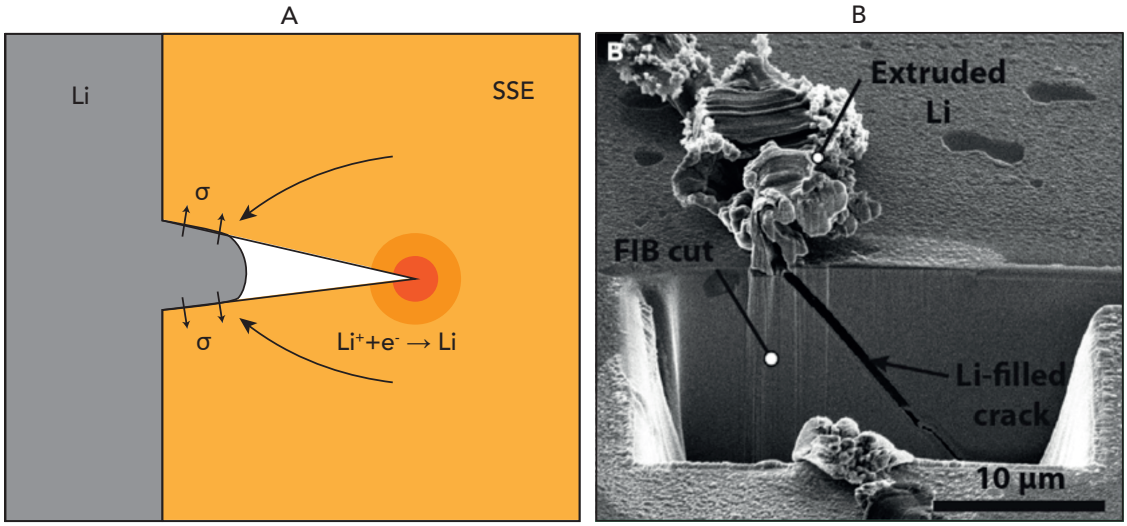


Figure 3.18: Relevance of nanoscale hardness to solid electrolyte fracture, due to lithium plating within cracks. (a) Schematic of stress concentration due to redistributed crack opening stress from lithium plated within a crack in a solid-state electrolyte SSE. (b) Image reproduced from Kazyak et al. [74] showing lithium-filled crack of width <500 nm in high-density $Li_7La_3Zr_2O_{12}$ (LLZO), and subsequent Li extrusion.

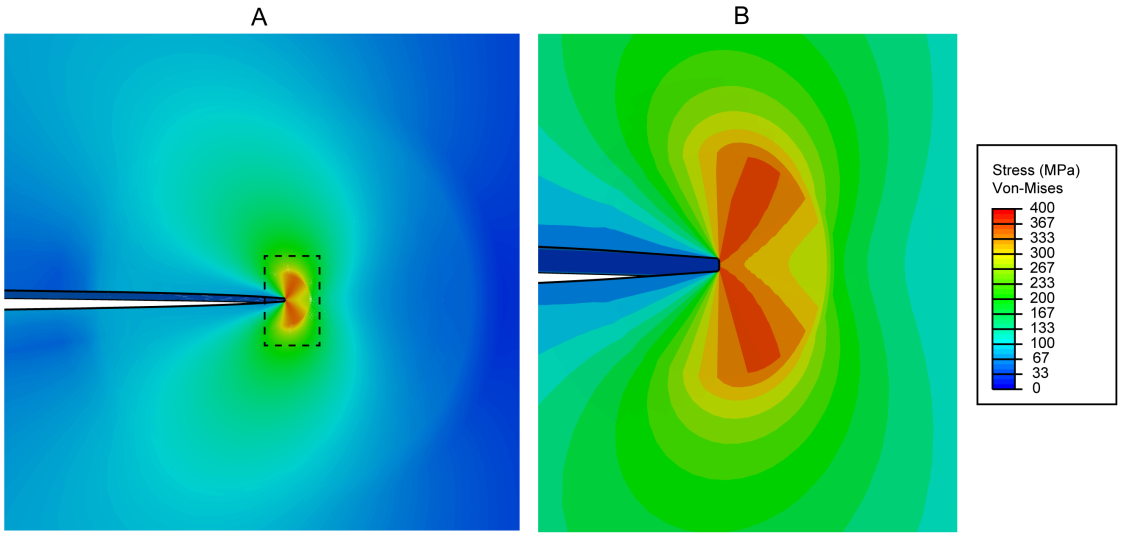


Figure 3.19: Simulated crack tip stress field for uniform opening pressure of 100 MPa on a 20-micron edge crack in a linear elastic material with a modulus of 100 GPa.

been highlighted in mechanical studies on lithium at length scales between 1 and 10 μm [82, 123, 125]. The data in this chapter demonstrates that on the ≈200 nm length scale relevant for lithium filaments, the hardness is approximately 100 MPa. The flow stress of nanoscale lithium can be approximated as a third of the measured hardness [179], approximately 30 MPa.

Previous experimental work has demonstrated crack propagation by lithium deposition within the crack under compressive stress – evidenced by subsequent viscoplastic extrusion of lithium out of the crack [74], a good example is reproduced in Figure 3.18B. If lithium is under compressive pressure, an equal opening pressure must be exerted on the solid electrolyte, this is shown schematically in Figure 3.18A. As ceramic solid electrolytes are stiff, the crack opening forces are redistributed leading to a stress concentration at the crack tip. Considering the simple filled crack case, linear elastic fracture mechanics equations for an edge crack experiencing internal pressure can be used [180, 181] ($K_1 = \Psi\sigma\sqrt{\pi a}$, where K_1 is the stress concentration at the crack tip, σ crack opening pressure, a crack length and Ψ a geometry factor of approximately one). To visualise this, a crack tip was modelled in Abaqus with a uniform opening pressure of 100 MPa on the inner faces of a 20 micron edge crack in a linear elastic material with a modulus of 100 GPa, the results are plotted in figure 3.19, with the characteristic butterfly crack tip stress concentration. Displacements have been scaled by a factor of 10 to show crack opening. Solid electrolytes are typically stiff ceramics, with low fracture toughness values (K_{1c}) in the range 0.5-1 MPa$\sqrt{m}$ [64, 182–184], with the notable exception of LiPON - which seems to have a high fracture toughness, although this could be an artefact of the sample being a thin film [183].

In addition to the simple observation that lithium has much higher hardness at the nanoscale, there are three additional considerations relevant to the observed fracture in ceramic solid electrolytes on lithium plating.

First, it may be for very high currents and very small crack diameters (<100 nm), the higher stresses evolved at higher strain rates than we have tested here, are sufficient to drive fracture. A crack opening stress of 200 MPa and a crack length of 5 μm will fracture materials with a fracture toughness below 0.8 MPa$\sqrt{m}$.

Second, to yield lithium out of a crack, forces at the lithium-ceramic interface will need to be overcome in addition to overcoming the material's intrinsic yield stress (von-Mises yield criterion). Assuming the adhesion between lithium and a solid electrolyte is similar to that observed with the diamond indenter tip, the

magnitude of the adhesion measured suggests frictional forces will be substantial. The situation is analogous to forging where the average pressure needed grows exponentially with the friction coefficient and aspect ratio.

Third, most experimental works demonstrating lithium filament propagation and concurrent electrolyte fracture, show a progressive degradation over successive cycles, instead of catastrophic fracture on the first [74, 185–187]. This matches the well-established concept of crack growth under a sub-critical but cyclic load, where the crack growth per cycle in the main (stage II) regime is described by the Paris-Erdogan law. As such, cyclic stresses caused by lithium plating and stripping from within a crack on successive cycles will propagate the crack across the electrolyte. Below a threshold stress concentration amplitude, crack growth is negligible in ceramics – this threshold value is a material property that should be investigated for candidate solid electrolyte materials. There are no current studies of this type on solid electrolyte materials.

3.11 Conclusions

In this chapter, I have quantified the mechanics of lithium at the nanoscale by nanoindentation. The measurements suggest stiffness tensor components of C_{11} = 13.3, C_{12} = 11.2, and C_{44} = 8.8 GPa. Clear size-dependent hardness is observed due to the stressed volume being small enough, so that few dislocations experience a shear stress and therefore less slip occurs than would for a bulk test. Hardness greater than 100 MPa is observed on the length scale of lithium filaments; this is two orders of magnitude higher than the measured bulk yield stress of 0.6 MPa. Linear elastic fracture mechanics suggest crack opening stresses of this order are likely to fracture current solid electrolyte materials due to their relatively low fracture toughness, especially over successive cycles.

The capability to EBSD map lithium metal was developed as a tool to enable the mechanical anisotropy of the metal to be measured. Microtome is a fast, effective method for producing smooth, fresh surfaces, ideal for EBSD and indentation. However, there is significant potential to build on this work, using

EBSD as a tool to gain an understanding of microstructural processes occurring within lithium metal in batteries. In recent years, cross-sectional imaging and in-operando characterisation techniques have played a fundamental role in developing an understanding of behaviours within a battery. Combining these, EBSD could be used in-operando to map evolving concentration gradients, strain gradients, and microstructural evolution during battery cycling. I've successfully demonstrated EBSD mapping for the heavier alkali metals of sodium and potassium using the same methodology as lithium.

Recent works have identified the correlation between lithium metal microstructure and electrochemical performance. Density functional theory (DFT) calculations show that the thermodynamic overpotential, and therefore nucleation kinetics, of plating and stripping vary by hundreds of mV based on the surface crystallographic orientation of lithium metal [188], and recent optical microscopy has shown varied pit nucleation rates and pit morphology dependent on the orientation of grains neighbouring grain boundaries [189]. There is an opportunity to use EBSD to further explore this link between lithium microstructure and electrochemical performance. This may be particularly useful with the trend towards multi-phase or alloy anodes, where the microstructure defines electrochemical performance.

EBSD and other backscattered imaging techniques such as electron channelling contrast imaging (ECCI) can be powerful tools in understanding the processes of plasticity in materials by enabling the mapping of dislocation density and strain gradients. Achieving this in lithium would require carefully optimised beam parameters and carefully chosen detectors. The role of dislocations in determining electrochemical performance remains unclear. They likely act as sinks for vacancies created during electrochemical stripping; and they, therefore, influence interfacial voiding. The role of plastic deformation in counteracting loss of contact at the interface is also unclear. Imaging of dislocations or strain fields in response to mechanical stress, such as by indentation, would allow a fundamental model of plasticity in lithium to be constructed to describe the role dislocations play in void formation/prevention. Achieving this requires at least an order of magnitude

improvement in the resolution of EBSD than we have achieved in this work; achievable by detecting backscattered electrons with lower energy; or by narrowing the energy window sampled.

Finally, microtome is a technique with significant promise in the preparation of lithium metal samples. The surface chemistry and morphology of lithium metal have a strong impact on its electrochemical performance [190]. Despite this, there is no standard method for preparing electrodes of known thickness, with a controlled surface morphology and freshly exposed surface. Machine microtome offers a reproducible, carefully controlled method of producing thin 1-60 $\pm$ 0.1 μm electrodes, with fresh surfaces. The thickness of electrodes prepared by the typical method of rolling/calendering is limited by friction, to a minimum of 100 micron – below which the lithium metal foil buckles and tears – this is equivalent to an areal capacity of 20.6 mAhcm^{-2}. As a result, studies tend to only partially cycle lithium metal anodes. To study the deep cycling of lithium metal, a method of preparing a layer of 25 micron (5 mAh cm^{-2}) is needed. I envisage a method whereby thin metal sections can be cut off a bulk ingot of lithium metal, like salami, and then die cut to the desired shape.

The mechanical strength of lithium observed gives a reasonable target opening stress within a crack which solid electrolyte materials must accommodate to prevent fracture and short circuiting. Considering linear elastic fracture mechanics, this essentially defines a maximum flaw size which is allowed to be present in solid electrolyte materials. Since completing this work, several studies have demonstrated that lithium propagation across a solid electrolyte is a crack-fracture mechanism, in line with the predictions of this work [79, 191]. The field as a whole is moving towards this as a consensus. Further work modelling the mechanical interaction between lithium metal and solid-state electrolytes would be helpful and I hope the results in this work can inform these models. In the meantime, higher fracture toughness electrolytes should be pursued. The hardness results in this work suggest that electrolytes that can tolerate cyclic loads of the order of 100 MPa, for as many cycles as the battery is intended to perform, should be pursued.

The development of solid electrolytes can be split into the fundamental materials development and processing. On the fundamental materials side, materials with a higher fracture toughness should be pursued. Novel concepts include toughening with bridging microfibers, the creation of composites with partially stabilised zirconia, or the addition of a high-toughness polymer. All of these are worthwhile pursuits to increase the fracture toughness value of the material.

More important is the reduction in the maximum flaw size within the manufactured material. With rare exceptions, solid electrolyte preparation methods such as cold-pressing lead to highly porous materials with continuous pore networks, and as a result short at very low current densities. The challenge is to develop scale-able methods to prepare thin solid electrolytes free from mechanical defects. Efforts to increase scale-ability, such as the preparation of polymer-ceramic composites tend to reduce the ionic conductivity and introduce many weak interfaces along which filaments can propagate, decreasing current density even further [192]. From this perspective, oxide-based ceramic electrolytes are of interest as they can be sintered in air and therefore binders used in the preparation of thin films can be burned out [193] to form relatively dense, thin films. Finally, solid electrolytes such as Li_2OHCl antiperovskite, which can be melted and resolidified are interesting as they can be made near defect-free; however, their ionic conductivity is orders of magnitude too low to be relevant. To accommodate the nanoscale hardness of lithium metal, the field must find cheap and scalable methods to produce thin, near defect-free solid electrolytes.

4

Developing an alloy anode investigation framework using the lithium magnesium alloy system.

Contents

4.1 Introduction 63
4.2 Synthesis of magnesium alloy anodes. 65
4.3 Characterisation of magnesium alloy anodes. 67
4.3.1 SEM Imaging 67
4.3.2 Electron backscattered diffraction. 67
4.3.3 X-ray diffraction. 71
4.4 Mechanical properties of lithium magnesium alloys. . 72
4.4.1 Elastic anisotropy 72
4.4.2 Plastic properties 74
4.4.3 Adhesion 76
4.4.4 Creep of lithium magnesium alloys 77
4.4.5 Summary of lithium magnesium mechanics. 85
4.5 Surface chemistry 86
4.5.1 Open-circuit voltage 86
4.5.2 Electrochemical Impedance Spectroscopy 87
4.6 Diffusion 94
4.6.1 PFG-NMR on ^{6}Li Alloys 94
4.6.2 Diffusivity measured by time of flight secondary ion mass spectrometry (TOF-SIMS). 97
4.7 Chronopotentiometry 97
4.8 Cross-sectional imaging of stripped lithium magnesium alloy anodes. 104

4.8.1 Cross-sectional imaging of stripped and plated lithium magnesium alloy anodes. 107
4.9 Conclusions. 108

4.1 Introduction

Much of the work reported in this chapter is in submission in Nature Materials (Pre-print - [194]).

Electrification of transport depends on an increase in battery energy density. On the anode side, this requires moving beyond graphite. Extensive work has focused on pure lithium metal anodes in combination with solid-state electrolytes. Lithium metal offers the highest theoretical energy density of 3860 $mAhg^{-1}$, but the material has slow self-diffusion kinetics (D_{Li} $\approx 3\times10^{-11} cm^2 s^{-1}$ at 298 K) meaning discharge currents for reasonable capacities are very limited. Slow transport kinetics lead to voiding and contact loss [72]. On plating, the morphology is unconstrained leading to shorts.

To overcome these fundamental limitations of lithium metal anodes, researchers are pursuing alternative anode materials that compromise energy density with the objective of improving performance. Recent works involving nano-structured anodes such as using aligned carbon nanotubes [195], deliver excellent performance compared to lithium metal, but these approaches are fundamentally hard to scale at the low cost needed for battery manufacture.

Lithium-rich alloys are of interest to overcome these challenges [94]. Alloying modifies the physical properties of lithium metal such as the diffusion rate [101–103], mechanics [104], chemistry at the interface, and the material microstructure; all of which can change the emergent electrochemical performance. This is achieved with only a small reduction of energy density compared to pure lithium [95].

Lithium-magnesium binary alloys have been considered one of the most promising alloy anode candidates [94] due to their high energy density, unique wide solid solubility in the lithium-rich phase (figure 4.1), and similarity in processing to

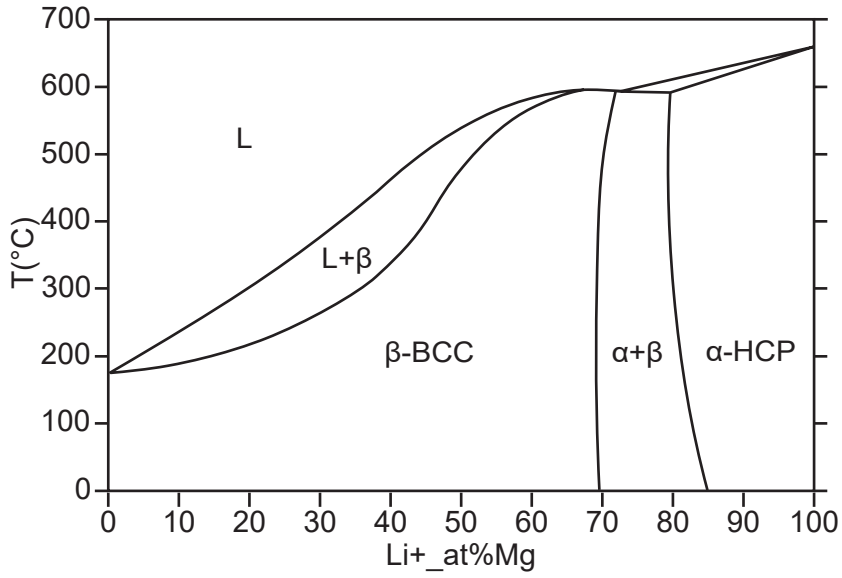


Figure 4.1: Phase diagram of lithium magnesium, redrawn based on Taylor et al. [196].

lithium metal. Conflicting literature reports on diffusivity [96] have contributed to this interest. Two works, using different methods, have identified similar decreases in lithium diffusivity with increasing magnesium alloy content [101, 102], but recently Krauskopf. et al. and Siniscalchi et al. [96, 102], both with an LLZO solid electrolyte, demonstrated improved stripping performance with increased magnesium content. This result is surprising and shows that measurement of the diffusivity alone is insufficient to understand the behaviour of alloy anodes. Diffusivity, mechanical properties, surface chemistry, and microstructure all contribute to the electrochemical performance.

Here I investigate the link between materials properties and electrochemical performance in the lithium-magnesium alloy system in combination with argyrodite, Li_6PS_5Cl, sulphide solid electrolyte. I synthesise and microstructurally characterise alloys of three magnesium compositions; then measure the mechanical hardness, stiffness, adhesion, and creep of these alloys by nanoindentation – quantifying the change with magnesium content. The effect of magnesium on interfacial chemistry is explored with impedance spectroscopy and x-ray photo-electron spectroscopy (XPS). Diffusivity is measured using ^{6}Li pulsed field gradient nuclear magnetic resonance spectroscopy (PFG-NMR). These properties are correlated with electrochemical tests

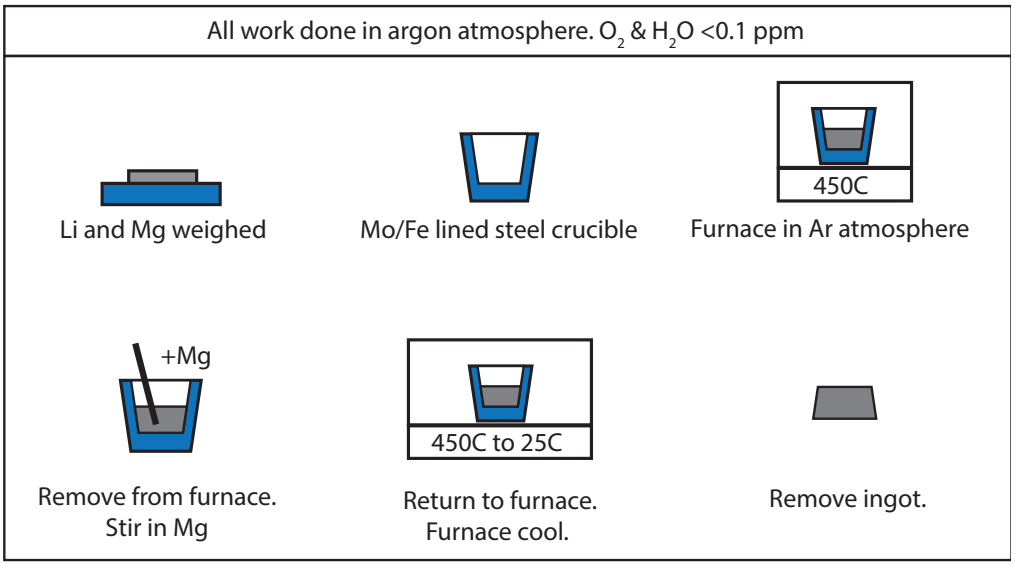


Figure 4.2: Synthesis of lithium magnesium alloys.

for varied magnesium content, performed in tightly controlled, realistic conditions (30°C, 50–100-micron thick anodes, 5 MPa stack pressure), with corresponding cross-sectional electron microscopy used to understand the underlying processes more clearly. The measure of diffusivity by electrochemistry and by NMR is compared. The work is presented as a framework that can be applied to other alloy systems, enabling the rapid development of alloy anodes and solid-state batteries.

4.2 Synthesis of magnesium alloy anodes.

There is little work in the literature documenting the method for producing lithium alloys. By building the capability in-house we are able to synthesise alloys of choice and are therefore able to investigate a wider array of alloys and can rapidly iterate until improvements are found.

Figure 4.2 shows the synthesis process of lithium magnesium alloys. Lithium metal (foil, 99.9%, Alfa Aesar) and magnesium metal (turnings, 99.98%, Alfa Aesar) were used for the casting of the Li-Mg alloys in a box furnace (MTI KSL-1200X-J-UL) within an argon-filled MBraun glovebox (O2 and H2O <0.1 ppm), this can be seen in Figure 4.3A. Lithium metal (around one gram) was heated to 450°C, well above the Li-Mg liquidus temperature, in a custom-made stainless-steel crucible,

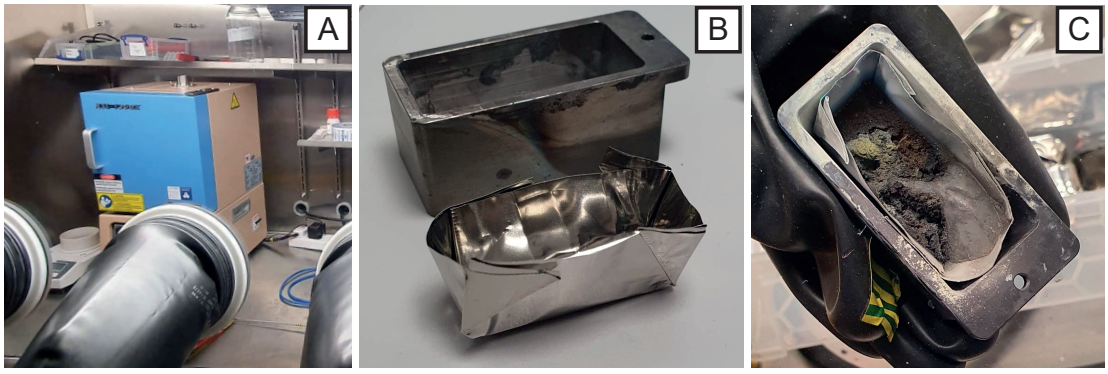


Figure 4.3: Furnace set up for alloy synthesis. (a) Photograph of furnace inside the cooled glovebox. (b) Photograph of foil-lined, custom-made crucible. (c) Photograph of stainless steel foil lined crucible after heating to 450°C with 20at%Mg content lithium-magnesium melt.

lined with molybdenum foil (Goodfellow), with a molybdenum foil lid. The molten lithium was removed from the furnace once at temperature, any slag was carefully removed with a stainless-steel spatula, and an appropriate mass of magnesium turnings were fully dissolved in the molten lithium using a stainless-steel spatula to stir. The crucible was then returned to the furnace for 2 hours at the same temperature before removing the melt from the furnace and air cooling to room temperature. The foil liner was removed from the ingot using pliers. Smaller volumes for experiments were cut from the bulk ingot using microtome blades (Thermo Scientific Epredia™ Shandon™ Premium High-profile Disposable Blades).

A custom stainless steel crucible figure 4.3B was designed and machined for synthesising lithium alloys. The crucible was designed to be near-impossible to tip over accidentally; easy to grip with tongs to allow it to be removed from the furnace at high temperature, with a trapezoidal prism internal volume to enable easy foil lining. An example of this lining folded from stainless steel is shown in figure 4.3B. For lithium magnesium alloys, molybdenum foil was used as stainless steel was observed to react with molten lithium magnesium at 450°C, as can be clearly observed in figure 4.3C.

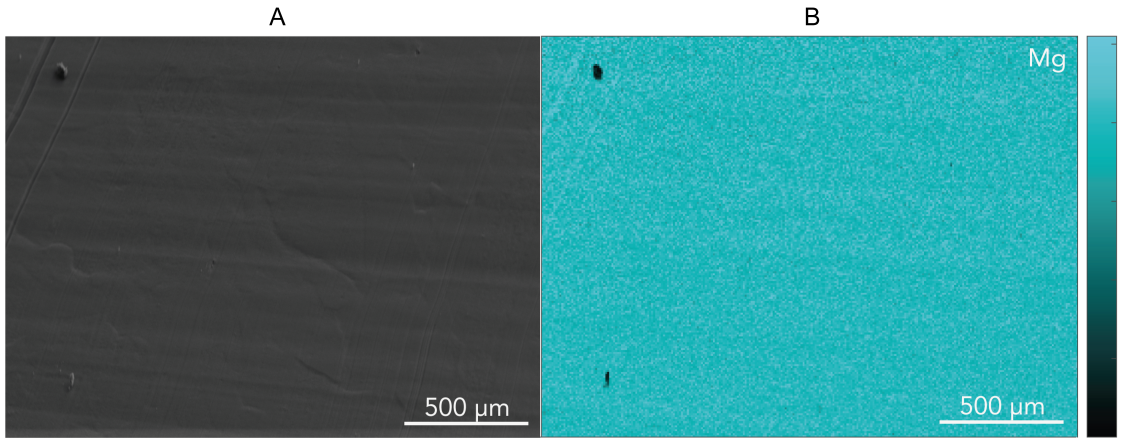


Figure 4.4: (a) SEM image of Li+5at%Mg sample surface. (b) Corresponding energy dispersive x-ray spectroscopy (EDX) map of Li+5at%Mg sample. Showing homogeneous Mg distribution throughout the sample.

4.3 Characterisation of magnesium alloy anodes.

4.3.1 SEM Imaging

Alloys were prepared for SEM in the same way as lithium metal, using a microtome blade. As can be seen in figure 4.4A, a secondary electron image of a Li+5at%Mg sample, the surfaces were flat except for cutting defects from the microtome blade (e.g. top left of image) and grooves which form on some grain boundaries. Energy dispersive x-ray spectroscopy (EDX) maps showed the distribution of magnesium in the sample was homogeneous, figure 4.4B. Suggesting any dendrite coring that occurred on solidification has homogenised. Based on the diffusivity values measured later, this is expected.

4.3.2 Electron backscattered diffraction.

To characterise the underlying grain structure, the samples were mapped using electron backscattered diffraction (EBSD). This was achieved by using microtome blades to prepare flat surfaces [156]. Representative maps of as-cast samples, allowed to solidify from 450°C outside of the furnace, are shown in figure 4.5A-C. All of the points indexed are the BCC phase. The conventional colour scheme has been used with red corresponding to an <001> surface normal, green corresponding to <110> and blue to <111>. There is a significant change in grain structure, the mean grain

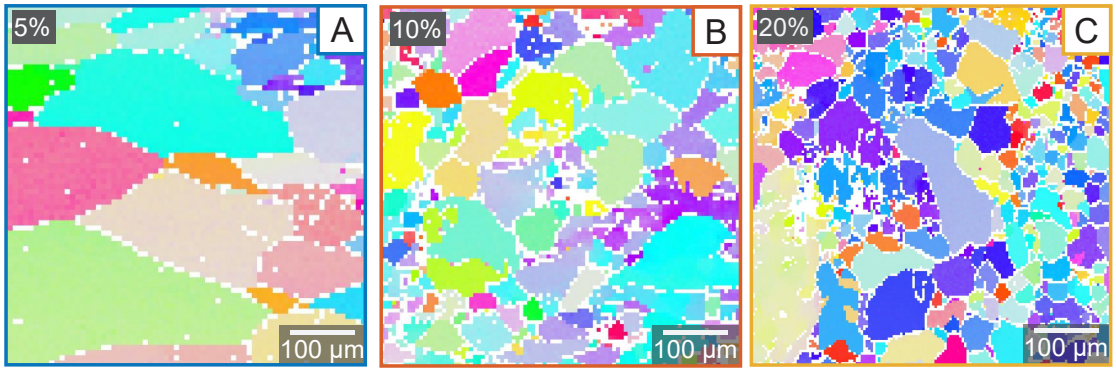


Figure 4.5: EBSD maps of air-cooled lithium magnesium alloys. (a) Li+5at%Mg. (b) Li+10at%Mg (c) Li+20at%Mg.

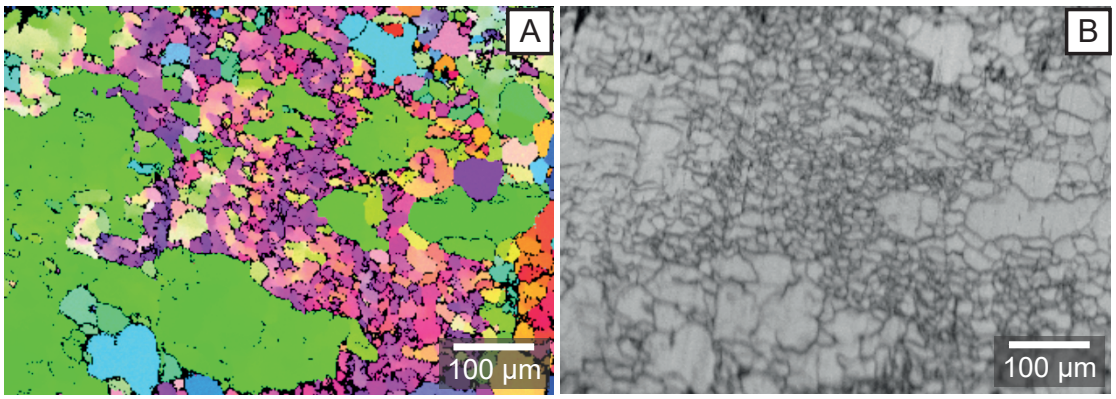


Figure 4.6: Slow-cooled 20at%Mg lithium magnesium microstructure, (a) grain orientation map (Z) (b) band contrast map.

diameters and standard deviations of the maps shown are 116.7±65.2 μm, 50.6±34.4 μm and 33.5±21.6 μm for the 5, 10 and 20% alloys respectively. It's worth noting that even in the 20% magnesium alloy, the grain size is still at least an order of magnitude too large for grain boundary diffusion to meaningfully contribute.

Increasing magnesium content leads to the stabilisation of finer microstructure, with the average grain size of the alloys decreasing. As-cast alloys are free from texture. With increased content, we observed a greater tendency for a dendritic microstructure, driven by constitutional super-cooling in solidification – especially when cooled very slowly. This leads to large regions with the same crystallographic orientation but with sub-grain boundaries of low band contrast – a small region plotted in light green can be observed in the bottom left corner of figure 4.5C. When the higher content lithium magnesium alloys are cooled more slowly (furnace

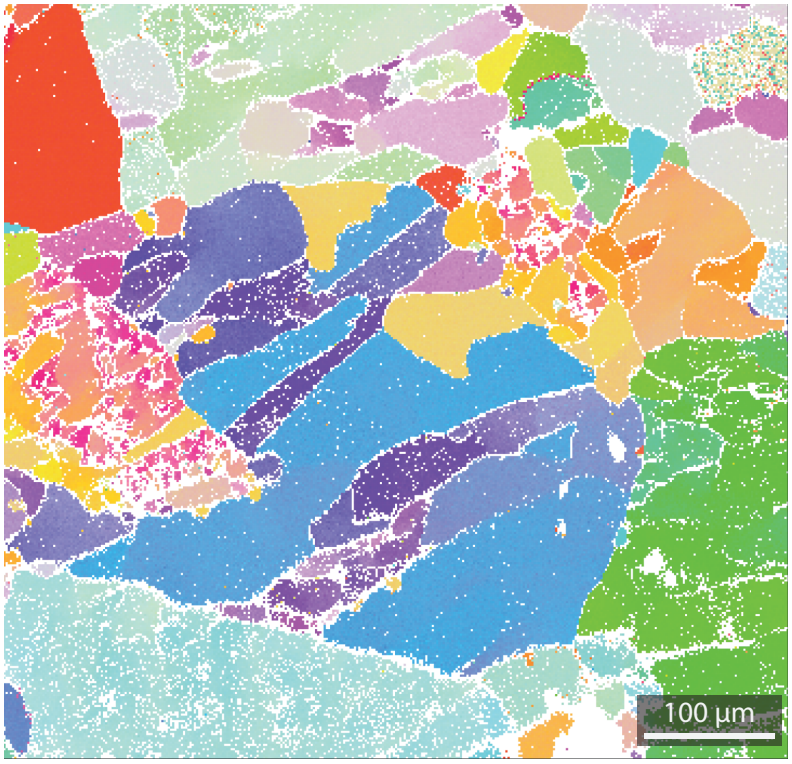


Figure 4.7: EBSD map of lithium 20% magnesium microstructure after anneal.

cooled), a dendritic solidification microstructure is more obvious, as can be observed in Figure 4.6. Large regions are observed with similar grain orientation but with boundaries of poor band contrast contained within them. This is typical of dendritic solidification caused by constitutional super-cooling. The 10 and 20 percent alloys were annealed for 24 hours at 150 °C to increase the grain size for the indentation experiment. An EBSD map of the annealed 20 percent alloy is shown in figure 4.7.

Considering the electron-cross section discussion in the earlier lithium section, the addition of magnesium significantly increases the EBSD signal and improves EBSD resolution. The modelled density of electron-sample interactions for backscattered electrons in lithium + 20% magnesium and pure lithium is plotted in Figure 4.8 A and B respectively. The plots are in sample coordinates, for a seventy-degree sample tilt, with a 30 kV incident electron beam. As can be seen, there is a significant decrease in penetration depth, which has the effect of increasing the resolution of EBSD.

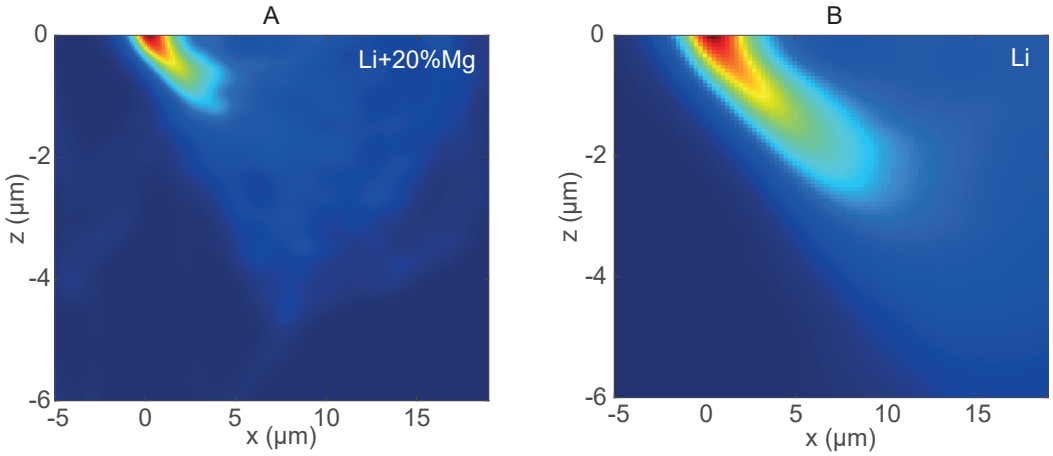


Figure 4.8: Modelled density of electron-sample interactions for backscattered electrons. (a) Lithium + 20% magnesium and (b) Pure lithium, using Casino [163]

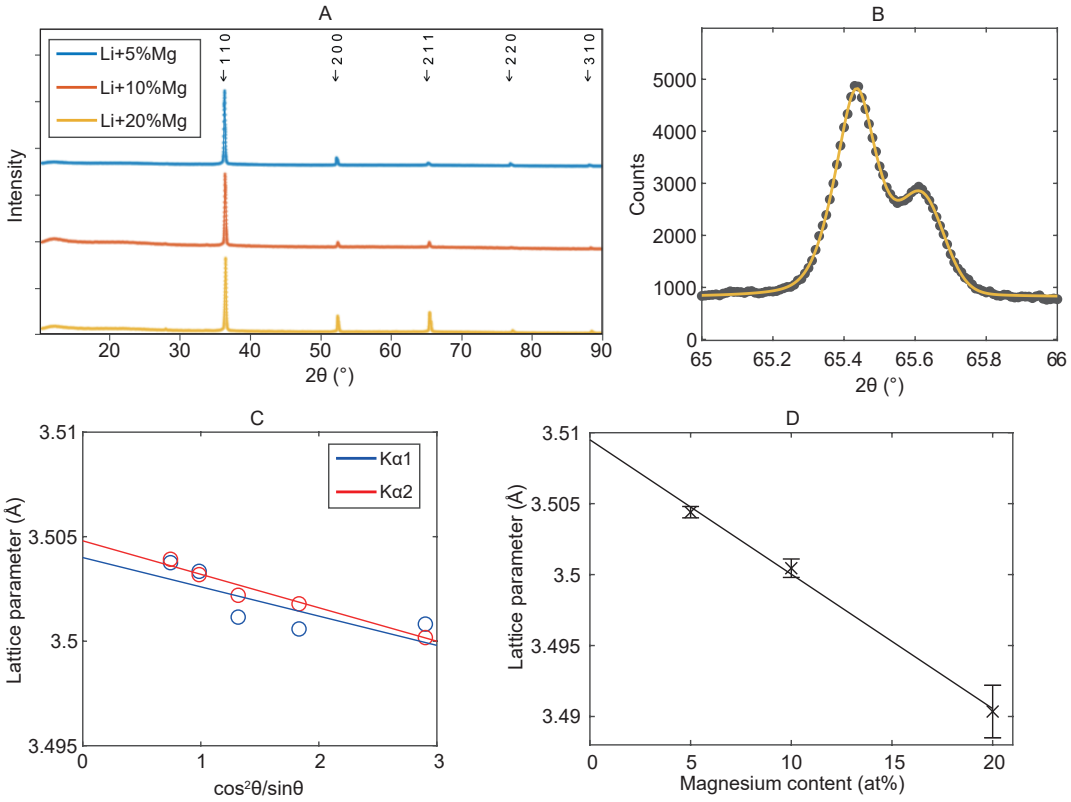


Figure 4.9: (a) Full XRD spectra of lithium alloys - y axes scaled for comparison. (b) Fitted peak example, 65 degree, Li+20%Mg (c) Extrapolation to theta = 0 for Kα1 and Kα2 peaks of Li+5at%Mg diffraction pattern. (d) Measured lattice parameters with magnesium content. Trendline = 3.5095 - 0.0009x Å, where x is %Mg.

4.3.3 X-ray diffraction.

XRD was performed on samples of the 5, 10 and 20% magnesium alloys with a Rigaku Miniflex. To create the samples, thin flakes were cut from the ingots using a microtome blade and mounted using petroleum jelly on a silicon single-crystal sample holder. The raw XRD data is shown in figure 4.9A. There is a peak shift due to the change in lattice parameter with the magnesium content. Each peak was fitted with a pair of Gaussian-Lorentzian sum peaks in Matlab with a constant background, the {211} peak is plotted in figure 4.9B as an example. The main source of errors in the measurement of peak position is the displacement of the sample surface from the diffractometer axis. To correct for this, the lattice parameters calculated from each fitted and indexed peak centre were plotted against $cos^2\theta/sin\theta$ and fit with a linear trend as shown in figure 4.9C for Li+5%Mg. This trend extrapolated to zero (large theta), gives the corrected lattice parameter. These lattice parameters from the $K\alpha 1$ and $K\alpha 2$ peaks were averaged to give the fitted lattice parameters in figure 4.9A, with the error bars showing the difference between the two values. The trend is linear, with a relationship of a = 3.5095 - 0.0009x Å, where x is %Mg.

The lithium magnesium system is single-phase, meaning the effect of microstructure on electrochemical performance is likely to be small. Looking forward to multi-phase alloys, the combined tools of XRD and SEM give a detailed picture of the alloy microstructure. XRD identifies the phases present in the sample and their crystal structure. Electron microscopy using EDX and EBSD provides the distribution of these phases within the material, the underlying grain structure, and the length scale of each phase. Such combined characterisation will be essential to unveil the link between microstructure and electrochemical performance. There is also scope for investigating the effect of processing techniques, such as rolling and annealing, on the microstructure.

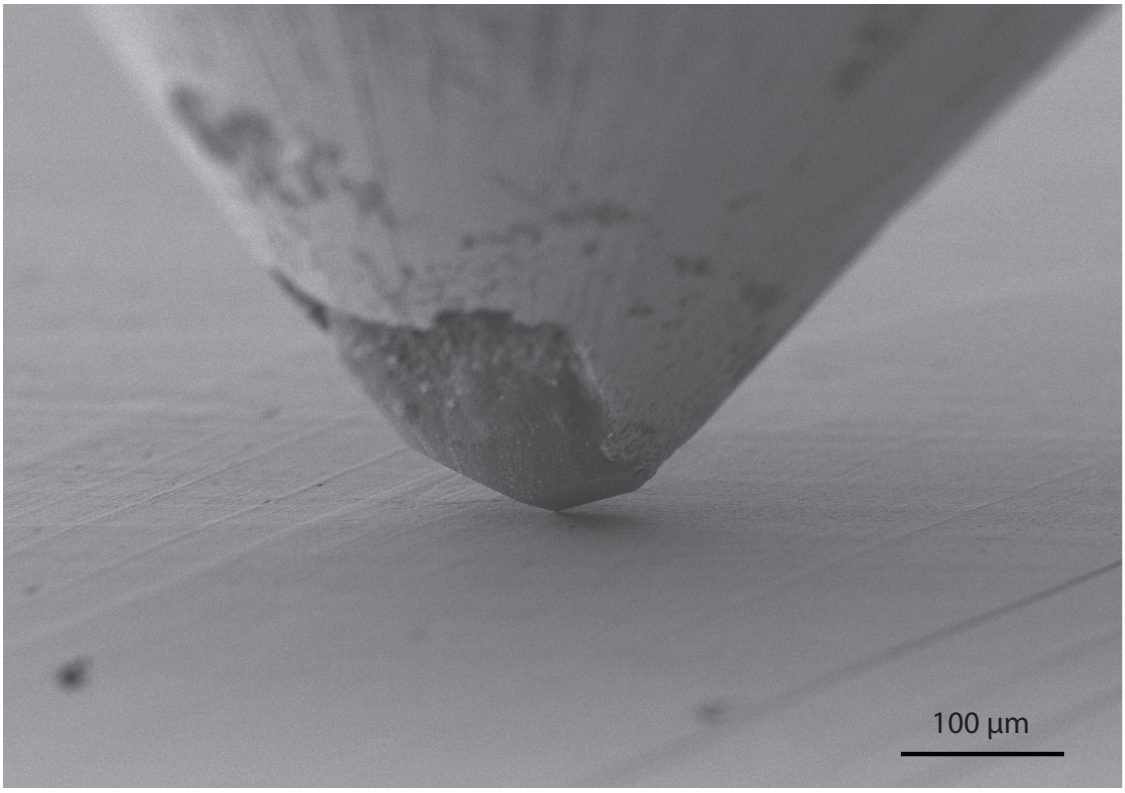


Figure 4.10: SEM micrograph of indenter tip in contact with surface of 5% magnesium alloy sample.

4.4 Mechanical properties of lithium magnesium alloys.

The methodology for mechanical testing outlined in the earlier chapter for lithium metal was repeated for binary lithium magnesium alloys of 5, 10 and 20 atomic percent. The samples were prepared by microtome as before. An SEM image of the indentation tip at the point it first made contact with a 5% Mg sample is shown in figure 4.10.

4.4.1 Elastic anisotropy

A series of indents around 1500 nm in depth were performed across grains with a range of crystallographic orientations to measure the modulus and hardness. The elastic results are presented in figure 4.11. In figure 4.11A, a linear increase in average indentation modulus was observed with increasing magnesium content, with approximately 0.5 GPa of stiffness increase per atomic percent magnesium

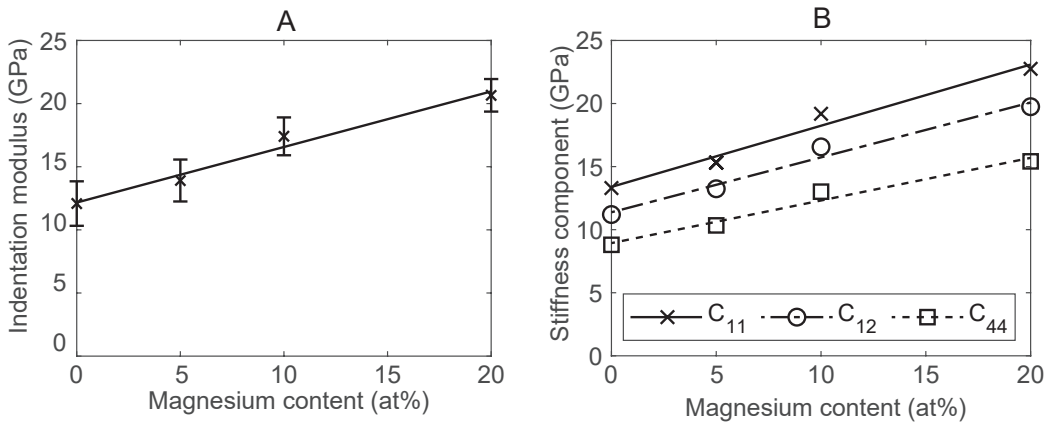


Figure 4.11: Elastic mechanical properties of lithium magnesium alloys. (a) Average Indentation modulus with magnesium content, error bars show standard deviation. (b) Elastic stiffness components with the magnesium content.

Alloy	C11	C12	C44	B	G*	E*	ν*
Li	13.3	11.2	8.8	11.9	4.0	10.7	0.35
5%Mg	15.3	13.2	10.3	13.9	4.4	12.0	0.36
10%Mg	19.2	16.6	13.0	17.5	5.6	15.1	0.36
20%Mg	22.8	19.7	15.4	20.7	6.6	17.8	0.36

Table 4.1: Elastic properties of lithium magnesium alloys measured by EBSD coupled indentation. *Hill polycrystal estimates. B = Bulk modulus, G = shear modulus, E = Young's modulus, ν=Poisson's ratio.

(M=0.44x+12.2 GPa, where x is the atomic percentage of Mg). This trend extrapolates to stiffness observed in magnesium-rich Beta alloys [197]. The error bars on figure 4.11A correspond to the standard deviation of the data sets, with different crystallographic orientations having different moduli. The EBSD coupled indentation method outlined in the lithium metal chapter was repeated to extract the three stiffness tensor components of each alloy which are plotted in figure 4.11B, and detailed in table 4.1 with the Hill (average of Voigt and Reuss) polycrystalline estimate values calculated. These results are in agreement with single crystal work investigating up to 4.2 at%Mg [104]. The elastic response to a general stress state can be calculated from these values. The orientation-dependent Young's moduli for the three alloy compositions are plotted with a common scale in figure 4.12.

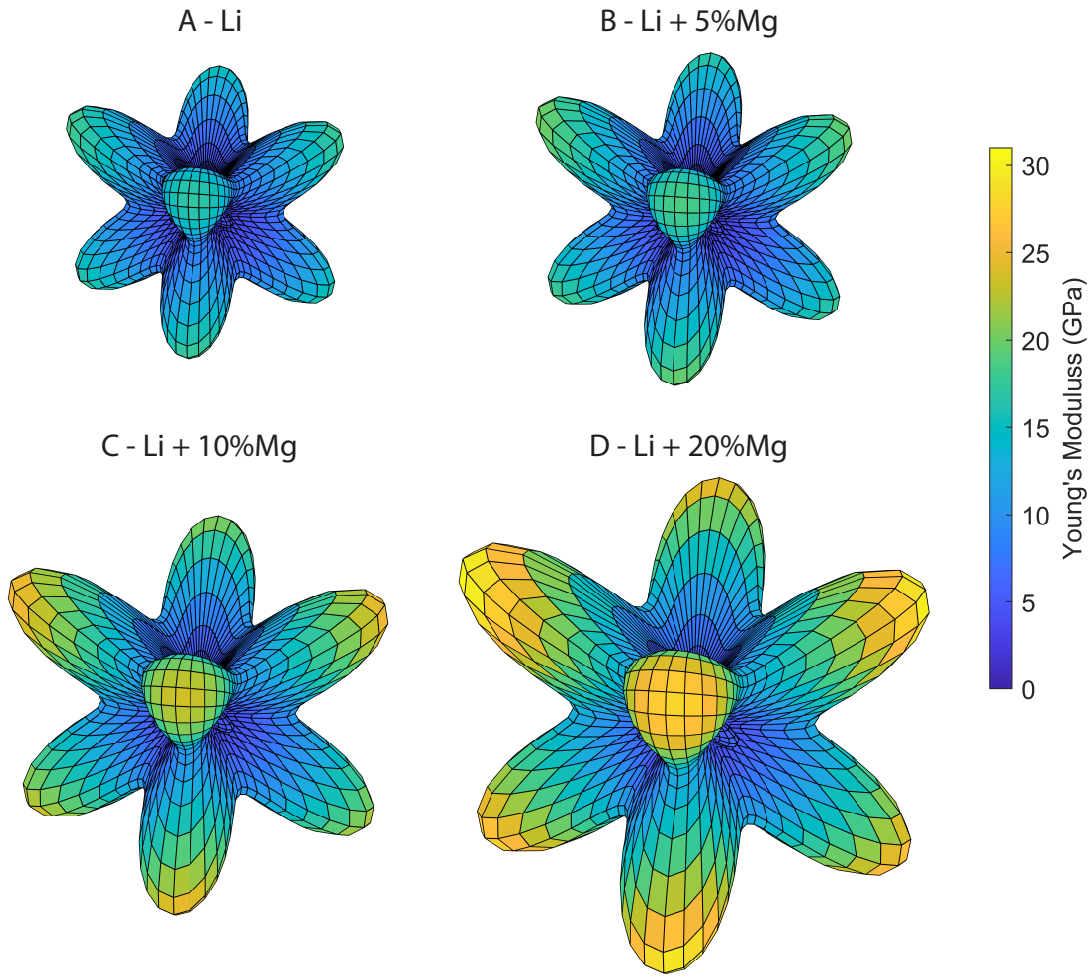


Figure 4.12: Orientation dependent Young's Modulus from measured stiffness tensor values. (a) Li, (b) Li+5at%Mg, (c) Li+10at%Mg, (d) Li+20at%Mg.

4.4.2 Plastic properties

Like pure lithium, strong size-dependent hardness is observed for lithium magnesium alloys. The average fitting curve for all indents at each composition is plotted in figure 4.13A with a representative data set, and the average fitting parameters are plotted in figure 4.13B. The observed hardness with indentation depth was fitted with equation 4.1 taken from Nix and Gao's seminal work [174], using data beyond 500 nm indent depth, such that the measured hardness decays towards H_0 with a characteristic decay length h*. A large increase in bulk hardness H_0 with magnesium content is observed, increasing from 2 MPa for pure lithium to over 57 MPa for the 20% alloy. This is reflected when handling the bulk ingots where

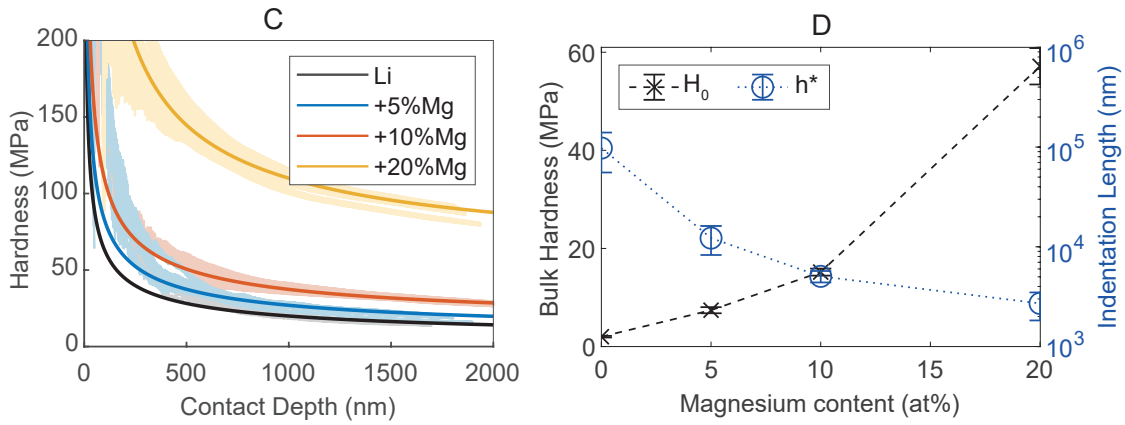


Figure 4.13: (a) Average size-dependent hardness curves for each alloy composition. (b) Fitting parameters for curves shown in C, showing bulk hardness (H_0) and characteristic decay length (h^*).

the high-content alloys require considerably more force to deform. The increasing trend is due to an increase in Peierl's stress that dislocations must overcome, lower thermal activity, and a greater dislocation density [167].

$$H = H_0\sqrt{1 + \frac{h^*}{h}} \tag{4.1}$$

A corresponding decrease in the characteristic decay length is observed (figure 4.13B), following the expected trend relative to the bulk hardness [174]. The dislocation density in the lattice of a material is inversely proportional to the measured decay length [198] meaning we expect the stored lattice dislocation density to be multiple times greater for the 5, 10 and 20% alloys, than for pure lithium. The role of dislocations in anode electrochemistry is unclear. A higher dislocation density will lead to a higher rate of vacancy absorption by dislocation climb. Depending on the rate at which this happens, it may lead to less voiding, which is caused by the aggregation of vacancies introduced during stripping at the solid electrolyte interface [72]. Improved contact retention has been observed by several works on the lithium-magnesium system, so it may be this is the case [96, 102, 199].

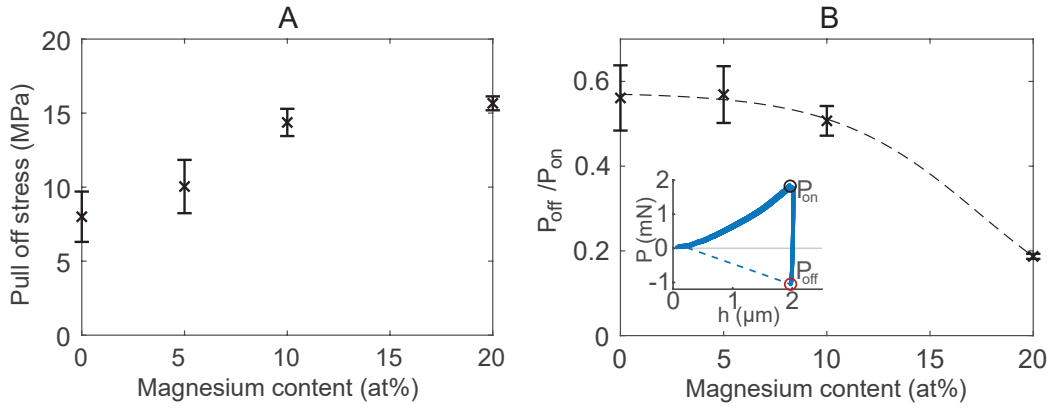


Figure 4.14: (a) Pull-off stress with the magnesium content. (b) Relative adhesion with alloy content, insert showing example load-displacement curve with pull-off force(P_{off}).

4.4.3 Adhesion

On indenter tip retraction, significant adhesion was observed for all indents, with a similar magnitude of force required to un-stick the indenter tip from each alloy as was needed to indent the sample. An example load-displacement graph is shown in the inset of figure 4.14B. The mean pull-off stress (retraction force/contact area) as a function of magnesium content is plotted in figure 4.14A. There is a clear increase in adhesion with the magnesium content. A numerical solution to calculate the work of adhesion for Berkovich indentation with extensive plastic deformation is yet to be found[200].

Considering a purely elastic assumption given by the Kendall model ($P_{off} = \sqrt{8A_c MW_{ad}R}$, $R = \sqrt{A_c/\pi}$), gives work of adhesion values of 9.61±0.03 mJ/m^2 for pure lithium and 15.00±0.57, 26.71±0.56 and 24.45±0.34 mJm^{-2} for the 5, 10 and 20 % alloys respectively. Again this should only be taken as an estimate as the purely elastic assumption is most likely to be invalid. Recent works have suggested higher anode-electrolyte adhesion leads to lower stack pressures being needed to prevent interfacial voiding on electrochemical stripping [100].

The ratio of peak indent load (P_{on}) and the retractive load required to overcome tip adhesion (P_{off}) is plotted in figure 4.14B. This value, equal to pull-off stress over hardness, can be considered as the relative strength of adhesion or effective adhesion of the material. Because the hardness of the alloys is higher, they physically are less

adhesive and are easier to work with, can be rolled thinner before rolling defects are observed, do not adhere to tweezers when handled.

4.4.4 Creep of lithium magnesium alloys

Lithium and lithium magnesium alloys are viscoplastic, meaning creep and stress relaxation are important components of their mechanical behaviour at room temperature. The electrochemical performance of a lithium anode is strongly dependent on the applied stack pressure. Higher extracted capacities on stripping are achieved with higher applied stack pressure attributed to the contribution of creep to the lithium flux towards the solid electrolyte-lithium interface[201]. On plating, increased stack pressure leads to lower critical current densities; perhaps due to creep contributing to the ingress of lithium into solid electrolyte flaws, increasing the risk of fracture. The quantification and understanding of creep, and how it can be modified with alloying, is therefore important.

Computational and experimental creep measurements for bulk polycrystalline samples of pure lithium, well below yield, show surprisingly strong agreement with a coefficient(n) of 6.4[202], 6.56[203] and 6.6 ± 0.7 [204] in the same stress and temperature regime ($\sigma/G \approx 10^{-}4$, 298K) indicating power law creep which is dislocation controlled. But lithium shows strong size-dependent hardness, with a characteristic length scale of 100 microns [156]. As bulk lithium creep is dislocation controlled; we may reasonably expect a change in creep behaviour at smaller length scales. A 5 mAhcm^{-2} capacity pure lithium metal anode has a thickness of $\approx$ 25 micron, and lithium filaments have a length-scale of as low as 100 nm; therefore creep behaviour in the 0.1-10 micron regime is highly relevant. More importantly, the changes in creep with alloying may contribute to observed differences in electrochemical performance. Broadly we expect less creep for the higher magnesium content alloys as the melting temperature and hardness both increase. In this subsection, the method of indentation creep has been developed with pure lithium and then measured with the lithium magnesium alloy range.

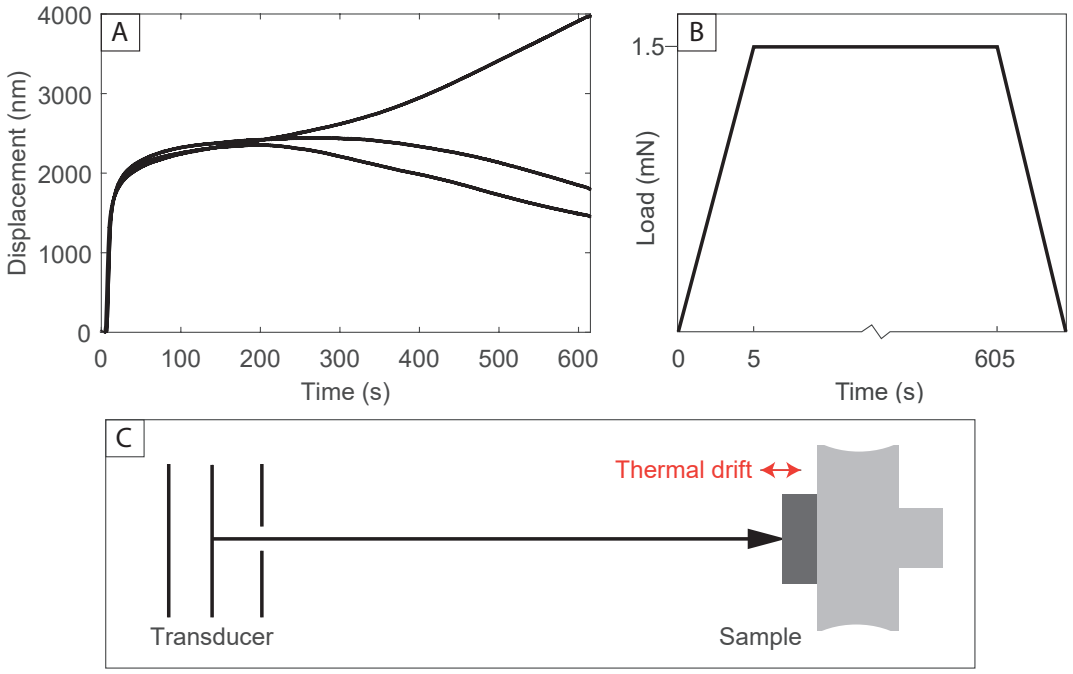


Figure 4.15: (a) Creep curves of pure lithium measured using quasistatic indentation technique. (b) Loading profile schematic. (c) Schematic of indentation measurement geometry showing thermal drift contribution to displacement measurement.

Quasistatic indentation creep

The PI88 indenter has two transducer options. The first is a low-load transducer with continual stiffness measurement; this can not change temperature. The second is a high-load transducer, this does not have continual stiffness measurement but is able to change temperature in the 20-800 °C range. Initially, to investigate creep I used the high-load stage, with the objective of independently determining the activation energy of creep using the Arrhenius relationship. A load-controlled trapezoidal loading scheme shown in figure 4.15B was used, with a peak load of 1.5 mN held for 600 seconds.

It can be seen from figure 4.15A that over time the creep curves diverge, and two of the three curves show apparent reverse creep. The significant error in the data is due to thermal drift, which is on the order of nanometres per second; compounding over the long experimental time. The schematic in figure 4.15C shows the geometry. The transducer holds the load constant at 1.5 mN during the hold period. The transducer block and sample surface are not perfectly fixed

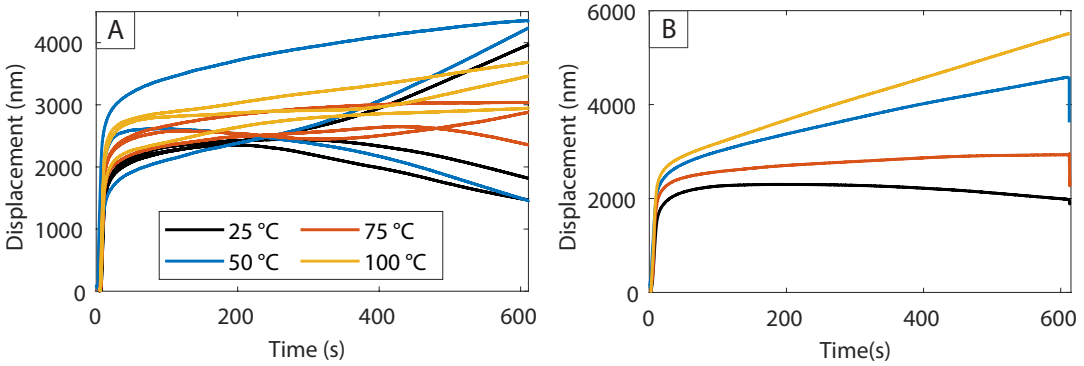


Figure 4.16: Quasistatic indentation creep. (a) Creep curves for 25, 50, 75 and 100 °C. (b) Averaged creep curves for each temperature.

relative to each other; and therefore some drift occurs during the course of the test. The transducer can not distinguish this displacement from the displacement due to the tip indenting into the sample.

Given thermal drift is a random property, accurate creep curves may in theory be obtained by performing sufficiently high numbers of creep tests such that the data could be averaged out. Six creep curves were performed successively at each of 25, 50, 75 and 100 °C. Three curves from each set are plotted in figure 4.16A showing very inconsistent data. The 6 creep curves measured for each temperature were interpolated across time, the results are plotted in figure 4.16B. The data set broadly shows the expected trend of increased creep with increased temperature. However, the 75°C and 50°C curves are in the wrong order. The 25°C curve is re-entrant. The relative hardness of each orientation will adversely affect data measured by this approach due to differences in the initial plastic indentation depth. To investigate this, EBSD was performed before and after the full set of heated indentations. However, the IPF Z maps in figure 4.17A and B show significant grain growth. Indent locations are marked with white triangles. The scanned regions are not identically aligned as the high-load indenter has a 3-axis, not 5-axis stage so the sample had to be removed and mounted on the standard SEM stage for EBSD. The significant grain growth is a result of both the high temperature and large number of introduced dislocations, and means that temperature-dependent creep measurements have significant challenges with attributing orientation to each indent.

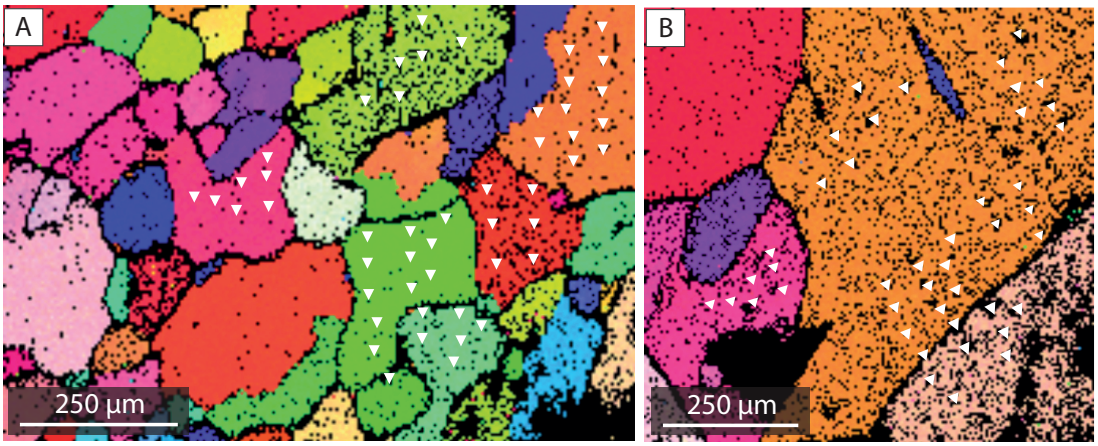


Figure 4.17: EBSD map of indented region, white triangles denote indent locations. (a) Before indentation. (b) After indentation.

I concluded from this work that this methodology would not succeed in accurately capturing the creep of lithium metal or its alloys at the nanoscale. A new methodology that accurately measures individual creep curves for each indent was necessary.

Thermal-drift independent indentation creep

A method for measuring creep, independent of thermal drift was recently outlined by Maier et al. [205]. This has since been built upon [206–209]. As the indentation tip is pyramidal, an increase in indentation depth is associated with an increase in the contact area. The relationship between contact area and measured stiffness is given by equation 4.2, and therefore the contact area, and subsequently indentation depth can be back-calculated from the measured stiffness as long as the indentation modulus of the material is known using equation 4.3. The mean indentation modulus for each composition was used throughout. As stiffness is measured at 10-300Hz, it is independent of thermal drift. The PI88 default settings only allow load-controlled tests at 220Hz, which does not work for lithium metal. However, in administrator mode, it is possible to change the frequency of load-controlled tests. 70Hz was used throughout the following work and gave less than 4 degrees of phase shift throughout the load-hold segment.

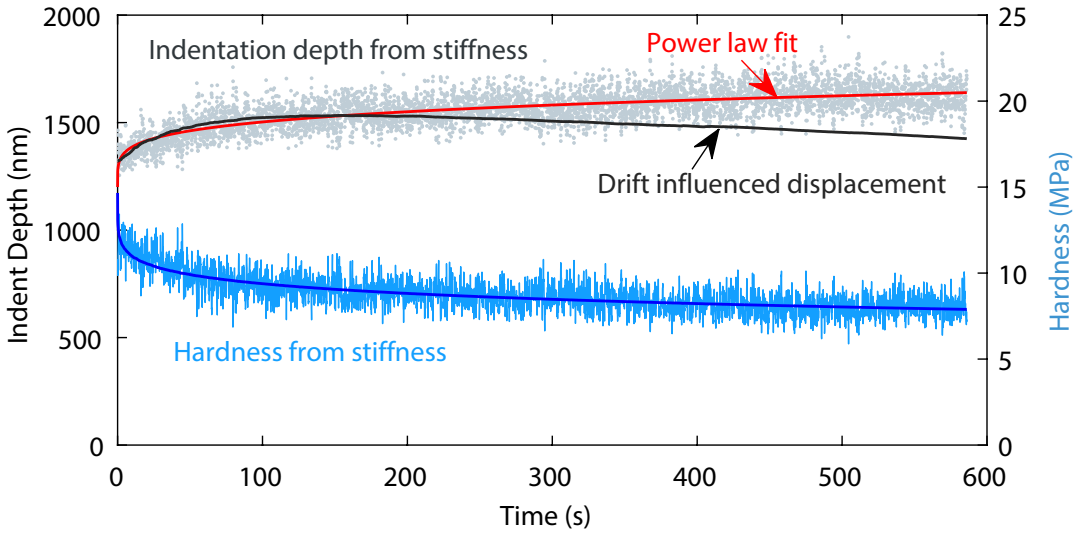


Figure 4.18: Processed creep curve for a 500 μN held load. The black line shows the direct displacement measure from the indenter, which is influenced by thermal drift. Grey points show calculated indentation depth from measured stiffness. Power law curve fit, shown in red. Hardness (load/contact area), calculated from the depth values, is plotted in blue.

$$S = \frac{2\beta}{\sqrt{\pi}} \cdot M \cdot \sqrt{A_c} \tag{4.2}$$

$$A_c = \frac{\pi}{4\beta^2} \cdot \frac{S^2}{M^2} \tag{4.3}$$

$$A_c = c_1 h_c^2 + c_2 h_c + c_3 h_c^{0.5} + c_4 h_c^{0.25} + ... \tag{4.4}$$

The contact area as measured by stiffness can then be used to determine a "true Hardness", by dividing the indentation load by this area.

In stiff, hard materials it is then worthwhile correcting for the difference between contact depth and indentation depth, using an epsilon value for a Berkovich tip of 0.75. In lithium due to its high E to H ratio, this makes little difference.

$$h = h_c + \epsilon \cdot \frac{P}{S} \tag{4.5}$$

The processed creep data for a 500 μN held load on pure lithium is shown in figure 4.18. The black line shows the direct displacement measure from the indenter,

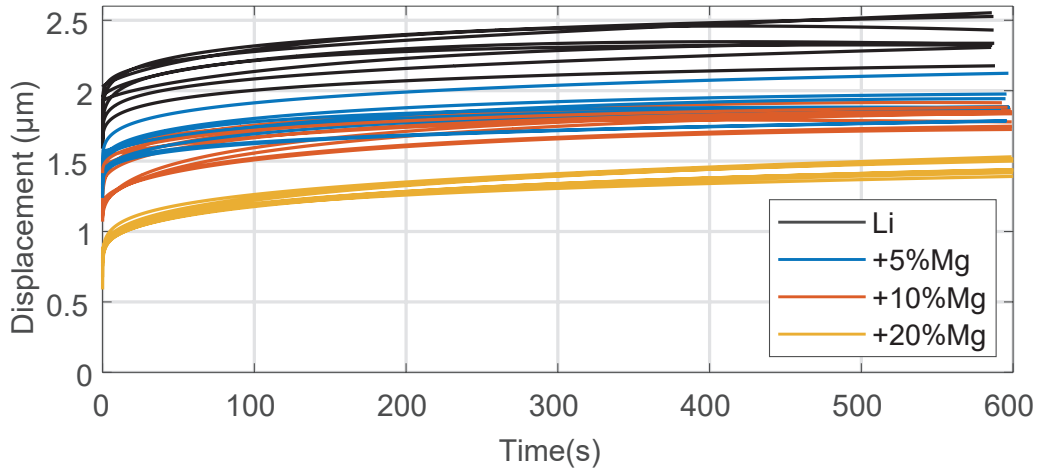


Figure 4.19: Constant force indentation power-law fit creep curves with the varied magnesium content.

which as established is influenced by thermal drift. The grey points show calculated indentation depth from measured stiffness using equation 4.3 and equation 4.4, with the indenter tip fitting parameters measured in the previous chapter. The data is noisy but can be fit with a power law curve ($h(t) = a \cdot t^b + c$), shown in red. Throughout, t = 0 was defined as the time at which the hold load was first reached. Hardness (load/contact area) is obtained from the depth values and is plotted in blue. The data shows that hardness is not a fixed value for a given load in viscoplastic materials such as lithium, but evolves over time. Different hardness is measured depending on the strain rate; with around a factor of two range. This is reflected in lithium metal's mechanical testing literature [156].

Indentation creep tests were performed on each of the alloy compositions, maintaining a constant load of 1000 μN with a Berkovich tip for 600 seconds, with stiffness continually measured [205]. The stiffness calculated depth-time data is relatively noisy and therefore figure 4.19 shows the result of each data set being fit with an empirical power law curve $h(t) = a \cdot t^b + c$. This gives an accurate reflection of the range of creep curves measured during the indentation tests and shows that the higher the magnesium content, the less creep occurs for the same load.

Finding creep parameters

Creep data from indentation is only useful insofar as it can be related to a general stress state. Su et. al. [210] outlined a methodology, building on the work of Bower et. al. [211] for going between indentation data and uniaxial test power law creep values, which can be input into mechanical models. Uniaxial creep is described by equation 4.6, whereas indentation creep values are defined by equation 4.7. It has been found experimentally that n=N, but that $\beta \neq \alpha$. Bower et al. proposed that the conversion could be done using equation 4.8, with c and F depending on the creep exponent n and the indentation tip shape. Su et. al. provides the parameterised values to calculate n and c for a Berkovich tip, the values for an equivalent cone angle of 70 degrees were used [210] and found experimentally that this conversion was valid across a range of materials.

$$\dot{\epsilon} = \alpha\sigma^n = A_c\sigma^n exp(-\frac{Q_c}{RT}) \tag{4.6}$$

$$\dot{\epsilon} = \frac{1}{h}\frac{dh}{dt} = \beta\sigma^N \tag{4.7}$$

$$\alpha = \frac{F^n c^{2n-1}}{tan\theta}\beta \tag{4.8}$$

Indentation creep parameters can be obtained by fitting a log-log plot of the displacement against time, using equation 4.10 obtained by taking the logarithm of equation 4.9 from [211]. There are alternative methods such as first fitting the displacement-time data with an empirical expression, then differentiating this function to calculate strain rate before plotting this against pressure on a log-log plot to obtain values[205]. I selected the first method, as it required fewer processing steps and therefore introduced less opportunity for processing error. An example fit can be seen in figure 4.20A, where except for at low times, the relationship is linear.

$$h = (2n\beta)^{\frac{1}{2n}}(\frac{P}{\pi \tan^2\theta})^{\frac{1}{2}} t^{\frac{1}{2n}} \tag{4.9}$$

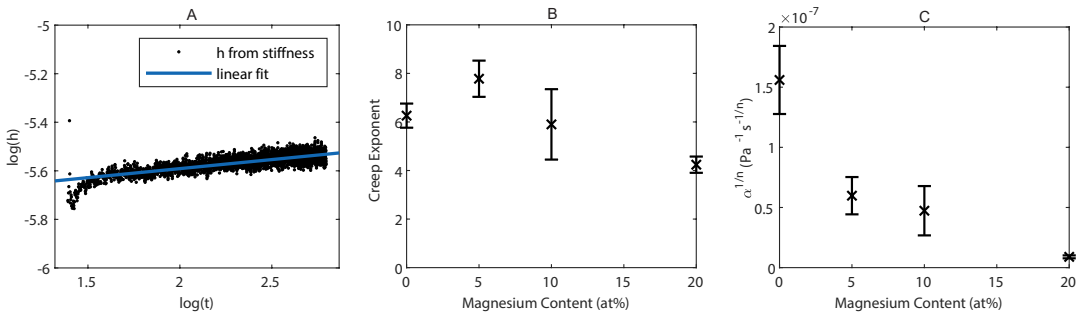


Figure 4.20: Indentation creep of lithium magnesium alloys. (a) Fit creep data for lithium metal indentation, giving n = N = 6.20 and $\beta = 2.01\times10^{-46}$, giving α= 2.32×10^{-43} $Pa^{-1}s^{-1/n}$. (b) Creep exponent, n, as a function of magnesium content. (c) Creep pre-factor, α, raised to 1/n as a function of magnesium content.

at%Mg	n	st. dev.(n)	$\alpha^{1/n}$	st. dev.($\alpha^{1/n}$)	α
0	6.26	0.497	1.56×10^{-7}	2.83×10^{-8}	2.29×10^{-43}
5	7.78	0.746	5.98×10^{-8}	1.55×10^{-8}	6.59×10^{-57}
10	5.90	1.45	4.73×10^{-8}	2.05×10^{-8}	6.08×10^{-44}
20	4.24	0.335	8.96×10^{-9}	1.22×10^{-9}	7.48×10^{-35}

Table 4.2: Fitted creep parameters with changing magnesium content.

$$log(h) = log\left((2n\beta)^{\frac{1}{2n}}(\frac{P}{\pi\tan^2\theta})^{\frac{1}{2}}\right) + \frac{1}{2n}log(t) \tag{4.10}$$

The creep exponent, n, for pure lithium, was measured to be 6.26 with a standard deviation of 0.497. This is in line with the bulk uniaxial test values for lithium of 6.4 [202], 6.56 [203] and 6.6 ± 0.7 [204]. Given the large exponent, and the stresses that drive creep being of the order of MPa, the pre-factor α is very small and varies significantly depending on the measured creep exponent. I found the value $\alpha^{1/n}$ far more consistent between indents. For pure lithium $\alpha^{1/n}$=1.56×10^{-7} $Pa^{-1}s^{-1/n}$, with a standard deviation of 2.8×10^{-8}. Using these values the pre-factor for lithium can be calculated as 2.29×10^{-43} $Pa^{-n}s^{-1}$. This is in strong agreement with the literature value of 2.95×10^{-43} $Pa^{-n}s^{-1}$ at 303 K [204]. This agreement validates the indentation methodology and suggests that the mechanisms of creep at the microscopic and macroscopic scales are the same.

The fit values for the lithium magnesium alloy samples are presented in figure 4.20B and C and in table 4.2. The creep exponent remains approximately

constant up to a magnesium content of 10%, and then is lower for the 20% sample. This follows from the hardness data which shows dislocation glide is substantially harder in the 20% sample. The creep exponent is in the range of 3-10 for all alloys suggesting the mechanism is dislocation glide. The measured pre-factors and exponents mean that higher magnesium content alloys, under the same stress, will have orders of magnitude lower creep rates than lower content alloys. The substantial increase in creep-resistance is a consequence of the increased hardness (figure 4.13B) and decreased thermal activity of the material with higher magnesium content, with the room temperature (298 K) to liquidus temperature decreasing from 0.69 for pure Li to below 0.6 for the 20% magnesium alloy, figure 4.1. Despite the strong agreement with pure lithium literature values, indentation creep isn't perfect, leading to scatter in the results. The technique has well-documented limitations [212], including only probing at high pressures, probing at a sub-grain level, an inability to discern between different stages of creep, and the processing needed to extract values from the data. The numerical values should be taken with a pinch of salt, but show a clear trend. Based on these findings, I'd expect smaller changes in electrochemical performance due to stress to be observed for electrodes made with lithium magnesium alloys than for pure lithium.

4.4.5 Summary of lithium magnesium mechanics.

Solid solution magnesium alloying of lithium leads to an increase in stiffness, hardness and creep resistance. In the wider context of metals, all the alloys are ductile and soft, pure aluminium for example, often regarded as a soft metal, has a hardness of around 250 MPa, whereas Li+20%Mg has a bulk hardness of 57 MPa. This means all of the studied alloys can be substantially deformed without embrittlement, such as in the rolling and attachment of electrodes. Nanoindentation is a powerful method to extract mechanical values from small samples. These alloys are an excellent example where preparing, storing and testing a statistically significant number of macroscopic test samples would be impractical. The numbers

gained are in line with the limited existing literature and show clear changes in mechanical properties with magnesium alloying.

4.5 Surface chemistry

The lithium metal anode has a very negative electrochemical reduction potential (-3.04 V versus standard hydrogen electrode). Due to this, the metal reduces all known solid electrolytes to form a solid electrolyte interphase layer (SEI). The SEI has an impact electrochemically, impeding lithium transport and therefore increasing the overpotential required to drive any current.

The surfaces in contact with the solid electrolyte are different when using lithium alloys and pure lithium. This may lead to changes in interfacial impedance. Differences may include the lithium activity and potential of the alloy compared to pure lithium leading to changes in the charge transfer resistance, the composition of any native layer on the alloy surface, and possibly the chemistry of the SEI formed [67]. By performing electrochemical impedance spectroscopy (EIS) at regular intervals throughout a period at open-circuit on multiple self-symmetric cells with an argyrodite solid electrolyte, we have quantified the interfacial resistance for the anode-electrolyte interface for each alloy, and its growth rate. This can then be correlated with the chemical characterisation of the interfacial layers using XPS.

4.5.1 Open-circuit voltage

A significant change in the open-circuit potential of an alloy could change the electrolyte reduction dynamics, leading to differences in SEI composition. Asymmetric solid-state cells for each of the alloys were assembled with a lithium metal counter electrode. The potential difference across the cell was measured over a 24-hour stabilisation period. The values are plotted in figure 4.21. As can be seen, there is a linear increase with magnesium content, but the increase is small, single millivolts in size. I therefore don't expect significant changes in the SEI formed by electrochemical electrolyte reduction.

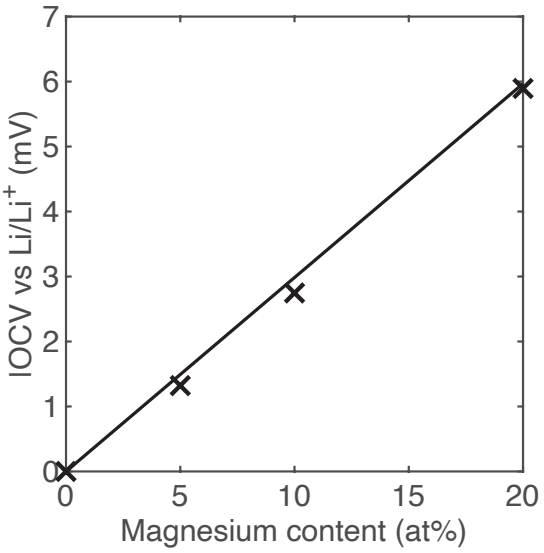


Figure 4.21: Open-circuit voltage measured against lithium metal counter electrode.

4.5.2 Electrochemical Impedance Spectroscopy

Electrochemical impedance spectroscopy (EIS) is a frequency-resolved technique. In a typical Nyquist impedance plot, the real and imaginary components of impedance, measured across a wide range of frequencies are plotted against each other. The current standard approach in the literature is to fit this data with an equivalent circuit that should be representative of the fundamental physics being measured. Processes leading to impedance have an associated timescale. The effects are cumulative with decreasing frequency, as high-frequency processes appear ohmic at lower frequencies.

EIS spectra were fit using the simplex method within the ZFit tool of the Biologic EC-Lab software using the equivalent circuit shown inset in figure 4.22A, with a finite ohmic resistance and two distinct depressed semicircles [93]. The smaller high-frequency component, attributed to grain boundaries or porosity within the solid electrolyte [90], was effectively constant throughout the OCV period and there is no significant trend of this or ohmic resistance with magnesium content. To enable consistency in accurately fitting changes in the interfacial semicircle, the solid-state electrolyte equivalent circuit element capacitance Q and resistance R were allowed to fit freely with all other values for an EIS spectrum in the middle of the OCV

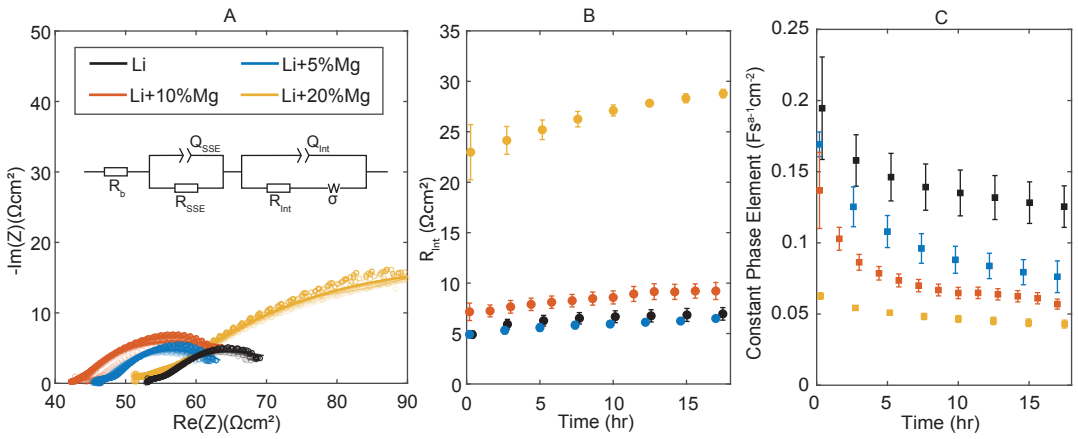


Figure 4.22: (a) AC electrochemical impedance spectroscopy of self-symmetric cells, higher saturation denotes longer time. Equivalent circuit inset. (b) Interface resistance against time. (c) Interface constant phase element against time.
Error bars in b and c show standard error across multiple samples.

period, and then these values were held constant to fit the remaining spectra in the series. The other values were allowed to fit freely throughout. The Warburg element is reflective of the transport within the anode and can be calculated from the anode diffusivity using equation 4.11. During fitting this value was fixed at 0.40, 0.55, 0.77, and 1.50 $\Omega s^{-1/2}$ for the 0, 5, 10 and 20% Mg anodes respectively, based on the diffusivity values at 303 K obtained by extrapolating ^{6}Li PFG-NMR trends reported later. Higher values for the Warburg element slightly decrease the fit interfacial resistance values, the change in measured interfacial resistance by using a Warburg value of 0 is small. As has been discussed in a recent paper [90] the larger, low-frequency component corresponds to the combined processes of charge transfer and transport through the interfacial layers. It was not possible to robustly separate these processes, so they are grouped together as a single total interfacial resistance. After fitting, resistance values were multiplied by the total area of the two electrodes to obtain an areal resistance, constant phase elements were divided by the total electrode area.

$$\sigma_w = \frac{RT}{Az^2F^2} \cdot \frac{1}{c_{Li}\sqrt{D_{Li}}} \tag{4.11}$$

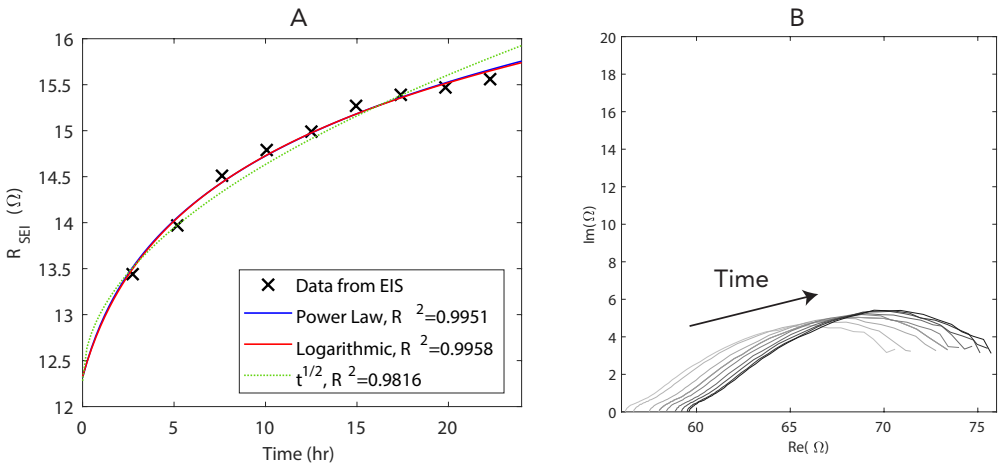


Figure 4.23: Growth of SEI resistance over time. (a) Increase in measured SEI resistance for a lithium metal self-symmetric cell. Fit with three functions discussed in the text. (b) Raw EIS data, fit to obtain values in A. Darker colours indicate later time.

The average areal interfacial resistance (R_{Int}) per electrode is plotted against time in figure 4.22B, with error bars indicating the standard error across the samples measured. The pure lithium and 5% samples are indistinguishable, but the 10% and 20% have a larger interfacial resistance which grows at a proportionally higher rate with time. There is a corresponding decrease over time in the size of the constant phase element Q_{Int}, figure 4.22C.

It is tempting to fit the growth over time with a function. In some works, diffusion-limited growth is assumed, leading to data being fit with a power law with an exponent of 0.5. This fit our data comparatively poorly (median R^2=0.966), overestimating resistance at longer times. Others have questioned this model's validity for SEI growth[213]. The data could be accurately fit with either a logarithmic expression, $R(t)=A\cdot\ln(1+b(t-t_0))$, or a power law with a free exponent $R(t) = A(t-t_0)^n$. As can be seen in figure 4.23, these two curves are nearly identical and the quality of the fit was indistinguishable (median R^2=0.991 and 0.990 respectively). The power law curve led to more consistent fitting parameters across samples. Within error, the growth exponent n was consistent for all alloy compositions at 0.11, with a standard deviation of 0.04, suggesting consistent interfacial resistance growth mechanisms despite changed magnesium content. However, these fits are entirely empirical and give little insight into the physical

process underpinning the change in resistance. They should not be extrapolated to times outside of the measured region, and don't capture any SEI growth during cycling. The change in the constant phase element in Figure 4.22C can be related to a change equivalent capacitance of the interface. From classic capacitance theory, the equivalent capacitance is inversely proportional to the layer thickness for a constant permittivity.

The interfacial resistance is due to the combination of charge transfer, transport through the native layer and SEI transport. The charge transfer resistance is proportional to the activity (c_i/c_i^{∞}) of the lithium in the metal electrodes (el) and solid electrolyte (se) raised to the charge transfer coefficients (a), as in equation 4.12 [214]. As it is a single electron reaction, the charge transfer coefficients will be approximately 0.5. Considering the 20% magnesium sample, the change in concentration should only account for approximately a 10% change in charge transfer resistance. This does not account for the size of the change in total interfacial resistance observed for the 20% sample. The charge transfer resistance should also remain constant over time at OCV.

$$i_0 = \frac{c_{el}}{c_{el}^{\infty}}^{a_{el}} \frac{c_{se}}{c_{se}^{\infty}}^{a_{se}} \cdot i_0^{c^{\infty}} \tag{4.12}$$

Considering the SEI transport, the change in potential with magnesium alloying is very small (figure 4.9), and therefore considering the SEI formation process as the electrochemical reduction of the solid electrolyte, we would expect near-identical electrochemical decomposition products.

To test this hypothesis, X-ray photo-electron spectroscopy (XPS) was performed using the in-situ sputtering method developed in a study for lithium metal[90]. XPS measurements were performed by Dr Sudarshan Narayanan using a PHI Versaprobe III instrument. The spectra were collected intermittently between periods of sputtering a very thin layer of magnesium metal onto the surface of an Li_6PS_5Cl pellet using an argon gun aimed at a magnesium foil sheet. The electrochemical potential of magnesium is well below the electrochemical stability window of the Li_6PS_5Cl solid electrolyte, therefore decomposition products form.

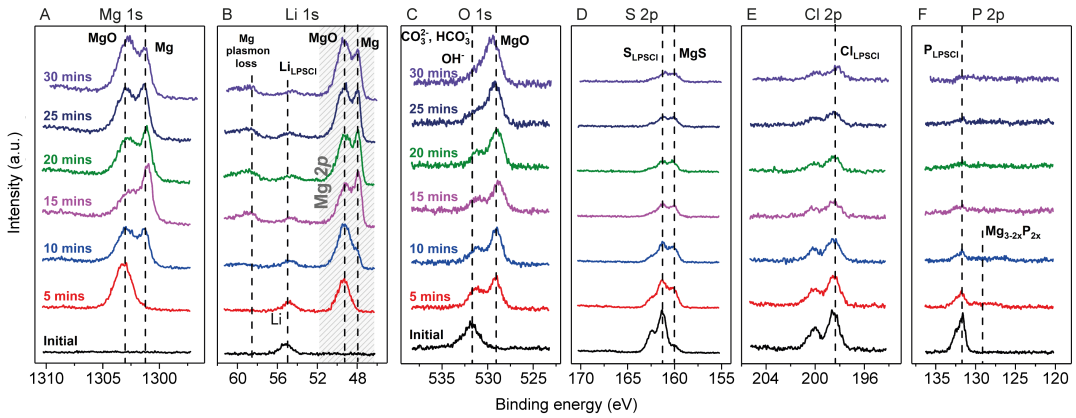


Figure 4.24: XPS data of Mg on Li6PS5Cl. Core-level XPS spectra collected at 5-minute intervals during Mg sputtering were conducted over a total period of 30 minutes. (a) Mg 1s, (b) Li 1s, (c) O 1s, (d) S 2p, (e) Cl 2p, and (f) P 2p transitions.

Figure 4.24A-B show core-level XPS spectra for the Mg 1s and Li 1s transitions from the surface of the Li_6PS_5Cl pellet, at various intervals during etching of a magnesium foil. The initial oxygen 1s spectra reveal the presence of surface contamination comprising typically of carbonates, bicarbonates and hydroxides, whose intensity reduces with increased Mg sputtering.

After just five minutes of sputtering (at an Ar^+ ion accelerating voltage of 4 kV) a peak characteristic of magnesium oxide appears at a binding energy (B.E.) of 1303 eV in the Mg 1s spectra, with an equivalent peak appearing in the oxygen 1s spectra at a B.E. of 529 eV [215]. Despite the very low oxygen content of the XPS chamber, the metallic magnesium layer deposited can easily react to form MgO [89, 155]. Further magnesium sputtering results in the appearance of another Mg 1s peak at a lower B.E. (∼1301 eV) characteristic of metallic magnesium, which increases in intensity as sputtering proceeds for longer periods. Li_6PS_5Cl reacts with lithium to form Li_2S, suggesting that the S^{2-} is weakly bound within the $PS_4{}^{3-}$ tetrahedron [93], therefore the growth of a peak at the lower B.E. shoulder (∼160 eV) in the S 2p spectra (figure 4.24D) could be indicative of the formation of MgS [216] but is indistinguishable from a Li_2S peak which we know will form as an electrolyte reduction product. A small amount of Li_2S can be seen in the initial spectra. The same issue is true in the Mg 1s spectra, where any MgS peak would be at a binding energy similar to that of MgO [217, 218]. The growth of this peak

after 15 minutes perhaps suggests the formation of MgS. No significant changes in the Cl 2p spectra were observed (figure 4.24E), likely due to the proximity in B.E. values for the Cl in argyrodite and that in $MgCl_2$, as has been noted previously for LiCl [93]. Lastly, in the P 2p spectra (figure 4.24F) there is a broad feature between 126-130 eV, ascribed to the formation of sub-phosphides which has equivalently been observed in the case of lithium sputtering [219], is present in very low intensities between five and ten minutes of sputtering.

This data demonstrates the limitations in XPS data in distinguishing compounds with overlapping peaks. There is no compelling evidence of magnesium products forming with reaction with the electrolyte when metallic magnesium is deposited and therefore the initial hypothesis that the SEI composition with the alloys is unchanged is not disproved. Of the possible decomposition products, all of the lithium compounds (Li_2S, LiCl, LiOH) are more thermodynamically stable than their magnesium equivalents (MgS, $MgCl_2$, $Mg(OH)_2$), with the exception that magnesium oxide ($\Delta G^{f,303K}_{MgO}$=-607.8 kJmol^{-1}) is more stable than lithium oxide ($\Delta G^{f,303K}_{Li_2O}$=-573.6 kJmol^{-1}).

The increased interfacial resistance and increased growth over time observed in EIS is most likely to be due to a change in the composition of the native layer on the electrodes due to the presence of magnesium in the electrode.

To investigate this, XPS was performed on the alloy samples, prepared in the same way as the cell electrodes. Figure 4.25D-F show the spectra for O 1s, Mg 2s, Li 1s and Mg 2p for the three alloy compositions after 60 minutes of sputtering into the native layer. Full spectra at different sputtering times are plotted in figure 4.26. Given the thermodynamics discussed, we attribute the Mg 2s peak (B.E. 86.7 eV) to magnesium oxide. The lithium 1s peak (B.E. 53.7 eV) is a combination of several compounds including lithium carbide [154, 220], oxide, hydroxide and others. All three alloy native layers consist of a combination of magnesium oxide and lithium compounds, but the relative fractions vary.

Figure 4.25C plots the relative intensity of the Mg 2s peak compared to the O 1s peak at a range of sputtering times. As can be seen, there is some variation

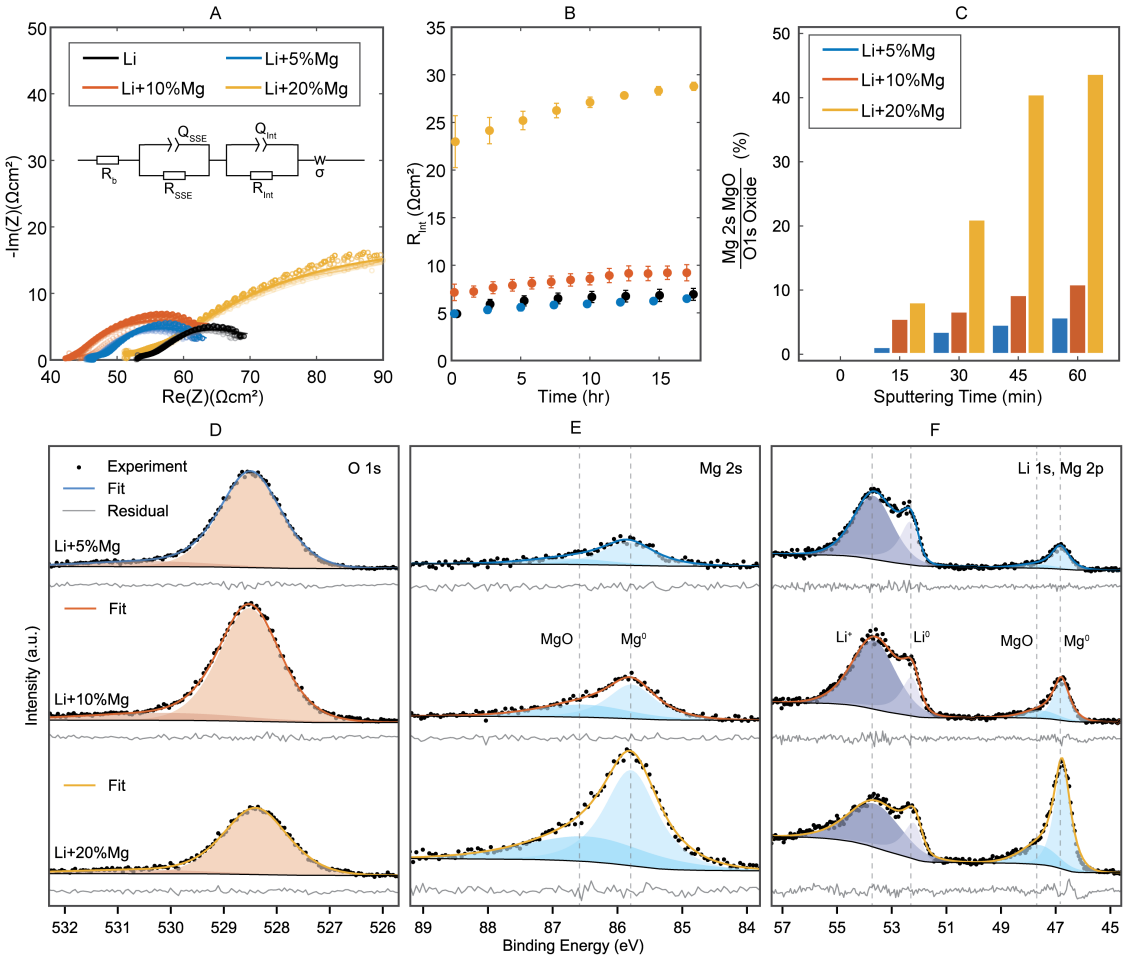


Figure 4.25: Interface chemistry (a-b) Repeated from figure 4.22. (c) Bar chart showing magnesium oxide fraction of total oxide at a series of sputtering depths. (d-f) XPS analysis to characterise native layer on the alloy surfaces. Core-level XPS spectra for each alloy composition for (d) O 1s, (e) Mg 2s, (f) Li 1s and Mg 2p.

in relative composition over the thickness of the layer, with more magnesium oxide present deeper into the layer, and more lithium compounds at the surface. This has been observed for native layers on pure lithium [215] and seems likely to reflect the formation kinetics of the layer. With a higher magnesium alloy content, a much greater fraction of magnesium oxide is observed in the native layer. The two formation energies are both similar and very negative, therefore where significant magnesium is present, they appear in approximately equal proportion. Given magnesium and lithium oxides do not form a solid solution, we expect the presence of magnesium oxide to inhibit lithium transport. The increased magnesium oxide content of the native layer therefore correlates well with the

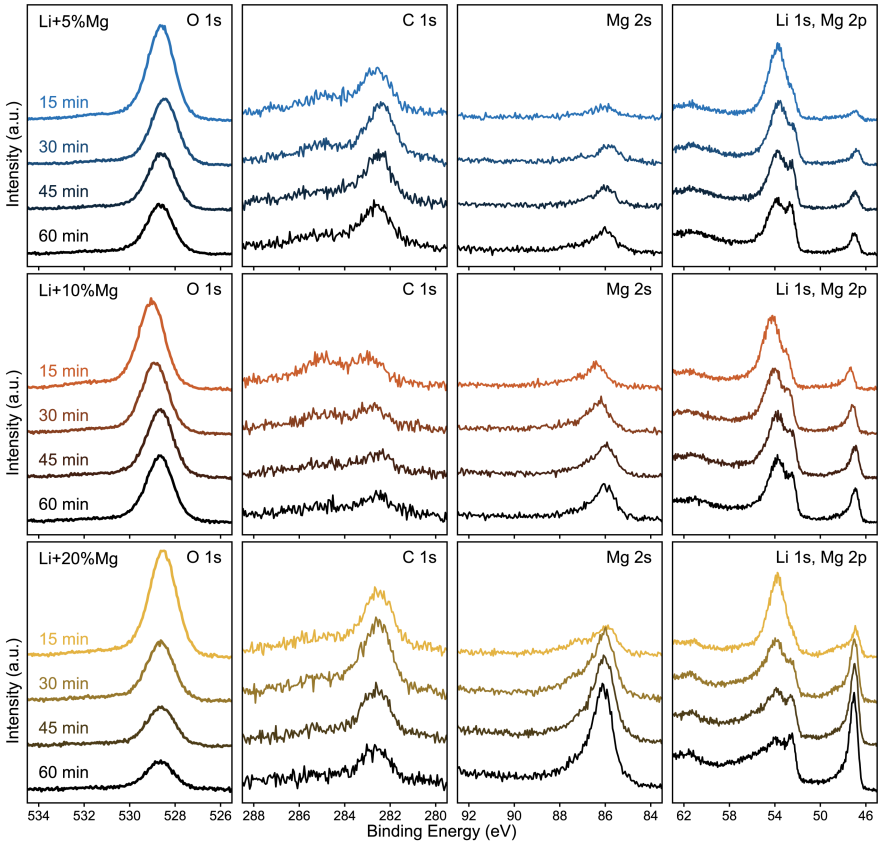


Figure 4.26: XPS spectra of native layer on alloy surface at a range of sputtering times. Core-level XPS spectra for each alloy composition for O 1s, C 1s, Mg 2s, Li 1s and Mg 2p.

increased interfacial impedance observed in EIS. The increase of 10 Ωcm^2 observed for the 20% sample over the others will meaningfully increase the overpotential needed to drive a high areal current.

4.6 Diffusion

4.6.1 PFG-NMR on ^{6}Li Alloys

The transport of lithium within a metal anode strongly influences electrochemical performance. As will be seen in this chapter there is a clear relationship between lithium diffusivity and accessible capacity at high discharge rates.

Self-diffusivity of lithium within pure lithium and alloy samples containing 5, 10 and 20% magnesium was measured using pulsed field gradient nuclear magnetic resonance spectroscopy (PFG-NMR) [221]. This measurement is challenging in naturally isotopic lithium (primarily ^{7}Li) due to the combination of slow ionic

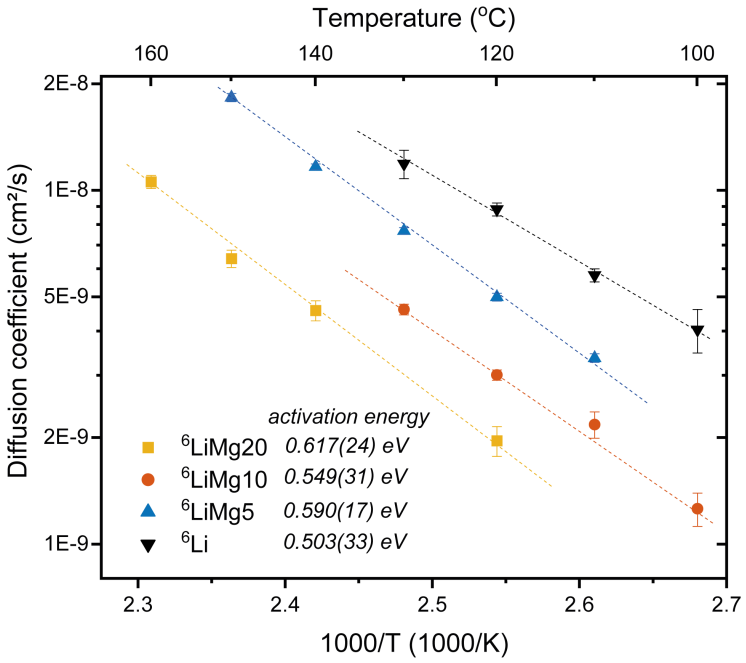


Figure 4.27: 6Li diffusion coefficient of pure lithium and LiMg alloy samples measured by PFG NMR.

diffusion and fast ^{7}Li spin relaxation caused by a quadrupolar interaction [222].To measure diffusivity in the magnesium alloy samples, ^{6}Li enriched alloy samples were synthesised as the ^{6}Li isotope has a much smaller nuclear electric quadrupole moment and therefore a longer relaxation time [223]. High temperatures were used to increase the diffusion rate to measurable values.

The alloy samples for nuclear magnetic resonance (NMR) tests were prepared with ^{6}Li-enriched lithium metal (95% ^{6}Li 5% ^{7}Li Chunks, Sigma Aldrich) following the same protocols as the normal lithium magnesium alloys. The metal ingots were then rolled and cut into small pieces and packed in NMR tubes that are sealed by J-Young's caps. The ^{6}Li PFG NMR experiments themselves were carried out by Dr Hua Guo on a Bruker AVANCE III HD spectrometer with a magnetic field of 9.4T (Larmor frequency of 6Li is 58.89 MHz) equipped with a 5 mm single-axis diffusion probe. A stimulated echo pulse sequence was applied with an effective gradient pulse duration (δ) of 2 ms, a diffusion time (Δ) between 300-800 ms, and gradient amplitudes varying between 0.02 and 25 T/m. A pulse delay of

1 s and a scan number of 128-512 were applied for each test. Each data point took approximately 10 hours to collect.

The results are shown in figure 4.27. The pure ^{6}Li-enriched lithium metal shows a diffusion coefficient of 8.83×10^{-9} cm^2s^{-1} at 393.1 K, and by fitting the diffusion coefficients at different temperatures with the Arrhenius equation, an activation energy of 0.503 ± 0.033 eV, which fits previous literature reports well [224]. Lower values of diffusivity and higher activation energies are measured for increasing magnesium content, with measured values of 0.590±0.017, 0.549±0.031, and 0.617±0.024 eV for the 5, 10, and 20% samples respectively, close to the previously reported value 0.63 eV for the Li+10%Mg alloy measured with the motional narrowing of ^{7}Li peaks [225].

The activation energy has two components, one due to the enthalpy of vacancy creation, and the second the enthalpy of vacancy hopping. An increase in vacancy creation enthalpy is expected with a higher melting point. An increase in hopping enthalpy with increasing magnesium content is expected with closer lattice packing and increased stiffness. There is some experimental error on the activation energy values, but the relationship appears linear (E_a=0.5242+ 0.0046·x eV, where x is at%Mg). The ^{6}Li diffusion coefficient of pure lithium and Li+20%Mg at room temperature (298 K) is calculated to be 7.55×10^{-11} and 5.63×10^{-12} cm^2s^{-1} by the extension of the Arrhenius plots, close to reported ^{8}Li NMR results [101] but slightly lower than time-of-flight secondary ion mass spectrometry (TOF-SIMS) results [102]. In addition, Shi et al reported diffusivity of lithium magnesium alloys from 10 to 40 at%Mg measured by chronoamperometry [103]. Their reported values are of the order of 10^{-8} cm^2s^{-1} at room temperature, however, their presented data for 40% magnesium gives a value of order 10^{-10} cm^2s^{-1}, which is in broad agreement with the other papers, and such electrochemical measurements of diffusivity can easily have very high errors.

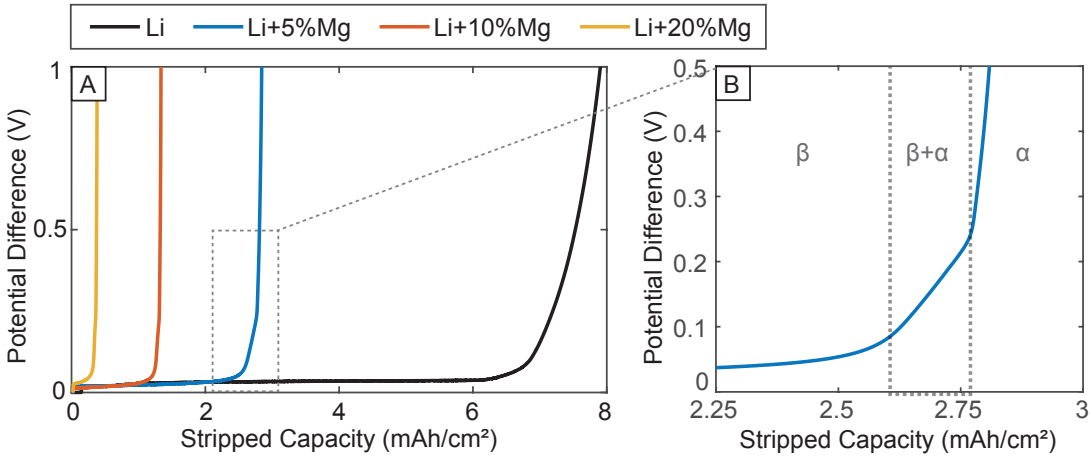


Figure 4.28: Electrochemical stripping of lithium magnesium alloys. (a) Chronopotentiometric stripping showing potential as a function of areal capacity at 0.31mAcm^{-2}. (b) Zoom on Li+5at%Mg potential increase.

4.6.2 Diffusivity measured by time of flight secondary ion mass spectrometry (TOF-SIMS).

Samples prepared as described were provided to Marco Siniscalchi to investigate the diffusivity of lithium in the alloys using time-of-flight secondary ion mass spectrometry (TOF-SIMS). The excellent work is published in ACS Energy Letters [102]. The results are in broad agreement and show a similar trend to the PFG-NMR values.

4.7 Chronopotentiometry

To investigate stripping performance, self-symmetric cells for each alloy composition were assembled and a constant current density of 0.31 mAcm^{-2} ran in a single direction until a cut-off voltage of 5V was reached. This current density was chosen as a compromise of reflecting realistic cell discharge conditions whilst considering the limitations of current solid electrolytes, where higher current densities lead to cell failure by shorting. The unidirectional stripping test is purposefully simple to allow for a clear comparison between different alloys.

Representative potential-capacity curves are plotted in figure 4.28. There is a clear trend of reduced stripping performance with increasing magnesium content.

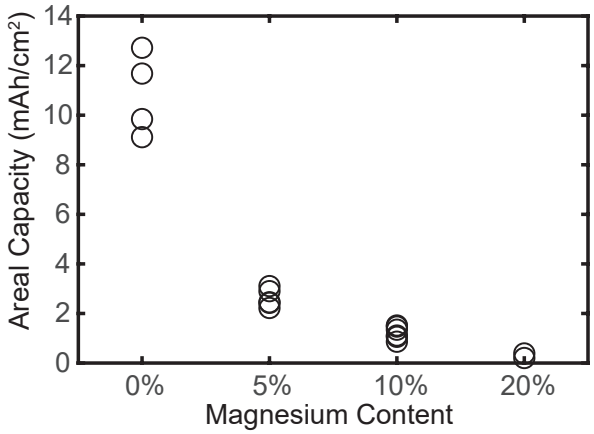


Figure 4.29: Extracted capacity for self-symmetric cells of varying alloy content showing the reproducibility of data in figure 4.28.

As can be seen in figure 4.28A, the shape of the cell potential increase in the alloys is different to the case of lithium failure. The zoomed figure 4.28B shows there are three distinct stages of potential increase for the alloys. The first, taking up most of the test time is a gradual increase. This corresponds to the increasing magnesium content of the alloy at the surface as a concentration gradient builds. This stage ends when a potential difference of approximately 70 mV is measured, which corresponds to the working potential of 69 at% magnesium-lithium alloy vs Li/Li+ [226]. The second stage is approximately linear, with a steeper gradient. After approximately 30 minutes, a third stage of rapid potential increase towards very large potentials is observed. The latter two stages correspond well to the 2-phase and alpha-phase region of the lithium magnesium phase diagram. The diffusivity of lithium in the alpha phase is approximately three orders of magnitude slower than that of the beta phase, therefore as the lithium-depleted surface layer transforms from BCC beta phase to HCP alpha phase; there is a dramatic increase in the concentration gradient required at the interface to supply the fixed current density (Fick's first law), and therefore a substantial increase in the transport overpotential within the anode. This leads to a rapid increase in measured potential. The custom cell design and careful electrochemistry led to very good reproducibility in the data, as can be seen in figure 4.29.

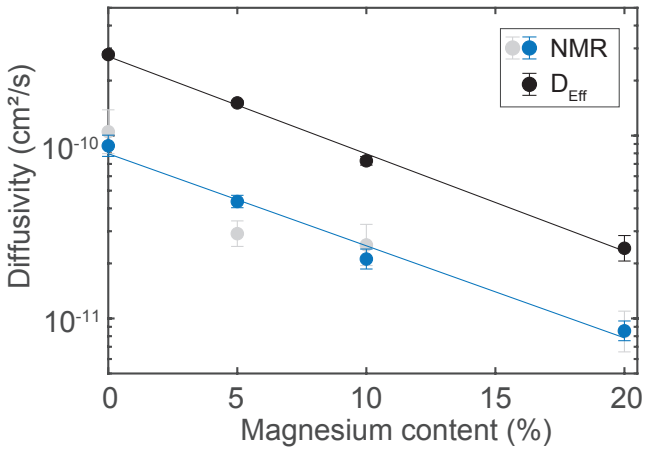


Figure 4.30: Calculated effective diffusivity plotted as a function of magnesium alloy content.

In the lithium-magnesium binary alloy samples, the increase in overpotential due to concentration changes is relatively easy to visualise and grasp. The lithium samples only have one component, so the process leading to an increase in potential is much harder to visualise. Others have discussed the process leading to lithium's overpotential increase elsewhere [227], but it isn't a solved problem. For lithium, there are no phase transformations and therefore the increase in potential is gradual. The effective diffusion limit is a progressive loss of contact between the lithium and the solid electrolyte; or the generation of voids (which impede transport), due to the grouping of vacancies. A final aspect to consider is that due to changes in volume associated with the removal of lithium, stress gradients will form, which will oppose transport (and therefore result in an overpotential). It's not obvious which of these processes is the most important. The exact dynamics are likely a balance. To accurately model and understand this, experimental values of stress relaxation and vacancy absorption are needed.

We observe higher magnesium content alloys have poorer stripping performance, which correlates well with the trend of reduced lithium diffusivity with increased magnesium content shown in figure 4.27. To investigate this further, I defined the time at which the first stripping stage ends as the point when the concentration of lithium at the alloy-electrolyte interface reaches the edge of the beta phase (31%)

and then calculated the effective diffusivity of each alloy anode within the beta phase region which corresponds to this lithium depletion time at the experimental stripping current density. This was achieved using a Crank-Nicolson finite element model, describing purely Fickian diffusion. These values are plotted in figure 4.30 in black. Extrapolated values from the NMR measurements presented earlier are plotted alongside the effective diffusivity values. Values obtained by extrapolating the individual Arrhenius expressions for each sample are plotted in grey, and values obtained by extrapolating from each data set's mean value using the linear trend of activation energy with magnesium content are plotted in blue.

The trend of effective diffusivity and the measured values shows the fundamental link between stripping performance and the lithium diffusivity of the material. Yet, there is a constant offset between measured material diffusivity and the effective diffusivity from the electrochemical experiments. The offset is most likely due to the role stress plays in modifying diffusion[228], but it could be a small systematic experimental error that I have not accounted for. I'd expect the applied compressive stress in the stripping direction to increase the driving force to flatten the concentration gradient of vacancies created during stripping. The mechanical and diffusivity data presented in this work should be sufficient to develop a fully coupled stress-diffusion model to calculate the impact of internal and externally applied stresses on diffusion behaviour. The electrochemical data can be used to validate the developed model.

The discrepancy between the two diffusivity values for the pure lithium case is often attributed to creep [229]. When lithium is stripped, there is no material left behind. Creep may therefore play a role, but the physical meaning of creep on the sub-micron length scale is hard to visualise, especially considering the presence of small-scale forces such as adhesion and friction which can prevent plastic flow as described by the Von-Mises criteria. In the alloy samples, creep is not expected as material is left even after lithium is stripped. This material remains under compression, so given this absence of a stress difference, we would not expect significant creep to occur. Second, the alloys are intrinsically more resistant to

creep than pure lithium. If creep were the dominant factor, we would expect the offset to decrease with magnesium content. It may therefore be that a simpler stress-coupled diffusion model, without a creep term, accurately describes transport of lithium within metallic anodes.

Notably, similar chronopotentiometry by other groups on the lithium-magnesium system [96, 102] do not see this characteristic diffusion-limited profile and see cell failure before a diffusion limit would be expected – suggesting that there is instead a loss of contact. It seems most likely that the lithium, bonded to the solid electrolyte by compressive stress during assembly, is stress relaxing over time and then debonding; the lithium doing so faster than the comparatively harder magnesium alloys due to its higher thermal activity. When a low but constant stack pressure is applied in this work, contact is maintained until a diffusion limit is reached.

Finite element modelling of diffusion.

To extract the diffusivity values presented in the previous section, finite element modelling was used as the analytical solution has a boundary condition problem [96]. Diffusion models are based upon Fick's second law of diffusion equation 4.13, which can be discretised for a given point in space and time in two ways either the implicit backward time, central space (BTCS) or the explicit forward time, central space (FTCS).

$$\frac{\partial C}{\partial t} = D\frac{\partial^2 C}{\partial x^2} \tag{4.13}$$

Backward time central space (BTCS):

$$\frac{C_j^{n+1} - C_j^n}{\Delta t} = D\frac{\frac{C_{j+1}^{n+1} - C_j^{n+1}}{\Delta x} - \frac{C_j^{n+1} - C_{j-1}^{n+1}}{\Delta x}}{\Delta x} \tag{4.14}$$

$$\frac{C_j^{n+1} - C_j^n}{\Delta t} = D\frac{C_{j+1}^{n+1} - 2C_j^{n+1} + C_{j-1}^{n+1}}{(\Delta x)^2} \tag{4.15}$$

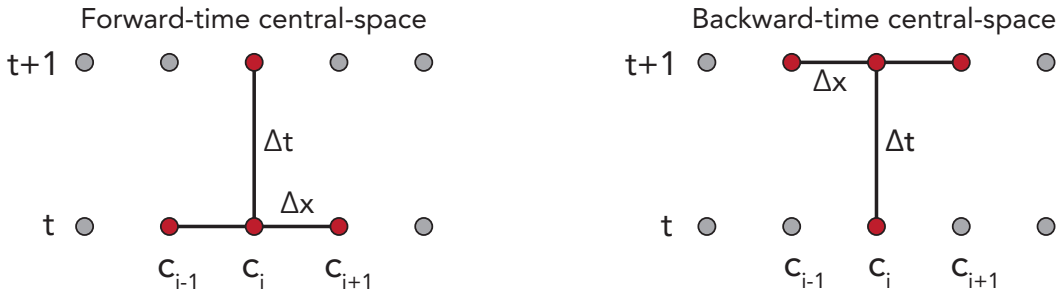


Figure 4.31: Schematic of two finite element methods.

Forward time central space (FTCS):

$$\frac{C_j^{n+1} - C_j^n}{\Delta t} = D\frac{C_{j+1}^n - 2C_j^n + C_{j-1}^n}{(\Delta x)^2} \tag{4.16}$$

The crank Nicolson method averages these two, giving an expression that is stable for a general time interval.

$$\frac{\partial C}{\partial t} = \frac{D}{2}\left\{\frac{\partial^2 C}{\partial x^2}_{BTCS} + \frac{\partial^2 C}{\partial x^2}_{FTCS}\right\} \tag{4.17}$$

$$\frac{C_j^{n+1} - C_j^n}{\Delta t} = \frac{D}{2}\left(\frac{C_{j+1}^n - 2C_j^n + C_{j-1}^n}{(\Delta x)^2} + \frac{C_{j+1}^{n+1} - 2C_j^{n+1} + C_{j-1}^{n+1}}{(\Delta x)^2}\right) \tag{4.18}$$

If we let $\alpha = \frac{D\Delta t}{(\Delta x)^2}$. Then rearrange to put all n+1 terms on the right hand side, and all n terms on the other.

$$-\frac{\alpha}{2}C_{j-1}^n + (1+\alpha)\,C_j^n - \frac{\alpha}{2}C_{j+1}^n = \frac{\alpha}{2}C_{j-1}^{n+1} + (1-\alpha)\,C_j^{n+1} + \frac{\alpha}{2}C_{j+1}^{n+1} \tag{4.19}$$

This set of simultaneous equations for C^1 to C^N can be written in matrix form. A compressed version of this is of the form:

$$\begin{bmatrix} 1+\alpha & -\frac{\alpha}{2} & 0 & 0 \\ -\frac{\alpha}{2} & 1+\alpha & -\frac{\alpha}{2} & 0 \\ 0 & -\frac{\alpha}{2} & 1+\alpha & -\frac{\alpha}{2} \\ 0 & 0 & -\frac{\alpha}{2} & 1+\alpha \end{bmatrix} \cdot \begin{bmatrix} C_1^n \\ \vdots \\ \vdots \\ C_N^n \end{bmatrix} = \begin{bmatrix} 1-\alpha & \frac{\alpha}{2} & 0 & 0 \\ \frac{\alpha}{2} & 1-\alpha & \frac{\alpha}{2} & 0 \\ 0 & \frac{\alpha}{2} & 1-\alpha & \frac{\alpha}{2} \\ 0 & 0 & \frac{\alpha}{2} & 1-\alpha \end{bmatrix} \cdot \begin{bmatrix} C_1^{n+1} \\ \vdots \\ \vdots \\ C_N^{n+1} \end{bmatrix} \tag{4.20}$$

The corners of this matrix differ due to boundary conditions. For insulative conditions:

$$C_{j-1}^{n} = C_{j}^{n} \tag{4.21}$$

$$\left(1+\frac{\alpha}{2}\right)C_{j}^{n} - \frac{\alpha}{2}C_{j+1}^{n} = \left(1-\frac{\alpha}{2}\right)C_{j}^{n+1} + \frac{\alpha}{2}C_{j+1}^{n+1} \tag{4.22}$$

A constant flux boundary was achieved computationally by modelling the right-hand boundary as insulative and then subtracting the correct amount based on the current density and time step from the boundary concentration values.

$$\begin{bmatrix} 1+\frac{\alpha}{2} & -\frac{\alpha}{2} & 0 & 0 \\ -\frac{\alpha}{2} & 1+\alpha & -\frac{\alpha}{2} & 0 \\ 0 & -\frac{\alpha}{2} & 1+\alpha & -\frac{\alpha}{2} \\ 0 & 0 & -\frac{\alpha}{2} & 1+\frac{\alpha}{2} \end{bmatrix} \cdot \begin{bmatrix} C_1^n \\ \vdots \\ \vdots \\ C_N^n \end{bmatrix} = \begin{bmatrix} 1-\frac{\alpha}{2} & \frac{\alpha}{2} & 0 & 0 \\ \frac{\alpha}{2} & 1-\alpha & \frac{\alpha}{2} & 0 \\ 0 & \frac{\alpha}{2} & 1-\alpha & \frac{\alpha}{2} \\ 0 & 0 & \frac{\alpha}{2} & 1-\frac{\alpha}{2} \end{bmatrix} \cdot \begin{bmatrix} C_1^{n+1} \\ \vdots \\ \vdots \\ C_N^{n+1} \end{bmatrix} \tag{4.23}$$

This expression can be rewritten as follows, and then C^{n+1} is solved by inversion and multiplication. Computationally this matrix was stored in the sparse datatype, as most of the values are zero.

$$M_L^n \cdot C^n = M_R^{n+1} \cdot C^{n+1} \tag{4.24}$$

$$C^{n+1} = \left(M_R^{n+1}\right)^{-1} \cdot M_L^n \cdot C^n \tag{4.25}$$

For this work, a 1D, concentration-independent diffusion model is adequate to capture the observed behaviour. However, this methodology is applicable to multi-dimensional systems and can integrate concentration-dependent diffusion or spatially varied diffusivity. The concentration was started at 73.28, 69.71 and 62.47 mmolcm^{-3} for the 5, 10 and 20% alloys respectively; and the diffusion limit point was defined as the solubility limit of the beta phase lithium (69%) or 25.20 mmolcm^{-3}. These concentrations were calculated using the lattice parameter trend from [230]. For the lithium case, the limit was defined as when the surface concentration reached zero, from a starting concentration of 76.83 mmolcm^{-3}. The time for the lithium

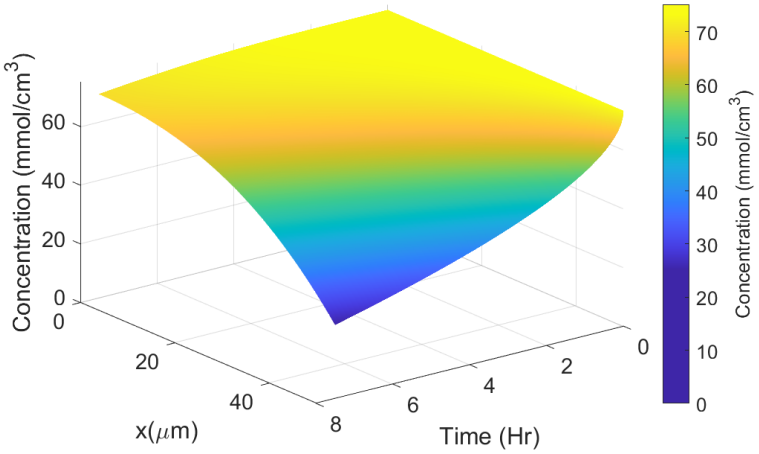


Figure 4.32: Modelled concentration profile over time in a lithium 5% magnesium alloy anode, with an effective diffusivity of $1.52 \times 10^{-10} cm^2 s^{-1}$. x-axis runs perpendicular to the electrode-electrolyte interface.

test agrees with the Cottrell equation. Diffusivity values were iterated such that the predicted time-to-limit matched experimental data, giving effective diffusivity.

Figure 4.32 shows the modeled evolving concentration gradient in a 50-micron thick lithium 5% magnesium alloy anode, with an effective diffusivity of $1.52 \times 10^{-10} cm^2 s^{-1}$, under the constant stripping current described previously. The concentration at the surface decreases until it reaches a value of 25.2 mmolcm^{-3}. As noted earlier, this simple diffusion model assumes the boundaries of the anode phase remain fixed, does not include the modification of the behaviour due to stress [231], and assumes the diffusivity remains constant despite the removed lithium. It's not surprising it overestimates performance. Modelers can use the mechanical values measured for these lithium magnesium alloys, the measured diffusivity values, and the chronopotentiometry data to make a more accurate model than has been described here.

4.8 Cross-sectional imaging of stripped lithium magnesium alloy anodes.

Impedance spectroscopy was taken before and after stripping for lithium metal (Figure 4.33A) and the alloys, for example, 20% (Figure 4.33B), show that interfacial

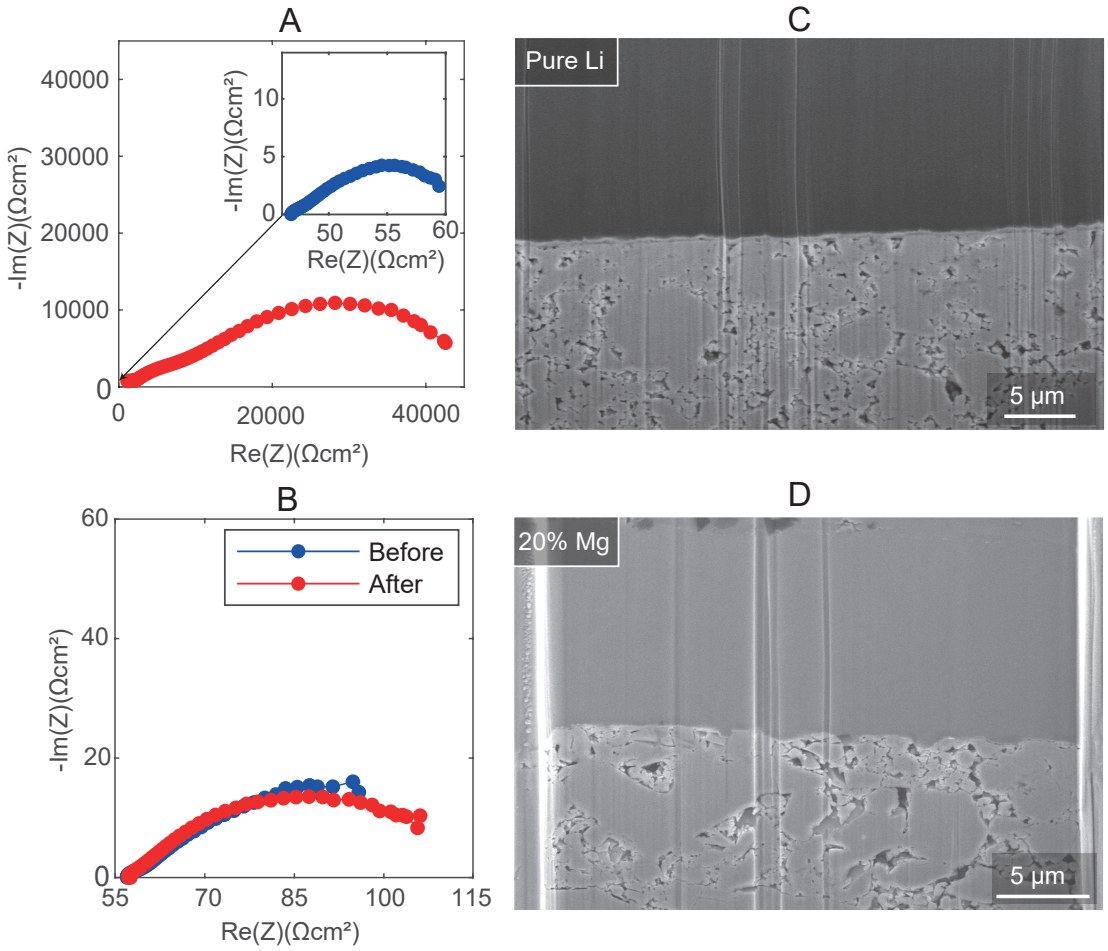


Figure 4.33: (a,b) Electrochemical impedance spectroscopy of lithium and 20%magnesium self-symmetric cells before and after chronopotentiometric stripping. (c,d) cross-sectional plasma focused ion beam images of the anode-electrolyte interface after stripping in lithium and 20% magnesium samples.

contact was maintained in the alloys, whereas the lithium cells have a significant increase in impedance, indicative of a loss of contact. This matches the potential versus time data which shows the increase in potential in the alloys is due to a diffusion limit and not a loss of contact. It is unclear whether there is a fundamental improvement in contact retention with magnesium alloying, or whether simply the decrease in diffusivity associated with the BCC to HCP phase transition introduces an earlier failure mode.

After stripping, the cells were disassembled and placed on stubs for microscopy characterisation. The samples were stored under Ar in a glovebox (H20 and O2 <0.1 ppm) until they could be transferred to the microscope using an airless transfer

vessel (Gatan iLoad) to the plasma FIB-SEM (Helios G4 PFIB CXe DualBeam, Thermo Scientific) for characterisation. All samples were sectioned using the same milling and polishing procedure, final ion beam polishing parameters of 30 kV and 15 nA were used as a trade-off between maximising milling rate and minimising beam damage. The alloys were milled at room temperature as they had been confirmed to not suffer excessive artefact creation at these temperatures, however, lithium samples were milled at cryogenic temperatures (-150 °C) using a cryogenic stage (Gatan) as lithium's low melting point leads to excessive image artefacts if milled at room temperature.

The figure shows two cross-sectional images of the electrolyte-anode interface after the described chronopotentiometry test, in a pure lithium (Figure 4.33C) and 20% alloy sample (Figure 4.33D). These were achieved by plasma-focused ion beam milling (PFIB) by Yvonne Chart and Emily Milan after cell disassembly. It can be seen in both cases that the metal anode is well conformed to the solid electrolyte despite the increased hardness of 20% magnesium sample – higher hardness alloys such as intermetallic phases may not do this, leading to the lower contact area and current focusing. The applied stack pressure of 5 MPa is insufficient to drive lithium's plastic flow/creep deep into these pores, as opposed to what has been observed in higher-pressure systems [186]. In both cases, the stripped anode is a solid block, with no internal porosity. This is different from other alloy systems where the formation of a porous scaffold has been identified [232]. The loss of contact, measured in EIS, is not obvious in the cross-sectional image, showing that caution should be exercised when drawing conclusions from PFIB data.

Practically the addition of magnesium makes PFIB easier. The increased melting point and hardness mean that cryogenic temperatures are not needed for any of the alloys. They may therefore be useful tools to study solid-state cell samples prepared by PFIB, including cross-sections and TEM samples which are not possible using pure lithium metal. One example is the imaging of the solid electrolyte interphase, which we expect to be similar due to the near-identical open-circuit voltage.

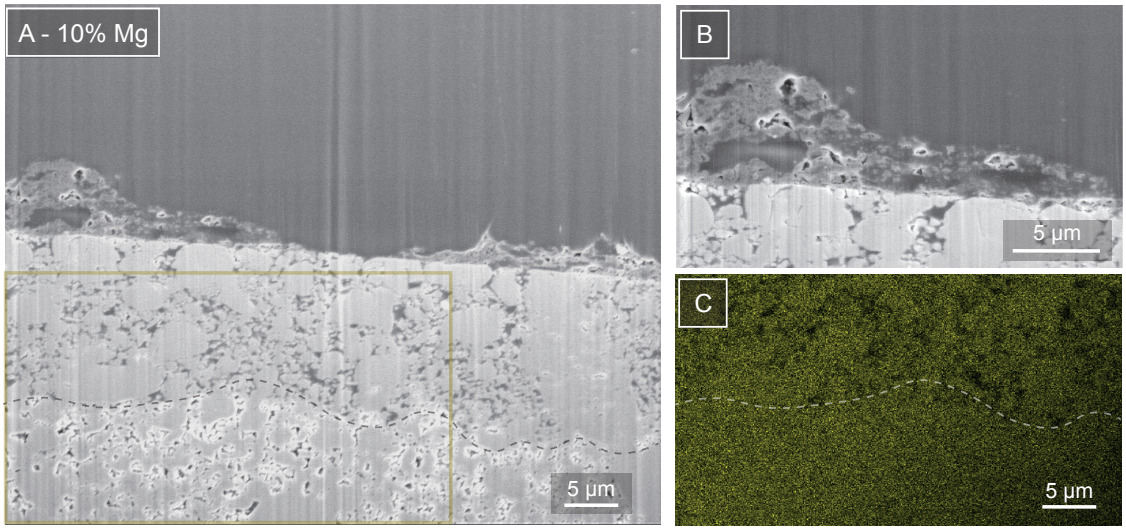


Figure 4.34: (a) Cross-sectional plasma focused ion beam image of 10% magnesium - electrolyte interface after stripping and plating at 0.31 $mAcm^{-2}$ to 5V limit. (b) zoomed image of A, (c) Sulphur EDX map of outlined region in A.

4.8.1 Cross-sectional imaging of stripped and plated lithium magnesium alloy anodes.

After the chronopotentiometry experiment described, where a constant current density of 0.31 $mAcm^{-2}$ was maintained until a voltage of 5 V, for a small number of cells we reversed the current density and replated the lithium until a -5 V limit was reached. The very large overpotential means that the system is far from equilibrium. Figure 4.34A shows a cross-sectional PFIB image of the interface between a 10%Mg electrode and the solid electrolyte after this experiment. 1.3 $mAhcm^{-2}$ of charge was passed.

Lithium plating within the porosity of the solid electrolyte can be observed, extending approximately 15 micron into the solid electrolyte. This can be seen by both the lack of charging in the SEM image A, and in the attenuation of the Sulphur signal at the filled pores in the EDX map shown in C. The plating of lithium within the pores is not good as it can ultimately lead to cell shorting. From an electrochemical perspective, it makes interpretation of the process challenging as the electrolyte-lithium contact area cannot be defined. This backs up our decision to only draw conclusions from unidirectional chronopotentiometry data, as the meaningful analysis of cyclic electrochemical data with such uncontrolled plating

is not possible. The processing of solid electrolytes is an area needing progress to control and constrain the plating morphology of lithium before meaningful, reproducible insights into the cyclic behaviour of lithium metal alloys can be made. Second, there is a region, highlighted in B on the electrode side of the interface which appears to be a partially filled void. These weren't observed in the stripped interfaces (although we cannot confirm their absence) so it could be a result of non-uniform lithium plating.

4.9 Conclusions.

The work reported in this chapter demonstrates that alloying lithium with magnesium significantly changes its microstructural, mechanical, kinetic, and chemical properties, which in turn impacts the electrochemical performance. The framework of experimentation from synthesis to cells is applicable to other lithium-rich alloy anodes. Electrochemically this work quantifies the clear correlation between diffusivity, and the cell performance on stripping, with an enhancement over a purely Fickian relationship attributed to the role of internal and externally applied stress on diffusion. To achieve target current densities and capacities, without excess stack pressure or temperature, anode materials with room temperature lithium diffusion coefficients higher than 5×10^{-9} cm^2s^{-1} should be pursued, necessitating the incorporation of a second phase. NMR is a valuable method to quickly screen candidate materials to find those with diffusivity values that can achieve the desired performance. In this case, ^{6}Li enrichment was necessary, but for most intermetallic phases ^{7}Li may be used. Once high diffusivity phases are found, the challenge of optimising the microstructure of the alloy to maximise the impact of these phases can be pursued. Having a high diffusivity alone is insufficient as contact must be maintained at the electrolyte interface, and reaction layers at the interface which significantly compromise electrochemical performance must be avoided, therefore mechanics and interfacial chemistry should be examined.

The mechanical properties of alloy anodes control four major battery properties. First, mechanics determine contact. Soft, adhesive, ductile metals such as those

investigated here, can be conformed to a non-uniform solid electrolyte surface by the application of mild pressures. Hard, non-adhesive materials will be more prone to losing contact. Second is the impact of mechanics on processing. Soft, ductile metals are best processed by rolling, whereas brittle materials are best processed by first ball-milling into a powder. Third, mechanics fundamentally underpin the durability of solid-state batteries with failure occurring due to the fracture of components under cyclic stress and nanoscale lithium intrusions [74, 231]; understanding the fundamental properties of candidate materials allows failure modes to be understood and resolved. Finally, several works [75] have demonstrated that stresses within batteries modify the transport of lithium atoms and ions. The fundamental mechanical values presented in this work enable stress-coupled models of lithium transport within lithium magnesium alloy anodes.

Current concentrations in lithium metal electrodes cause several problems in solid-state cells including dendrite growth and contact loss. The addition of just 5% magnesium to lithium makes the electrode's stripping dynamics essentially independent of stress. This is potentially very useful, leading to greater performance stability and safety. The low magnesium regime is worth exploring to find an optimal balance between performance, which is made worse due to decreased diffusivity, and minimising stress sensitivity.

Despite the nearly identical operating potential, impedance spectroscopy shows an increased interfacial resistance for the alloys compared to pure lithium, which grows over time, attributable primarily to changes in the alloy passivation layer composition. The combined tools of XPS and EIS allow changes in interfacial chemistry to be identified and understood. In other alloy systems much larger interfacial impedance may be observed, which could have a significant electrochemical impact.

Finally, a consistent theme we observed throughout this work, is that just 5% magnesium content makes many characterisation methods easier – increased atomic number leads to improved EBSD resolution, XRD signal and stability in PFIB, as well as making the alloys far easier to handle in cell assembly. If researchers carefully consider the changes to the properties identified in this work;

using a lithium magnesium alloy may allow characterisation currently impossible with pure lithium. This will enable the behaviour of the pure metal to be better understood. For example, as the open circuit potential is so close to lithium metal, it seems inevitable that a very similar solid electrolyte interphase (SEI) will form on the lithium magnesium alloys, as on pure lithium. The XPS results support this hypothesis. The alloys may therefore be useful to allow SEM and TEM characterisation of the SEI, without needing the cryogenic conditions that are necessary for FIB of pure lithium.

5

Indium lithium alloys as a counter/reference electrode.

Contents

5.1 Introduction 112
5.2 Synthesising phase pure InLi. 113
5.3 Mechanical characterisation 115
5.3.1 Berkovich Indentation 115
5.3.2 Cube corner indentation 117
5.4 Diffusion of InLi intermetallic. 119
5.5 In metal on charge 120
5.5.1 First cycle coulombic efficiency of pure indium metal . . 124
5.6 Indium-lithium on discharge 125
5.6.1 Cast indium lithium two-phase alloy electrode 126
5.6.2 In + InLi two layer alloy electrode 131
5.6.3 Characterising delithiated microstructure 134
5.7 Electrodes formed by combining indium and lithium foils 138
5.8 Cycling two-layer InLi electrode. 142
5.8.1 Electrochemical Impedance Spectroscopy before cycling 143
5.8.2 Cycling two-layer InLi electrode 144
5.9 Conclusions 147

5.1 Introduction

When using a lithium metal electrode, current-generation solid-state batteries have very low critical current densities (current density above which cell shorts occur). This is particularly true of solid electrolytes produced by scale-able methodologies such as tape casting [192]. Current evidence suggests this is due to high electrolyte porosity, which enables solid electrolyte fracture under the stresses generated by lithium metal plating [156]. Solving this issue by advancing solid-state manufacturing of electrolytes, and progressing novel strategies such as interlayers [193], is important.

In the meantime, the low current densities achievable with a lithium metal electrode are holding back the rate of progress in electrode development, specifically solid-state composite cathodes and initially lithium-free anodes which form lithium metal on the first charge. An alternative counter electrode is needed that can cycle relevant capacities at higher current densities, without shorting. Ideally, this material would be a good reference electrode; with a constant potential over a wide capacity range at a high charge/discharge rate.

The lithium-indium alloy system has gained popularity in this role [118, 233, 234], but there is little understanding of the mechanism underpinning the performance or the limitations of the electrode. In many cases, this has led to misleading conclusions. The region of interest is the wide two-phase region between indium and the InLi intermetallic which can be seen on the phase diagram in figure 5.1. In this study, we investigate the fundamental materials properties of the InLi intermetallic phase, and then by producing electrodes with different microstructures, gain an understanding of the processes underpinning observed electrochemical performance.

The material properties of indium metal are relatively well understood. Chemically it is stable, especially compared to other battery materials (E = -0.34 V vs SHE). Mechanically indium is very similar to lithium [235], a soft metal (E = 12.7 GPa, G = 3.8 GPa, ν=0.45 σ_y=0.93 MPa) which due to its low melting point (Tm = 156.6 $^{\circ}C$) is prone to creep and stress relaxation [236]. The diffusion kinetics of indium are relatively sluggish, with a bulk self-diffusion coefficient ($D_{self}^{297.6K} = 5.7 \times 10^{-14} cm^2 s^{-1}$) [235], which is three orders of magnitude lower than

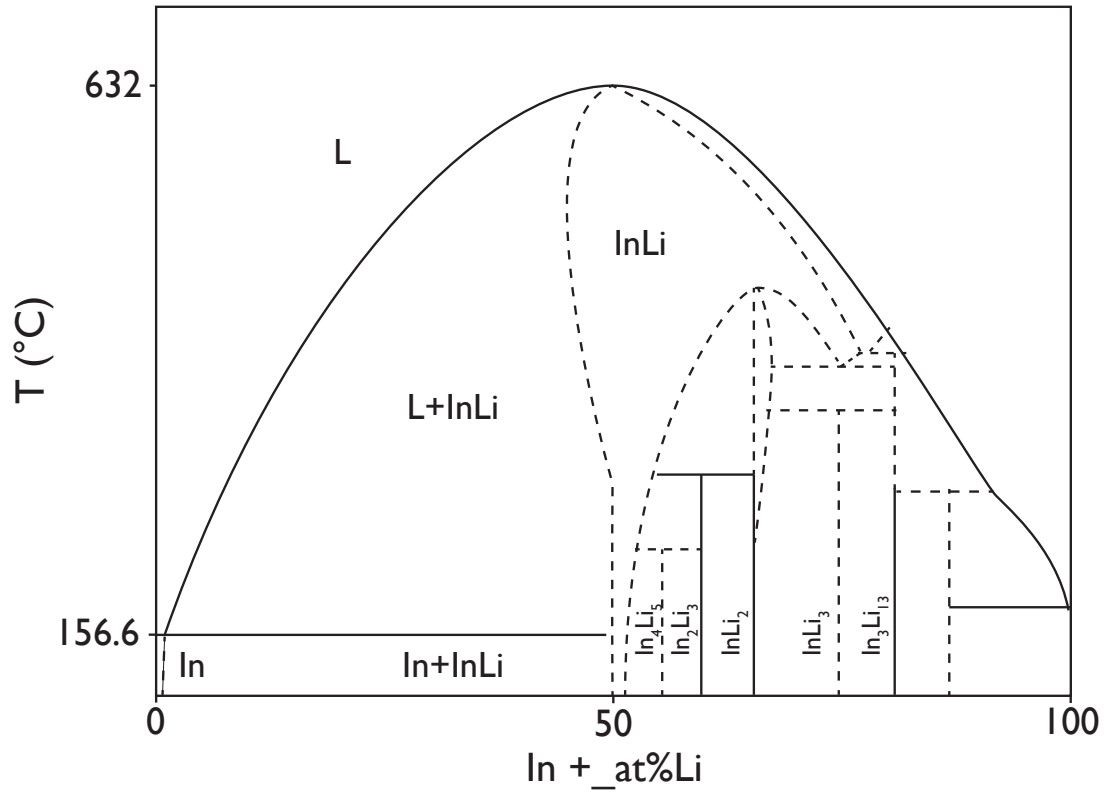


Figure 5.1: Phase Diagram of indium lithium binary system. Redrawn from [118]

lithium's self diffusivity. Indium's use in practical batteries is limited by its very high density of 7.31 gcm^{-3}. The material properties of the second phase in this system, the InLi intermetallic are poorly understood.

5.2 Synthesising phase pure InLi.

Indium (Sigma Aldrich, lump) and lithium (99.9% Alfa Aesar) were weighed (MTI PCB-200) to make a 50:50 atomic ratio. These were put into a steel foil lined stainless steel crucible. The melting point of the InLi intermetallic is 632°C figure 5.1. The mixture was heated to 700°C. Once molten the crucible was removed from the furnace, stirred with a spatula, and then returned to the furnace for 2 hours before furnace cooling.

After removing the cooled crucible from the furnace, some of the solidified crystals were shattered. Presumably, this occurred due to a substantial contraction during cooling. The material was entirely detached from the steel foil liner, was

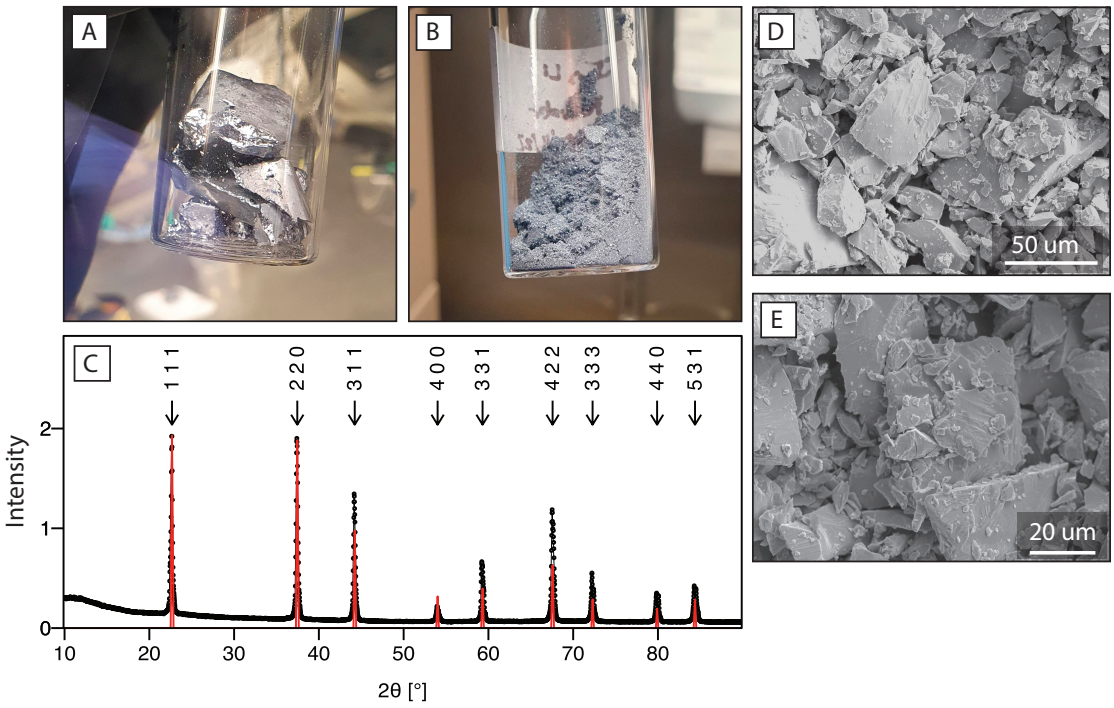


Figure 5.2: InLi intermetallic synthesis. (a) Photograph of InLi intermetallic after casting. (b) InLi after hand milling in pestle and mortar. (c) XRD of hand milled powder with InLi pattern and peaks labelled. (d) SEM image of hand-milled powder particles. (e) Second SEM image of hand-milled powder particles

opaque, and was a purple-grey in colour. A photograph of the 'as-cast' InLi can be seen in figure 5.2A.

This material was milled by hand using a pestle and mortar. A photograph of the milled powder is shown in figure 5.2B. The XRD pattern of this powder shown in figure 5.2C, taken using a Rigaku Miniflex, within a nitrogen glovebox, reflects the predicted pattern of the material, with no un-indexed peaks. This suggests the synthesised material is phase-pure. InLi has a cubic B32 crystal structure, a space group of $Fd\bar{3}m$, composed of two diamond sublattices with a unit cell size of 6.78 Å. To characterise the approximate particle size distribution, SEM images of the powder were taken, with the sample prepared using double-sided copper tape. These are shown in figure 5.2D and E. The largest particles are 50 micron in diameter, and the smallest are below 5 micron.

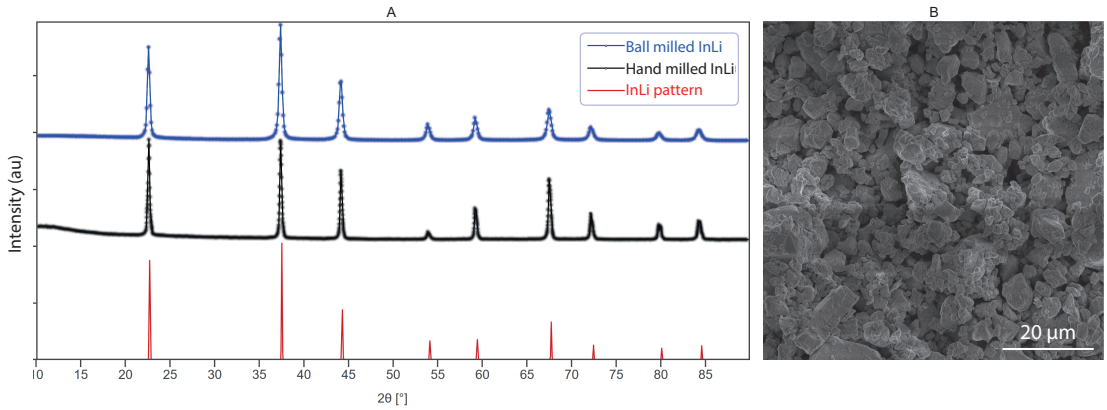


Figure 5.3: Ball milled InLi powder. (a) XRD spectra of InLi powder before and after ball milling. (b) Secondary electron SEM image of ball-milled powder.

Ball milling of InLi

The hand-milled powder was ball milled. A Fritsch Pulverisette 7 ball mill, within an argon glovebox, was used with a zirconia jar and 60 zirconia balls, with parameters of 600 revolutions per minute (rpm), alternating 5 minutes on, 5 minutes rest for 60 cycles, with alternating cycle directions. XRD spectra of the ball-milled powder showed the same peaks as the hand-milled powder indicating no phase change. The peaks are slightly broader for the ball-milled sample. SEM images in Figure 5.3B showed a reduced particle size compared to the hand-milled powder, with particle size ranging from 20 micron down to below 1 micron.

5.3 Mechanical characterisation

5.3.1 Berkovich Indentation

An InLi intermetallic chunk was mounted on a custom aluminium stub and polished using silicon carbide sanding paper from 800-4000 grit. In an ideal world, a smoother sample surface would be prepared, but the final 4000 grit sandpaper provided a mirror finish to the sample suitable for indentation. Two indentation transducers were used to characterise the intermetallic mechanically, the first a 'low-load' indenter up to 25 mN with continual stiffness measurement (CSM); the second a 'high-load' indenter up to 500 mN without continual stiffness measurement.

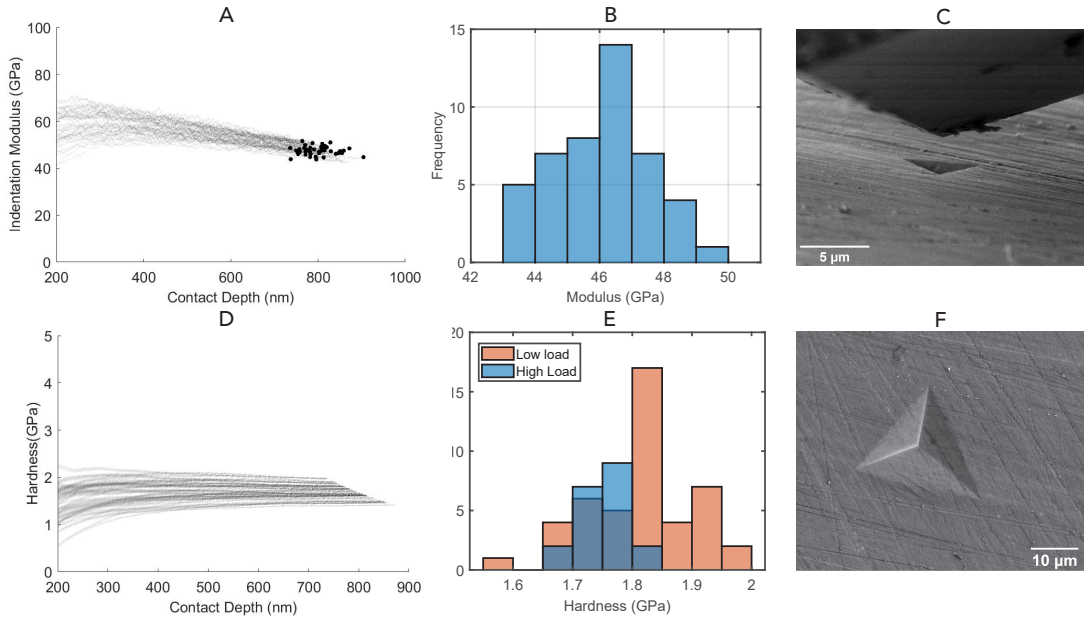


Figure 5.4: Mechanical characterisation of InLi intermetallic. (a) Indentation modulus versus depth using CSM method (lines) with quasistatic unload fits plotted as dots. (b) Histogram of CSM indentation modulus values averaged. (c) SEM image of indent after CSM indentation. (d) Hardness versus depth for low-load indentation. (e) Hardness distributions for low load measured by CSM and high load impression size. (f) Indent impression viewed normally, used to calculate hardness.

The indentation modulus measured by the low-load CSM technique on 50 indents is plotted in figure 5.4A. From this, the elastic modulus can be calculated. The mean value for over 600 nm is 47.5±1.6 GPa. Using the simple load-displacement unload curve the stiffness can be measured and modulus calculated, giving a value of 46.1 ± 1.4 GPa. The same was done for the high-load load-displacement curve giving a Young's modulus value of 46.6 ± 3.4 GPa.

The hardness measured by the low-load CSM technique on 50 indents is plotted in figure 5.4D. The mean value sampled over 600 nm is 1.68±0.16 GPa. Due to surface roughness and other errors, there is an error in the displacement measured by the indenter which gives an average maximum depth of 742.7 nm with a standard deviation of 87.4 nm and a range of 388.3 nm. This is not reflective of reality, as observed in the near-identical impression size. After indenting, the impression area was measured to be 14.06 square micrometres, with a standard deviation of 0.66 square micrometres. The maximum load was 25.463 mN, with a standard

deviation of 0.023 mN. Giving a hardness of 1.82±0.08 GPa. The difference in size between the impressions is lower than the error in area measurement. They are effectively identical. The measured hardness is essentially independent of depth. The impression size methodology was repeated using the same tip on the high-load transducer, 20 indents were performed, and an example impression can be seen in figure 5.4F. A hardness value of 1.755 ± 0.008 GPa was obtained. This last value is the most accurate hardness value; and is in agreement with the others. Notably, even at large indentation loads of 500 mN, no indentation fracture was observed; suggesting a fracture toughness of at least 5 MPa$\sqrt{m}$. Indium lithium is a cubic material, and therefore there may be slight elastic or plastic anisotropy that I have not captured in this test. I measured hardness of 1.76 GPa and an elastic modulus (E) of 47 GPa. These are substantially higher than those of both pure indium and lithium metal.

5.3.2 Cube corner indentation

The side of a piece of solidified InLi was found to be smooth enough for EBSD. This was mounted onto an SEM stub and indented using a cube corner indentation tip at 500 mN of load, the maximum of the indenter figure 5.5A. The loading curves are smooth, with no clear pop-in. After indentation, one of the indents was mapped using EBSD to enable the orientation of the observed slip bands to be calculated. From the EBSD map, we know the surface normal and sample x and y axes in crystal coordinates. We can therefore calculate the vectors that trace the slip bands on the sample surface, from their angle. On the SEM image figure 5.5B, the $\{\bar{1}01\}$ planes have been marked, as these are typically the active slip planes in cubic intermetallics. These align well with the observed slip bands. Crystallographic misorientations in the sample Z vector are plotted in the figure 5.5D and E, showing misorientation of around 2 degrees immediately around the indent in the areas which visibly have piled up in the tilted image of the indent in figure 5.5C. The scratch on the bottom left of the indent is due to insufficiently retracting the indenter tip before moving it after indentation.

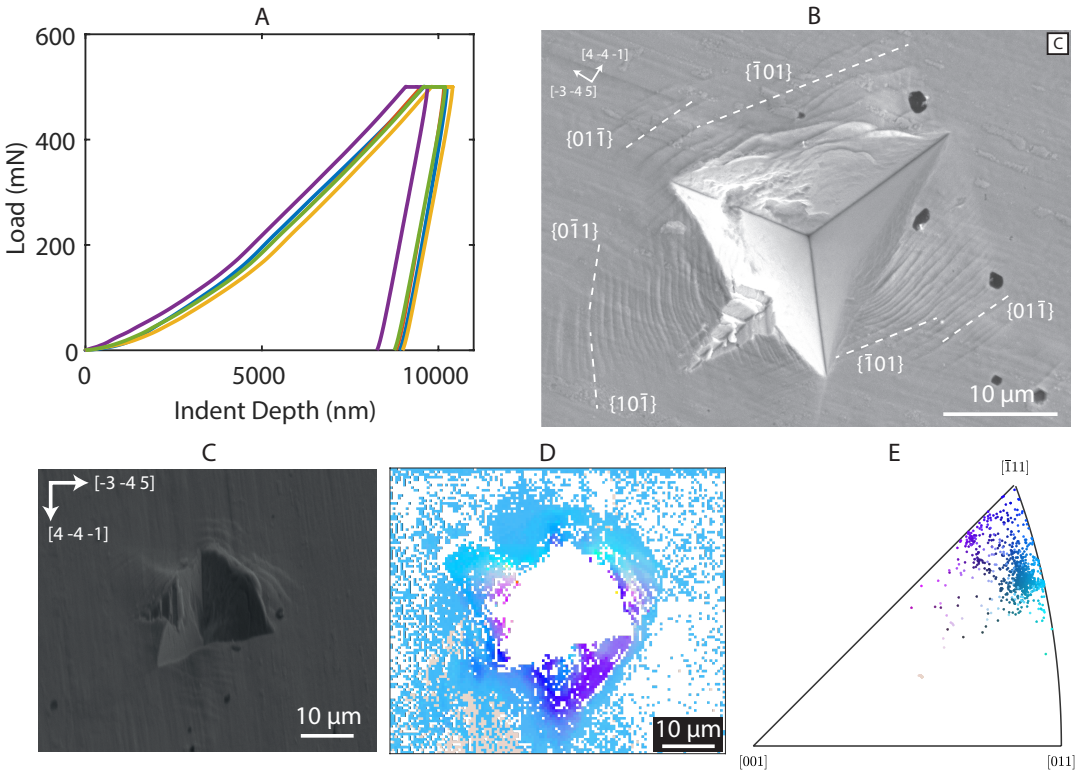


Figure 5.5: Cube corner indentation of InLi. (a) Load-displacement data for five 500 mN indents into InLi, no pop-in from fracture. (b) SEM micrograph of indent showing no fracture and clear slip bands. (c) SEM of indent in EBSD position. (d) IPF Z EBSD map of crystallographic orientation around indent. (e) IPF Z pole figure for the map in D showing grain orientation.

The interesting insight here is that under high load at the nanoscale, significant plasticity is observed, with no clear fracture. The plasticity seems limited to a single set of slip planes - leading to very clear slip bands. This is distinct from the macroscopic behaviour, where the material is brittle. Macroscopic fracture may occur at grain boundaries; with the limited number of slip systems leading to stress concentrations at the boundaries where deformation can't be accommodated. Second, it may be at the nanomechanical scale, the flaws present are insufficient for fracture to occur. In the context of battery materials, these both suggest that at the nanoscale, this material is resistant to fracture.

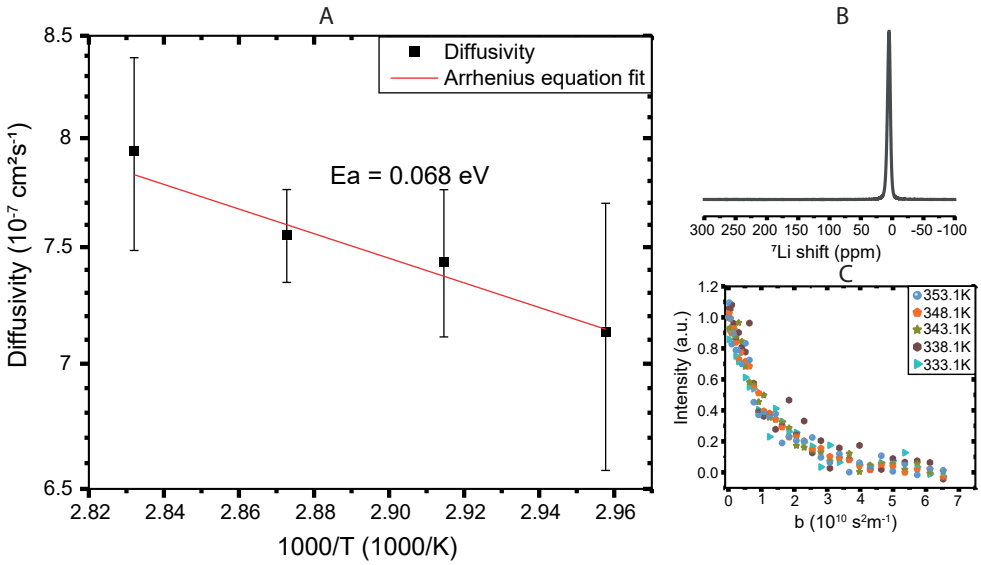


Figure 5.6: ^{7}Li PFG-NMR of InLi intermetallic. (a) Fitted Arrhenius line to diffusivity values. (b) Knight shift of InLi intermetallic. (c) Relaxation curves.

5.4 Diffusion of InLi intermetallic.

As identified in the previous chapter on lithium magnesium alloys, the most impactful material property influencing its electrochemical lithium stripping performance is the rate of lithium diffusion. To this end, the self-diffusion coefficient of InLi was investigated using PFG-NMR. The ground powder was used for this, NMR experiments were performed by Dr Hua Guo.

Diffusivity was measured as a function of temperature, with reliable data observed above 334K (T2 < 10 ms). These are plotted in figure 5.6B. The data between 338 K and 354 K fit with the Arrhenius equation giving a very low activation energy of 0.068±0.037 eV (figure 5.6C). The trend line extrapolates to give a room temperature lithium diffusivity of 5.5±1×10^{-}7 cm^2/s.

Our data shows diffusivity values about a factor of two lower than work done by Tarczon et al in 1988, which reports D_0 values from 7.7 ×10^{-6} to 3.5×10^{-5} cm^2/s across a range of Li:In compositions (47% to 53% In) due to changes in vacancy concentration, with very similar activation energies of 0.086 to 0.061 eV [237]. For diffusivity measurements taken 35 years apart, a factor of two difference is very strong agreement. More recently, computational work has sought

to understand the diffusion mechanism in this intermetallic alongside other indium-lithium intermetallics and the comparable lithium tin system [238]. The work compares two theoretical mechanisms of atom hopping, interstitial diffusion with an activation energy of 0.25 eV and vacancy diffusion with an activation energy of 0.015 eV. Our experimentally observed activation energy of 0.068 eV comprises both the vacancy hopping energy and the vacancy creation energy. Assuming the computational work is accurate, subtracting the hopping energy from our total value gives a vacancy creation activation energy of 0.053 eV. The material shows a small positive Knight shift of 5 ppm figure 5.6B, reflecting it is metallic in character. The second takeaway from this plot is that the peak is narrow, showing the fast diffusivity of lithium in this material.

Lithium diffusion in this InLi intermetallic is at least four orders of magnitude faster than self-diffusion in lithium at room temperature (1×10^{-10} cm^2s^{-1}). The diffusivity of an intermetallic is not determined by the diffusivity of its constituent pure metals but is instead highly dependent on the specific crystal structure and bond character.

5.5 In metal on charge

When using lithium metal as a counter electrode, shorting is commonly observed, especially at high current densities. This is caused by lithium filaments propagating across the solid electrolyte. Even before this, significant instability is observed due to freshly plated lithium reducing newly-contacted solid electrolyte. The use of lithium as a counter electrode is therefore holding back the development of both cathodes and anodes. The operating potential of an indium/InLi electrode is 622 mV above Li/Li^+ [118]. This high alloying potential is a substantial thermodynamic barrier to lithium metal plating and therefore the electrode should be highly resistant to cell shorting. To investigate this, solid-state cells were assembled with a lithium metal electrode (100 μm foil) and an indium metal foil counter electrode (127 μm Sigma Aldrich). Constant areal current densities between 0.3 and 5 $mAcm^{-2}$ were applied driving lithium ions to the indium metal electrode, and the cell potential

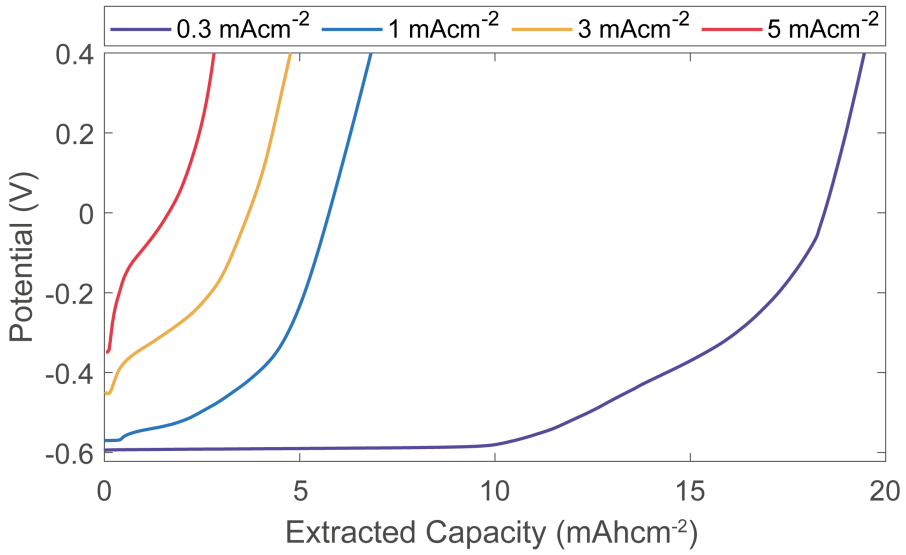


Figure 5.7: Chronopotentiometric stripping of lithium with indium metal counter electrode showing potential as a function of extracted areal capacity at 0.3, 1, 3 and 5 $mAcm^{-2}$.

was monitored over time. Figure 5.7 shows the cells ran stably with no shorting; even at high cell potentials and large extracted capacities.

Using indium metal as a counter electrode allows the measurement of lithium metal performance at a relevant range of current densities for battery development (0.1 - 5 $mAcm^{-2}$) in solid-state cells. The performance limits on stripping the lithium metal electrode are clear, with a significant increase in cell potential observed over the experiment in all cases, with the increase occurring at lower capacities for higher current densities. Lithium metal does not meet the performance requirements of commercial solid-state batteries which are estimated to be capable of a discharge rate of 1C, with low overpotentials, for an areal capacity of 5 $mAhcm^{-2}$. This data can be used to understand transport within the lithium metal anode. A study consisting of lithium against indium metal, at a range of current densities, and at a range of pressures (1-10 MPa), would be very valuable to the community as a whole.

The origin of the performance is not simply the high operating potential of the two phase region, else many alloys would work, but is due to the way in which the microstructure evolves such that the system remains near equilibrium, thereby giving very low overpotentials. The lithiation mechanism was investigated using

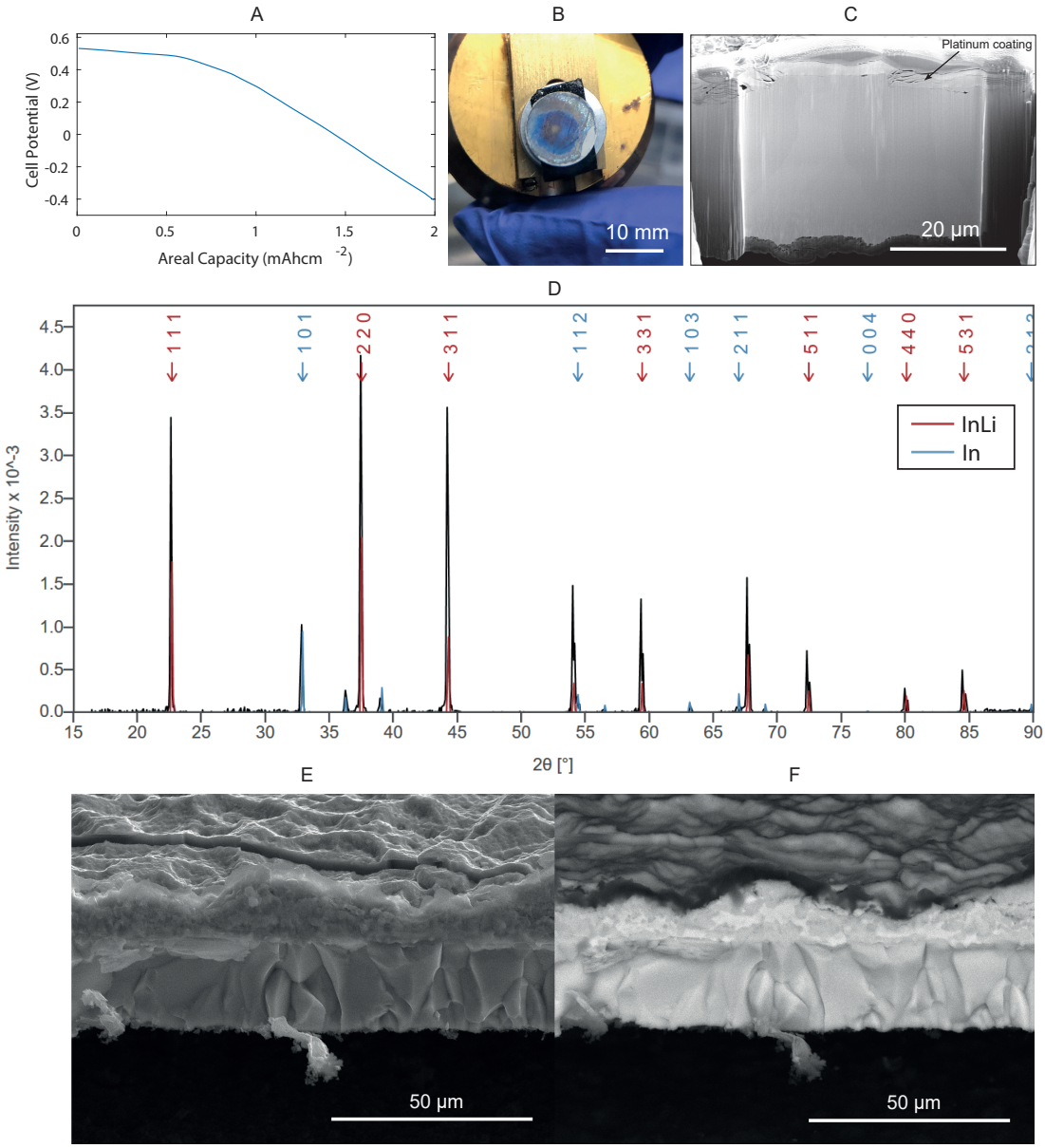


Figure 5.8: Characterisation of partially lithiated indium metal foil. (a) Chronopotentiometric lithiation of 2mAhcm^{-2} at 1 mAcm^{-2} of 20 μm indium metal foil from lithium metal counter electrode. (b) Photograph of partially lithiated indium foil from current-collector facing side. (c) Cross-sectional PFIB image of centre of partially lithiated indium foil. (d) XRD pattern of partially lithiated indium foil from current-collector facing side, In blue, InLi red. (e,f) SEM image of microtome cross-section of partially lithiated foil, secondary electron (e) and backscattered sem image (f) showing two-phase microstructure.

plasma-focused ion beam (PFIB) cross-sectional imaging and XRD. Better PFIB results are obtained for thin samples as these reduce the time taken to prepare the cross-section and reduce image artefacts such as shadowing. A thin indium foil (20-micron) was lithiated with 2 $mAhcm^{-2}$ of lithium at a current density of 1 $mAcm^{-2}$ in a solid-state cell. 20 microns of indium requires approximately 3.4 $mAhcm^{-2}$ to convert all of it to InLi intermetallic. The chronopotentiometry data for the cell is shown in figure 5.8A.

The cell stack was removed from the containing Macor cylinder using a 10 mm diameter piston in a press. The nickel foil current collector was removed easily. Figure 5.8B shows a photograph of the lithiated indium metal electrode. Clear colour variations can be observed, with the centre blue and the edge grey, suggesting in-homogeneous lithiation. It is well established that compressive pressure enhances the stripping performance within lithium metal. Considering a forging analogy, the internal pressure is likely concentrated at the centre of the lithium metal counter-electrode, leading to in-homogeneity. This is not widely considered in studies of lithium performance and should be investigated further.

SEM was performed to investigate the microstructural distribution of the two phases. Figure 5.8C shows a cross-sectional secondary electron image of the electrode, taken near the centre. The cross-section was prepared using plasma-FIB by Yvonne Chart. No phase contrast could be observed in the SEM, images were taken with both back-scattered and secondary electron imaging modes at a range of beam voltages. The thickness of this region is 27.5 μm. There is a volume increase of 51% on lithiation (V_m^{In}=15.76, V_m^{InLi}=23.82 cm^3). I believe the cross-section is InLi throughout, making the original foil slightly thinner than 20 microns. A second cross-sectional hole was prepared at the edge of the sample, the thickness at this region was 22.7 μm, confirming the inhomogeneity of the sample. There was insufficient time to polish the cross-section for meaningful imaging.

After cross-sectional PFIB, the partially lithiated In foil came off from the solid electrolyte. This in itself suggests the electrode-facing surface is primarily InLi intermetallic instead of the more adhesive indium metal. The electrode was

scanned in the XRD mounted with the electrolyte-facing side pointing down. The data shown in figure 5.8D shows the sample is primarily InLi, with some indium metal phase. No other phases are present.

A microtome blade was used to cut the lithiated electrode. Compared to cross-sectional PFIB, this does not prepare so flat a surface on brittle materials such as InLi but leads to a much larger cross-sectional area, and avoids imaging artifacts from shadowing, and artefacts from milling. Figure 5.8E and F show secondary electron (left) and backscattered electron (right) images of part of the cross-section, with the electrolyte-facing side at the bottom. A clear two-layer morphology can be observed. The fracture morphology and darker Z-contrast of the lower layer suggest it is InLi, whereas the top layer is primarily indium metal. The BSE image suggests there may be some InLi islands within the In layer. The two-layer morphology suggests there is an InLi-In phase boundary which has propagated through the electrode thickness as more lithium is added. Given the very fast diffusion kinetics of the InLi phase, the electrode should be able to be charged at very high current densities before significant transport overpotentials are observed, giving the excellent performance observed.

5.5.1 First cycle coulombic efficiency of pure indium metal

Indium can be charged at a high rate, leading to the growth of an InLi layer facing the solid electrolyte. Given the electrode expands during lithiation, it's reasonable to expect good contact retention with the solid electrolyte. It's interesting therefore what fraction of the capacity of that layer can be extracted on a subsequent discharge cycle. To investigate this pure indium foil was used as one electrode, with the other the two-layer architecture obtained by first cold-pressing an argyrodite solid electrolyte pellet (370 MPa, 1 minute), then cold-pressing (370 MPa, 5 minutes) 70 mg of ball-milled phase pure InLi intermetallic onto the surface, then attaching an indium metal foil disc (127 micron thick) to the outer surface (80 MPa, 1 minute) with a nickel foil current collector. This electrode architecture is discussed later. A schematic of the cell is shown in figure 5.9B. A 1 $mAcm^{-2}$ current was applied

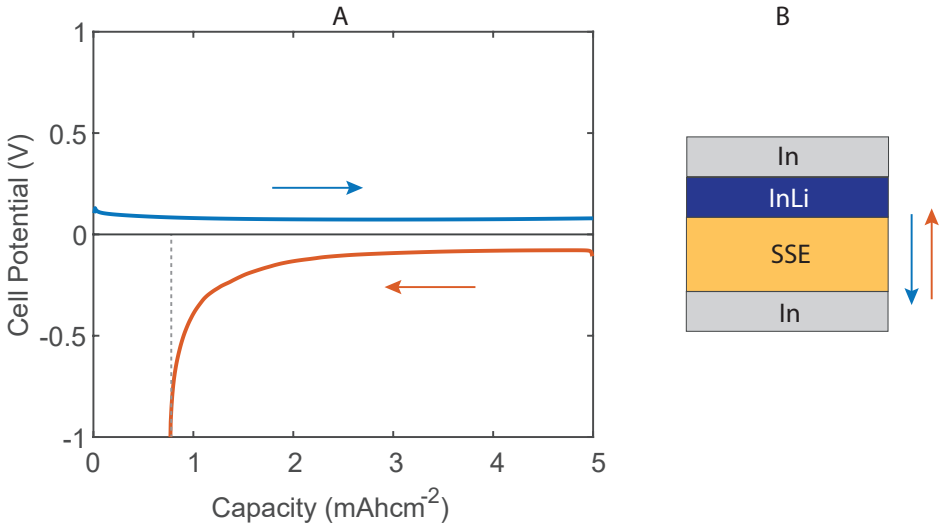


Figure 5.9: First cycle efficiency of indium metal lithiation. (a) Chronopotentiometry of charge and subsequent discharge of indium metal from ball-milled InLi powder and indium foil counter/reference electrode. (b) Cell schematic

to charge the indium foil with 5 $mAhcm^{-2}$ of capacity. After one hour of open circuit, an equal but opposite current was applied until a cell potential of -2.5 V was reached, figure 5.9A. The returned capacity, using the cut-off voltage of -2.5 V was 4.25 $mAhcm^{-2}$, giving a first cycle coulombic efficiency of 85.0%. This is relatively high, but far from unity, meaning pure indium would be a poor counter-electrode to investigate capacity fade in initially lithiated electrodes.

5.6 Indium-lithium on discharge

As demonstrated, the discharge performance of lithium metal is poor, especially at high rates; with large polarisation and limited capacity. The discharge performance of lithiated indium is promising, but not unity. There is, therefore, a need for a counter/reference electrode that has larger capacities and lower polarisations on discharge. As lithium is removed, the InLi -> In + Li^+ + e^- reaction will occur, leading to a progressive change in the electrode microstructure. The microstructure of the initial electrode significantly impacts the achievable performance.

5.6.1 Cast indium lithium two-phase alloy electrode

Indium + 25% Lithium

The first indium lithium electrode investigated was a two-phase electrode, directly in the centre of the two-phase In + InLi region. Indium and lithium were weighed (MTI PCB-200) to make a 75:25 atomic ratio, to make an alloy in the middle of the two-phase region. These were put into a molybdenum foil-lined stainless steel crucible. The melting point of the InLi intermetallic is 632°C so the mixture was heated to 700°C. Once molten the crucible was removed from the furnace, stirred with a spatula, and then returned to the furnace for 2 hours. The crucible was removed from the furnace and turned upside down above the stainless steel glovebox base. The melt rapidly solidified on contact with the glovebox base, forming a relatively fine microstructure.

A sample, taken from the centre of the solidified ingot was calendered and mounted onto an SEM stub. A backscattered electron image can be seen in Figure 5.10A. The microstructure consists of InLi particles within an indium metal matrix. This occurs due to the InLi particles forming first, leading to a progressive lithium depletion of the liquid melt, which eventually solidifies as nearly pure indium. The microstructure as-cast is similar.

Looking more closely at the precipitates; they contain pockets of indium internally; suggesting the formed precipitate was supersaturated with indium on initial solidification; which then drove the internal nucleation of indium pockets. This is in agreement with literature phase diagrams which show a wide solid-solubility region of the InLi phase at high temperature, which reduces to around 3at% in width at room temperature. The same is true of the predominantly indium regions, which contain smaller precipitates of InLi.

X-ray diffraction was performed on the 2-phase alloy Figure 5.10B, confirming the presence of indium metal (navy) and the InLi intermetallic (red).

Two self-symmetric cells were assembled with the alloy, which was easy to calendar down to a foil. The same cell assembly was used as in the previous lithium-magnesium study, with the same Li_6PS_5Cl solid electrolyte, 5 MPa of stack

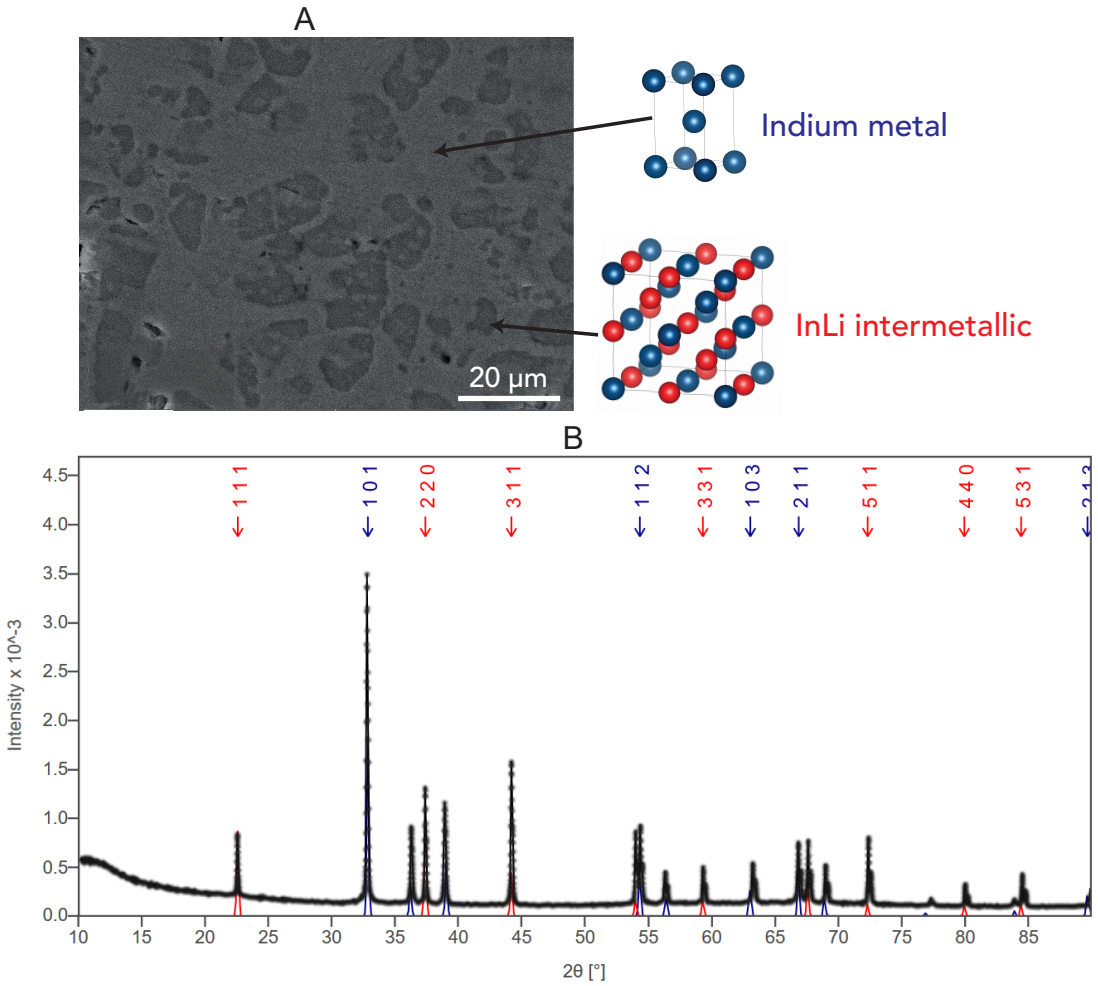


Figure 5.10: Characterisation of two phase In+25at%Li alloy. (a) Back-scattered electron image of alloy microstructure after calendering. (b) XRD pattern of two-phase alloy with reference patterns, InLi (red), In(blue).

pressure, and the same electrochemical procedure of extracting 0.31 $mAcm^{-2}$ of current until failure. As before, a 24-hour stabilisation period at open-circuit was run before the chronopotentiometry, during which EIS spectra were collected at regular intervals. Electrochemical impedance spectroscopy performed every 2.44 hours during open circuit, shows that there is a progressive growth in the interface impedance for this electrode architecture, with a single suppressed semicircle. This could be due to changes in the interface reaction layer or microstructural evolution at the interface. The interface resistance values are approximately double that observed for lithium metal cells [93], perhaps due to the lithium-containing InLi phase occupying below 50% of the contact area.

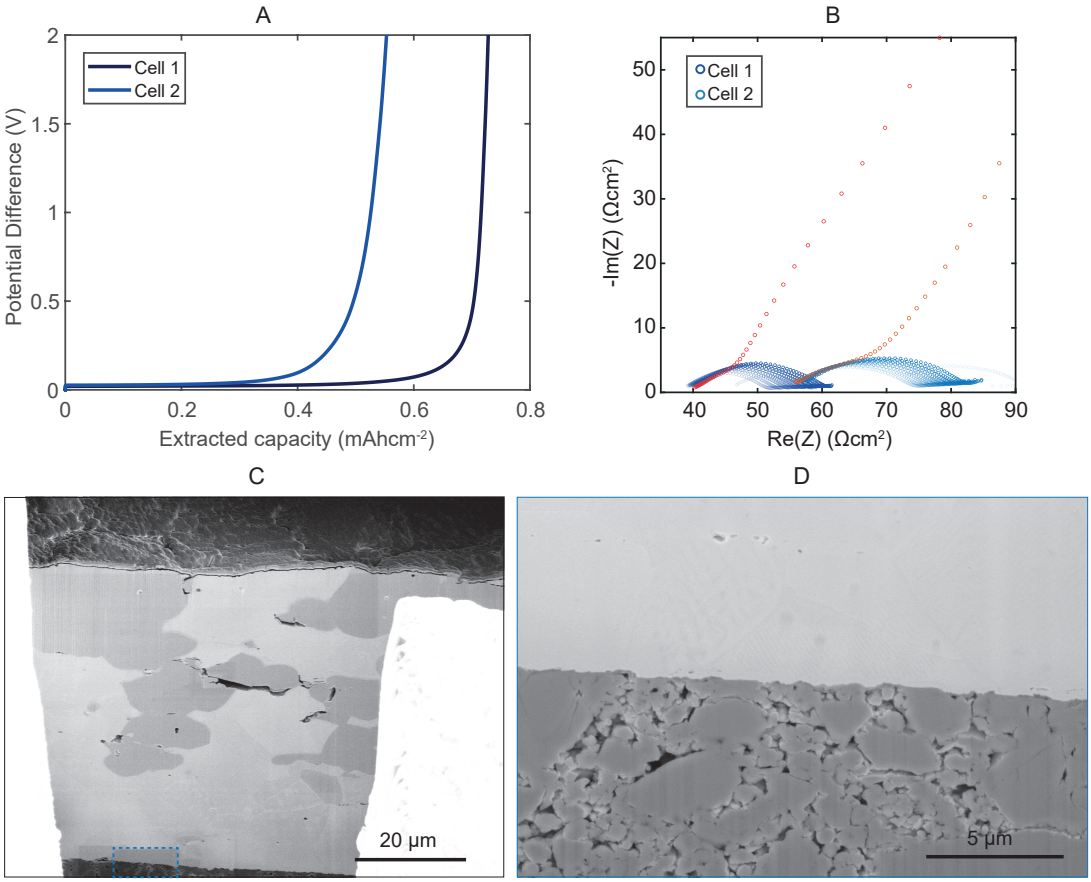


Figure 5.11: (a) Chronopotentiometric stripping showing potential as a function of areal capacity at 0.31 $mAcm^{-2}$ (b) Electrochemical impedance spectroscopy before (navy/blue, more opaque colour indicating a longer time at OCV) and after chronopotentiometry (red/orange). (c) Cross-sectional PFIB image of In+25%Li alloy after chronopotentiometric stripping, full electrode thickness secondary electron image. (d) Higher magnification image of the region highlighted in A, showing electrode-electrolyte interface.

The extracted capacity from both cells was low as can be seen in figure 5.11A. The increase in potential is fairly rapid, which is indicative of a diffusion limit. Impedance spectra taken after the stripping spectra (orange and red in figure 5.11B) follow the final spectra collected during the OCV period (blues in figure 5.11B); except that there is a linear tail to the spectra. This shows that the bulk and interface resistance is unchanged, but that there is a transport limit in at least one of the electrodes. Physically this suggests that the electrodes remain well-contacted to the electrolyte (else the ohmic and interface resistance would change), but that the InLi intermetallic which has fast transport at the interface has been consumed, leaving only indium metal. This result suggests that the diffusion of

lithium in indium metal is very slow.

After chronopotentiometry, one of the cells was disassembled and imaged using a cross-sectional PFIB. The cross-section was prepared by Yvonne Chart. The two phases are distinguishable in Figure 5.11C due to atomic number contrast, with the indium phase appearing bright and the InLi intermetallic phase significantly darker. The solid electrolyte interface is visible at the base of the image. The image agrees with the electrochemical data, showing depletion of InLi near the interface has occurred, with approximately 15 micron without any InLi phase. Regions of the metal near the interface appear scarred; this could be an indication of where the InLi->In phase transformation has occurred. Figure 5.11D shows a zoomed section highlighted in A, showing intimate contact between the indium metal and the solid electrolyte, in agreement with the EIS data.

Indium + 40% Lithium

Given the poor stripping performance in the 25% lithium alloy, a higher content alloy of 40% lithium was synthesised and tested in the same way. Figure 5.12A shows the chronopotentiometry data. There is a significant improvement in extracted areal capacity over the 25% sample. However, the amount extracted is still small, and the overpotential throughout the stripping cycle is too large for the alloy to be a useful counter/reference electrode. The increase is more gradual than in the prior alloy case, suggesting there is a progressive loss of contact instead of a surface depletion mechanism. This is confirmed by the impedance spectra for the cells shown in figure 5.12B and C, with before in blue and after in red; which shows a substantial increase in interface resistance, indicative of a loss of contact.

Microscopy on the raw ingot (figure 5.12D and E, with the left and right panels of D showing the secondary electron and backscattered signals respectively, show that the alloy is primarily InLi intermetallic with a fine microstructure. The ingot is calendered prior to electrochemical testing to form a foil. A secondary electron image of the calendered foil is shown in figure 5.12F. Due to the material being predominantly hard, stiff InLi intermetallic, it does not smoothly calendar

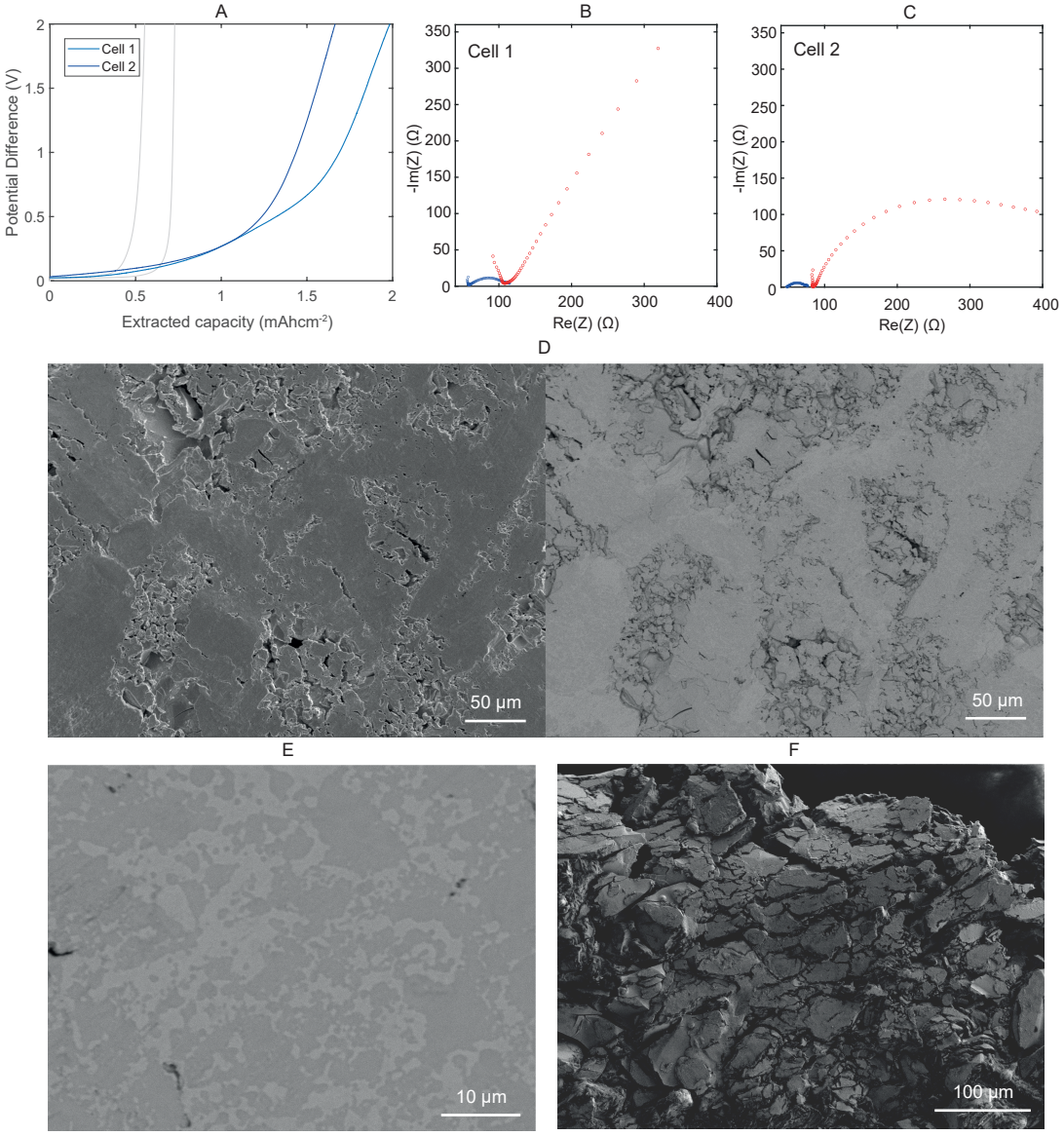


Figure 5.12: (a) Chronopotentiometric stripping showing potential as a function of areal capacity at 0.31 $mAcm^{-2}$ (b, c) Electrochemical impedance spectroscopy before (blue) and after chronopotentiometry (red) for each cell. (d) Secondary electron and backscattered electron of a microtomed surface of In+40%Li alloy ingot (e) High magnification backscattered electron image of ingot showing two-phase microstructure (f) Secondary electron image of calendered In+40%Li foil.

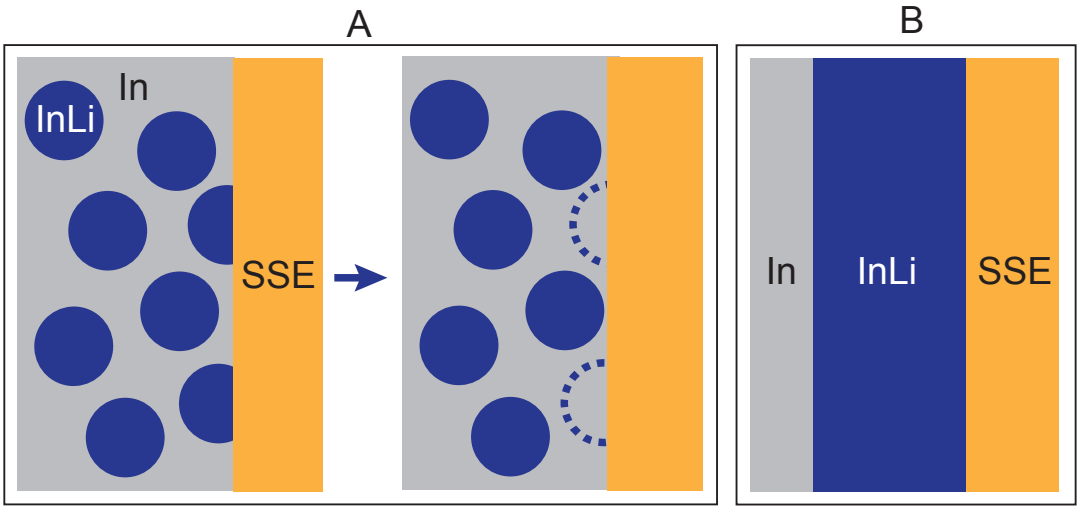


Figure 5.13: Electrode de-lithiation schematics. (a) Cast alloy. (b) Two-layer electrode.

but instead fractures into flakes. The mechanics of the intermetallic phase, high hardness, and low adhesion, are not well suited to processing by calendering or helpful in maintaining electrode-electrolyte contact.

The production of In and InLi two-phase electrodes by casting is not an effective method to produce electrodes that give high capacity on discharge. Alternatives will now be explored. However, the advantage of the casting methodology is that it produces a metallic foil, which is easy to work with, and has excellent stability. It could therefore be useful as a stable reference electrode in a 3-electrode setup.

5.6.2 In + InLi two layer alloy electrode

Based on the findings with the cast alloys, as depicted in figure 5.13A only a small fraction of the lithium was accessible during discharge, an alternative architecture consisting of two layers was conceived. In this new electrode architecture indium metal was layered behind an InLi intermetallic layer facing the electrode, this is shown in figure 5.13B. As both phases are present, the open-circuit potential will be 0.622 V vs Li/Li^+, but the material facing the electrolyte starts as 100% InLi intermetallic (with some porosity); therefore maximising the transport kinetics. On lithium removal from the electrode, a balance exists between the nucleation and growth of indium metal pockets within the InLi phase.

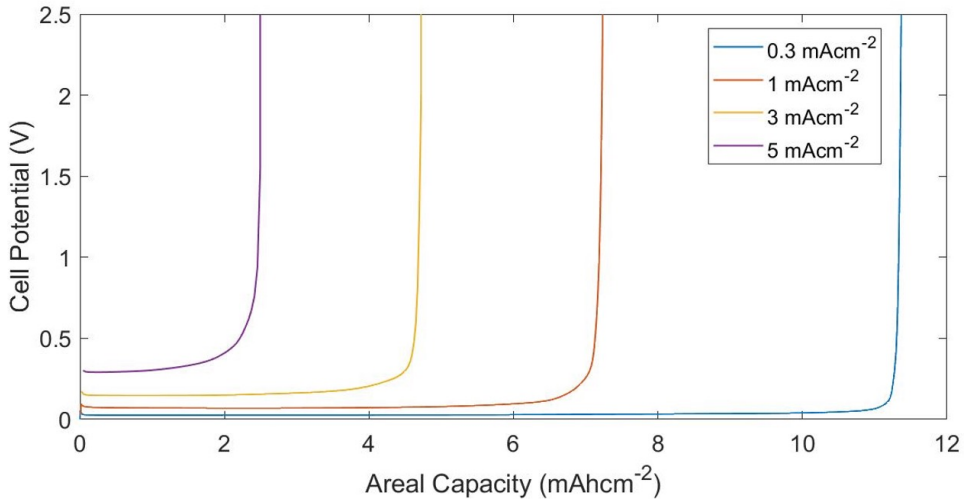


Figure 5.14: Electrochemical stripping of two layer In+InLi electrodes. Chronopotentiometric stripping showing potential as a function of areal capacity at 0.3, 1, 3 and 5 $mAcm^{-2}$.

The two-layer electrode architecture was obtained by first cold-pressing (370 MPa, 5 minutes) 70 mg of ball-milled phase pure InLi intermetallic onto the surface of the 10 mm cold-pressed argyrodite solid electrolyte pellet (370 MPa, 1 minute), before attaching a 10 mm indium metal foil disc (127 micron thick) to the outer surface (80 MPa, 1 minute) with a nickel foil current collector.

The unidirectional chronopotentiometry experiment was performed, using an indium metal counter electrode at 0.3, 1, 3 and 5 $mAcm^{-2}$. The measured potential vs extracted capacity is plotted in figure 5.14. As can be observed, the extracted capacities for each current density are higher than both the cast 25%Li alloy, and lithium metal. Compared to lithium metal, the potential profiles are much flatter for the same current density. This is near-ideal behaviour for a combined counter and reference electrode.

The theoretical capacity of 70 mg of InLi intermetallic is equivalent to 19.9 $mAhcm^{-2}$. All of the cells delivered below this. If indium precipitate nucleation was very difficult for the system, then the existing In/InLi planar interface would move through the material and a continuous InLi pathway would be maintained, leading to a full-capacity extraction. The below-theoretical capacity suggests instead that pockets of indium metal nucleate and grow within the InLi layer, leading to

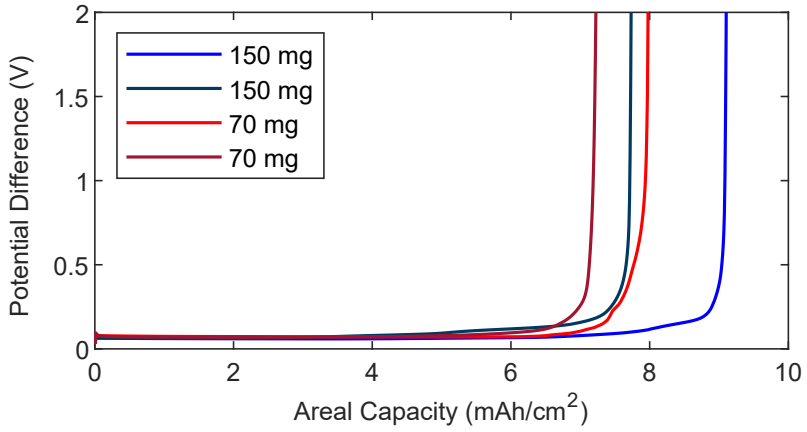


Figure 5.15: Chronopotentiometry at 1 mAcm^{-2} of self-symmetric cells with two layer In+InLi electrodes with 70 and 150 mg InLi loading. Chronopotentiometric stripping showing potential as a function of areal capacity at 0.3, 1, 3 and 5 mA/cm2.

the progressive blocking of lithium transport through the electrode; contributing to an increasing observed potential.

The hockey stick capacity-potential curves suggest that whilst there are continuous pathways of InLi intermetallic through the electrode, lithium-ion transport is fast and therefore the overpotential is very low. When these continuous pathways are blocked by indium metal, the overpotential rapidly increases. The potential increase happens at a lower extracted capacity at higher current densities, suggesting the formation of indium precipitates in the InLi matrix is more localised to the surface. For low current densities, the lithium depletion profile will be near-uniform throughout the electrode, and therefore indium precipitate nucleation will be less likely at the surface. At high current densities, the lithium depletion profile will have a high concentration gradient near the electrolyte interface. Therefore the initial precipitation of indium will be more localised to the surface. As more lithium is extracted, these precipitates will grow.

A higher mass loading of InLi was investigated. Either 70 or 150 mg of ball-milled InLi intermetallic powder was cold pressed onto both sides of the solid electrolyte pellet. Onto this 10 mm disc of indium metal (Sigma Aldrich, 127 μm, 99.99% purity) were attached at 80 MPa, with a nickel foil current collector. Two other cells were assembled with 70 mg of the powder. These self-symmetric cells were

tested unidirectionally at 1 mA cm^{-2}. Figure 5.15 shows the chronopotentiomtry data of two cells for each mass loading. The increase in extracted capacity observed for twice the mass loading is very small, 7.60±0.38 to 8.42±0.69 $mAhcm^{-2}$ for 70 and 150 mg of InLi respectively.

5.6.3 Characterising delithiated microstructure

The full lithium content of the InLi used in the electrode is not accessible due to the nucleation of indium metal blocking transport routes. The mechanism behind this will be similar to any metallurgy nucleation problem. Due to the removal of lithium during electrochemical stripping, a concentration gradient builds in the InLi phase. The fast diffusion kinetics of InLi are such that this gradient extends deep into the electrode, particularly at low current densities. The lithium depletion in the InLi phase leads to a thermodynamic driving force for the nucleation of indium metal, which is most likely at microstructural defects such as InLi particle boundaries and the growth of existing indium precipitates. The formation of indium metal from depleted InLi returns the remaining InLi to its equilibrium composition, see equation 5.1. This process continues over time with existing indium precipitates growing and new ones being formed; with the effective composite diffusivity of the electrode decreasing as the indium volume fraction increases. The microstructural distribution of newly formed indium determines the electrochemical performance observed, therefore characterisation of cells after reaching a voltage limit on discharge is worthwhile.

$$InLi_{1-x} \rightarrow In_{1-x}Li_{1-x} + xIn \tag{5.1}$$

First, a cell with a working electrode of 70 mg of InLi powder with 120-micron thick indium foil was discharged to a cut-off potential of 2.5 V as before. The cell was disassembled and the nickel current collector was removed before an electrode cross-section was prepared as shown in the backscattered electron image figure 5.16A. The phase boundary between indium metal (top), the discharged InLi layer (middle) and the solid electrolyte (dark, bottom) can be seen. A higher

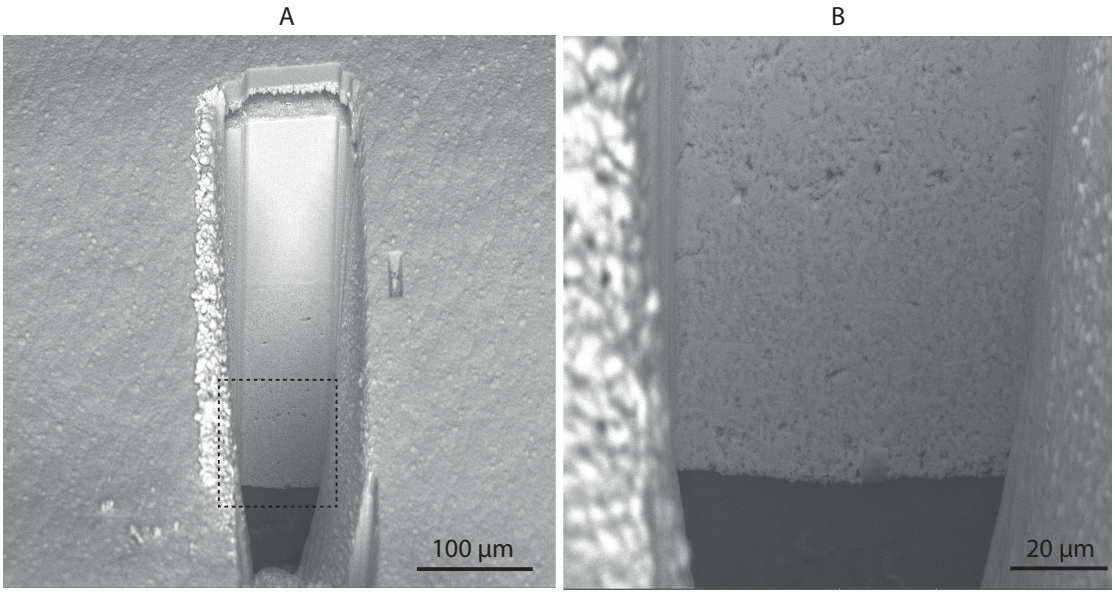


Figure 5.16: PFIB cross-section of two-layer electrode. (a) Backscattered SEM image of PFIB trench. (b) Higher magnification backscattered SEM image of the area highlighted in A.

magnification backscattered electron image of the discharged InLi layer is shown in figure 5.16B, where some phase contrast is arguably visible. It is however impossible to make convincing arguments about the distribution of the indium and InLi phases. This is due primarily to the degree of back-scattered electron shadowing from the deep trench.

Plasma FIB was repeated except a twenty-micron indium foil was used when assembling the cell. The much thinner indium layer reduces the depth of the trench required to image the electrode, thereby reducing the degree of shadowing and improving the data quality. An overall 20 kV backscattered electron (BSE) image is shown in figure 5.17A. The locations of other images shown in the figure are marked and labelled. Overall the cross-section of the electrode has three layers. From top to bottom, there is primarily indium metal, then primarily InLi with significant porosity, and then in contact with the solid electrolyte, a dense layer primarily of indium metal.

A schematic illustration of the delithiation microstructure, based on the PFIB observations is shown in figure 5.18. There are three main locations of indium growth.

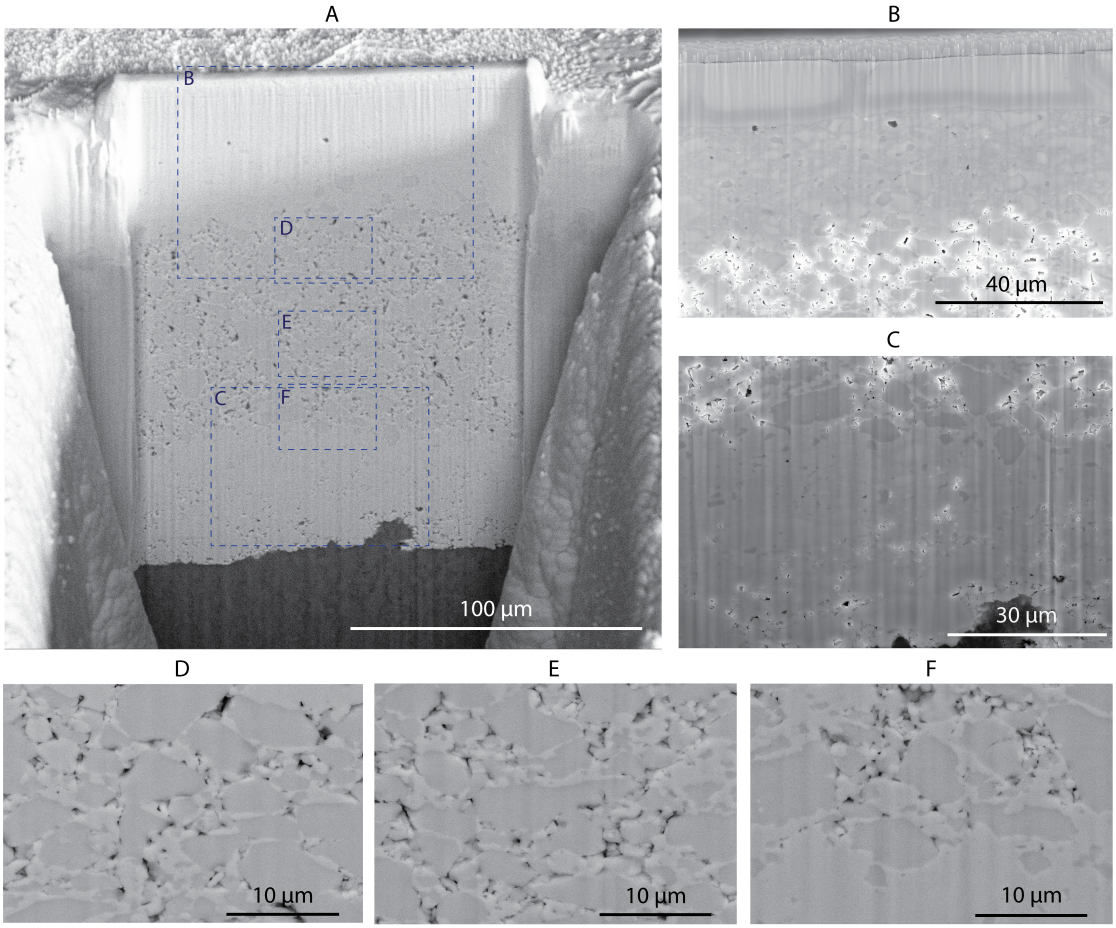


Figure 5.17: Cross-sectional PFIB of InLi electrode delithiated to 2.5 V at 1 mAcm^{-2}. (a) Overall 20 kV backscattered electron (BSE) image. Overlays of other image locations. (b) 30 kV secondary electron (SE) image of top. (c) 30 kV SE image of bottom of layer. (d, e, f) 20 kV BSE image of central two-phase region.

First, the existing indium metal-InLi interface due to the indium foil has propagated into the InLi layer. This can be seen most clearly in figure 5.17B, where the 20-micron indium foil can be clearly seen at the top. Below this is a layer of indium metal, in which the previously InLi particle boundaries can be seen. Some InLi particles, distinguishable by their darker colour in the BSE image, have been occluded within the newly formed indium layer. The cross-section is low in porosity in this layer due to the softness of indium allowing it to yield under the 5 MPa stack pressure within the cell during discharge.

Second, InLi has nucleated throughout the InLi block. As can be seen in figure 5.17D, E and F this primarily occurs on the surface of former InLi particles,

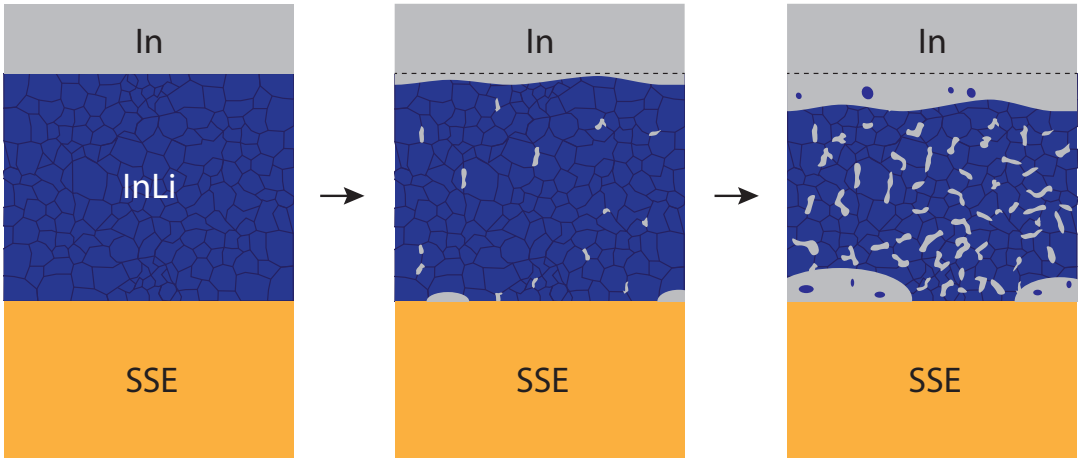


Figure 5.18: Schematic showing indium nucleation morphology during discharge.

leading to a two-phase microstructure. Because of the volume change on delithiation, and the high hardness of InLi, the porosity already present in the InLi layer is exacerbated. The diffusivity of the two-phase microstructure is reduced from that of pure InLi, due to ion-conducting pathways becoming tortuous. It's not clear that there is a significant difference in the ratio of InLi and indium metal between the three images.

Third, there is a thick layer of indium at the solid electrolyte interface, visible in figure 5.17C. This layer is too thick for lithium to diffuse through, therefore it's likely that this is a large indium pocket that has nucleated at the surface and grown over the discharge process. As it is nearest the surface, it grows quickly. The previous figure 5.16 did not have this layer, suggesting, as is schematically depicted in figure 5.18, these pockets do not cover the whole the electrode interface - else lithium could not be extracted from the anode in the moments before the 2.5 V limit was reached.

These three locations of indium formation affect the cell performance differently. The first location, with the existing indium-InLi interface propagating into the InLi layer, does nothing to degrade cell performance as continuous InLi pathways from the solid electrolyte to this interface remain. The second mechanism of indium nucleation within the InLi bulk is detrimental to cell performance, as the diffusivity of the two-phase microstructure is reduced compared to the pristine.

This leads to the depletion concentration gradient being more localised to the electrode-electrolyte interface, accelerating the rate of conversion to InLi here. The final location of indium pockets at the interface with the solid electrolyte is the most detrimental as this leads to an increase in the effective current density through the remaining InLi in contact with the solid electrolyte, again leading to a steeper concentration gradient and more likelihood of further indium nucleation near this interface. The relative contributions of these three locations change with current density, as evidenced by the varied extracted capacity.

There is significant scope to improve the microstructural characterisation of this electrode to better understand the distribution of the two phases through the electrode, including the impact of current density on the plating location. An interesting approach would be transmission powder XRD of a discharged cell, where the relative volume fraction of the two phases can be mapped as a function of distance from the electrolyte interface, or X-ray computed tomography after discharge, enabling the full microstructure to be imaged in 3D. The resolution of the PFIB shown here is far greater than what is achievable by either of these techniques, making the techniques complementary.

5.7 Electrodes formed by combining indium and lithium foils

Using the InLi intermetallic powder to assemble the electrodes is effective, but many labs do not have this material. I, therefore, investigated whether comparable performance electrodes could be assembled using indium and lithium metal foils. Thin foils of indium metal (127 μm, Sigma Aldrich) and lithium metal (Calendered to 49 μm, Sigma Aldrich), figure 5.19B, were layered and co-calendered. The two metals do not immediately react, but over several days, a solid-state reaction occurs leading to a purple/grey layer forming figure 5.19C. Lithium that has not yet reacted can be easily peeled off. XRD of the sample is shown in figure 5.19A, with both the indium and InLi phase present.

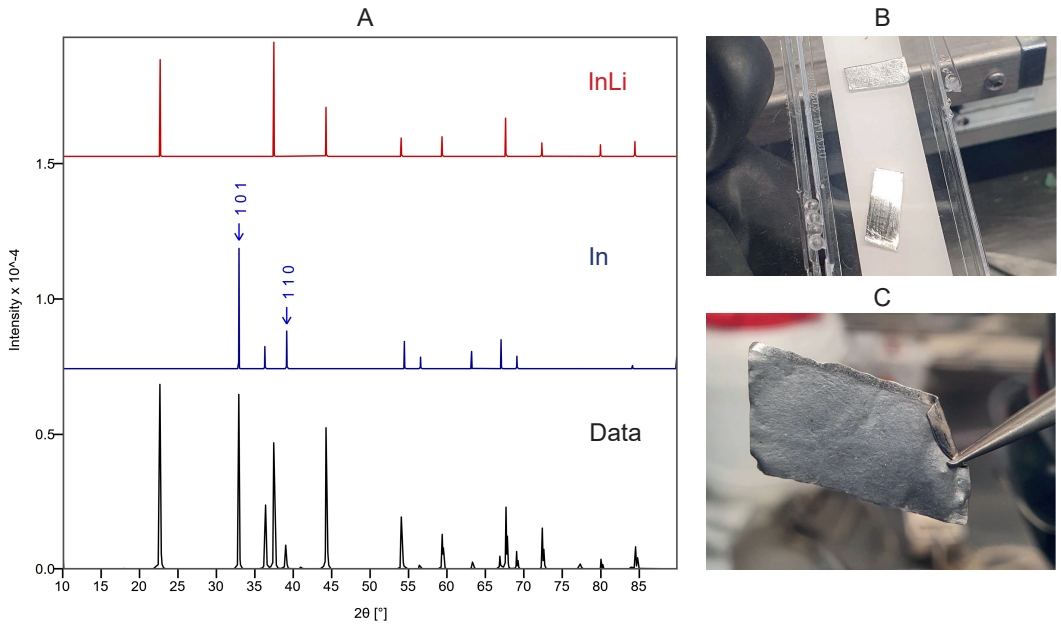


Figure 5.19: (a) XRD of reacted indium and lithium foils. (b) Photograph of indium and lithium foil pieces before calendaring. (c) Image of foil after 2 days.

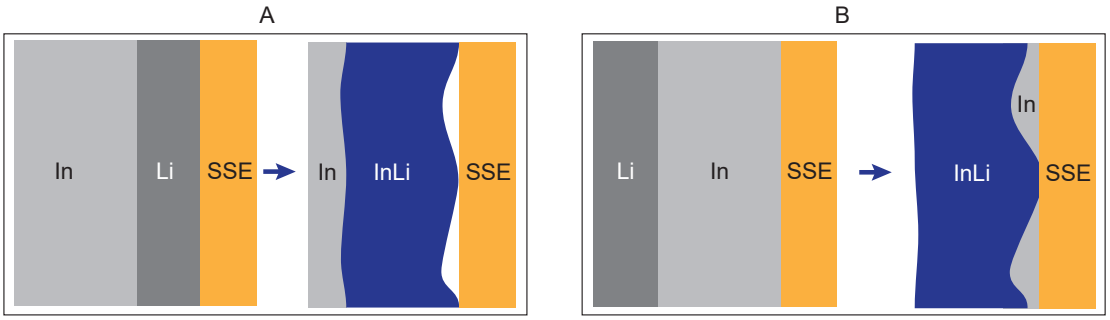


Figure 5.20: Schematic of two foil electrodes. (a) Lithium on the inside. (b) Indium on the inside.

10 mm diameter discs of lithium (4.6 mg, approximately 100 micron), then indium metal (144 mg, approximately 200 micron) giving an approximate In:Li ratio of 2:1, were pressed with 80 MPa pressure onto cold-pressed solid electrolyte pellet to form self-symmetric cells. Three cells were assembled with a 5 MPa stack pressure and left at OCV for 48 hours. Electrochemical impedence spectra were collected every two hours. As can be seen in figure 5.21A, the OCV was initially zero volts, but was then unstable, tending towards zero volts at long times. Given the cells are self-symmetric, the variation in open-circuit voltage suggests varied reaction kinetics to form the InLi phase. EIS results are shown

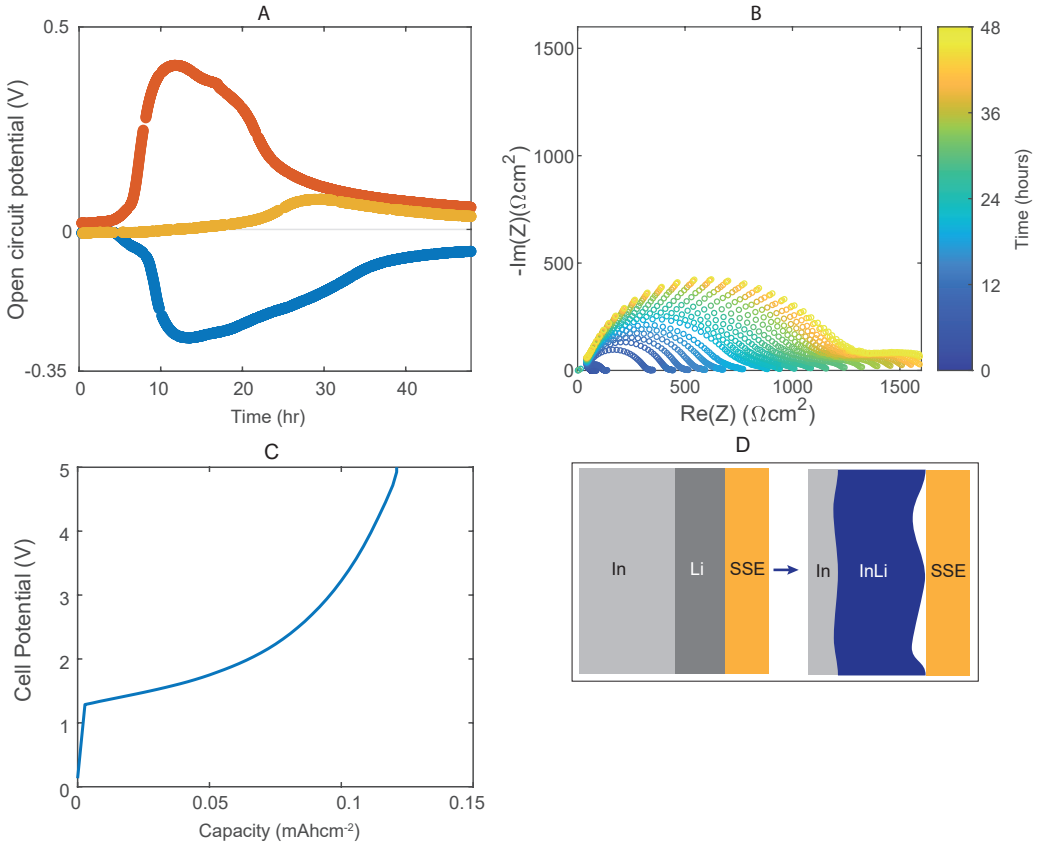


Figure 5.21: Two foil electrodes, lithium on inside. (a) Open circuit voltage of self-symmetric cells over two days. (b) Electrochemical impedance spectroscopy of self-symmetric two foil cell. (c) Chronopotentiometry of self-symmetric cell at 1 mAcm^{-2}. (d) Schematic of the reaction process leading to loss of contact.

in figure 5.21B initially is typical of a lithium metal self-symmetric cell, with an interface impedance resistance of 9.9 Ωcm^2. Over time, the suppressed semicircle attributable to interface impedance increased to over 1200 Ωcm^2 after 48 hours. This implies a progressive loss of contact between the anode and the solid electrolyte. On reacting from indium (15.76 $cm^3 mol^{-1}$) and lithium metal (13.02 $cm^3 mol^{-1}$) to form InLi intermetallic (23.82 $cm^3 mol^{-1}$), there is a volume shrinkage of 17%. As the formed intermetallic is a hard, stiff, non-adhesive material, the 5 MPa of applied stack pressure is insufficient to retain good contact. This scenario is depicted schematically in figure 5.21D. The continual change in impedance over the 48-hour period suggests that the reaction is incomplete. On attempting to draw current, the impedance is very large so just 0.12 mAhcm^{-2} capacity can be extracted at

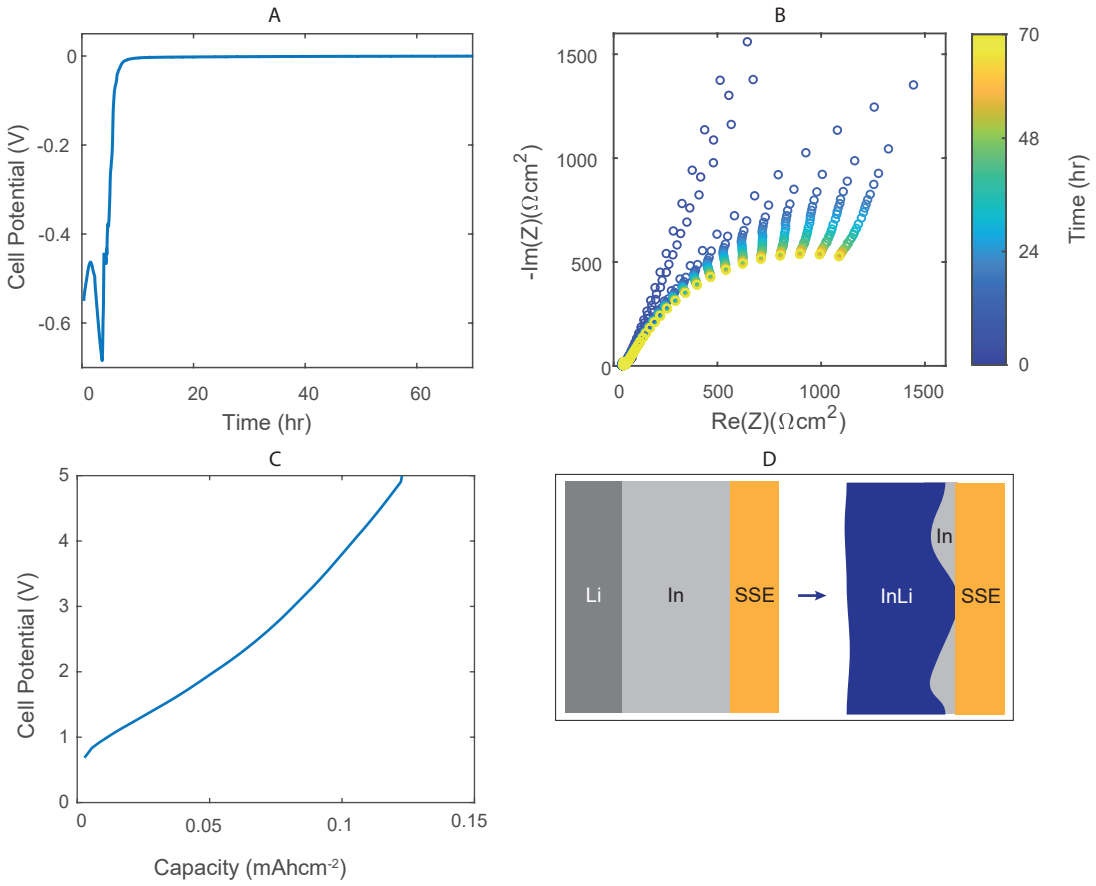


Figure 5.22: Two foil electrodes, indium on the outside. (a) Open circuit voltage of self-symmetric cell over 70 hours. (b) Electrochemical impedance spectroscopy of self-symmetric two foil cell. (c) Chronopotentiometry of self-symmetric cell at 1 $mAcm^{-2}$. (d) Schematic of the reaction process.

1 $mAcm^{-2}$ before the 5V voltage limit is reached.

Alternatively [118] proposed assembling electrodes where the indium metal is on the inside, facing the solid electrolyte and lithium metal on the outside. Using this approach they demonstrate a cycled capacity of 1 $mAcm^{-2}$. Based on the findings in this chapter, this approach seems counter-intuitive as the indium metal layer will block lithium transport. A self-symmetric cell was assembled in the same way as the prior experiment, but with the indium on the inside. Figure 5.22A shows the OCV of the self-symmetric cell starts at -0.6 V and goes to within 10 mV of zero volts after 8 hours before continuing to decrease towards zero over the following 62 hours. The EIS data shown in figure 5.22B starts with a straight line showing the diffusion limit we'd expect from indium at the interface. As time

passes, the warburg tail curves over - suggesting some InLi contact at the interface. Even after 70 hours at OCV, the impedance remains very large. Figure 5.22C shows unidirectional chronopotentiometry at 1 $mAcm^{-2}$. A small capacity of 0.12 $mAhcm^{-2}$ is extracted, again suggesting a small amount of InLi contact at the interface. This performance is much worse than that reported in the prior work. In the cell I tested, an In:Li ratio of approximately 2:1 was used. If a smaller ratio was used, closer to 1:1, the inhomogeneity of the indium-lithium reaction will mean that some InLi phase is in contact with the solid electrolyte, enabling a meaningful capacity to be extracted as reported by Santhosha et. al. [118]. This is depicted schematically in figure 5.22D. As reported in the supplementary information of the Santhosha paper, using too small of an In:Li ratio e.g. 1.23:1 reduces the extractable capacity before the electrode moves out of the In/InLi two-phase composition range, leading to unstable potential. Optimising the thickness of indium and lithium foil so that meaningful capacity can be extracted is hard.

The solid-state reaction of indium and lithium metal foils can be used to synthesise In/InLi two-phase electrodes. This reaction is relatively slow, as illustrated by the continual change in impedance over 48 hours shown in figure 5.21. Compared to the cold-pressing of phase pure InLi powder, producing electrodes in this manner is much harder experimentally and much less reproducible. The cold-pressing methodology leads to excellent solid electrolyte contact, immediately stable potential and immediately stable impedance, all of these are valuable in a counter/reference electrode. Therefore this is a superior methodology compared to preparing the electrode by reacting the two metal foils.

5.8 Cycling two-layer InLi electrode.

Although a great deal of information can be gained from unidirectional chronopotentiometry, many battery applications require sustained performance over multiple cycles. Therefore a solid-state counter/reference electrode that is capable of superior sustained performance over multiple cycles is valuable. Cycling experiments can be very time-consuming, especially if small charge/discharge rates are used. By

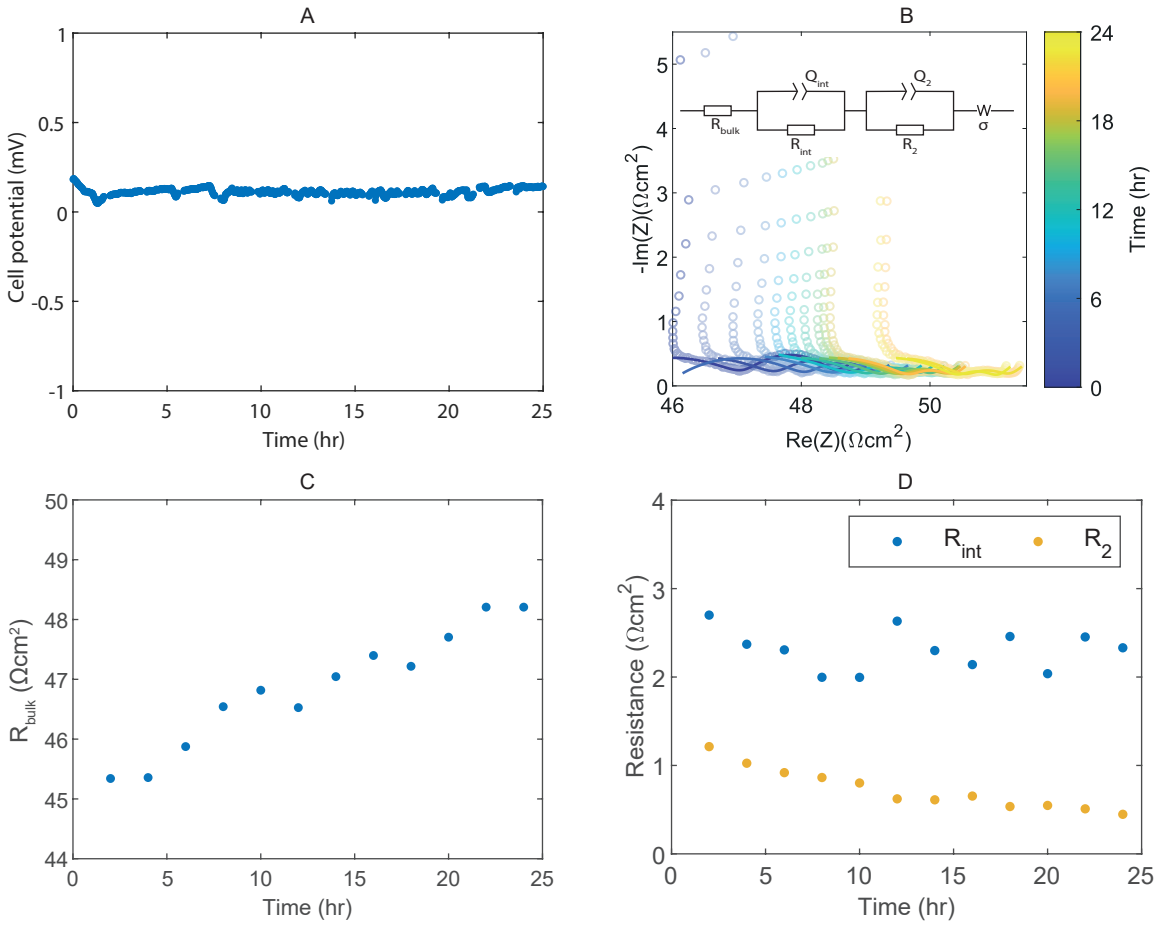


Figure 5.23: Electrochemical impedance spectroscopy during open-circuit of symmetric two-layer electrode cell. (a) Open circuit voltage with time. (b) Fit EIS spectra. Inset of equivalent circuit used to fit curves. (c) Bulk/ohmic resistance with time. (d) Moderate (R_{int})and low frequency (R_2) interface resistance terms over time.

performing experiments at high discharge rates, failure modes for electrodes can be established and understood whilst minimising experiment duration.

5.8.1 Electrochemical Impedance Spectroscopy before cycling

Self-symmetric cells with electrodes of 70 mg of InLi powder with 120-micron thick indium foil were assembled as described previously. Before cycling, electrochemical impedance spectra were collected every two hours over a twenty-five-hour period at an open circuit. The cell potential is shown in figure 5.23A with a mean value and standard deviation of 0.1135 and 0.0194 mV. The fitted EIS curves are shown in

figure 5.23B. The spectra were fit using the equivalent circuit inset into figure 5.23B, and the high-frequency tail (>20 kHz) was excluded. As can be seen in figure 5.23C the bulk resistance increases slightly over the course of the OCV period. Given the potential of the In/InLi electrode (0.622 V vs Li/Li^+) is still well below the thermodynamic stability window of the argyrodite [239], it is likely that a layer of decomposition products such as Li_2S and Li_3P forms to passivate the interface by blocking electrons, preventing further degradation [240]. The growth of this layer could be the origin of the increased ohmic resistance R_{bulk} in figure 5.23C.

The impedance curves have two clear suppressed semicircles, the first at a moderate frequency of 5 kHz, and the second at a low frequency of 5 Hz. The size of the two semicircles is small at around 2.3 and 1 Ωcm^2, the fit values are plotted in figure 5.23D. These resistances are smaller than are typically observed for lithium-argyrodite symmetric cells, as was shown in figure 4.22. Unlike the Li system, there is not a large impedance component that significantly grows over time, which we attributed to the SEI formed with the solid electrolyte and lithium [194]. In figure 5.23D, the low-frequency component decreases in resistance towards zero over the course of the OCV period, whereas the moderate frequency component is essentially constant, with a mean value of 2.31 Ωcm^2. The moderate frequency component is all that remains after cycling and can be attributed to the charge transfer process at the solid-electrolyte electrode interface.

5.8.2 Cycling two-layer InLi electrode

The unidirectional chronopotentiometry for the cold-pressed two-layer electrode presented in figure 5.14 shows a hockey-stick type shape, with very low and stable electrode overpotential until a sharp increase is reached. Based on this data, I selected a test cycling capacity of 3 $mAcm^{-2}$ and capacity of 3 $mAhcm^{-2}$. This considerable current density and near-limit capacity allows the identification and mechanistic understanding of electrode performance degradation during cycling. Figure 5.24 shows cycling data for a self-symmetric cell assembled with 70 mg of InLi intermetallic cycled at a current density of 3 $mAcm^{-2}$ and capacity of 3

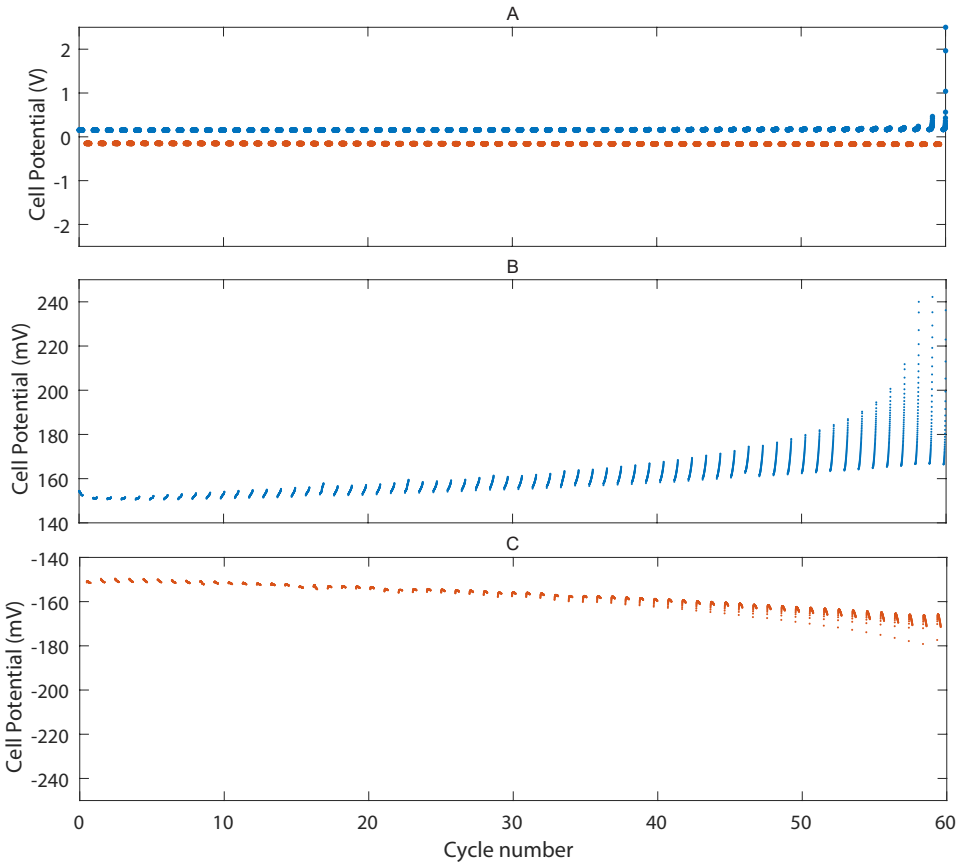


Figure 5.24: Cycling of two-layer electrode at 3mAcm^{-2}, 3mAhcm^{-2}. (a) Overall. (b) Discharge cycles. (c) Charge cycles.

mAhcm^{-2} at a temperature of 303 K and a stack pressure of 5 MPa. The cell was at OCV for one hour after each charge and each discharge step including a twenty-minute EIS measurement. The working electrode is defined as the electrode discharged (Li stripped) first. Figure 5.24A shows that 60 cycles are achieved before a voltage limit of 2.5 V is reached on the discharge cycle. Up to 50 cycles, the overpotentials are low, even with such a high current density. The cell is limited by the working electrode, with much larger overpotentials on discharge than charge, demonstrating that there is scope to improve the pristine electrode manufacturing to optimise the initial microstructure. Overall the cycling data show a progressive worsening of performance instead of a sudden failure.

Figure 5.25 shows EIS data collected following each discharge and charge cycle. In line with the cycling potential data, there is a progressive increase in impedance

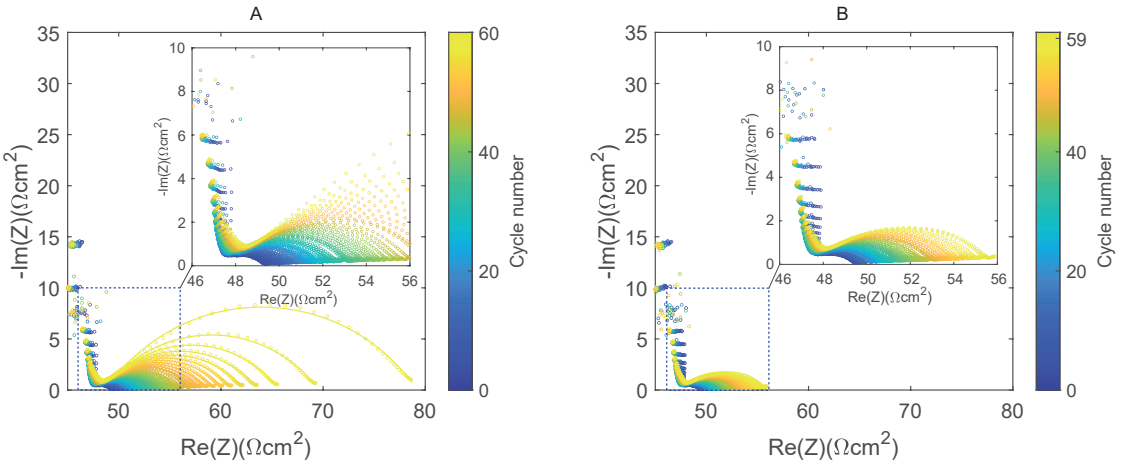


Figure 5.25: Electrochemical impedance spectroscopy during cycling of two-layer electrode at 3mAcm^{-2}, 3mAhcm^{-2}. (a) After discharge. (b) After charge.

after each discharge cycle. The lower frequency and high frequency impedance components which were clearly separate in the OCV electrochemical impedance spectroscopy were not separable after cycling. With the high-frequency tail excluded from the fit, the simple equivalent circuit model, shown in figure 5.26D fit the data well. The fit values for fitting all 119 impedance curves are plotted in figure 5.26A and B. The bulk resistance is approximately constant, which suggests interface contact is maintained over successive cycles and is not the main mechanism of performance degradation. By contrast, the interface resistance grows progressively over successive cycles. This is not primarily due to the growth of an SEI, as this would persist after recharging. I hypothesise that it is due to the growth of pockets of indium metal, such as the one observed in figure 5.17, at the solid electrolyte interfaces, as the indium is ion-blocking, this leads to a reduction in the contact area between the solid electrolyte and the lithium-ion transporting InLi phase.

The mean interface resistance value during OCV is 2.31 Ωcm^2. If it is assumed this reflects perfect contact between the solid electrolyte and InLi intermetallic, this value can be divided by the interface resistance after each charge and discharge to obtain the contact area fraction of InLi. This value, plotted in figure 5.26C decreases near linearly with cycle number. After the final cycle, where a threshold potential of 2.5 V is reached, a contact area fraction of below 10% remains.

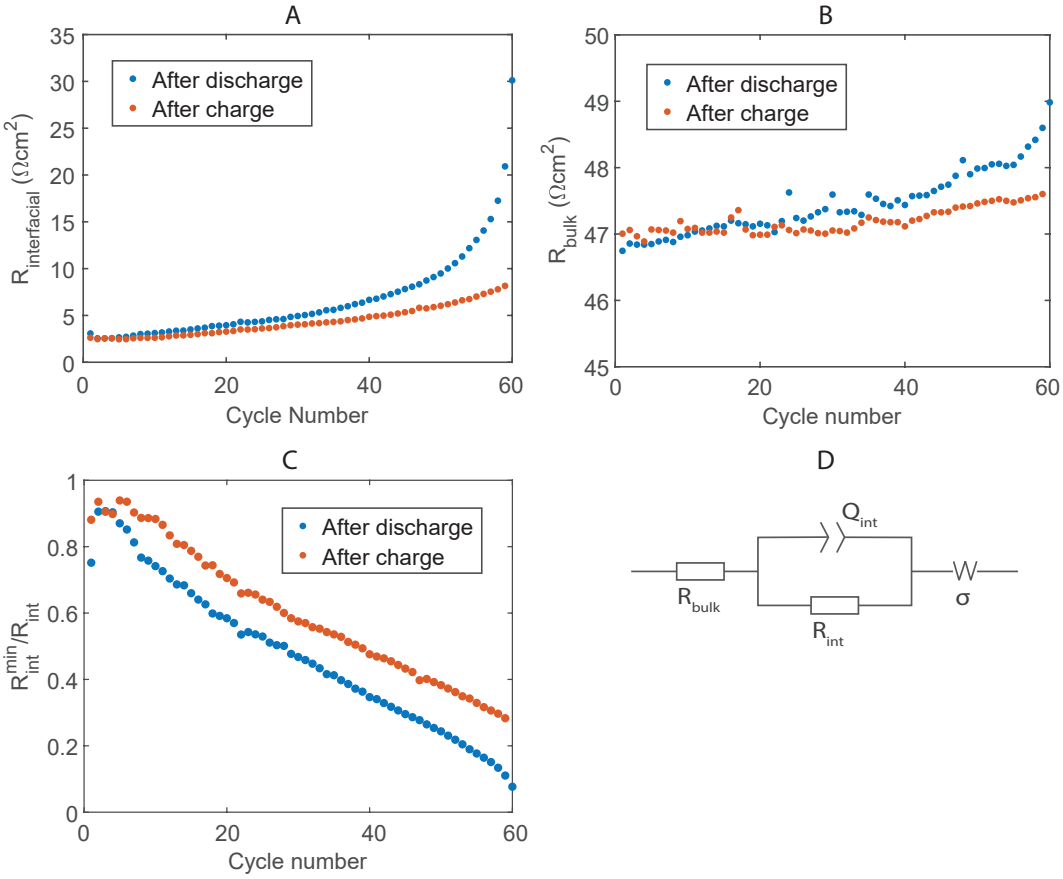


Figure 5.26: Equivalent circuit values of EIS data presented in figure 5.25 with cycle life. (a) Interface resistance. (b) Bulk resistance. (c) Interface InLi fraction. (d) Equivalent circuit used to fit EIS data.

This data shows the failure mechanism of this electrode over successive cycles due to the accumulation of indium metal at the interface with the solid electrolyte. This behaviour is predictable and measurable from impedance spectroscopy.

5.9 Conclusions

Electrodes operating in the InLi/In the two-phase region are effective counter/reference electrodes. They should play a helpful role in accelerating research into electrode materials for solid-state batteries. The diffusion kinetics in the InLi intermetallic are incredibly fast, whereas the diffusion kinetics in the In metal phase are very slow. Lithium transport within the electrode is therefore dependent on the microstructure, which evolves due to lithiation/delithiation. Further work should seek to optimise

the manufacturing method of indium/lithium electrodes to minimise the nucleation of indium metal pockets at the electrolyte interface and within the fast diffusing InLi such that a continuous network of intermetallic can be maintained for greater extracted capacities than was achieved in this work. The success of changes in the evolving microstructure could be investigated using X-ray tomography in-operando. The coupled problem of indium precipitation and transport within the electrode seems ideal for a phase field model to describe. This could guide further improvement of this electrode architecture and its manufacture. Perhaps more simply, a composite electrode could be produced by incorporating solid electrolyte particles into the InLi layer to provide ion-conducting pathways deep into the electrode. A compromise must then be found between discharge potential profile flatness and the accessible capacity at high rates.

Considering alloys more broadly, intermetallics are an interesting and under-studied materials class for lithium batteries; with unique mechanical, chemical, and transport properties. There are analogous lithium-rich intermetallics with very high diffusivity which have an equilibrium two-phase region with lithium metal. Fast discharge performance superior to that of lithium metal may be achieved if electrodes can be made incorporating these materials.

6
Conclusions

In Chapter 3 I developed EBSD of lithium metal and used it to quantify the orientation-dependent mechanics of lithium by nanoindentation. The surface preparation technique of microtome is ideal for lithium metal and its alloys due to their high reactivity and low hardness. It leads to very low roughness and avoids contamination or significant surface modification.

The indentation measurements suggest stiffness tensor components of C_{11}=13.3, C_{12}=11.2, C_{44}=8.8 GPa. Clear size-dependent hardness is observed due to the stressed volume being small enough so that few dislocations experience a shear stress and therefore less slip occurs than would for a bulk test. Hardness greater than 100 MPa is observed on the length scale of lithium filaments, this is two orders of magnitude higher than the bulk yield stress of around 0.6 MPa [82]. Linear elastic fracture mechanics suggest crack opening stresses of this order are likely to fracture current solid electrolyte materials due to their relatively low fracture toughness, especially over successive cycles. Higher toughness solid electrolyte materials, and processing techniques to achieve low porosity in solid electrolytes should be pursued.

In Chapter 4 I demonstrated that alloying lithium with magnesium significantly changes its microstructural, mechanical, kinetic, and chemical properties, which in turn impacts the electrochemical performance. The framework of experimentation

from synthesis to cells is applicable to any lithium-rich alloy anode. Electrochemically this work shows there is a clear correlation between diffusivity, and the cell performance on stripping, with an enhancement over a purely Fickian relationship attributable to the role of stack pressure. To achieve target current densities and capacities, without excess stack pressure or temperature, anode materials with room temperature lithium diffusion coefficients in excess of 10^{-9} cm^2s^{-1} should be pursued, necessitating the incorporation of a second phase. NMR is a valuable method to quickly screen candidate materials to find those with diffusivity values that can achieve the desired performance. In this case, ^{6}Li enrichment was necessary, but for most intermetallic phases ^{7}Li may be used. Once high diffusivity phases are found, the challenge of optimising the microstructure of the alloy to maximise the impact of these phases can be pursued. Having a high diffusivity alone is insufficient as contact must be maintained at the electrolyte interface, and reaction layers at the interface which significantly compromise electrochemical performance must be avoided, therefore mechanics and interfacial chemistry should be examined. The mechanical properties of alloy anodes control four major battery properties. First, mechanics determine contact. Soft, adhesive, ductile metals such as those investigated here, can be conformed to a non-uniform solid electrolyte surface by the application of mild pressures. Hard, non-adhesive materials will be more prone to losing contact. Second is the impact of mechanics on processing. Soft, ductile metals are best processed by rolling, whereas brittle materials are best processed by first ball-milling into a powder. Third, mechanics fundamentally underpin the durability of solid-state batteries with failure occurring due to the fracture of components under cyclic stress and nanoscale lithium intrusions [74, 231]; understanding the fundamental properties of candidate materials allows failure modes to be understood and resolved. Finally, several works [75] have demonstrated that stresses within batteries modify the transport of lithium atoms and ions. The fundamental mechanical values presented in this work enable stress-coupled models of lithium transport within lithium magnesium alloy anodes.

Despite the nearly identical operating potential, impedance spectroscopy shows an increased interfacial resistance for the alloys compared to pure lithium, which grows over time, attributable primarily to changes in the alloy passivation layer composition. The combined tools of XPS and EIS allow changes in interfacial chemistry to be identified and understood. In other alloy systems, especially those which operate at higher or variable potentials where reversible electrolyte red-ox may occur – much larger interfacial impedance may be observed, which will have a significant electrochemical impact. Finally, a consistent theme we observed throughout this work, is that just 5% magnesium content makes many characterisation methods easier – increased atomic number leads to improved EBSD resolution, XRD signal and stability in PFIB, as well as making the alloys far easier to handle in cell assembly. If researchers carefully consider the changes to the properties identified in this work; using a lithium magnesium alloy may allow characterisation currently impossible with pure lithium. This will enable the behaviour of the pure metal to be better understood.

In the final experimental chapter, I studied the indium/InLi two-phase region as a counter/reference electrode for solid-state batteries. The diffusion kinetics in the InLi intermetallic are incredibly fast, whereas the diffusion kinetics in the In metal phase are very slow. Lithium transport within the electrode is strongly dependent on the microstructure, which evolves as a result of lithiation/delithiation. This sets up an interesting two-phase problem. A two-layer electrode architecture is proposed which leads to very flat discharge profiles even at very high rates at relevant capacities. Considerable cycling stability is demonstrated, with a clear degradation mechanism.

Overall the work in this thesis moves the field of solid-state battery development forward by providing a deeper understanding of the material properties, the resultant electrochemical performance, and the link between the two. I hope others continue to build on the ideas discussed in this work to develop high-performance solid-state batteries.

References

[1] *The Road to Zero*. Tech. rep. July. Department for Transport, 2018.

[2] *Emissions of air pollutants from transport*. Tech. rep. European Environment Agency, 2018.

[3] *Car Registration Data*. 2019. URL: https://www.smmt.co.uk/vehicle-data/car-registrations/.

[4] Eric Wolff et al. "Climate Change Evidence & Causes An overview from the Royal Society". In: (2020).

[5] George Crabtree, Elizabeth Kócs, and Lynn Trahey. "The energy-storage frontier: Lithium-ion batteries and beyond". In: *MRS Bulletin* 40.12 (2015), pp. 1067–1076.

[6] Heebyung Koh and Christopher L. Magee. "A functional approach for studying technological progress: Extension to energy technology". In: *Technological Forecasting and Social Change* 75.6 (2008), pp. 735–758.

[7] Jon Moore. *BNEF Executive Factbook*. Tech. rep. Bloomberg, 2020.

[8] *Valuation of energy use and greenhouse gas*. Tech. rep. April. Department for Business, Energy & Industrial Strategy, 2019.

[9] Graeme Hill et al. "The role of electric vehicles in near-term mitigation pathways and achieving the UK's carbon budget". In: *Applied Energy* 251.April (2019).

[10] Charlie Bloch et al. *Breakthrough Batteries - Powering the Era of Clean Electrification*. Tech. rep. Rocky Mountain Institute, 2019.

[11] Andreas W Schäfer et al. "Technological, economic and environmental prospects of all-electric aircraft". In: *Nature Energy* 4.2 (2019), pp. 160–166. URL: http://dx.doi.org/10.1038/s41560-018-0294-x.

[12] Dingchang Lin, Yayuan Liu, and Yi Cui. "Reviving the lithium metal anode for high-energy batteries". In: *Nature Nanotechnology* 12.3 (2017), pp. 194–206. URL: http://dx.doi.org/10.1038/nnano.2017.16.

[13] Gilbert N Lewis and Frederick G Keyes. "The Potential of the Lithium Electrode". In: *Journal of the American Chemical Society* 33.9 (1913), pp. 340–344.

[14] Raymond Jasinski. "A summary of patents on organic electrolyte batteries". In: *Journal of Electroanalytical Chemistry* 26.2-3 (1970), pp. 189–194.

[15] M Stanley Whittingham and Arthur H Thompson. "Intercalation and lattice expansion in titanium disulfide". In: *The Journal of Chemical Physics* 62.4 (1975), p. 1588.

[16] M Stanley Whittingham and Fred R Gamble. "The lithium intercalates of the transition metal dichalcogenides". In: *Materials Research Bulletin* 10.5 (1975), pp. 363–371.

[17] S Basu et al. “Synthesis and properties of lithium-graphite intercalation compounds”. In: *Materials Science and Engineering* 38.3 (1979), pp. 275–283.

[18] M Zanini, S Basu, and J E Fischer. “Alternate synthesis and reflectivity spectrum of stage 1 lithium-graphite intercalation compound”. In: *Carbon* 16.3 (1978), pp. 211–212.

[19] R Yazami and Ph Touzain. “A reversible graphite-lithium negative electrode for electrochemical generators”. In: *Journal of Power Sources* 9.3 (1983), pp. 365–371.

[20] E Peled. “The Electrochemical Behavior of Alkali and Alkaline Earth Metals in Nonaqueous Battery Systems—The Solid Electrolyte Interphase Model”. In: *Journal of the Electrochemical Society* 126.12 (1979), pp. 2047–2051.

[21] K MIZUSHIMA et al. “LixCoO2 (0<x1): A new cathode material for batteries of high energy density”. In: *Solid State Ionics* 3-4.4 (Aug. 1981), pp. 171–174. URL: https://linkinghub.elsevier.com/retrieve/pii/0167273881900771.

[22] Akira Yoshino, Kenichi Sanechika, and Takayuki Nakajima. *Secondary battery.* 1986. URL: https://patents.google.com/patent/US4668595.

[23] M Stanley Whittingham. “History, evolution, and future status of energy storage”. In: *Proceedings of the IEEE* 100.SPL CONTENT (2012), pp. 1518–1534.

[24] Chen Xi Zu and Hong Li. “Thermodynamic analysis on energy densities of batteries”. In: *Energy and Environmental Science* 4.8 (2011), pp. 2614–2624.

[25] Teyeb Ould Ely, Dana Kamzabek, and Dhritiman Chakraborty. “Batteries Safety: Recent Progress and Current Challenges”. In: *Frontiers in Energy Research* 7.September (2019).

[26] Doron Aurbach et al. “A short review of failure mechanisms of lithium metal and lithiated graphite anodes in liquid electrolyte solutions”. In: *Solid State Ionics* 3.148 (2002), pp. 405–416.

[27] Raimund Koerver et al. “Chemo-mechanical expansion of lithium electrode materials-on the route to mechanically optimized all-solid-state batteries”. In: *Energy and Environmental Science* 11.8 (2018), pp. 2142–2158.

[28] J.-M. Tarascon and M Armand. “Issues and challenges facing rechargeable lithium batteries”. In: *Nature* 414.6861 (Nov. 2001), pp. 359–367.

[29] John B Goodenough and Youngsik Kim. “Challenges for rechargeable Li batteries”. In: *Chemistry of Materials* 22.3 (2010), pp. 587–603.

[30] Jack Ewing. *Volkswagen Hopes Fresh Logo Signals an Emission-Free Future.* Sept. 2019. URL: https://www.nytimes.com/2019/09/08/business/volkswagen-trademark-electric-vehicles.html.

[31] Andrew Ulvestad. “A Brief Review of Current Lithium Ion Battery Technology and Potential Solid State Battery Technologies”. In: (2018). URL: http://arxiv.org/abs/1803.04317.

[32] Melanie J Loveridge et al. “Looking deeper into the galaxy (Note 7)”. In: *Batteries* 4.1 (2018), pp. 1–11.

[33] *Events with smoke, fire, extreme heat or explosion involving lithium batteries.* Tech. rep. FAA Office of Security and Hazardous Materials Safety, 2019.

[34] Wu Xu et al. “Lithium metal anodes for rechargeable batteries”. In: *Energy and Environmental Science* 7.2 (2014), pp. 513–537.

[35] Dongping Lu et al. “Failure mechanism for fast-charged lithium metal batteries with liquid electrolytes”. In: *Advanced Energy Materials* 5.3 (2015), pp. 1–7.

[36] Bingbin Wu et al. “The interplay between solid electrolyte interface (SEI) and dendritic lithium growth”. In: *Nano Energy* 40.July (2017), pp. 34–41.

[37] Ju Hsiang Cheng et al. “Visualization of Lithium Plating and Stripping via in Operando Transmission X-ray Microscopy”. In: *Journal of Physical Chemistry C* 121.14 (2017), pp. 7761–7766.

[38] Chengcheng Fang et al. “Quantifying inactive lithium in lithium metal batteries”. In: *Nature* 572.7770 (2019), pp. 511–515. URL: `http://dx.doi.org/10.1038/s41586-019-1481-z`.

[39] J. R. Dahn, J. C. Burns, and D. A. Stevens. “Importance of coulombic efficiency measurements in R & D efforts to obtain long-lived li-ion batteries”. In: *Electrochemical Society Interface* 25.3 (2016), pp. 75–78.

[40] Jingxu Zheng et al. “Chem Soc Rev Regulating electrodeposition morphology of lithium : towards commercially relevant secondary Li metal batteries”. In: (2020).

[41] Abdul Rahman O Raji et al. “Lithium Batteries with Nearly Maximum Metal Storage”. In: *ACS Nano* 11.6 (2017), pp. 6362–6369.

[42] Yong-gun Lee et al. “composite anodes”. In: *Nature Energy* March (2020).

[43] Gilbert N. Lewis and Frederick G. Keyes. “The Potential of the Lithium Electrode”. In: *Journal of the American Chemical Society* 33.9 (1913), pp. 340–344.

[44] J B Bates et al. “Electrical properties of amorphous lithium electrolyte thin films”. In: *Solid State Ionics* 53-56.PART 1 (1992), pp. 647–654.

[45] Charles Monroe and John Newman. “The Impact of Elastic Deformation on Deposition Kinetics at Lithium/Polymer Interfaces”. In: *Journal of The Electrochemical Society* 152.2 (2005), A396.

[46] Jürgen Janek and Wolfgang G. Zeier. “A solid future for battery development”. In: *Nature Energy* 1.9 (Sept. 2016).

[47] Mauro Pasta et al. “2020 roadmap on solid-state batteries”. In: *JPhys Energy* 2.3 (Aug. 2020), p. 032008.

[48] Chunwen Sun et al. “Recent advances in all-solid-state rechargeable lithium batteries”. In: *Nano Energy* 33 (Mar. 2017), pp. 363–386.

[49] Noriaki Kamaya et al. “A lithium superionic conductor”. In: *Nature Materials* 10.9 (2011), pp. 682–686. URL: `http://dx.doi.org/10.1038/nmat3066`.

[50] Wenjia Zhao et al. “Solid-State Electrolytes for Lithium-Ion Batteries: Fundamentals, Challenges and Perspectives”. In: *Electrochemical Energy Reviews* 2.4 (2019), pp. 574–605. URL: `https://doi.org/10.1007/s41918-019-00048-0`.

[51] Edmund J Cussen. “Structure and ionic conductivity in lithium garnets”. In: *Journal of Materials Chemistry* 20.25 (2010), pp. 5167–5173.

[52] O Bohnke, C Bohnke, and J L Fourquet. “Mechanism of ionic conduction and electrochemical intercalation of lithium into the perovskite lanthanum lithium titanate”. In: *Solid State Ionics* 91.1-2 (1996), pp. 21–31.

[53] Yusheng Zhao and Luke L Daemen. “Superionic conductivity in lithium-rich anti-perovskites”. In: *Journal of the American Chemical Society* 134.36 (2012), pp. 15042–15047.

[54] Ohmin Kwon et al. “Synthesis, structure, and conduction mechanism of the lithium superionic conductor Li10+δGe1+δP2-δS12”. In: *Journal of Materials Chemistry A* 3.1 (2015), pp. 438–446.

[55] Kunimitsu Kataoka. “Oxide single crystals with high lithium-ion conductivity as solid electrolytes for all-solid-state lithium secondary battery applications”. In: *Journal of the Ceramic Society of Japan* 128.1 (Jan. 2020), pp. 7–18. URL: https://www.jstage.jst.go.jp/article/jcersj2/128/1/128_19094/_article.

[56] Fudong Han et al. “High electronic conductivity as the origin of lithium dendrite formation within solid electrolytes”. In: *Nature Energy* 4.3 (2019), pp. 187–196. URL: http://dx.doi.org/10.1038/s41560-018-0312-z.

[57] William D Richards et al. “Interface Stability in Solid-State Batteries”. In: *Chemistry of Materials* 28.1 (2016), pp. 266–273.

[58] Arumugam Manthiram, Xingwen Yu, and Shaofei Wang. “Lithium battery chemistries enabled by solid-state electrolytes”. In: *Nature Reviews Materials* 2.4 (2017), pp. 1–16. URL: http://dx.doi.org/10.1038/natrevmats.2016.103.

[59] Linus Froboese et al. “Effect of Microstructure on the Ionic Conductivity of an All Solid-State Battery Electrode”. In: *Journal of The Electrochemical Society* 166.2 (2019), A318–A328.

[60] James A Dawson et al. “Toward Understanding the Different Influences of Grain Boundaries on Ion Transport in Sulfide and Oxide Solid Electrolytes”. In: *Chemistry of Materials* 31.14 (2019), pp. 5296–5304.

[61] Ying Zhao et al. “A review on modeling of electro-chemo-mechanics in lithium-ion batteries”. In: *Journal of Power Sources* 413.October 2018 (2019), pp. 259–283. URL: https://doi.org/10.1016/j.jpowsour.2018.12.011.

[62] Jitti Kasemchainan et al. “Critical stripping current leads to dendrite formation on plating in lithium anode solid electrolyte cells”. In: *Nature Materials* 18.October (2019). URL: http://dx.doi.org/10.1038/s41563-019-0438-9.

[63] Lukas Porz et al. “Mechanism of Lithium Metal Penetration through Inorganic Solid Electrolytes”. In: *Advanced Energy Materials* 1701003.20 (2017), pp. 1–12.

[64] Jeff Wolfenstine et al. “Mechanical behavior of Li-ion-conducting crystalline oxide-based solid electrolytes: a brief review”. In: *Ionics* 24.5 (May 2018), pp. 1271–1276.

[65] Xin Zhang et al. “Rethinking How External Pressure Can Suppress Dendrites in Lithium Metal Batteries”. In: *Journal of The Electrochemical Society* 166.15 (2019), A3639–A3652.

[66] Jürgen Janek and Wolfgang G. Zeier. “Challenges in speeding up solid-state battery development”. In: *Nature Energy* 8.March (2023), pp. 230–240.

[67] Sudarshan Narayanan et al. “In situ and operando characterisation of Li metal – Solid electrolyte interfaces”. In: *Current Opinion in Solid State and Materials Science* 26.2 (2022), p. 100978. URL: https://doi.org/10.1016/j.cossms.2021.100978.

[68] Abhik Banerjee et al. *Interfaces and Interphases in All-Solid-State Batteries with Inorganic Solid Electrolytes*. 2020.

[69] Thorben Krauskopf et al. “The Fast Charge Transfer Kinetics of the Lithium Metal Anode on the Garnet-Type Solid Electrolyte Li6.25Al0.25La3Zr2O12”. In: *Advanced Energy Materials* 10.27 (July 2020), p. 2000945.

[70] William S. LePage et al. “Lithium mechanics: Roles of strain rate and temperature and implications for lithium metal batteries”. In: *Journal of the Electrochemical Society* 166.2 (2019), pp. 89–97.

[71] Yang Lu et al. *Critical Current Density in Solid-State Lithium Metal Batteries: Mechanism, Influences, and Strategies*. 2021.

[72] Jitti Kasemchainan et al. “Critical stripping current leads to dendrite formation on plating in lithium anode solid electrolyte cells”. In: *Nature Materials* 18.10 (Oct. 2019), pp. 1105–1111.

[73] Sebastian Wenzel et al. “Interphase formation on lithium solid electrolytes - An in situ approach to study interfacial reactions by photoelectron spectroscopy”. In: *Solid State Ionics* 278 (2015), pp. 98–105.

[74] Eric Kazyak et al. “Li Penetration in Ceramic Solid Electrolytes: Operando Microscopy Analysis of Morphology, Propagation, and Reversibility”. In: *Matter* 2.4 (2020), pp. 1025–1048.

[75] Ying Zhao et al. “A review on modeling of electro-chemo-mechanics in lithium-ion batteries”. In: *Journal of Power Sources* 413 (Feb. 2019), pp. 259–283.

[76] Jared Tippens et al. “Visualizing Chemomechanical Degradation of a Solid-State Battery Electrolyte”. In: *ACS Energy Letters* 4.6 (2019), pp. 1475–1483.

[77] Fengyu Shen et al. “Effect of Pore Connectivity on Li Dendrite Propagation within LLZO Electrolytes Observed with Synchrotron X-ray Tomography”. In: *ACS Energy Letters* 3.4 (2018), pp. 1056–1061.

[78] Chen Xu et al. “Enhanced strength and temperature dependence of mechanical properties of Li at small scales and its implications for Li metal anodes”. In: *Proceedings of the National Academy of Sciences of the United States of America* 114.1 (2017), pp. 57–61.

[79] Cole D. Fincher et al. “Controlling dendrite propagation in solid-state batteries with engineered stress”. In: *Joule* 6.12 (2022), pp. 2794–2809.

[80] R Schultz. *Lithium: Measurement of Young’s Modulus*. Tech. rep. November. Fermi National Accelerator Laboratory, 2002.

[81] Thorben Krauskopf et al. “Toward a Fundamental Understanding of the Lithium Metal Anode in Solid-State Batteries - An Electrochemo-Mechanical Study on the Garnet-Type Solid Electrolyte Li 6.25 Al 0.25 La 3 Zr 2 O 12”. In: *ACS Applied Materials and Interfaces* 11.15 (2019), pp. 14463–14477.

[82] Cole D. Fincher et al. “Mechanical properties of metallic lithium: from nano to bulk scales”. In: *Acta Materialia* 186 (Mar. 2020), pp. 215–222.

[83] Alvaro Masias et al. “Elastic, plastic, and creep mechanical properties of lithium metal”. In: *Journal of Materials Science* 54.3 (2019), pp. 2585–2600.

[84] Yizhou Zhu, Xingfeng He, and Yifei Mo. “Origin of Outstanding Stability in the Lithium Solid Electrolyte Materials: Insights from Thermodynamic Analyses Based on First-Principles Calculations”. In: *ACS Applied Materials and Interfaces* 7.42 (2015), pp. 23685–23693.

[85] Mei chin Pang et al. *Interactions are important: Linking multi-physics mechanisms to the performance and degradation of solid-state batteries*. Apr. 2021.

[86] Andrew L. Davis et al. “Operando Analysis of Interphase Dynamics in Anode-Free Solid-State Batteries with Sulfide Electrolytes”. In: *Journal of The Electrochemical Society* 168.7 (July 2021), p. 070557.

[87] Sebastian Wenzel et al. “Interphase formation on lithium solid electrolytes - An in situ approach to study interfacial reactions by photoelectron spectroscopy”. In: *Solid State Ionics* 278 (2015), pp. 98–105. URL: http://dx.doi.org/10.1016/j.ssi.2015.06.001.

[88] William D. Richards et al. “Interface Stability in Solid-State Batteries”. In: *Chemistry of Materials* 28.1 (2016), pp. 266–273. URL: http://dx.doi.org/10.1038/s41578-019-0157-5.

[89] Kevin N. Wood et al. “Operando X-ray photoelectron spectroscopy of solid electrolyte interphase formation and evolution in Li2S-P2S5 solid-state electrolytes”. In: *Nature Communications* 9.1 (June 2018), p. 2490. URL: https://www.nature.com/articles/s41467-018-04762-z.

[90] Sudarshan Narayanan et al. “Effect of current density on the Li-Li 6 PS 5 Cl solid electrolyte interphase”. In: (2022), pp. 1–11.

[91] Hongyao Zhou et al. “Protective coatings for lithium metal anodes: Recent progress and future perspectives”. In: *Journal of Power Sources* 450.November 2019 (2020), p. 227632. URL: https://doi.org/10.1016/j.jpowsour.2019.227632.

[92] Jun Pu et al. *Advanced: In situ technology for Li/Na metal anodes: An in-depth mechanistic understanding*. 2021.

[93] Sebastian Wenzel et al. “Interfacial reactivity and interphase growth of argyrodite solid electrolytes at lithium metal electrodes”. In: *Solid State Ionics* 318.February 2017 (2018), pp. 102–112. URL: https://doi.org/10.1016/j.ssi.2017.07.005.

[94] John A. Lewis et al. “The promise of alloy anodes for solid-state batteries”. In: *Joule* 6.7 (2022), pp. 1418–1430. URL: https://doi.org/10.1016/j.joule.2022.05.016.

[95] Song Jin et al. “Solid-Solution-Based Metal Alloy Phase for Highly Reversible Lithium Metal Anode”. In: *Journal of the American Chemical Society* 142.19 (2020), pp. 8818–8826.

[96] Thorben Krauskopf et al. “Diffusion Limitation of Lithium Metal and Li–Mg Alloy Anodes on LLZO Type Solid Electrolytes as a Function of Temperature and Pressure”. In: *Advanced Energy Materials* 9.44 (Nov. 2019).

[97] Xin Zhang et al. “Pressure-Driven Interface Evolution in Solid-State Lithium Metal Batteries”. In: *Cell Reports Physical Science* (2020), p. 100012. URL: https://doi.org/10.1016/j.xcrp.2019.100012.

[98] John A. Lewis et al. “Linking void and interphase evolution to electrochemistry in solid-state batteries using operando X-ray tomography”. In: *Nature Materials* 20.4 (2021), pp. 503–510. URL: http://dx.doi.org/10.1038/s41563-020-00903-2.

[99] Dominic Spencer Jolly et al. “Temperature Dependence of Lithium Anode Voiding in Argyrodite Solid-State Batteries”. In: *ACS Applied Materials and Interfaces* 13.19 (2021), pp. 22708–22716.

[100] Ieuan David Seymour and Ainara Aguadero. “Suppressing void formation in all-solid-state batteries: The role of interfacial adhesion on alkali metal vacancy transport”. In: *Journal of Materials Chemistry A* 9.35 (2021), pp. 19901–19913.

[101] A. Korblein et al. “Diffusion processes in solid Li-Mg and Li-Ag alloys and the spin-lattice relaxation of 8Li”. In: *Journal of Physics F: Metal Physics* 15.3 (1985), pp. 561–577.

[102] Marco Siniscalchi et al. “On the Relative Importance of Li Bulk Diffusivity and Interface Morphology in Determining the Stripped Capacity of Metallic Anodes in Solid-State Batteries”. In: *ACS Energy Letters* (2022), pp. 3593–3599.

[103] Zhong Shi et al. “Electrochemical properties of Li-Mg alloy electrodes for lithium batteries”. In: *Journal of Power Sources* 92.1-2 (2001), pp. 70–80.

[104] J. Trivisonno and Charles S. Smith. “Elastic constants of lithium-magnesium alloys”. In: *Acta Metallurgica* 9.12 (1961), pp. 1064–1071.

[105] Wei Jun Zhang. “A review of the electrochemical performance of alloy anodes for lithium-ion batteries”. In: *Journal of Power Sources* 196.1 (2011), pp. 13–24.

[106] Robert A Huggins. “Lithium alloy negative electrodes”. In: *Journal of Power Sources* 81-82 (1999), pp. 13–19.

[107] J O Besenhard, J Yang, and M Winter. “Will advanced lithium-alloy anodes have a chance in lithium-ion batteries?” In: *Journal of Power Sources* 68.1 (1997), pp. 87–90.

[108] Wei Jun Zhang. “A review of the electrochemical performance of alloy anodes for lithium-ion batteries”. In: *Journal of Power Sources* 196.1 (2011), pp. 13–24. URL: http://dx.doi.org/10.1016/j.jpowsour.2010.07.020.

[109] Ji Heon Ryu et al. “Failure modes of silicon powder negative electrode in lithium secondary batteries”. In: *Electrochemical and Solid-State Letters* 7.10 (2004), pp. 306–309.

[110] M R Wagner et al. “Electrolyte decomposition reactions on tin- And graphite-based anodes are different”. In: *Electrochemical and Solid-State Letters* 7.7 (2004).

[111] L Y Beaulieu et al. “Colossal reversible volume changes in lithium alloys”. In: *Electrochemical and Solid-State Letters* 4.9 (2001), pp. 7–10.

[112] Xiao Hua Liu et al. “Size-dependent fracture of silicon nanoparticles during lithiation”. In: *ACS Nano* 6.2 (2012), pp. 1522–1531.

[113] Maziar Ashuri, Qianran He, and Leon L Shaw. “Silicon as a potential anode material for Li-ion batteries: Where size, geometry and structure matter”. In: *Nanoscale* 8.1 (2016), pp. 74–103.

[114] Md Arafat Rahman et al. “Nanostructured silicon anodes for high-performance lithium-ion batteries”. In: *Advanced Functional Materials* 26.5 (2016), pp. 647–678.

[115] Matea Raić et al. “Nanostructured silicon as potential anode material for Li-ion batteries”. In: *Molecules* 25.4 (2020).

[116] Kai Yan et al. “Selective deposition and stable encapsulation of lithium through heterogeneous seeded growth”. In: *Nature Energy* 1.3 (2016).

[117] Cheol Min Park, Heechul Jung, and Hun Joon Sohn. “Electrochemical behaviors and reaction mechanism of nanosilver with lithium”. In: *Electrochemical and Solid-State Letters* 12.9 (2009).

[118] A. L. Santhosha et al. “The IndiumLithium Electrode in Solid-State Lithium-Ion Batteries: Phase Formation, Redox Potentials, and Interface Stability”. In: *Batteries and Supercaps* 2.6 (2019), pp. 524–529.

[119] Yuhgene Liu et al. “Aluminum foil negative electrodes with multiphase microstructure for all-solid-state Li-ion batteries”. In: *Nature Communications* 14.1 (2023).

[120] Harry C. Nash and Charles S. Smith. “Single-crystal elastic constants of lithium”. In: *Journal of Physics and Chemistry of Solids* 9.2 (1959), pp. 113–118.

[121] T. Slotwinski and J. Trivisonno. “Temperature dependence of the elastic constants of single crystal lithium”. In: *Journal of Physics and Chemistry of Solids* 30.5 (1969), pp. 1276–1278.

[122] R. A Felice, J Trivisonno, and D. E Schuele. “Temperature and pressure dependence of the single-crystal elastic constants of Li and natural lithium”. In: *Physical Review B* 16.12 (1977), pp. 5173–5184.

[123] Chen Xu et al. “Enhanced strength and temperature dependence of mechanical properties of Li at small scales and its implications for Li metal anodes”. In: *Proceedings of the National Academy of Sciences of the United States of America* 114.1 (2017), pp. 57–61.

[124] P W Bridgman. “The Electrical Resistance of Metals under Pressure”. In: *Proceedings of the American Academy of Arts and Sciences* 57.3 (1922), pp. 41–66.

[125] Erik G Herbert, Stephen A Hackney, and Nancy J Dudney. “Nanoindentation of high-purity vapor deposited lithium fi lms : The elastic modulus”. In: (2018), pp. 1335–1346.

[126] W. M. Robertson and D. J. Montgomery. “Elastic modulus of isotopically-concentrated lithium”. In: *Physical Review* 117.2 (1960), pp. 440–442.

[127] S Tariq et al. “Li Material Testing - Fermilab Antiproton Source Lithium Collection Lens”. In: *Proceedings of the 2003 Particle Accelerator Conference.* 2003, pp. 1452–1454.

[128] Masayuki Kamaya. "A procedure for estimating Young's modulus of textured polycrystalline materials". In: *International Journal of Solids and Structures* 46.13 (2009), pp. 2642–2649. URL: http://dx.doi.org/10.1016/j.ijsolstr.2009.02.013.

[129] D. Hull and H. M. Rosenberg. "The deformation of lithium, sodium and potassium at low temperatures: Tensile and resistivity experiments". In: *Philosophical Magazine* 4.39 (1959), pp. 303–315.

[130] Jungwoo Z Lee et al. "Cryogenic Focused Ion Beam Characterization of Lithium Metal Anodes". In: *ACS Energy Letters* 4.2 (2019), pp. 489–493.

[131] B. R.S. Rogne and C. Thaulow. "Strengthening mechanisms of iron micropillars". In: *Philosophical Magazine* 95.16-18 (2015), pp. 1814–1828.

[132] E Peled and S Menkin. "Review - SEI: Past, present and future". In: *Journal of the Electrochemical Society* 164.7 (2017), A1703–A1719.

[133] Wanli Xu, Sri S Vegunta, and J C Flake. "Modified Solid Electrolyte Interphase of Silicon Nanowire Anodes for Lithium-Ion Batteries". In: (2011), pp. 55–61.

[134] Jie Zhang et al. "Direct observation of inhomogeneous solid electrolyte interphase on MnO anode with atomic force microscopy and spectroscopy". In: *Nano Letters* 12.4 (2012), pp. 2153–2157.

[135] Hosop Shin et al. "Component-/structure-dependent elasticity of solid electrolyte interphase layer in Li-ion batteries: Experimental and computational studies". In: *Journal of Power Sources* 277 (2015), pp. 169–179. URL: http://dx.doi.org/10.1016/j.jpowsour.2014.11.120.

[136] Sang Pil Kim, Adri C.T.Van Duin, and Vivek B Shenoy. "Effect of electrolytes on the structure and evolution of the solid electrolyte interphase (SEI) in Li-ion batteries: A molecular dynamics study". In: *Journal of Power Sources* 196.20 (2011), pp. 8590–8597. URL: http://dx.doi.org/10.1016/j.jpowsour.2011.05.061.

[137] Shun Li Shang et al. "Lattice dynamics, thermodynamics and elastic properties of monoclinic Li 2CO 3 from density functional theory". In: *Acta Materialia* 60.13-14 (2012), pp. 5204–5216. URL: http://dx.doi.org/10.1016/j.actamat.2012.06.006.

[138] Kada Bidai et al. "First principle study of mechanical stability and thermodynamic properties of anti-fluorite Li2O and Rb2O under pressure and temperature effect". In: *Chinese Journal of Physics* 54.5 (2016), pp. 678–694. URL: http://dx.doi.org/10.1016/j.cjph.2016.08.010.

[139] Ziyang Ning et al. "Dendrite initiation and propagation in lithium metal solid-state batteries". In: *Nature* 618.7964 (June 2023), pp. 287–293. URL: https://doi.org/10.1038/s41586-023-05970-4%20https://www.nature.com/articles/s41586-023-05970-4.

[140] Kaihui Nie et al. "Interfaces Between Cathode and Electrolyte in Solid State Lithium Batteries: Challenges and Perspectives". In: *Frontiers in Chemistry* 6 (Dec. 2018), pp. 1–19.

[141] E. Peled and S. Menkin. "Review - SEI: Past, present and future". In: *Journal of the Electrochemical Society* 164.7 (2017), pp. 1703–1719.

[142] Jeff Wolfenstine et al. “Mechanical behavior of Li-ion-conducting crystalline oxide-based solid electrolytes: a brief review”. In: *Ionics* (2017), pp. 1–6.

[143] Peng Shi et al. “A Review of Composite Lithium Metal Anode for Practical Applications”. In: 1900806 (2019), pp. 1–15.

[144] Hee Dae Lim et al. *A review of challenges and issues concerning interfaces for all-solid-state batteries*. 2020.

[145] Angus J. Wilkinson and T. Ben Britton. “Strains, planes, and EBSD in materials science”. In: *Materials Today* 15.9 (2012), pp. 366–376. URL: http://dx.doi.org/10.1016/S1369-7021(12)70163-3.

[146] T. B. Britton et al. “Tutorial: Crystal orientations and EBSD - Or which way is up?” In: *Materials Characterization* 117 (2016), pp. 113–126. URL: http://dx.doi.org/10.1016/j.matchar.2016.04.008.

[147] W.C. Oliver and G.M. Pharr. “An improved technique for determining hardness and elastic modulus using load and displacement sensing indentation experiments”. In: *Journal of Materials Research* 7.6 (1992), pp. 1564–1583.

[148] Benoit Merle, Wesley H. Higgins, and George M. Pharr. “Critical issues in conducting constant strain rate nanoindentation tests at higher strain rates”. In: *Journal of Materials Research* i (2019).

[149] P. Sudharshan Phani, W. C. Oliver, and G. M. Pharr. “Understanding and modeling plasticity error during nanoindentation with continuous stiffness measurement”. In: *Materials and Design* 194 (2020), p. 108923. URL: https://doi.org/10.1016/j.matdes.2020.108923.

[150] Alexandros Ch Lazanas and Mamas I. Prodromidis. “Electrochemical Impedance SpectroscopyA Tutorial”. In: *ACS Measurement Science Au* (2022).

[151] Shangshang Wang et al. “Electrochemical impedance spectroscopy”. In: *Nature Reviews Methods Primers* 1.1 (2021).

[152] Christofer Sångeland et al. “Probing the interfacial chemistry of solid-state lithium batteries”. In: *Solid State Ionics* 343.September (2019), p. 115068. URL: https://doi.org/10.1016/j.ssi.2019.115068.

[153] Neal Fairley et al. “Systematic and collaborative approach to problem solving using X-ray photoelectron spectroscopy”. In: *Applied Surface Science Advances* 5 (2021), p. 100112. URL: https://doi.org/10.1016/j.apsadv.2021.100112.

[154] Kiyoshi Kanamura et al. “X-Ray Photoelectron Spectroscopic Analysis and Scanning Electron Microscopic Observation of the Lithium Surface Immersed in Nonaqueous Solvents”. In: *Journal of The Electrochemical Society* 141.9 (1994), pp. 2379–2385.

[155] Joshua S. Gibson et al. “Gently does it!: in situ preparation of alkali metal-solid electrolyte interfaces for photoelectron spectroscopy”. In: *Faraday Discussions* 236 (2022), pp. 267–287.

[156] Jack Aspinall, David E.J. Armstrong, and Mauro Pasta. “EBSD coupled indentation: Nanoscale mechanics of lithium metal”. In: *Materials Today Energy* 110 (Oct. 2022), p. 101183. URL: https://doi.org/10.1016/j.tet.2021.131932%20https://linkinghub.elsevier.com/retrieve/pii/S2468606922002416.

[157] Nicolas Brodusch, Karim Zaghib, and Raynald Gauvin. "Electron backscatter diffraction applied to lithium sheets prepared by broad ion beam milling". In: *Microscopy Research and Technique* 78.1 (2015), pp. 30–39.

[158] S. Shim et al. "Effects of focused ion beam milling on the compressive behavior of directionally solidified micropillars and the nanoindentation response of an electropolished surface". In: *Acta Materialia* 57.2 (2009), pp. 503–510. URL: http://dx.doi.org/10.1016/j.actamat.2008.09.033.

[159] James F. Ziegler, M. D. Ziegler, and J. P. Biersack. "SRIM - The stopping and range of ions in matter (2010)". In: *Nuclear Instruments and Methods in Physics Research, Section B: Beam Interactions with Materials and Atoms* 268.11-12 (2010), pp. 1818–1823. URL: http://dx.doi.org/10.1016/j.nimb.2010.02.091.

[160] H. Azza et al. "Thermodynamic Reassessment of the Gallium–Lithium Phase Diagram". In: *Journal of Phase Equilibria and Diffusion* 38.5 (2017), pp. 788–795.

[161] A. J. Gallagher et al. "Dynamic tensile properties of human skin". In: *2012 IRCOBI Conference Proceedings - International Research Council on the Biomechanics of Injury* (2012), pp. 494–502.

[162] J. Xu et al. "Atomic force microscopy and nanoindentation characterization of human lamellar bone prepared by microtome sectioning and mechanical polishing technique". In: *Journal of Biomedical Materials Research - Part A* 67.3 (2003), pp. 719–726.

[163] Dominique Drouin et al. "CASINO V2.42 - A fast and easy-to-use modeling tool for scanning electron microscopy and microanalysis users". In: *Scanning* 29.3 (2007), pp. 92–101.

[164] Andrew Deal, Tejpal Hooghan, and Alwyn Eades. "Energy-filtered electron backscatter diffraction". In: *Ultramicroscopy* 108.2 (2008), pp. 116–125.

[165] S. X. Ren et al. "Exploring spatial resolution in electron back-scattered diffraction experiments via Monte Carlo simulation". In: *Microscopy and Microanalysis* 4.1 (1998), pp. 15–22.

[166] Abhishek Bhattacharyya and John A. Eades. "Use of an energy filter to improve the spatial resolution of electron backscatter diffraction". In: *Scanning* 31.3 (2009), pp. 114–121.

[167] Faming Gao. "Hardness of cubic solid solutions". In: *Scientific Reports* 7.August 2016 (2017), pp. 1–6. URL: http://dx.doi.org/10.1038/srep40276.

[168] Joost J. Vlassak and W.D. Nix. "Measuring the Elastic Properties of Materials By Means of Indentation". In: *J. Mech. Phys. Solids* 42.8 (1994), pp. 1223–1245.

[169] Joost J. Vlassak and W. D. Nix. "Indentation modulus of elastically anisotropic half spaces". In: *Philosophical Magazine A: Physics of Condensed Matter, Structure, Defects and Mechanical Properties* 67.5 (1993), pp. 1045–1056.

[170] D. M. Barnett and J. Lothe. "Dislocations and line charges in anisotropic piezoelectric insulators". In: *Physica Status Solidi (B)* 67.1 (1975), pp. 105–111.

[171] Antoine Delafargue and Franz Josef Ulm. "Explicit approximations of the indentation modulus of elastically orthotropic solids for conical indenters". In: *International Journal of Solids and Structures* 41.26 (2004), pp. 7351–7360.

[172] Jeffrey C. Lagarias et al. “Convergence properties of the Nelder-Mead simplex method in low dimensions”. In: *SIAM Journal on Optimization* 9.1 (1998), pp. 112–147.

[173] Feifei Shi et al. “Strong texturing of lithium metal in batteries”. In: *Proceedings of the National Academy of Sciences of the United States of America* 114.46 (2017), pp. 12138–12143.

[174] William D. Nix and Huajian Gao. “Indentation size effects in crystalline materials: A law for strain gradient plasticity”. In: *Journal of the Mechanics and Physics of Solids* 46.3 (1998), pp. 411–425.

[175] George M. Pharr, Erik G. Herbert, and Yanfei Gao. “The indentation size effect: A critical examination of experimental observations and mechanistic interpretations”. In: *Annual Review of Materials Research* 40 (2010), pp. 271–292.

[176] Gerolf Ziegenhain, Herbert M. Urbassek, and Alexander Hartmaier. “Influence of crystal anisotropy on elastic deformation and onset of plasticity in nanoindentation: A simulational study”. In: *Journal of Applied Physics* 107.6 (2010).

[177] Yan Jin et al. “Challenges and recent progress in the development of Si anodes for lithium-ion battery”. In: *Advanced Energy Materials* 7.23 (2017), pp. 1–17.

[178] Yijie Jiang, David S. Grierson, and Kevin T. Turner. “Flat punch adhesion: Transition from fracture-based to strength-limited pull-off”. In: *Journal of Physics D: Applied Physics* 47.32 (2014).

[179] Jeremy T. Busby, Mark C. Hash, and Gary S. Was. “The relationship between hardness and yield stress in irradiated austenitic and ferritic steels”. In: *Journal of Nuclear Materials* 336.2-3 (2005), pp. 267–278.

[180] I. N. Sneddon and H. A. Elliot. “The opening of a Griffith crack under internal pressure”. In: *Quarterly of Applied Mathematics* 4.3 (1946), pp. 262–267.

[181] Makoto Sakamoto. “An Elastic Layer with a Penny-Shaped Crack Subjected to Internal Pressure.” In: *JSME International Journal Series A* 46.1 (2003), pp. 10–14. URL: http://www.jstage.jst.go.jp/article/jsmea/46/1/46_1_10/_article.

[182] Spencer D. Jackman and Raymond A. Cutler. “Effect of microcracking on ionic conductivity in LATP”. In: *Journal of Power Sources* 218 (2012), pp. 65–72. URL: http://dx.doi.org/10.1016/j.jpowsour.2012.06.081.

[183] Sergiy Kalnaus et al. “Resistance to fracture in the glassy solid electrolyte Lipon”. In: *Journal of Materials Research* 36.4 (2021), pp. 787–796.

[184] Juliane Franciele Nonemacher et al. “Micromechanical assessment of Al/Y-substituted NASICON solid electrolytes”. In: *Ceramics International* 45.17 (2019), pp. 21308–21314.

[185] Shuai Hao et al. “Tracking lithium penetration in solid electrolytes in 3D by in-situ synchrotron X-ray computed tomography”. In: *Nano Energy* 82.October 2020 (2021), p. 105744. URL: https://doi.org/10.1016/j.nanoen.2021.105744.

[186] Ziyang Ning et al. “Visualizing plating-induced cracking in lithium-anode solid-electrolyte cells”. In: *Nature Materials* 20.8 (2021), pp. 1121–1129. URL: http://dx.doi.org/10.1038/s41563-021-00967-8.

[187] Lukas Porz et al. “Mechanism of Lithium Metal Penetration through Inorganic Solid Electrolytes”. In: *Advanced Energy Materials* 7.20 (Oct. 2017).

[188] Kyle S Nagy et al. “Thermodynamic Overpotentials and Nucleation Rates for Electrodeposition on Metal Anodes”. In: *ACS Applied Materials and Interfaces* 11.8 (2019), pp. 7954–7964.

[189] Adrian J Sanchez et al. “Lithium stripping: anisotropic evolution and faceting of pits revealed byoperando3-D microscopy”. In: *Journal of Materials Chemistry A* 9.37 (2021), pp. 21013–21023.

[190] Jens Becking et al. “Lithium-Metal Foil Surface Modification: An Effective Method to Improve the Cycling Performance of Lithium-Metal Batteries”. In: *Advanced Materials Interfaces* 4.16 (2017), pp. 1–9.

[191] Geoff McConohy et al. “Mechanical regulation of lithium intrusion probability in garnet solid electrolytes”. In: *Nature Energy* (2023). URL: https://doi.org/10.1038/s41560-022-01186-4.

[192] Soochan Kim et al. “Thin Solid Electrolyte Separators for Solid-State Lithium-Sulfur Batteries”. In: *Nano Letters* 22.24 (2022), pp. 10176–10183.

[193] Ju Sik Kim et al. “Surface engineering of inorganic solid-state electrolytes via interlayers strategy for developing long-cycling quasi-all-solid-state lithium batteries”. In: *Nature Communications* 14.1 (2023).

[194] Jack Aspinall et al. “Lithium magnesium alloys : a framework for investigating lithium alloy anodes for solid state batteries”. 2023.

[195] Yuming Chen et al. “Li metal deposition and stripping in a solid-state battery via Coble creep”. In: *Nature* 578.7794 (Feb. 2020), pp. 251–255.

[196] Richard H. Taylor, Stefano Curtarolo, and Gus L.W. Hart. “Ordered magnesium-lithium alloys: First-principles predictions”. In: *Physical Review B - Condensed Matter and Materials Physics* 81.2 (2010), pp. 1–8.

[197] Taylor W. Cain and Joseph P. Labukas. “The development of β phase Mg–Li alloys for ultralight corrosion resistant applications”. In: *npj Materials Degradation* 4.1 (2020). URL: http://dx.doi.org/10.1038/s41529-020-0121-2.

[198] S. Graça et al. “Determination of dislocation density from hardness measurements in metals”. In: *Materials Letters* 62.23 (2008), pp. 3812–3814.

[199] Ling Long Kong et al. “Lithium–Magnesium Alloy as a Stable Anode for Lithium–Sulfur Battery”. In: *Advanced Functional Materials* 29.13 (2019).

[200] Congrui Jin and Donna M. Ebenstein. “Nanoindentation of compliant materials using Berkovich tips and flat tips”. In: *Journal of Materials Research* 32.2 (2017), pp. 435–450.

[201] Jean-marie Doux et al. “Stack Pressure Considerations for Room Temperature All- Solid-State Lithium Metal Batteries”. In: (2019), pp. 0–20.

[202] P M Sargent and M F Ashby. “Deformation mechanism maps for alkali metals”. In: *Scripta Metallurgica* 18.2 (1984), pp. 145–150.

[203] Alvaro Masias et al. “Elastic, plastic, and creep mechanical properties of lithium metal”. In: *Journal of Materials Science* 54.3 (2019), pp. 2585–2600. URL: https://doi.org/10.1007/s10853-018-2971-3.

[204] William S LePage et al. “Lithium mechanics: Roles of strain rate and temperature and implications for lithium metal batteries”. In: *Journal of the Electrochemical Society* 166.2 (2019), A89–A97.

[205] Verena Maier et al. “An improved long-term nanoindentation creep testing approach for studying the local deformation processes in nanocrystalline metals at room and elevated temperatures”. In: *Journal of Materials Research* 28.9 (2013), pp. 1177–1188.

[206] Verena Maier et al. “Thermally Activated Deformation Behavior of ufg-Au: Environmental Issues During Long-Term and High-Temperature Nanoindentation Testing”. In: *JOM* 67.12 (Dec. 2015), pp. 2934–2944. URL: http://link.springer.com/10.1007/s11837-015-1638-7.

[207] Olena Prach et al. “A new nanoindentation creep technique using constant contact pressure”. In: *Journal of Materials Research* 34.14 (2019), pp. 2492–2500.

[208] X. D. Hou and N. M. Jennett. “Defining the limits to long-term nano-indentation creep measurement of viscoelastic materials”. In: *Polymer Testing* 70.July (2018), pp. 297–309. URL: https://doi.org/10.1016/j.polymertesting.2018.07.022.

[209] J. Dean et al. “A procedure for extracting primary and secondary creep parameters from nanoindentation data”. In: *Mechanics of Materials* 65 (2013), pp. 124–134. URL: http://dx.doi.org/10.1016/j.mechmat.2013.05.014.

[210] Caijun Su et al. “Measurement of power-law creep parameters by instrumented indentation methods”. In: *Journal of the Mechanics and Physics of Solids* 61.2 (2013), pp. 517–536.

[211] A. F. Bower et al. “Indentation of a power law creeping solid”. In: *Proceedings - Royal Society of London, A* 441.1911 (1993), pp. 97–124.

[212] R. Goodall and T. W. Clyne. “A critical appraisal of the extraction of creep parameters from nanoindentation data obtained at room temperature”. In: *Acta Materialia* 54.20 (2006), pp. 5489–5499.

[213] Peter M. Attia, William C. Chueh, and Stephen J. Harris. “ Revisiting the t 0.5 Dependence of SEI Growth ”. In: *Journal of The Electrochemical Society* 167.9 (2020), p. 090535.

[214] John Newman and Karen E Thomas-Alyea. *Electrochemical Systems*. 3rd ed. 2001, p. 700.

[215] Svenja K. Otto et al. “In-Depth Characterization of Lithium-Metal Surfaces with XPS and ToF-SIMS: Toward Better Understanding of the Passivation Layer”. In: *Chemistry of Materials* 33.3 (2021), pp. 859–867.

[216] Michael Salama et al. “Metal-Sulfur Batteries: Overview and Research Methods”. In: *ACS Energy Letters* 4.2 (2019), pp. 436–446.

[217] J. Lahtinen et al. “Studies of Mg-O overlayers on Co(0001): growth mode and CO chemisorption properties”. In: *Surface Science* 245.3 (1991), pp. 244–254.

[218] B. P. Vinayan et al. "Performance study of magnesium-sulfur battery using a graphene based sulfur composite cathode electrode and a non-nucleophilic Mg electrolyte". In: *Nanoscale* 8.6 (2016), pp. 3296–3306.

[219] Tammo K. Schwietert et al. "Clarifying the relationship between redox activity and electrochemical stability in solid electrolytes". In: *Nature Materials* 19.4 (2020), pp. 428–435. URL: http://dx.doi.org/10.1038/s41563-019-0576-0.

[220] Ronja Haas and Jürgen Janek. "The Influence of Oxygen Dissolved in the Liquid Electrolyte on Lithium Metal Anodes". In: *Journal of The Electrochemical Society* 169.11 (2022), p. 110527.

[221] Kee Sung Han et al. "Pulsed Field Gradient Nuclear Magnetic Resonance and Diffusion Analysis in Battery Research". In: *Chemistry of Materials* 33.22 (2021), pp. 8562–8590.

[222] J. M. Titman and B. M. Moores. "Nuclear spin relaxation and translational diffusion in dilute alloys of lithium". In: *Journal of Physics F: Metal Physics* 2.3 (May 1972), pp. 592–604. URL: https://iopscience.iop.org/article/10.1088/0305-4608/2/3/026.

[223] J. Cederberg et al. "Nuclear electric quadrupole moment of 6Li". In: *Physical Review A* 57.4 (Apr. 1998), pp. 2539–2543. URL: https://link.aps.org/doi/10.1103/PhysRevA.57.2539.

[224] A. Lodding, J. N. Mundy, and A. Ott. "Isotope Inter-Diffusion and Self-Diffusion in Solid Lithium Metal". In: *physica status solidi (b)* 38.2 (Jan. 1970), pp. 559–569. URL: http://doi.wiley.com/10.1002/pssb.19700380206.

[225] D. G. Hughes. "Nuclear magnetic resonance in lithium and dilute lithium-Magnesium alloys". In: *Philosophical Magazine* 5.53 (May 1960), pp. 467–471. URL: http://www.tandfonline.com/doi/abs/10.1080/14786436008238298.

[226] Y Iwadate et al. "Electrochemical study of mass transfer in Li-Mg and Li-Mg-Al alloys". In: *Journal of Applied Electrochemistry* 17.2 (Mar. 1987), pp. 385–397. URL: http://link.springer.com/10.1007/BF01023304.

[227] Thorben Krauskopf et al. "Lithium-Metal Growth Kinetics on LLZO Garnet-Type Solid Electrolytes". In: *Joule* 3.8 (2019), pp. 2030–2049.

[228] Xiangchun Zhang, Wei Shyy, and Ann Marie Sastry. "Numerical simulation of intercalation-induced stress in Li-Ion battery electrode Particles". In: *Journal of the Electrochemical Society* 154.10 (2007).

[229] Xin Zhang et al. "Pressure-Driven Interface Evolution in Solid-State Lithium Metal Batteries". In: *Cell Reports Physical Science* (2020), p. 100012. URL: https://doi.org/10.1016/j.xcrp.2019.100012.

[230] L D Firth, N H A Nowaira, and W Scott. "Lattice parameters of lithium-magnesium and lithium-silver alloys". In: *Journal of Physics F: Metal Physics* 4.September (1974), pp. 9–11.

[231] Isaac Capone et al. "Electrochemo-Mechanical Properties of Red Phosphorus Anodes in Lithium, Sodium, and Potassium Ion Batteries". In: *Matter* 3.6 (2020), pp. 2012–2028.

[232] Sang Yun Han et al. "Porous Metals from Chemical Dealloying for Solid-State Battery Anodes". In: *Chemistry of Materials* 32.6 (2020), pp. 2461–2469.

[233] Weitao Jing et al. "Li-Indium alloy anode for high-performance Li-metal batteries". In: *Journal of Alloys and Compounds* 924 (2022), p. 166517. URL: https://doi.org/10.1016/j.jallcom.2022.166517.

[234] Shuting Luo et al. "Growth of lithium-indium dendrites in all-solid-state lithium-based batteries with sulfide electrolytes". In: *Nature Communications* 12.1 (Nov. 2021), p. 6968. URL: https://www.nature.com/articles/s41467-021-27311-7.

[235] Fereshteh Mallakpour et al. "Length-scale-dependent stress relief mechanisms in indium at high homologous temperatures". In: *Journal of Materials Research* 36.12 (2021), pp. 2444–2455. URL: https://doi.org/10.1557/s43578-021-00186-6.

[236] B. N. Lucas and W. C. Oliver. "Indentation power-law creep of high-purity indium". In: *Metallurgical and Materials Transactions A* 30.3 (1999), pp. 601–610.

[237] J. C. Tarczon et al. "Vacancy-antistructure defect interaction diffusion in β-LiAl and β-LiIn". In: *Materials Science and Engineering A* 101.C (May 1988), pp. 99–108. URL: https://linkinghub.elsevier.com/retrieve/pii/092150938890055X.

[238] Jiale Qu et al. "High Rate Transfer Mechanism of Lithium Ions in Lithium-Tin and Lithium-Indium Alloys for Lithium Batteries". In: *Journal of Physical Chemistry C* 124.45 (2020), pp. 24644–24652.

[239] Georg F. Dewald et al. "Experimental assessment of the practical oxidative stability of lithium thiophosphate solid electrolytes". In: *Chemistry of Materials* 31.20 (2019), pp. 8328–8337.

[240] Qing Zhang et al. "Sulfide-Based Solid-State Electrolytes: Synthesis, Stability, and Potential for All-Solid-State Batteries". In: *Advanced Materials* 31.44 (2019), pp. 1–42.